# Novel compounds from chemistry to druggable candidates

**Edited by**
Peter Rose, Yi Zhun Zhu and Jawad Nasim

## About Frontiers

Frontiers is more than just an open access publisher of scholarly articles: it is a pioneering approach to the world of academia, radically improving the way scholarly research is managed. The grand vision of Frontiers is a world where all people have an equal opportunity to seek, share and generate knowledge. Frontiers provides immediate and permanent online open access to all its publications, but this alone is not enough to realize our grand goals.

## Frontiers journal series

The Frontiers journal series is a multi-tier and interdisciplinary set of open-access, online journals, promising a paradigm shift from the current review, selection and dissemination processes in academic publishing. All Frontiers journals are driven by researchers for researchers; therefore, they constitute a service to the scholarly community. At the same time, the *Frontiers journal series* operates on a revolutionary invention, the tiered publishing system, initially addressing specific communities of scholars, and gradually climbing up to broader public understanding, thus serving the interests of the lay society, too.

## Dedication to quality

Each Frontiers article is a landmark of the highest quality, thanks to genuinely collaborative interactions between authors and review editors, who include some of the world's best academicians. Research must be certified by peers before entering a stream of knowledge that may eventually reach the public – and shape society; therefore, Frontiers only applies the most rigorous and unbiased reviews. Frontiers revolutionizes research publishing by freely delivering the most outstanding research, evaluated with no bias from both the academic and social point of view. By applying the most advanced information technologies, Frontiers is catapulting scholarly publishing into a new generation.

## What are Frontiers Research Topics?

Frontiers Research Topics are very popular trademarks of the *Frontiers journals series*: they are collections of at least ten articles, all centered on a particular subject. With their unique mix of varied contributions from Original Research to Review Articles, Frontiers Research Topics unify the most influential researchers, the latest key findings and historical advances in a hot research area.

Find out more on how to host your own Frontiers Research Topic or contribute to one as an author by contacting the Frontiers editorial office: frontiersin.org/about/contact

# Novel compounds from chemistry to druggable candidates

**Topic editors**

Peter Rose — University of Nottingham, United Kingdom
Yi Zhun Zhu — Macau University of Science and Technology, SAR China
Jawad Nasim — Saarland University, Germany

# Table of contents

# Editorial: Novel compounds from chemistry to druggable candidates

Pete Rose[1]*, Jawad Nasim[2] and Yi-Zhun Zhu[3]*

[1]School of Bioscience, University of Nottingham, Nottingham, United Kingdom, [2]School of Pharmacy, Saarland University, Saarbrücken, Saarland, Germany, [3]School of Pharmacy, University of Macau, Taipa, Macau Region, China

Editorial on the Research Topic
Novel compounds from chemistry to druggable candidates

For decades natural product and novel compound research has been at the for front of drug discovery and has produced a spectrum of therapeutics that underpin modern day treatment regimes. Molecules of natural origin are often low molecular weight compounds, playing important biological functions in their host species, but once isolated or modified have value in drug discovery programmes. Other novel species that are inspired by nature have equal value in drug discovery streams especially given recent shifts towards computational chemistry and newer, greener routes of chemical synthesis. Advances in analytical chemistry applications has driven efficient molecular characterisation and isolation platforms, that when combined with genomic and biotechnological systems circumvents many of the barriers that hindered drug discovery approaches in previous decades. These developments are creating new opportunities in drug discovery research and importantly are allowing for the characterisation and isolation of novel molecules from a spectrum of differing organismal sources or synthetic libraries. The current topics "*Novel Compounds from Chemistry to Druggable Candidates*"discusses some of the recent work of colleagues in drug discovery research that are designed to identify or develop novel therapeutics. Several research articles are presented in the current topics, with additional reviews that cover antiviral compounds, marine derived sesquiterpenes, plant phytochemicals, computational chemistry and use in drug development and screening. Hopefully, the current topic issue and associated articles will facilitate interest in researchers to instigate additional drug discovery research programmes with the aim of developing future therapeutics.

In the current edition several research have contributed their valuable work that describes some of fascinating work being conducted around the world on natural products, novel compounds and drug discovery. In the review by Guo et al. the authors summarize the progress of natural products research in supporting the identification of novel antiviral agents that overcome some of the limitation and drug resistance seen over the last 2 decades. This article describes the effects of different structural types of natural products on antiviral activity thereby providing a foundation for the development of novel antiviral drugs in the future. Points of interest are descriptions of recently discovered alkaloids like isatigotindolediosides in root extracts of *Isatis indigotica*, and diterpenoids forsyqinlingine isolated from *Forsythia suspensa*, with promising antiviral properties. Also described are other molecules isolated from natural sources including examples of quinones, flavonoids and polysaccharides. In the review of Li et al. a comprehensive

overview of the compound is leonurine, a molecule isolated and characterized in the tissues of *Herb leonuri* is provided. In recent years, scientists have assessed the bioactive properties of this compound that describe potent antioxidant, anti-apoptotic, and anti-inflammatory properties. Therein, are described efficient synthetic routes and isolation procedures and more recent efforts to make structural modifications of leonurine to enhance its pharmacological properties. Another fascinating field of research is in the characterisation and assessment of animal derived compounds for use in pharmacological research. Ye et al. shifts the narrative towards traditional Chinese medicines and the exploration of toad venom-derived agents (TVAs) for use in cancer research. Ye et al. reports on the various bioactivities of amphibian derived compounds and provides an overview of bufadienolides, the major bioactive components in TVAs. Descriptions of the molecular mechanisms of action provides coverage of a range of cellular targets spanning descriptions of their impacts on Na$^+$/K$^+$-ATPase and voltage-gated potassium channels, through to impacts on apoptotic and cell cycle pathways. In the review by Cai et al. the authors summarized recent updates in click and computational chemistry for drug discovery. Key aspects covered include development of clicking to effectively synthesize druggable candidates, synthesis and modification of natural products, targeted delivery systems, and computer-aided drug discovery for target identification, seeking out and optimizing lead compounds, and ADMET prediction. These approaches are now becoming more common place in novel compound research and with aid in optimising drug discovery streams using computational strategies. In the final review paper by Halma et al. the narrative provides an overview of novel opportunities in the development and identification of novel compounds for the inhibition of SARS-CoV-1 and SARS-CoV-2 helicases. While many studies have focused on the SARS-CoV-2 spike protein interest is also shifting to the development of replication inhibitors like, for example, the SARS-CoV-2 helicase (nsp13). This helicase shares 99.8% similarity with its SARS-CoV-1 homolog and was shown to be essential for viral replication. Halma et al. described computational studies and identified molecules that show potency to this target. These studies potentially being of interest in the anti-viral research field.

In addition to the review articles the primary research articles highlight a breadth of research in novel compound drug discovery. These articles turn attention towards the characterisation and testing of novel compounds using various chemical routes. Zhang et al. describes a genomic mining strategy to confirm the presence of genes involved in Acorane-type sesquiterpenes biosynthesis in a deep-sea derived *Penicillium bilaiae* F-28 fungus. Subsequently, 20 acorane sesquiterpenes were characterised following the large-scale fermented of fungal isolates. Importantly, of the identified molecules, 18 sesquiterpenes, namely, bilaiaeacorenols A–R were new to science. Following pharmacological assessment in an anti-inflammatory model, compound **18** exhibited the capacity to reduce NO production in LPS-induced BV-2 macrophages. These properties were dose-dependent and appeared to correlate with the capacity to inhibit LPS-induced NF-κB activation. In the article by Gao et al. the narrative shifts towards modification of the plant derived anti-malarial, artemisinin. The labile lactone structure of artemisinin is responsible for the instability of this

molecule. Using strategies involving biotransformation, stains of *Cunninghamella echinulata* CGMCC 3.4879 and *Cunninghamella elegans* CGMCC 3.4832, were used to transform 10-deoxyartemisinin, a chemically modified form of artemisinin, to several novel metabolites. These products were separated and identified and tested for antimalarial activity against *Plasmodium falciparum* 3D7. This paper highlighting the novel approaches in which chemical synthesis is coupled to use of biotransformation platforms to generate novel metabolites for use in screening systems. Other articles cover refined analytical methods, computation and other *in silico* technologies to assist in drug discovery. Yu et al. focuses on plant derived compounds with a study describing the development of an UPLC-MS/MS quantification method to study the preclinical pharmacokinetics of *N*-demethylsinomenine, a potential novel analgesic candidate. Niazi et al. contributes a description of a combined synthetic chemistry and computational docking method and molecular dynamics (MD) simulation to identify small molecular modulators capable of targeting Mdm2 and Pirh2, two critical regulators of the tumour suppressor protein p53. Following screen, two synthetic lead compound MMs02943764, and MMs03738126 were found to have significant anti-proliferative effects across a range of cancer cell lines. These findings correlating with the capacity of the compounds to modulate p53 inhibitor complexes, as explored using computational platforms. Molecules were found to promote cell cycle arrest at the SubG0/G1, S, and G2 phases. This study, highlighting how multidisciplinary strategies can underpin the characterisation of novel chemicals for cancer therapy.

To summarize, this topic covers the frontiers of novel compounds in drug discovery and development. Many of the included studies raise the need for multi-disciplinary approaches that combine both synthetic or traditional 'wet chemistry approaches' coupled with computational or other *in silico* systems. Furthermore, these approaches are complemented by the use of robust validated biological molecules to determine compound efficacy. With the ever-rapid development of newer computation approaches, green synthetic routes, and breadth of biological screening assays, it is clear the new therapeutics will emerge in coming years using these systems.

## Author contributions

PR: Writing–original draft, Writing–review and editing. JS: Writing–original draft, Writing–review and editing. YZ: Writing–original draft, Writing–review and editing.

## Funding

## Conflict of interest

The authors declare that the research was conducted in the absence of any commercial or financial relationships that could be construed as a potential conflict of interest.

## Publisher's note

All claims expressed in this article are solely those of the authors and do not necessarily represent those of their affiliated organizations, or those of the publisher, the editors and the reviewers. Any product that may be evaluated in this article, or claim that may be made by its manufacturer, is not guaranteed or endorsed by the publisher.

# Research progress on the antiviral activities of natural products and their derivatives: Structure–activity relationships

Yajing Guo[1], Anna Ma[1], Xinyan Wang[1], Chen Yang[1], Xi Chen[2]*, Gen Li[1]* and Feng Qiu[1,3]

[1]School of Chinese Materia Medica, Tianjin University of Traditional Chinese Medicine, Tianjin, China, [2]School of Pharmaceutical Engineering of Traditional Chinese Medicine, Tianjin University of Traditional Chinese Medicine, Tianjin, China, [3]Tianjfin State Key Laboratory of Modern Chinese Medicine, Tianjin University of Traditional Chinese Medicine, Tianjin, China

Viruses spread rapidly and are well-adapted to changing environmental events. They can infect the human body readily and trigger fatal diseases. A limited number of drugs are available for specific viral diseases, which can lead to non-efficacy against viral variants and drug resistance, so drugs with broad-spectrum antiviral activity are lacking. In recent years, a steady stream of new viral diseases has emerged, which has prompted development of new antiviral drugs. Natural products could be employed to develop new antiviral drugs because of their innovative structures and broad antiviral activities. This review summarizes the progress of natural products in antiviral research and their bright performance in drug resistance issues over the past 2 decades. Moreover, it fully discusses the effect of different structural types of natural products on antiviral activity in terms of structure–activity relationships. This review could provide a foundation for the development of antiviral drugs.

KEYWORDS

natural products, antiviral, derivatization, resistance, structural-activity relationship

**Abbreviations:** Adv, adenovirus; AS, Acetylshikonin; Atg12, autophagy-related gene 12; Atg5, autophagy-related gene five; CA, Caffeic acid; $CC_{50}$, cytotoxic concentration of extracts to cause death to 50% of viable cells; CCR5, C-C chemokine receptor five; CDV, Canine distemper virus; CHA, Chlorogenic acid; CHB, chronic HBV; CHIKV, Chikungunya virus; COVID-19, Coronavirus disease 2019; CVA16, coxsackievirus A16; CVB3, coxsackievirus B3; DENV, Dengue virus; EBV, Epstein-Barr virus; $EC_{50}$, half-maximal effective concentration; $ED_{50}$, median effective dose; EV71, enterovirus 71; GA, Glycyrrhetinic acid; GaLA, galacturonic acid; GL, Glycyrrhizin; H3N2, influenza virus A3/Beijing/30/95; HBeAg, hepatitis B virus e antigen; HBsAg, hepatitis B virus surface antigen; HBV, hepatitis B virus; HBx, HBV X; HCMV, Human cytomegalo vrius; HCoV-NL63, human coronavirus NL63; HCV, hepatitis C virus; HIV, human immunodeficiency virus; HIV-1RT, HIV-1 reverse transcriptase; HSV, herpes simplex viruses; IAV, influenza A virus; $IC_{50}$, half-maximal inhibitory concentration; IFN-α, interferon-α; Keap1/Nrf2, Kelch-like ECH-associated protein 1/Nuclear factor (erythroid-derived 2)-like two; LC3-II, autophagy-related protein light chain three; MDCK, Madin-Darby canine kidney; NNRTI, non-nucleoside reverse transcriptase inhibitor; NPs, Natural products; OA, Oleanolic acid; SARS-CoV-2, severe acute respiratory syndrome-coronavirus two; SFTSV, severe fever with thrombocytopenia syndrome virus; SI, selectivity index; TMV, tobacco mosaic virus; UA, Ursolic acid; ZIKV, Zikavirus.

# 1 Introduction

Recently, numerous viral diseases originating from wildlife hosts have posed a serious threat to the life of humans. These viruses have included the Ebola virus (Zhu et al., 2020), human immunodeficiency virus (HIV) (Yonekawa et al., 2019), and influenza A virus (IAV) (Joseph et al., 2017). Close contact between humans and domestic animals and populations of wild animals has increased the risk of virus transmission between species. The International Committee on Taxonomy of Viruses approved and promulgated the latest classification of viruses in 2021, which contains 9,110 viruses (Walker et al., 2021). The increasing number of viruses demonstrates their biological diversity and rapid adaptability, and reflects the potential harmfulness of viruses.

Viruses destroy the structure and function of host cells and cause serious damage to the host by multiplying. They also evolve at a fast rate to adapt to the host's internal environment. For example, there were 2,682 male and 2,455 female deaths from infection by the Dengue virus (DENV) and its variants over the past 3 decades in Brazil, with symptoms of severe internal bleeding, circulatory collapse, and shock (Nunes et al., 2019). Many diseases caused by viral infections are transmissible, lethally harmful, and difficult to cure.

Vaccines and antiviral drugs are the two main strategies for fighting viruses. In general, vaccines are considered the best means for preventing viral infections. However, vaccine development requires rigorous processes, which are time-consuming. Also, the vaccination rates and outcome data are not impressive in older populations, which necessitates use of antiviral agents to complement vaccines (Demicheli et al., 2018). Only a few antiviral drugs have been developed to prolong the life of patients, but they had significant disadvantages: high price, resistance, and non-efficacy against viral variants. Coronavirus disease 2019 (COVID-19) occurs due to infection by severe acute respiratory syndrome-coronavirus 2 (SARS-CoV-2) infection. COVID-19 continues to wreak havoc on healthcare and economic systems worldwide. The number of infections and deaths due to SARS-CoV-2 keeps rising, new strains of the virus are emerging, and definite efficacious treatment is not available (Barlow et al., 2020). Existing therapeutics cannot stop infection by or transmission of viruses, and humankind cannot wait for the research and development of new antiviral drugs.

"Natural products" (NPs) are chemical substances of natural origin. They have complicated structures and a wide variety of biological activities (Newman and Cragg, 2016). Many active components of NPs and their derivatives possess antiviral activity, such as alkaloids, quinones, flavonoids, terpenoids, glycans, organic acids, and others (Supplementary Table S1). Newman et al. concluded that, in the last 28 years, the drugs developed based on NPs were 63.1% of all small-molecule drugs (Newman and Cragg, 2020). That figure demonstrates the great
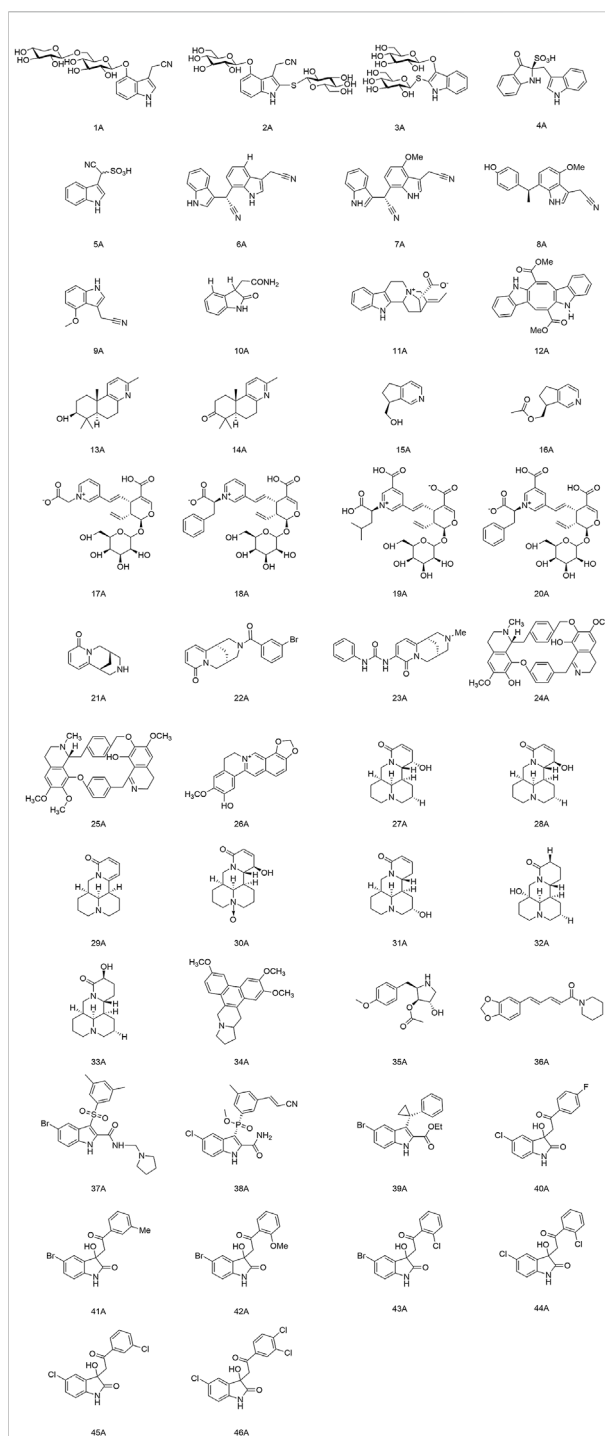


FIGURE 1
Structures of alkaloids (and their derivatives) with antiviral activity.

potential of NPs and their derivates in the development of new drugs. Wright suggested continuation of exploration of NPs as a source for drug development based on existing research. He suggested avoiding the complicated steps of synthesis "from

scratch" and rationalizing application of resources for solving threats to the life and health of humans (Wright, 2019).

Up to now, to our knowledge, there is no reported data to conclude the relationships between the structure of each natural product component and its antiviral activity. This review summarized the research progress of antiviral NPs and their derivatives in the past 2 decades. We focused on the structure-activity relationships between various types of active ingredients in NPs and their antiviral activity, mainly alkaloids, quinones, flavonoids, terpenoids, glycans, organic acids and others. We also discussed the development potential of natural products in resolving drug resistance problems, and provided a rationale for in-depth development of antiviral drugs.

# 2 Alkaloids

Alkaloids represent a structurally diverse group of nitrogen-containing bases. Most of them show significant pharmacological activities. In particular, the alkaloids with antiviral activity mainly include the following categories: indole, terpenoid, quinolinine, isoquinoline, indolizidine, quinolizidine, pyrrolidine and piperidine. The structures of alkaloids and their derivatives mentioned in this review are shown in Figure 1.

## 2.1 Indole alkaloids

Meng and colleagues discovered two new indole alkaloid diglycosides, isatigotindolediosides C (1A) and isatigotindolediosides E (2A), along with one known analog Calanthoside (3A), isolated from an aqueous extract of *Isatis indigotica* roots (Meng et al., 2017b). (1A) and (2A) showed equal inhibitory activity to the (3A) for coxsackievirus B3 (CVB3), with an $IC_{50}$ of 33.3 μM. Also, Meng's team separated eight additional indole alkaloid sulfonic acids from the aqueous extract of *I. indigotica* roots, including isatibisindosulfonic acid B (4A) and isatindosulfonic acid B (5A), which had activity against CVB3 and influenza virus A, respectively (Meng et al., 2017a). Chen's team identified seventeen alkaloids from the aqueous extract of *I. indigotica* roots. Compounds (6A), (7A), (8A), and (9A) had activity against influenza viruses, and (10A) inhibited CVB3 replication with an $IC_{50}$ value of 6.87 μM (Chen et al., 2012). Moradi and his team discovered that the total alkaloids of an extract of *Peganum harmala* seeds had a highly inhibitory effect upon IAV replication in Madin-Darby canine kidney (MDCK) cells. They could restrain the RNA replication and polymerase activity of the IAV without affecting its hemagglutination inhibition and virucidal activity, so they could be developed as agents against the IAV (Moradi et al., 2017). Zhang and his colleagues isolated a novel indole alkaloid, 17-nor-excelsinidine (11A), from *Alstonia scholaris* and it was significantly more potent than acyclovir against the herpes

simplex virus (HSV) and adenoviruses, with an $EC_{50}$ of 1.09 and 0.94 μg/ml, respectively (Zhang et al., 2014). Esteves and his team isolated caulerpin (12A) from the marine green alga *Caulerpa racemose*, and showed anti-Chikungunya virus (CHIKV) activity, and its derivatives were promising as anti-CHIKV drugs (Esteves et al., 2019). Macedo and coworkers revealed that (12A) can inhibit the alpha and beta phases of the replication cycle of the herpes zoster type-1 virus, as well as could be a substitute for acyclovir (Macedo et al., 2012).

## 2.2 Terpenoid alkaloids

Li and his team isolated two diterpenoid forsyqinlingines (13A), (14A) and two C9-monoterpenoid alkaloids (15A), (16A) from *Forsythia suspensa*, all of them showed antiviral effects against the IAV and respiratory syncytial virus *in vitro* (Li W. et al., 2021; Li et al., 2022). Yu and his collaborates separated and identified nine new alkaloids from the aqueous extract of *Lonicera japonica* flower buds. Compounds (17A), (18A), (19A), and (20A) demonstrated activity against influenza viruses, and (18A) inhibited replication of coxsackieviruses (Yu et al., 2013).

## 2.3 Quinolinine and isoquinolinine alkaloids

(−)-Cytisine (21A) is a quinoline alkaloid with antiviral activity. It is mainly isolated from plants of the Leguminosae family (Gotti and Clementi, 2021). The structural modifications of (21A) have focused on its secondary nitrogen atom and 2-pyridone core. Tsypysheva and collaborators revealed that derivative (22A) with introduction of *m*-bromobenzamide on the secondary nitrogen atom and (23A) with an aryl-substituted urea moiety on the 2-pyridone core could improve the anti-influenza-virus activity of (21A) ($ED_{50}$ = 109 μg/ml) with $ED_{50}$ values of 44 and 57 μg/ml, respectively. They provided a reference for further targeting and optimizing of the antiviral activity of quinoline alkaloids (Tsypysheva et al., 2013). In addition, they discovered that (−)-cytisine derivatives have activity against DENV-2. The attachment and entry of E proteins targeting the DENV could be inhibited by introduction of a substituted thioamide or thiocarbamide fragment at the 3-position of the 2-pyridone core, as well as insertion of a fragment that formed a donor–acceptor bond (Tsypysheva et al., 2021). Silva and colleagues extracted a bisbenzylisoquinoline alkaloid, warifteine (24A), from the rhizomes of *Cissampelos sympodialis*, which proved to be an anti-DENV (da Silva et al., 2021a). Subsequently, they found that (24A) and methylwarifteine (25A) had strong effects against the Zika virus *in vitro*, and could be used as a pharmacophore or lead compounds to counteract Zika-virus infection (da Silva et al.,
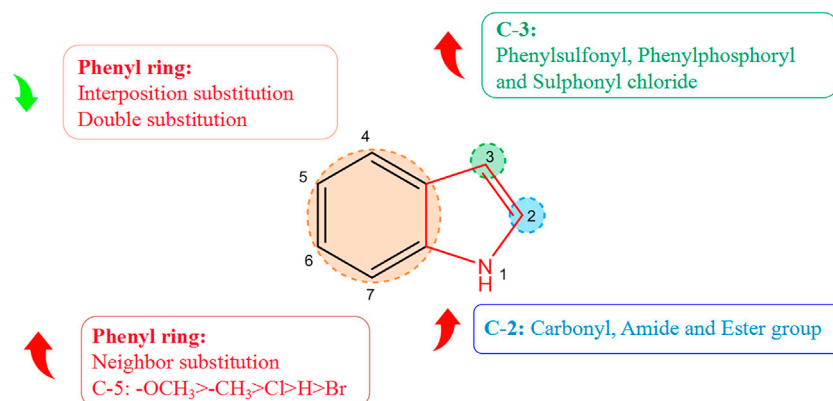
**FIGURE 2**
Structure−activity relationship of alkaloids with respect to viruses.

2021b). Zeng's team identified that dehydrocheilanthifoline (26A) had anti-hepatitis B virus (HBV) activity *in vitro*, making it a promising drug candidate for the treatment of HBV infection (Zeng et al., 2013).

## 2.4 Indolizidine and quinolizidine alkaloids

Pan's team discovered that several bitter ginseng alkaloids, such as compounds (27A), (28A), and (29A) inhibited replication of influenza viruses, whereas compounds (30A), (31A), (32A), and (33A) showed activity against CVB3 (Pan et al., 2015). Xi and colleagues suggested that Tylophorine B (34A) had high affinity for the RNA of the tobacco mosaic virus (TMV) and the starting point of its oriRNA assembly, with an $IC_{50}$ of 2.4 nM against TMV RNA. Presumably, (34A) contributed to the viral-suppressive effect by binding to oriRNA and interfering with viral assembly (Xi et al., 2006).

## 2.5 Pyrrolidine alkaloids and piperidine alkaloids

Quintana and collaborators demonstrated that anisomycin (35A) (derived from *Botrytis cinerea*) had activity against the DENV and Zika virus by inhibiting viral replication (Quintana et al., 2020). Huang et al. discovered significant inhibition of SARS-CoV-2 replication in Vero E6 cells at the nanomolar level with relatively non-toxic concentrations of (35A) (Huang et al., 2020). Jiang's group discovered that piperine (36A) had anti-HBV activity and could inhibit secretion of hepatitis B virus surface antigen (HBsAg) and hepatitis B virus e antigen (HBeAg), thereby suggesting a *rationale* for development of new drugs that can prevent and treat HBV infection (Jiang et al., 2013).

## 2.6 Structure−activity relationship of alkaloids with respect to virus activity

Derivatization of alkaloids with respect to antiviral features had focused mainly on indole alkaloids. Nitrogen-containing heterocycles have shown high antiviral activity. The structure–activity relationship with regard to the antiviral activity of indole alkaloids is summarized in Figure 2, where positions 2, 3, and five of the indole ring are the essential active sites for indole alkaloids to exert antiviral effects. Introduction of hydrophilic groups such as amide, carbonyl, and ester at the 2-position, the phenyl ring at the 3-position terminus, and a halogen group at the 5-position can enhance the antiviral activity of indole alkaloids. Derivative (37A) of indole alkaloids synthesized by Regina and colleagues showed potent activity against HIV-1 reverse transcriptase (RT) and HIV-1 with an $IC_{50}$ value of 1.3 nM (La Regina et al., 2011). Dousson and coworkers revealed that aryl phosphorindole (38A) was a potent non-nucleoside reverse transcriptase inhibitor (NNRTI) of the HIV with an $IC_{50}$ value of 0.34 μM, and that (37A) and (38A) shared a similar pharmacophore profile (Dousson et al., 2016). Hassam and collaborators used a cyclopropylindole derivative as the basic backbone to synthesize NNRTIs of the HIV by introducing amide, carboxyl, and ester groups at the 2-position. Experimental results indicated that the amide and ester groups could enhance the antiviral activity of these compounds. Compound (39A) showed the most potent antiviral activity ($IC_{50}$ = 0.066 μM), whereas the carboxyl group was not as effective in inhibiting the HIV, presumably because of the poor permeability of the carboxyl group, which was ionized at physiological pH (Hassam et al., 2012). Chander and his colleagues derivatized 3-hydroxy-3-(2-oxo-2-phenylethyl)indolin-2-one as a basic backbone and evaluated its anti-HIV-1 activity *in vitro*. Substitution with bromine or chlorine at position 5 (R1) of the oxindole ring enhanced its antiviral activity significantly. Compound (40A) with a chlorine substitution had higher antiviral activity ($IC_{50}$ =
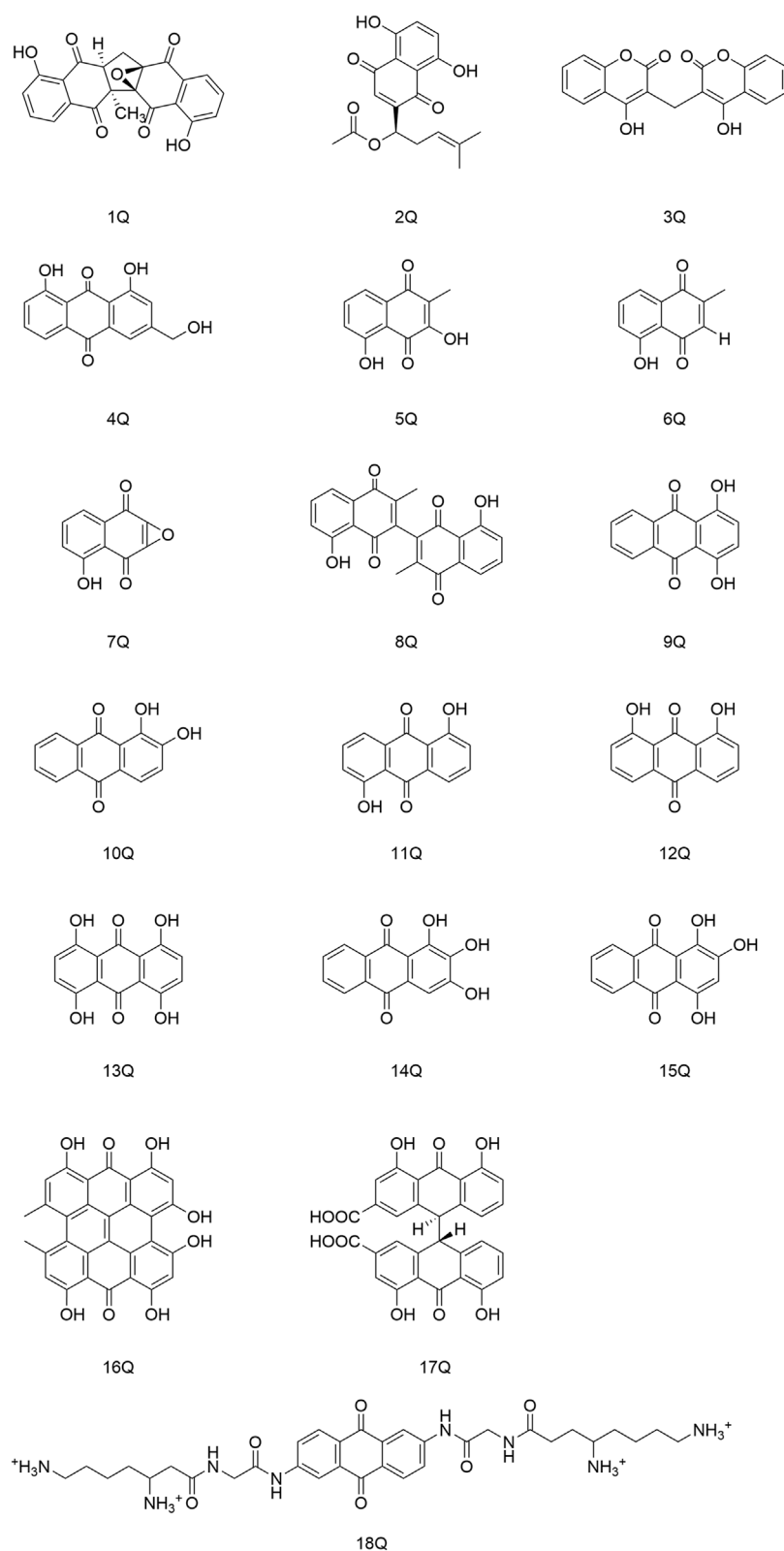
**FIGURE 3**
Quinones (and their derivatives) with antiviral activity.

5.92 μM), whereas little antiviral potency was observed in case of substitution of bromine on the oxindole ring with hydrogen (Chander et al., 2018). Moreover, the antiviral activity varied depending on the type and position of the substituents on the benzene ring. The electron-donating methyl (41A), methoxy (42A), and halogenated chlorine groups (43A) increased their antiviral inhibition ($IC_{50}$ = 1.38, 0.82, and 2.03 μM, respectively), with the methoxy group having the most significant antiviral activity. Comparison of the antiviral activity of o-substituted (44A) ($IC_{50}$ = 0.76 μM), inter-substituted (45A) ($IC_{50}$ = 34.25 μM), and double-substituted (46A) ($IC_{50}$ = 68.86 μM) revealed that o-substitution could strengthen the inhibitory ability of the compounds against viruses, whereas inter-substitution and double substitution had a negative effect on antiviral activity.

# 3 Quinones

## 3.1 Antiviral activity of quinones

Quinones are a class of aromatic organic compounds with two double bonds and a cyclic diketone structure with six carbon atoms. Quinones can be categorized into four groups based on their structure: benzoquinone, naphthoquinone, anthraquinone, and phenanthrenequinone (Patel et al., 2021), in which the main ones with antiviral activity are anthraquinone and naphthoquinone (Figure 3).

Cetina and coworkers discovered that the naphthoquinone compound zeylanone epoxide (1Q), isolated from *Diospyros anisandra*, could exert activity against influenza-A and -B viruses. Compound (1Q) could reduce viral titers and block the extra-nuclear transport of viral nucleoprotein, and could be a promising drug against influenza viruses (Cetina-Montejo et al., 2019). Liu and his team established that acetylshikonin (2Q) could inactivate viral particles directly at relatively low concentrations to block the uptake or entry of coxsackievirus A16 (CVA16) *in vitro*. Hence, (2Q) could protect cells from CVA16, and inhibit *in vivo* and *ex vivo* infection by CVA16 (Liu X. et al., 2019). Cheng and collaborators identified that dicoumarol (3Q) could inhibit the transcription of covalently closed circular-DNA by promoting degradation of the targeted viral protein (HBx), thereby combating chronic infection with the hepatitis B virus (Cheng S. T. et al., 2021). Parvez and his colleagues identified the potential of aloe-emodin (4Q) in hepatocellular carcinoma cells, likely through inhibition of the polymerase activity of the HBV (Parvez et al., 2019).

## 3.2 Structure–activity relationships of quinones with respect to viruses

Most of the quinones that display antiviral activity are naphthoquinone and anthraquinone compounds, and the structure–activity relationship of their antiviral effects is depicted in Figure 4.

Montejo's team observed that the naphthoquinone compound droserone (5Q) possessed weak activity against influenza viruses as well as cytotoxicity. Plumbagin (6Q) (in which the 2-position hydroxyl group is replaced with hydrogen) showed antiviral activity, and it was assumed that the 2-position hydroxyl group inhibited the antiviral activity of naphthoquinone (Cetina-Montejo et al., 2019). However, 2,3-epoxiplumbagin (7Q) and the naphthoquinone dimer 3,3-biplumbagin (8Q), which are structurally similar and contain an epoxide structure, reduced their cytotoxicity to different degrees, and (1Q) (which has an epoxide structure and a naphthoquinone backbone) showed the most significant activity against influenza viruses, with an $IC_{50}$ value of 0.65 ± 0.01 μM. They hypothesized that the presence of epoxide structures and naphthoquinone multimers in naphthoquinone compounds could enhance their antiviral activity.

Thus, the antiviral activity of anthraquinones appears to be related to the number and location of phenolic hydroxyl groups in their structures. Also, formation of a keto-phenol system on the same benzene ring is the key to their antiviral activity. Furuta and his colleagues showed that derivative (9Q) inhibited hepatitis C virus (HCV) replication ($IC_{50}$ = 54 μM) mainly by suppressing the activity of NS3 decarboxylase. The activity of (9Q) was superior to that of (10Q), (11Q), or (12Q) (Furuta et al., 2015). Also, increasing the number of hydroxyl groups on the same benzene ring and the number of pairs of keto-phenol systems could further improve the inhibitory activity. They found that (13Q) had the most potent inhibitory activity ($IC_{50}$ = 6 μM), and that (14Q) and (15Q) had similar abilities to inhibit NS3 decyclase, with $IC_{50}$ values of 18 and 11 μM, respectively. Anti-HCV activity was also augmented significantly by multimerization of hydroxyanthraquinones, such as (16Q) and (17Q), both of which had a double-anthraquinone backbone structure with $IC_{50}$ values of three and 0.8 μM, respectively. In addition, the antiviral activity of anthraquinones might be potentiated to some extent by insertion of a group capable of inhibiting the activity of viral proteins into the anthraquinone structure. Frecentese and coworkers discovered that positions two and six of the anthraquinone ring were crucial for the synthesis of HIV-1 nucleocapsid inhibitors, and synthesized the compound (18Q), which provided the groundwork for development of new anti-HIV drugs (Frecentese et al., 2016).

# 4 Flavonoids

"Flavonoids" is a general term for compounds with a C6-C3-C6 skeleton based on 2-phenylchromanone as the parent nucleus (Liu et al., 2021). Flavonoids can be divided into flavonoids, flavonols, isoflavones, and dihydroflavonoids according to the degree of oxidation of the C3 chain and position of the benzene-ring linkage (Fang et al., 2015).
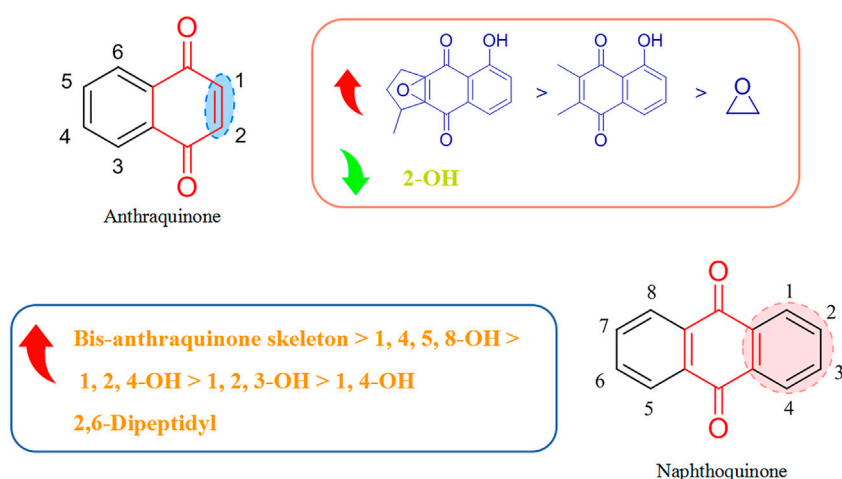
**FIGURE 4**
Structure−activity relationship of quinones with respect to viruses.

Zandi and his team showed that flavonoids have activity against DENV-2 in Vero cells. Autophagy, the inflammation-related nuclear factor-kappa B pathway, and Toll-like receptor pathway might be the major molecular targets of flavonoids against viruses (Zandi et al., 2011; Cheng C. et al., 2021). We have described some representative flavonoids with significant antiviral activity in this review. The structures of flavonoids (and their derivatives) that possess antiviral activity are shown in Figure 5.

## 4.1 Flavonoids and flavonols

### 4.1.1 Quercetin and rutin

Quercetin (1F) is the most common flavonol compound with notable antiviral effects found in nature (Li et al., 2016). Xu and coworkers demonstrated that (1F) had good protective effects against the cardiomyocyte damage wrought by CVB3 infection. Shohan and collaborators used (1F) in combination with the antiviral drugs raltegravir and famipiravir to treat critically ill inpatients with neocoronary pneumonia, and (1F) showed a more significant effect than that observed using raltegravir alone or famipiravir alone (Xu et al., 2021; Shohan et al., 2022). Rutin (2F) is a flavonol ligand composed of (1F) and rhamnoglucoside. (2F) has been shown to exert activity against the HBV, influenza viruses, human noroviruses, and the DENV (Li K. et al., 2021). Kim and her colleagues investigated the antiviral activity of (1F), (2F), and isoquercetin (3F) against influenza-A and B viruses. (3F) showed the highest antiviral activity ($ED_{50}$ = 1.2 μM), even

better than that of the positive control drug amantadine ($ED_{50}$ = 1.4 μM) (Kim et al., 2010).

### 4.1.2 Baicalin and baicalein

Baicalin (4F) is a glycoside flavonoid with high polarity. Baicalein (5F) is the aglycone part of (4F). Lani's team revealed that (5F) had stronger intracellular antiviral activity in the post-entry phase of CHIKV replication, with an $IC_{50}$ value of 1.891 μg/ml and selectivity index (SI) of 188.4, much stronger than that of the positive control, ribavirin ($IC_{50}$ = 11.07 μg/ml, associated SI = 54.2) (Lani et al., 2016).

(5F) also possesses anti-CHIKV activity, in which the hydroxyl group at position seven on the baicalin ring A is replaced with a glucouronoid ($EC_{50}$ = 7 μM). It inhibits different stages of the replication cycle of the CHIKV as well as the production and expression of CHIKV protein, thereby eliciting direct viral killing (Oo et al., 2018). Zhu's group showed that (5F) had anti-influenza virus A3/Beijing/30/95 (H3N2) activity, mainly through inhibition of formation of the autophagy-related gene 5 (Atg5)–autophagy-related gene 12 (Atg12) complex and autophagy-related protein light chain 3 (LC3-II) expression, as well as reducing virus replication by suppressing the influenza virus-induced autophagy pathway (Zhu et al., 2015).

## 4.2 Other flavonoids

Hesperidin (6F) is a glycoside formed by hesperetin and rhamnoglucoside. (6F) is a dihydroflavonoid derivative. Meneguzzo and colleague suggested that (6F) could interfere with different stages of the invasion and replication of

**FIGURE 5**
Flavonoids (and their derivatives) that possess antiviral activity.
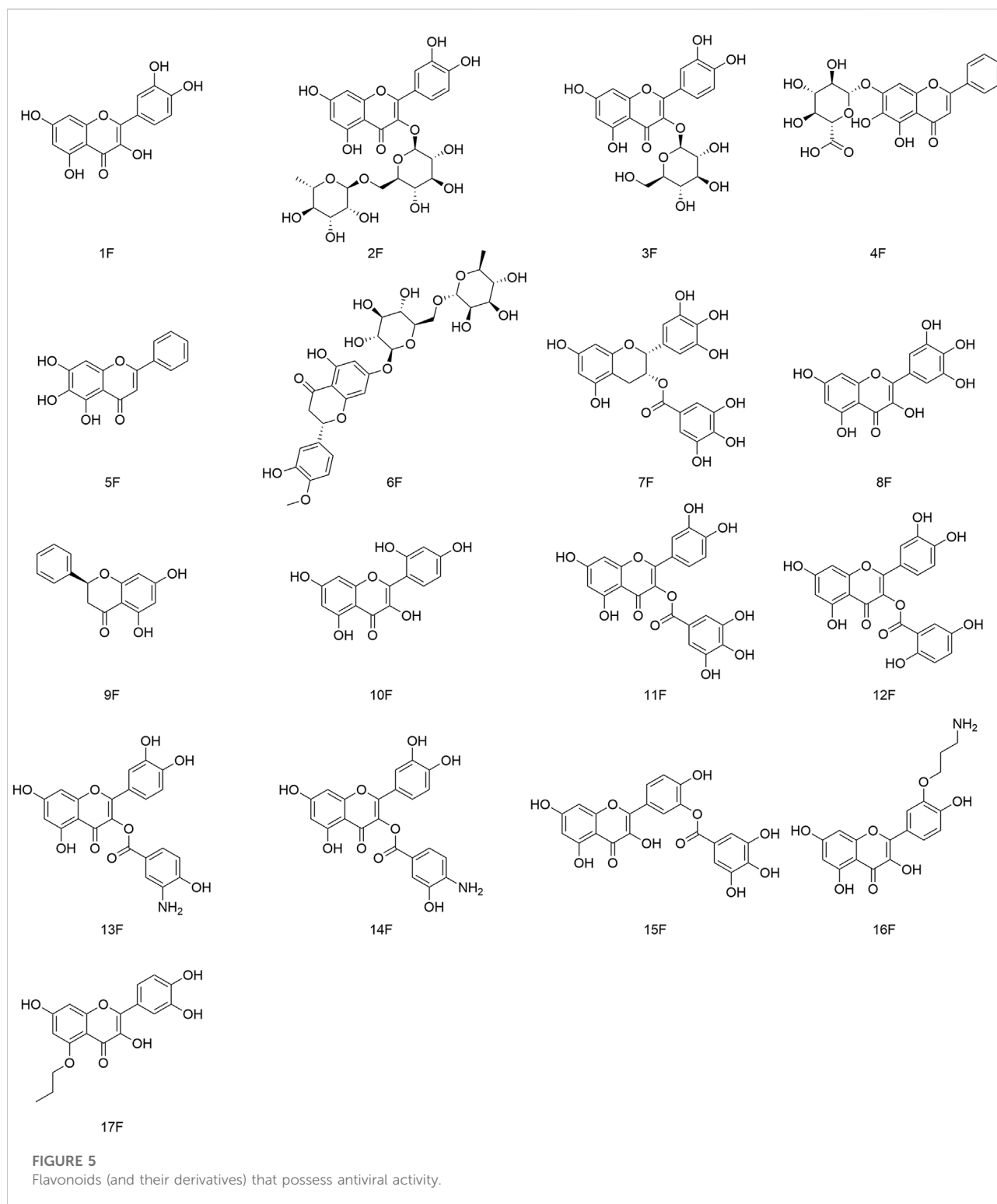
coronaviruses. (6F) has extremely strong binding capacity to the receptors for SARS-CoV-2 (Meneguzzo et al., 2020). Epigallocatechin-3-gallate (EGCG) (7F) is a major component of tea. Pang and colleagues observed that (7F) had anti-HBV activity.

Treatment of HepG2 2.2.15 cells with (7F) (50 µg/ml) for 6 days could repress secretion of HBsAg and HBeAg significantly (53% and 44% inhibition, respectively) and inhibition of HBsAg was stronger than that of the positive control lamivudine (Pang et al., 2014).

**FIGURE 6**
Structure−activity relationships with respect to the antiviral activity of flavonoids.
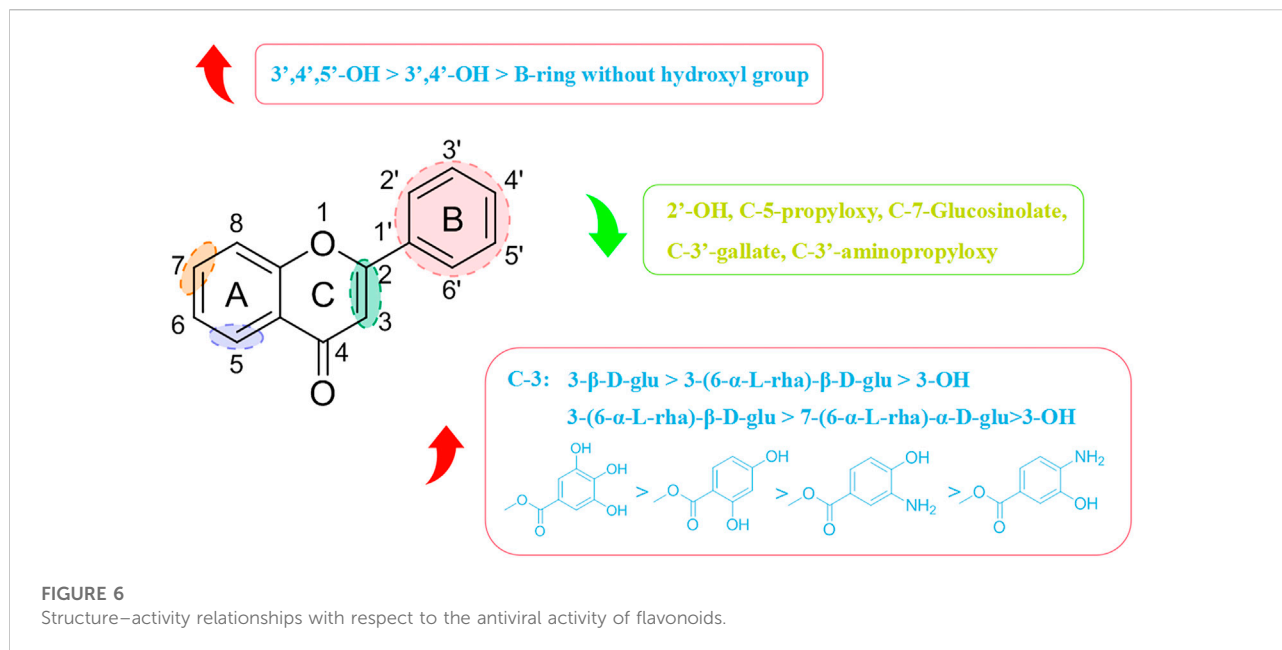
## 4.3 Structure−activity relationship of flavonoids with respect to viruses

Most flavonoids possess a C6-C3-C6 skeleton. The type and position of substituent groups can affect their antiviral activity. The specific structure–activity relationships are shown in Figure 6. Pasetto and his team discovered that myricetin (8F) had the highest activity against HIV-1 *in vitro* ($IC_{50}$ = 20.43 μM), which was about four-times that of (1F) ($IC_{50}$ = 88.98 μM) and 16-times that of pinocembrin (9F) ($IC_{50}$ = 346.75 μM) under identical conditions (Pasetto et al., 2014). (8F) has $3'$, $4'$, and $5'$ hydroxyl groups, whereas (1F) has two adjacent hydroxyl groups at $3'$ and $4'$ positions, and no hydroxyl group is present in any of these positions in (9F). The relationship between their structure and antiviral activity has been hypothesized to be $3',4',5'$-OH > $3',4'$- OH > B-ring without OH. The greater the number of hydroxyl groups on the B-ring, the more potent is the antiviral activity of flavonoid compounds. Besides the number of hydroxyl groups on the B-ring, the position of hydroxyl groups on the B-ring can also influence their antiviral activity. Morin (10F) and (1F) are flavonol compounds containing two free hydroxyl groups on the B-ring, but they are present in different positions, with (10F) having a $2',4'$ interposition dihydroxy group and (1F) having a $3',4'$ neighboring dihydroxy group. Carvalho's group revealed that the anti-Canine distemper virus (CDV) activity of mulberry pigment was weaker than that of (1F). They speculated that the $2'$ hydroxyl group on the B ring might influence its antiviral activity (Carvalho et al., 2013). Tahpa's group modified the C-3, C-5, and C-$3'$ hydroxyl groups on (1F). They concluded that introduction of gallate, dihydroxybenzoate, and aminohydroxybenzoate at C-3 improved the antiviral activity of (1F), with (11F) showing the most potent antiviral activity ($ED_{50}$ = 9.1 μM), which was similar to (4F) activity ($ED_{50}$ = 8.3 μM). In contrast, introduction of gallate, aminopropoxy, and propoxy at C-5 and C-$3'$ curtailed the antiviral activity of (1F), presumably because $3'$-OH and 5-OH were the active groups involved in the antiviral action of (1F) (Thapa et al., 2012).

Flavonoids are combined with carbohydrates to form glycosides in plants. The linkage position and type of sugar affects their antiviral activity. Carvalho and his colleagues showed that both (2F) and (7F) had stronger anti-CDV viral activity than (1F) (Carvalho et al., 2013). They postulated that the glycosylation of (2F) and (7F) could enhance their antiviral activity, and that the degree of improvement in antiviral activity was related to the glycosylation site, with (2F) glycosylation at C-3 being distinctly superior to (7F) glycosylation at C-7. Thapa and collaborators demonstrated that (3F) containing 3-β-D-glu had considerable antiviral activity ($ED_{50}$ = 1.2 μM), which was superior to that of (2F) containing 3-(6-α-L-rha)-β-D-glu ($ED_{50}$ > 100 μM) (Thapa et al., 2012). However, not all flavonoid glycosides have stronger antiviral activity than their aglycones. In terms of activity against DENV-2, (5F) is weaker than (6F). 7-OH might be an important moiety for the antiviral activity of (6F) (Moghaddam et al., 2014).

## 5 Terpenoids

Terpenoids are a group of hydrocarbons occurring naturally in plants. They can be classified as monoterpenes, sesquiterpenes,
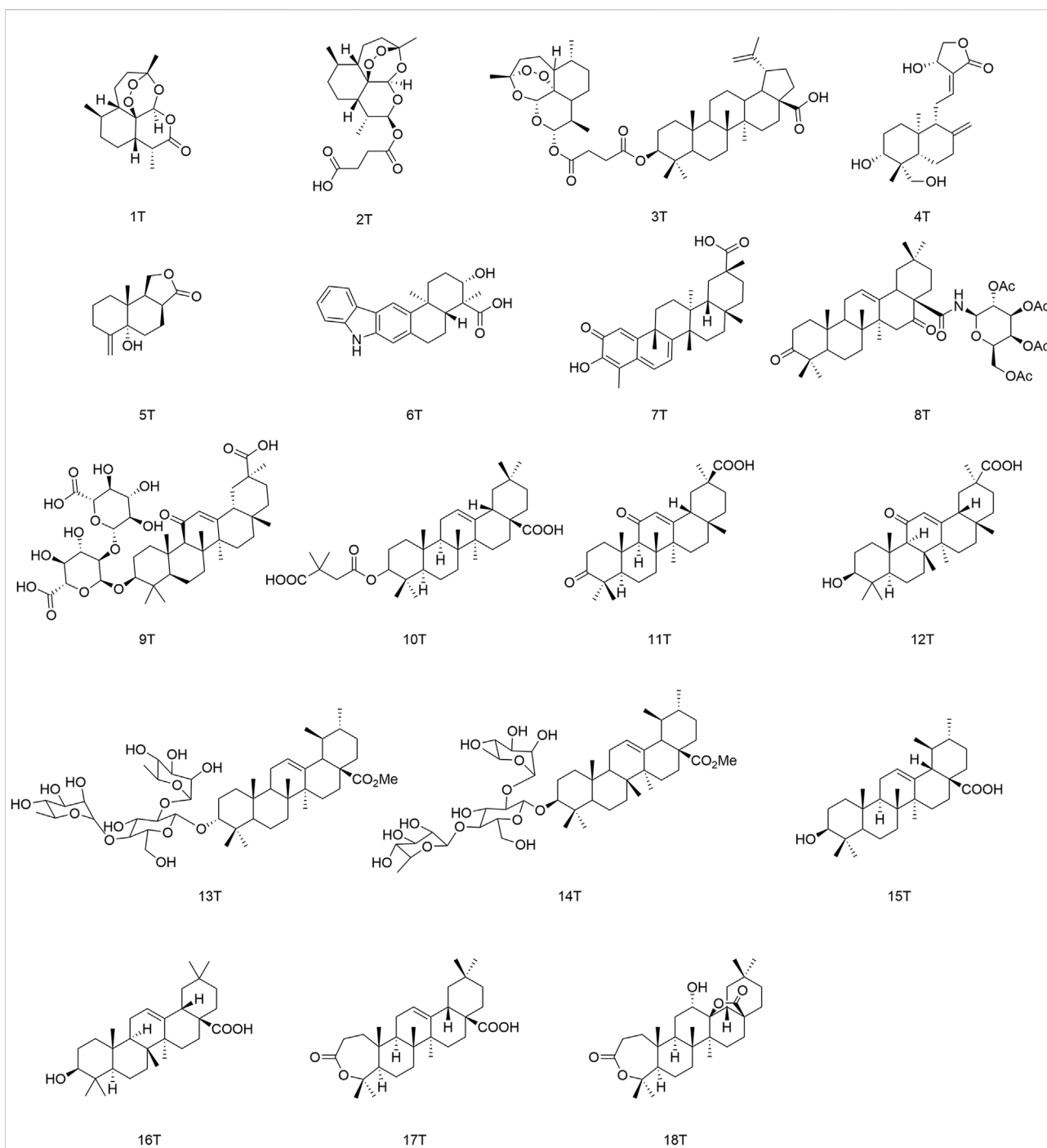
**FIGURE 7**
Terpenoids (and their derivatives) with antiviral activity.

triterpenes, and polyterpenes according to the number of isoprene units in the molecule (Zhang et al., 2018). Thanks to research into new antiviral drugs, the essential oils of plants have become popular due to their high efficiency, safety, and resistance (Zhang et al., 2021). The structures of terpenoids with antiviral activity are presented in Figure 7.

## 5.1 Monoterpenes and sesquiterpenes

The monoterpenes present in the essential oils of plants include monoterpene alcohols and monoterpene aldehydes, which having slightly higher antiviral activity than monoterpene alcohols (Astani et al., 2010). Artemisinin (1T)

is a sesquiterpene lactone, and its derivatives have shown inhibitory effects against the human cytomegalovirus (HCMV), HBV, and HCV. In particular, artesunate (2T) can control secretion of HBsAg with an $IC_{50}$ of 2.3 μmol/L and reduce gene expression of the HBV with an $IC_{50}$ of 0.5 μmol/L (Wohlfarth and Efferth, 2009). Karagoz and collaborators showed that derivative (3T) presented high anti-HCMV activity ($EC_{50}$ = 0.24 μM), which was 15-times higher than the antiviral activity of betulinic acid and 23-times that of (2T), as well as being superior to the clinically used anti-HCMV drug ganciclovir (Karagoz et al., 2019). Panraksa and colleagues showed that andrographolide (4T) displayed appreciable anti-DENV activity in Hep G2 and HeLa cells, with $EC_{50}$ values of 21.304 and 22.739 μM, respectively (Panraksa et al., 2017). Liu and his team identified a new 14-demethylamino-based sesquiterpene, phomanolide (5T), with high activity against influenza A virus (HIN1) ($IC_{50}$ = 2.96 ± 0.64 μg/ml), which was first isolated from *Aconitum vilmorinianum.* (Liu S. S. et al., 2019). Ding et al. isolated a pentacyclic indole sesquiterpene named xiamycin (6T) from *Streptomyces* species with moderate anti-HIV activity. (6T) blocked the entry of C-C chemokine receptor 5 (CCR5)-tropic HIV-1, indicating that the pentacyclic carbazole system might be an effective backbone for antiviral agents (Ding et al., 2010).

## 5.2 Triterpenes

Triterpenoids are composed mainly of six isoprene units, of which pentacyclic triterpenes are the most common and exhibit strong antiviral activity. The main types of pentacyclic triterpene skeletons are oleanolane, ursolidane, lupinane, and corkolidane (Miranda et al., 2022).

Tseng and coworkers showed that celastrol (7T) could induce gene expression of heme oxygenase-1, which led eventually to HCV inhibition (Tseng et al., 2017). Si and collaborators discovered that (8T) (a derivative of echinocystic acid combined with acetylated galactose) exerted prominent effects against the Ebola virus, with $IC_{50}$ values of 59.2 ± 1.6 nM (Si et al., 2018). Matsumoto and colleague demonstrated that glycyrrhizin (9T) possessed anti-HCV activity ($EC_{50}$ = 16.5 μM) and that its mechanism of action involved controlling the release of infectious HCV particles (Matsumoto et al., 2013).

## 5.3 Structure−activity relationships of pentacyclic triterpenoids with respect to viruses

Pentacyclic triterpenoids influence antiviral activity mainly at C-3, C12−C13, and C-28 positions (Fan et al., 2020) (Figure 8). Introducing of glycosyl groups, 3′,3′-dimethylsuccinic acid, and acyl groups at C-3 can enhance antiviral activity. Cai's group

observed that the pentacyclic triterpene parent nucleus and glucose molecules were essential in upgrading the activity of compounds against influenza viruses (Cai et al., 2022). Yu and collaborators concluded that derivative (10T) containing a 3′,3′-dimethylsuccinic acid moiety had an $EC_{50}$ value of 0.32 μM against HIV-1, whereas derivatives containing 3′,3′-dimethylpentanedioic acid showed no antiviral activity (Yu et al., 2006). Wang and colleagues reported that (11T) was oxidized to a ketone group, and its ability to inhibit secretion of HBsAg protein ($IC_{50}$ = 432.54 μM) proved to be much weaker than that of glycyrrhetinic acid (12T) ($IC_{50}$ = 20.86 μM), presumably because the 3-ketone group suppresses the antiviral activity of triterpenoids (Wang L. J. et al., 2012). Moreover, the C-3 configuration proffered different advantages in the prevention of different viral species. Ma and his team demonstrated that β-configuration substituent-containing derivatives of oleanolic acid were superior to the α-configuration counterparts in terms of anti-HCV activity (Ma et al., 2009). Song's team revealed that (13T) containing an α-configuration hydroxyl group could maintain activity against influenza A virus (H5N1) and reduce cytotoxicity against MDCK cells greatly, stronger than the β-configuration (14T) (Song et al., 2015).

The free hydroxyl group at the C-3 position and free carboxyl group at the end of the side-chain at the C-28 position are crucial moieties for the antiviral activity of triterpenoids (Sun et al., 2002) such as ursolic acid (15T) and oleanolic acid (16T), which both showed high anti-HCV activity (Kong et al., 2013). Liao and colleagues discovered that introducing of an amide group in the side-chain at the C-28 position was beneficial for enhancing antiviral activity and reducing cytotoxicity. The antiviral activity of aromatic amine derivatives was obviously better than that of aromatic methylamines, which suggests that the distance between the benzene ring and nitrogen atom is too long to depress antiviral activity (Liao et al., 2019). It was possible to improve the anti-H5N1 activity of aromatic amine compounds containing methoxy or chlorine atoms substituted at adjacent/opposite positions in the side-chain in preference to those containing inter-substituted aromatic amines. Li's team synthesized a series of triterpenoid derivatives of 3,4-lactones, among which derivative (17T) with a C12−C13 double bond developed stronger inhibition of secretion of the HBV protein HBeAg ($IC_{50}$ = 0.86 μM), whereas the antiviral activity of (18T) with an oxidized double bond decreased ($IC_{50}$ = 149.1 μM), thereby suggesting that the C12−C13 double bond played an important role in the maintenance of activity (Li et al., 2018).

## 6 Polysaccharides

Polysaccharides are natural macromolecules with a wide range of origin. In general, polysaccharides consist of >10 monosaccharide molecules that have been polymerized,

**FIGURE 8**
Structure–activity relationship of pentacyclic triterpenoids with regard to viruses.
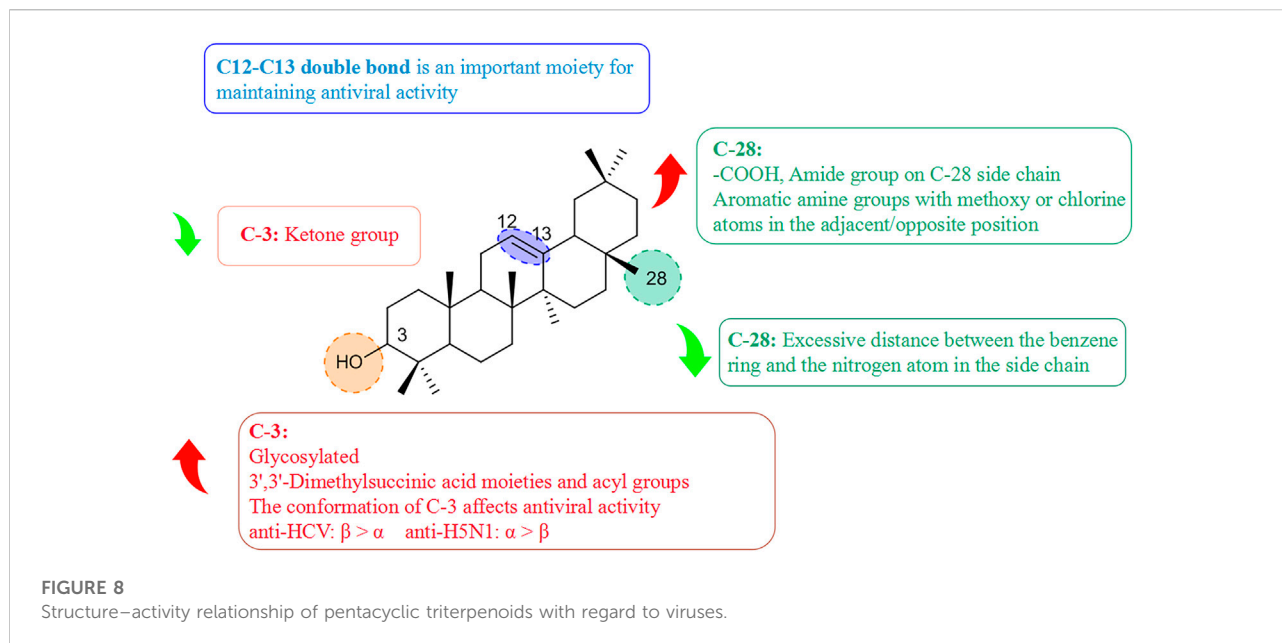
which contain multiple chiral centers and most are non-cytotoxic (Muralidharan et al., 2019). Polysaccharides and their derivatives display prominent suppressive effects against the HIV, HSV, enteroviruses, and influenza viruses, and become a focus of research (Wang C. R. et al., 2011; Saha et al., 2012; de Godoi et al., 2014; Wu et al., 2016).

## 6.1 Plant-derived polysaccharides

Plants are the main natural source of polysaccharides. Oliveira and coworkers found that the crude aqueous and alkaline extracts of *Stevia rebaudiana* leaves possessed activity against HSV-1 *in vitro* (de Oliveira et al., 2013). Ceole and collaborators noticed that anti-HSV-1 activity was more pronounced in the crude fraction, which was related directly to the interaction between the *S. rebaudiana*-derived polysaccharide and viral glycoprotein, not to cellular receptors (Ceole et al., 2020). Su's team demonstrated that distilled-water and 95%-ethanol extracts of *Ardisia chinensis* Benth exerted varying degrees of activity against CVB3 *in vitro*, with the aqueous extract being more active (IC$_{50}$ = 3.9 μg/ml) (Su et al., 2006). This antiviral activity was derived mainly from a neutral polysaccharide with d-glucose as the main glycoside.

### 6.1.1 Ginseng polysaccharides
Baek and colleagues showed that two ginseng pectin polysaccharides suppressed rotavirus-induced cell death in a dose-dependent manner. They inhibited the binding of rotaviruses to host cells (IC$_{50}$ = 15 and 10 μg/ml), with the hairy region possibly being its functional site (Baek et al.,

2010). Yoo's group showed that ginseng polysaccharides boosted the survival of H1N1- and H3N2 influenza-infected mice, demonstrating that ginseng polysaccharides could be used as therapeutic agents against infections by influenza viruses (Yoo et al., 2012).

### 6.1.2 *Houttuynia cordata* polysaccharides
Cheng and his team revealed that *H. cordata* polysaccharides possessed activity against human noroviruses by deforming and swelling viral particles, thereby inhibiting virus penetration into target cells (Cheng et al., 2019). Zhu and coworkers found that treatment with *H. cordata* polysaccharides could improve the survival chances of mice infected with IAV-H1N1, protecting them from lung and intestinal damage as well as reducing viral replication. *H. cordata* polysaccharides might have potential as an alternative drug for treatment of human IAV infection (Zhu et al., 2018).

### 6.1.3 Other polysaccharides
Kim's team discovered that one polysaccharide from dried roots of *Sanguisorba officinalis* was efficient in treatment of Enterovirus 71 (EV71) infections (Kim et al., 2022). Vinicius and coworkers found that polysaccharides from *Leptospermum* species could influence the initial replication of poliovirus type 1 and bovine herpes zoster virus and had high antiviral activity (Rincao et al., 2012). Lin and collaborators identified a polysaccharide fraction in *Platycladus orientalis (L.) Franco* with anti-HBV activity, primarily via repression of expression of HBsAg and HBeAg and interfering with replication of HBV DNA, with IC$_{50}$ values of 1.33 ± 0.12, 1.67 ± 0.13, and 0.80 ± 0.03 mg/ml, respectively (Lin et al., 2016).

## 6.2 Sulfated derivatives

Sulfated polysaccharides are natural and semi-synthetic acidic polysaccharides formed by substitution of a hydroxyl group for a sulfate group on a monosaccharide in a macromolecular chain (Lu et al., 2021). Usually, sulfated polysaccharides have high activity because the negatively charged sulfate group can bind to glycoproteins in the viral envelope, thereby prohibiting the viral particle from binding to and penetrating the target cell. Sulfated modifications appear to be critical for polysaccharides, with sulfated polysaccharides having greater potential for antiviral activity. For example, the sulfated polysaccharides from *Auricularia auricula* and *Tremella* species have strong activity against the Newcastle disease virus (Zhao et al., 2011; Nguyen et al., 2012). Ma and coworkers isolated a new partially sulfated polysaccharide, PSP-2B, with low cytotoxicity and activity against HSV-1 ($IC_{50}$ = 69 μg/ml) and HSV-2 ($IC_{50}$ = 49 μg/ml) (Ma et al., 2016). Galhardi and colleagues evaluated the activity of *Azadirachta indica* polysaccharides (P1 and P2) and their sulfated derivatives (P1S and P2S) against the poliovirus and herpes zoster virus: P1S was the most active and interacted mainly in the initial stages of viral replication (Faccin-Galhardi et al., 2012). Godoi and collaborators investigated the activity of sulfated polysaccharides from *Adenanthera pavonina* seeds against poliovirus type 1, and concluded that they repressed poliovirus type 1 at several steps of replication and had low cytotoxicity (de Godoi et al., 2014). LJ04 is an acidic polysaccharide that can inactivate EV71 within 2 h at 37°C (Yue et al., 2017). The sulfate group is vital to the antiviral activity of LJ04 (Li et al., 2020). Mukherjee and collaborators chemically vulcanized arabinoxylan (1P) from the seed husks of *Plantago ovata* and found that the sulfate group of arabinoxylan (2P) conferred activity against HSV-1 (Mukherjee et al., 2021). Kappa carrageenan (3P) is present in red algae plants. Kappa carrageenan (3P) and its sulfated derivatives have high inhibitory effects against IAV replication *in vitro* and *in vivo* (Wang W. et al., 2012). Oral or nasal sprays containing kappa gum have been shown inactivate SARS-CoV-2 infection in cultures of human airway epithelial cells (Schutz et al., 2021).

## 6.3 Structure−activity relationship of polysaccharides with regard to viruses

The type of functional group in polysaccharides is closely related to their antiviral activity. Cai's team demonstrated that pectic polysaccharides derived from the above-ground parts of *Portulaca oleracea L.* could restrain viral penetration and possessed anti-HSV-2 activity. It has highly methyl-esterified and partially acetylated residues of galacturonic acid in its structure. Its anti-HSV-2 activity ceases after removal of esterification; the methyl esterification or acetylation of galacturonic acid (GalA) residues might be responsible for the

FIGURE 9
Factors affecting the antiviral activity of sulfated polysaccharides.
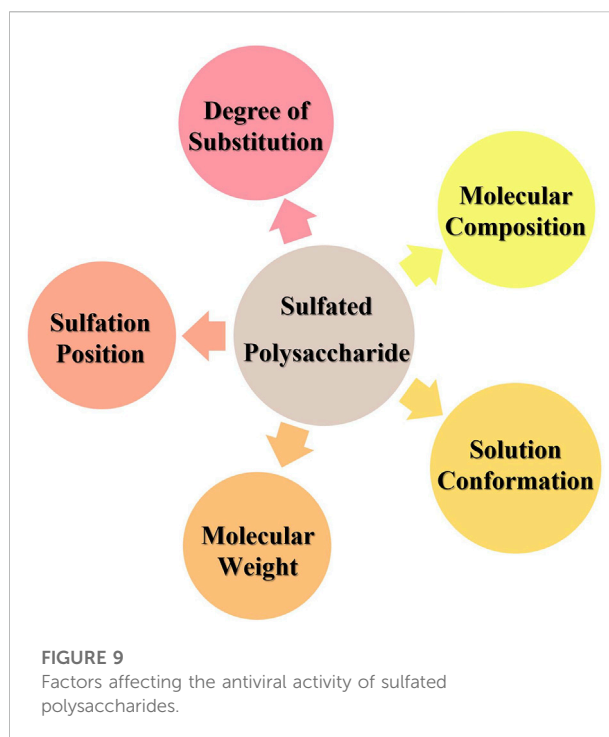
antiviral effect (Dong et al., 2010). Liu and collaborators subjected neutral polysaccharides extracted from *Polygonatum cyrtonema Hua* to sulfation, phosphorylation, carboxymethylation, acetylation, or sulfonylation. Phosphorylation or sulfation could intensify the inhibitory activity of neutral polysaccharides against the HSV. The sulfonylated derivative had identical activity to that of neutral polysaccharides. Acetylation or carboxymethylation depressed the antiviral activity of neutral polysaccharides (Liu et al., 2011).

Sulfation is the most common approach to chemical derivatization of polysaccharides. Various factors influence the antiviral activity of sulfated polysaccharides: the degree of substitution, sulfation position, molecular composition, molecular weight, and solution conformation of the polysaccharide (Ghosh et al., 2009) (Figure 9). The number of sulfate groups is correlated closely with antiviral activity in polysaccharides. Jiao and his colleagues isolated four polysaccharides from several Atlantic Canadian seaweeds, all of which had activity against influenza viruses. The activity of these four polysaccharides decreased as their sulfate content increased (Jiao et al., 2012). However, the antiviral activity of the polysaccharides did not follow a simple linear relationship with the degree of sulfation. Wang's group revealed that the anti-IAV activity of carrageenan oligosaccharides was significantly different despite possessing similar sulfate content. K-keratan gum oligosaccharide had the highest activity at a sulfate content of 0.8–1.0 mol/mol of disaccharide and a molecular weight of 1–3 kDa, thereby indicating that sulfation sites also influenced

antiviral activity (Wang W. et al., 2012). Thuy and coworkers reported that fucoidan isolated from three species of brown seaweed possessed distinctive anti-HIV activity. However, the anti-HIV activity of compounds with different degrees of sulfation and sulfate sites was very similar to each other, which suggested that the molecular weight and type of glycosidic bond of fucoidan were the main factors affecting their antiviral activity (Thuy et al., 2015).

In addition, the molecular weight and conformational changes of a polysaccharide can affect its antiviral activity. Witvrouw and his team revealed that dextran sulfate of higher molecular weight had higher antiviral activity than that of dextran sulfate of lower molecular weight if the molecular-weight range was 1–500 kDa (Witvrouw and De Clercq, 1997). Lopes and collaborators analyzed the activity of seven chemically modified sulfated polysaccharides from green seaweed against the HSV. SU1F1 (a heterosaccharide with a molecular weight of 34 kDa) provided clearly superior antiviral activity to that of SU1F2 (molecular weight <5 kDa) (Lopes et al., 2017). Tuvaanjav's group sulfated two water-soluble polysaccharides from *Cynomorium songaricum Rupr.* They noted that the sulfated polysaccharide could inhibit HIV infection with an $EC_{50}$ value of 0.3–0.4 μg/ml. They postulated that sulfation changed the conformation of the polysaccharide and enhanced the electrostatic interaction of sulfate groups (Tuvaanjav et al., 2016).

# 7 Organic acids

The main organic acids involved in the antiviral activity of NPs are ferulic acid, cinnamic acid, chlorogenic acid, and caffeic acid.

Carvalho and his colleagues discovered that cis-cinnamic acid (1R) and ferulic acid (2R) had high anti-CDV activity, and that the antiviral effect of ferulic acid (2R) was stronger than that of (1R) (Carvalho et al., 2013). *Trans-*cinnamic acid (3R) is structurally similar to (2R), but did not show activity against the CDV, probably owing to the substituents at the C-4 and C-5 positions of (2R). Chlorogenic acid (4R) had antiviral activity, especially in fighting the herpes virus and CVB3 (Yu, 2017). Ding's group discovered that (4R) exhibited activity against influenza viruses, with $EC_{50}$ values of 44.87 μM against the H1N1 virus and 62.33 μM against the H3N2 virus (Ding et al., 2017). Caffeic acid (5R) is a degradation product of (4R) and appears to be widespread in plants (Boerjan et al., 2003). Shen and his collaborators reported that (5R) could inhibit HCV replication by activating the Kelch-like ECH-associated protein 1/Nuclear factor (erythroid-derived 2)-like 2 (Keap1/Nrf2) pathway and led to an increase in protein expression of p62, with an $IC_{50}$ value of 100 ± 20 μM (Shen et al., 2018). Ogawa and coworkers found that (5R) could inhibit severe fever with thrombocytopenia syndrome virus (SFTSV) infection with an

$IC_{50}$ of 0.048 mM. The mechanism of action was mainly through suppression of binding of the SFTSV to cells rather than dependence upon its acidity (Ogawa et al., 2018). Weng's team discovered that the activity of (5R) was higher than (4R) in elderberry extracts against human coronavirus NL63, with an IC50 of 3.54, and 43.45 μM, respectively (Weng et al., 2019).

# 8 Others

Tatanan A (1O) is a novel sesquiterpene lignan. It was first identified in the ethanol extract of *Acorus calamus L.* roots (Ni et al., 2011). Yao and colleagues found that (1O) could oppress the translation and early RNA synthesis of DENV-2, thereby resulting in new activity against DENV-2 ($EC_{50}$ = 3.9 μM) (Yao et al., 2018). Cui and collaborators demonstrated that manassantin B (2O) (a lignan-like compound derived from the roots of *Saururus chinensis*) conferred high activity against replication of the Epstein-Barr virus (EBV) with an $EC_{50}$ of 1.72 μM, thereby providing the first evidence of an anti-EBV effect in lignans (Cui et al., 2014). Pang and coworkers reported the anti-HBV activity of lutein (3O). It blocked secretion of HBsAg and the amount of extracellular HBV DNA in HepG2 cells in a dose-dependent manner (Pang et al., 2010). Ratnoglik and coworkers characterized the high anti-HCV activity of pyropheophorbide (4O) from *Morinda citrifolia* leaves. It induced inhibition of RNA replication and protein synthesis of the HCV with antiviral effects at entry and post-entry steps with an $IC_{50}$ of 0.2 μg/ml (Ratnoglik et al., 2014). An enhanced interferon-α (IFN-α) anti-HCV agent, diosgenin (5O) (steroidal saponin of plant origin) was identified by Wang and collaborators as having anti-HCV activity with an $EC_{50}$ of 3.8 μM. A possible mechanism of action may be related to inhibition of expression of signal transducer and activator of transcription-3 (Wang Y. J. et al., 2011).

# 9 Conclusion

Viruses pose a serious challenge to the health and quality of life of humans. Their general spread and rapid mutation has severely compromised the efficacy of antiviral drugs, thereby stimulating research and development of new antiviral drugs (Owen et al., 2022).

Antiviral drugs were developed to be used as a "second step" after vaccination. Use of antiviral agents enables rapid clinical use during outbreaks of viral diseases if vaccines are not available. This strategy can control the spread of viral diseases and protect the lives and health of humans. Vaccine are designed to be virus-specific and to treat individual viruses, but fail to deliver the full range of antiviral effects, including low (or no) effects against mutant strains of a virus (Jefferson et al., 2014). Drug resistance is

also an emerging problem. For instance, almost all prevalent influenza strains are mutated with resistance to adamantanes, which suggests an urgent need to reinvigorate development of antiviral drugs (Van Poelvoorde et al., 2020).

In recent years, NPs have emerged as new sources for development of antiviral drugs, with the potential to be developed into broad-spectrum antiviral drugs. The large number of compounds, comprehensive antiviral activity, and low cytotoxicity could be the advantages of using NPs as antiviral drugs (Mast et al., 2020). Most studies on antiviral agents have focused on the activity of NPs, which can inhibit different types of viruses. However, studies on related structural modifications and derivatization are relatively scarce, and the structure–activity relationship between NPs and their antiviral effects is seriously lacking, which can not well guide the synthesis of antiviral drugs derived from NPs.

This review surveyed NPs with antiviral activity and their derivatives in the past 2 decades, and summarized one hundred and twelve compounds' structures and their antiviral activities. On this basis, we systematically explored the conformational relationships of different structural types of NPs in antiviral aspects. Alkaloids, quinones, flavonoids and terpenoids showed bright performance in exerting antiviral activity. Meanwhile, the derivatives of indole alkaloids, anthraquinones, naphthoquinones, flavonols and pentacyclic triterpenes could be substantially enhanced in their antiviral activities by appropriate structural modifications. These structural skeletons are very promising for the development of novel antiviral drugs and deserve further investigation. The positions 2, 3, and five on the indole ring were found to be important sites for antiviral activity in indole alkaloids. The introduction of amide and ester groups at the 2-position could enhance their antiviral activity, and the oxindole backbone formed by the introduction of carbonyl groups was also unique in antiviral. The number of hydroxyl groups in anthraquinones would correlate with their ability to exert antiviral activity. It was possible to enhance the inhibition of viruses by increasing the number of hydroxyl groups and keto-phenol systems on the same benzene ring. In addition, the introduction of epoxide structures in naphthoquinone compounds and the synthesis of naphthoquinone multimers could be employed for antiviral derivatization. The type and position of the substituent in the NP could have an effect on the antiviral activity of the compound. In some sites, the introduction of some groups would weaken the antiviral activity of natural products. For example, the introduction of $2'$ hydroxyl groups on the B ring of flavonoids and 3-ketone groups in pentacyclic triterpenoids would have a detrimental effect upon antiviral activity. This knowledge could provide some ideas and directions for derivatization of the NP and strongly help to design and synthesize more antiviral drugs.

Drug resistance is a very challenging factor in the development of antiviral drugs. NPs offer great potential to combat this problem. Compared with drugs with single-spectrum antiviral activity, the multi-targeting of NPs could elicit more possibilities for antiviral agents. A combination of NPs with antiviral drugs could enhance the inhibitory and synergistic activity of antiviral drugs against drug-resistant strains. Artesunate (a derivative of artemisinin) has been shown to have activity against HCMV-susceptible, ganciclovir-resistant sublines, and clinical isolates without cross-resistance. Artesunate could offer a new approach to clinically refractory HCMV infections if standard antiviral therapies fail (Efferth et al., 2002; Schnepf et al., 2011). Studies have suggested that a combination of artesunate with the established antiviral drugs ganciclovir, cidofovir, maribavir, or phosphonate provide synergistic inhibition of the HCMV and reduce resistance to antiviral drugs (Drouot et al., 2016). Heredia and collaborators found that resveratrol increased the anti-HIV activity of tenofovir by 10-fold and restored susceptibility of TFV-resistant viruses. (Heredia et al., 2013). Kim's team revealed that isoquercetin was highly effective in treatment of influenza viruses (even better than the positive control, amantadine). Moreover, isoquercetin could act in synergy with amantadine against influenza viruses and reduce resistance to amantadine (Kim et al., 2010). Haidari and his team discovered that a combination of pomegranate polyphenol extract and oseltamivir increased the anti-influenza effect of oseltamivir synergistically, and inhibited replication of the human influenza-A virus and H3N2 influenza virus *in vitro* (Haidari et al., 2009). Propolis is a non-toxic NP. Propolis and acyclovir have a strong synergistic effect against the herpes virus; perhaps a component of propolis affects cell division and increases the efficacy of acyclovir (Yildirim et al., 2016).

Current research on the actions of NPs against viruses has limitations. Many compounds have antiviral activity, but most of the active ingredients are present in low concentrations and difficult to isolate from NPs. Most studies have focused on the isolation and identification of active ingredients, but few studies have explored structural modifications. Many studies on antiviral activity showed only preliminary screening for antiviral activity and little research on the mechanisms and targets of NPs against viruses. Conducting clinical trials to demonstrate their efficacy and toxicity *in vivo* is not ethical, so most studies have been at the cellular level. This problem has restricted the development of antiviral drugs. Further research is required to assess the feasibility of NPs being used as antiviral drugs in clinical practice. It has been proposed that the antiviral activity of NPs could be deepened through a combination of technologies, such as high-throughput screening, synthetic biology, metabolic engineering, and medicinal chemistry. In recent years, artificial intelligence has been applied gradually for the

discovery and development of drugs. Computer-aided drug design as well as artificial intelligence drug discovery and design have started to become the core technologies for innovative drug research because they have a short development cycle and high hit rate. These technologies could provide a new impetus to develop safe and efficacious antiviral drugs faster, and drive the development of innovative drugs.

## Author contributions

YG: Conceptualization and writing (original draft). AM, XW, and CY: Writing (review and editing). XC, GL, and FQ: Supervision.

## Funding

## References

Astani, A., Reichling, J., and Schnitzler, P. (2010). Comparative study on the antiviral activity of selected monoterpenes derived from essential oils. *Phytother. Res.* 24 (5), 673–679. doi:10.1002/ptr.2955

Baek, S. H., Lee, J. G., Park, S. Y., Bae, O. N., Kim, D. H., and Park, J. H. (2010). Pectic polysaccharides from panax ginseng as the antirotavirus principals in ginseng. *Biomacromolecules* 11 (8), 2044–2052. doi:10.1021/bm100397p

Barlow, A., Landolf, K. M., Barlow, B., Yeung, S. Y. A., Heavner, J. J., Claassen, C. W., et al. (2020). Review of emerging pharmacotherapy for the treatment of coronavirus disease 2019. *Pharmacotherapy.* 40 (5), 416–437. doi:10.1002/phar.2398

Boerjan, W., Ralph, J., and Baucher, M. (2003). Lignin biosynthesis. *Annu. Rev. Plant Biol.* 54, 519–546. doi:10.1146/annurev.arplant.54.031902.134938

Cai, M., Shao, L., Yang, F., Zhang, J. H., and Yu, F. (2022). Design, synthesis of pentacyclic triterpenoid glucose conjugate and *in vitro* activity against influenza virus. *Chin. J. Org. Chem.* 42 (05), 1453–1462. doi:10.6023/cjoc202111008

Carvalho, O. V., Botelho, C. V., Ferreira, C. G., Ferreira, H. C., Santos, M. R., Diaz, M. A., et al. (2013). *In vitro* inhibition of canine distemper virus by flavonoids and phenolic acids: Implications of structural differences for antiviral design. *Res. Vet. Sci.* 95 (2), 717–724. doi:10.1016/j.rvsc.2013.04.013

Ceole, L. F., Companhoni, M. V. P., Lopes, S. M. S., de Oliveira, A. J. B., Goncalves, R. A. C., Dias, B. P., et al. (2020). Anti-herpes activity of polysaccharide fractions from Stevia rebaudiana leaves. *Nat. Prod. Res.* 34 (11), 1558–1562. doi:10.1080/14786419.2018.1516662

Cetina-Montejo, L., Ayora-Talavera, G., and Borges-Argaez, R. (2019). Zeylanone epoxide isolated from Diospyros anisandra stem bark inhibits influenza virus *in vitro*. *Arch. Virol.* 164 (6), 1543–1552. doi:10.1007/s00705-019-04223-y

Chander, S., Tang, C. R., Penta, A., Wang, P., Bhagwat, D. P., Vanthuyne, N., et al. (2018). Hit optimization studies of 3-hydroxy-indolin-2-one analogs as potential anti-HIV-1 agents. *Bioorg. Chem.* 79, 212–222. doi:10.1016/j.bioorg.2018.04.027

Chen, M. H., Gan, L. S., Lin, S., Wang, X. L., Li, L., Li, Y. H., et al. (2012). Alkaloids from the root of Isatis indigotica. *J. Nat. Prod.* 75 (6), 1167–1176. doi:10.1021/np3002833

Cheng, C., Zhang, W., and Shi, L, Y. (2021). Progress on the active ingredients and molecular targets of traditional Chinese medicine with antiviral property. *Chin. J. Tradit. Chin. Med. Pharm.* 36 (10), 5997–6001.

Cheng, D. Q., Sun, L., Zou, S. Y., Chen, J., Mao, H. Y., Zhang, Y. J., et al. (2019). Antiviral effects of houttuynia cordata polysaccharide extract on murine norovirus-1 (MNV-1)A human norovirus surrogate. *Molecules* 24 (9), 1835. doi:10.3390/molecules24091835

Cheng, S. T., Hu, J. L., Ren, J. H., Yu, H. B., Zhong, S., Wong, V. K. W., et al. (2021). Dicoumarol, an NQO1 inhibitor, blocks cccDNA transcription by promoting degradation of HBx. *J. Hepatology* 74 (3), 522–534. doi:10.1016/j.jhep.2020.09.019

Chiu, Y. H., Chan, Y. L., Tsai, L. W., Li, T. L., and Wu, C. J. (2012). Prevention of human enterovirus 71 infection by kappa carrageenan. *Antivir. Res.* 95 (2), 128–134. doi:10.1016/j.antiviral.2012.05.009

Cui, H., Xu, B., Wu, T. Z., Xu, J., Yuan, Y., and Gu, Q. (2014). Potential antiviral lignans from the roots of Saururus chinensis with activity against epstein–barr virus lytic replication. *J. Nat. Prod.* 77 (1), 100–110. doi:10.1021/np400757k

da Silva, P. G., Fonseca, A. H., Ribeiro, M. P., Silva, T. D., Grael, C. F. F., Pena, L. J., et al. (2021a). Bisbenzylisoquinoline alkaloids of Cissampelos sympodialis with antiviral activity against Dengue virus. *Nat. Prod. Res.* 35 (24), 6129–6133. doi:10.1080/14786419.2020.1827404

da Silva, P. G., Fonseca, A. H., Ribeiro, M. P., Silva, T. D., Grael, C. F. F., Pena, L. J., et al. (2021b). Bisbenzylisoquinoline alkaloids of Cissampelos sympodialis with *in vitro* antiviral activity against Zika virus. *Front. Pharmacol.* 12, 743541. doi:10.3389/fphar.2021.743541

de Godoi, A. M., Faccin-Galhardi, L. C., Lopes, N., Rechenchoski, D. Z., de Almeida, R. R., Ricardo, N., et al. (2014). Antiviral activity of sulfated polysaccharide of *Adenanthera pavonina* against poliovirus in HEp-2 cells. *Evidence-Based Complementary Altern. Med.* 2014, 1–6. doi:10.1155/2014/712634

de Oliveira, A. J. B., Cordeiro, L. M. C., Goncalves, R. A. C., Ceole, L. F., Ueda-Nakamura, T., and Iacomini, M. (2013). Structure and antiviral activity of arabinogalactan with (1 -> 6)-beta-D-galactan core from Stevia rebaudiana leaves. *Carbohydr. Polym.* 94 (1), 179–184. doi:10.1016/j.carbpol.2012.12.068

Demicheli, V., Jefferson, T., Di Pietrantonj, C., Ferroni, E., Thorning, S., Thomas, R. E., et al. (2018). Vaccines for preventing influenza in the elderly. *Cochrane Database Syst. Rev.* 2, CD004876. doi:10.1002/14651858.CD004876.pub4

Ding, L., Münch, J., Goerls, H., Maier, A., Fiebig, H.-H., Lin, W.-H., et al. (2010). Xiamycin, a pentacyclic indolosesquiterpene with selective anti-HIV activity from a bacterial mangrove endophyte. *Bioorg. Med. Chem. Lett.* 20 (22), 6685–6687. doi:10.1016/j.bmcl.2010.09.010

## Conflict of interest

The authors declare that the research was conducted in the absence of any commercial or financial relationships that could be construed as a potential conflict of interest.

## Publisher's note

All claims expressed in this article are solely those of the authors and do not necessarily represent those of their affiliated organizations, or those of the publisher, the editors and the reviewers. Any product that may be evaluated in this article, or claim that may be made by its manufacturer, is not guaranteed or endorsed by the publisher.

## Supplementary material

The Supplementary Material for this article can be found online at: https://www.frontiersin.org/articles/10.3389/fchem.2022.1005360/full#supplementary-material

Ding, Y., Cao, Z. Y., Cao, L., Ding, G., Wang, Z. Z., and Xiao, W. (2017). Antiviral activity of chlorogenic acid against influenza A (H1N1/H3N2) virus and its inhibition of neuraminidase. *Sci. Rep.* 7 (1), 45723. doi:10.1038/srep45723

Dong, C. X., Hayashi, K., Lee, J. B., and Hayashi, T. (2010). Characterization of structures and antiviral effects of polysaccharides from Portulaca oleracea L. *Chem. Pharm. Bull.* 58 (4), 507–510. doi:10.1248/cpb.58.507

Dousson, C., Alexandre, F. R., Amador, A., Bonaric, S., Bot, S., Caillet, C., et al. (2016). Discovery of the aryl-phospho-indole IDX899, a highly potent anti-HIV non-nucleoside reverse transcriptase inhibitor. *J. Med. Chem.* 59 (5), 1891–1898. doi:10.1021/acs.jmedchem.5b01430

Drouot, E., Piret, J., and Boivin, G. (2016). Artesunate demonstrates *in vitro* synergism with several antiviral agents against human cytomegalovirus. *Antivir. Ther.* 21 (6), 535–539. doi:10.3851/Imp3028

Efferth, T., Marschall, M., Wang, X., Huong, S. M., Hauber, I., Olbrich, A., et al. (2002). Antiviral activity of artesunate towards wild-type, recombinant, and ganciclovir-resistant human cytomegaloviruses. *J. Mol. Med.* 80 (4), 233–242. doi:10.1007/s00109-001-0300-8

Esteves, P. O., de Oliveira, M. C., Barros, C. D., Cirne-Santos, C. C., Laneuvlille, V. T., and Paixao, I. C. P. (2019). Antiviral effect of caulerpin against Chikungunya. *Nat. Prod. Commun.* 14 (10), 1934578X1987829–6. doi:10.1177/1934578x19878295

Faccin-Galhardi, L. C., Yamamoto, K. A., Ray, S., Ray, B., Linhares, R. E. C., and Nozawa, C. (2012). The *in vitro* antiviral property of Azadirachta indica polysaccharides for poliovirus. *J. Ethnopharmacol.* 142 (1), 86–90. doi:10.1016/j.jep.2012.04.018

Fan, B, Z., Wang, Y, X., Lian, X, T., Xie, W, S., Yu, Y., and Liang, J, H. (2020). Structure-activity relationships and mechanisms of triterpenoids against virus. *CIESC. J.* 71 (9), 4071–4101.

Fang, Y, J., Xu, A, C., An, M, M., Wang, F., and Jiang, Y, Y. (2015). Research advances in pharmacokinetics and pharmacological effects of flavonoids. *pcar.* 15 (1), 6–9. doi:10.5428/pcar20150102

Frecentese, F., Sosic, A., Saccone, I., Gamba, E., Link, K., Miola, A., et al. (2016). Synthesis and *in vitro* screening of new series of 2, 6-Dipeptidyl-anthraquinones: Influence of side chain length on HIV-1 nucleocapsid inhibitors. *J. Med. Chem.* 59 (5), 1914–1924. doi:10.1021/acs.jmedchem.5b01494

Furuta, A., Tsubuki, M., Endoh, M., Miyamoto, T., Tanaka, J., Salam, K. A., et al. (2015). Identification of hydroxyanthraquinones as novel inhibitors of hepatitis C virus NS3 helicase. *Int. J. Mol. Sci.* 16 (8), 18439–18453. doi:10.3390/ijms160818439

Ghosh, T., Chattopadhyay, K., Marschall, M., Karmakar, P., Mandal, P., and Ray, B. (2009). Focus on antivirally active sulfated polysaccharides: From structure-activity analysis to clinical evaluation. *Glycobiology* 19 (1), 2–15. doi:10.1093/glycob/cwn092

Gotti, C., and Clementi, F. (2021). Cytisine and cytisine derivatives. More than smoking cessation aids. *Pharmacol. Res.* 170 (1-3), 105700. doi:10.1016/j.phrs.2021.105700

Haidari, M., Ali, M., Casscells, S. W., and Madjid, M. (2009). Pomegranate (punica granatum) purified polyphenol extract inhibits influenza virus and has a synergistic effect with oseltamivir. *Phytomedicine* 16 (12), 1127–1136. doi:10.1016/j.phymed.2009.06.002

Hassam, M., Basson, A. E., Liotta, D. C., Morris, L., van Otterlo, W. A. L., and Pelly, S. C. (2012). Novel cyclopropyl-indole derivatives as HIV non-nucleoside reverse transcriptase inhibitors. *ACS Med. Chem. Lett.* 3 (6), 470–475. doi:10.1021/ml3000462

Heredia, A., Davis, C. E., Reitz, M. S., Le, N. M., Wainberg, M. A., Foulke, J. S., et al. (2013). Targeting of the purine biosynthesis host cell pathway enhances the activity of tenofovir against sensitive and drug-resistant HIV-1. *J. Infect. Dis.* 208 (12), 2085–2094. doi:10.1093/infdis/jit395

Huang, C. T., Chao, T. L., Kao, H. C., Pang, Y. H., Lee, W. H., Hsieh, C. H., et al. (2020). Enhancement of the IFN-Beta-Induced host signature informs repurposed drugs for COVID-19. *Heliyon* 6 (12), e05646. doi:10.1016/j.heliyon.2020.e05646

Jefferson, T., Jones, M., Doshi, P., Spencer, E. A., Onakpoya, I., and Heneghan, C. J. (2014). Oseltamivir for influenza in adults and children: Systematic review of clinical study reports and summary of regulatory comments. *BMJ* 348, g2545. doi:10.1136/bmj.g2545

Jiang, Z. Y., Liu, W. F., Zhang, X. M., Luo, J., Ma, Y. B., and Chen, J. J. (2013). Anti-HBV active constituents from piper longum. *Bioorg. Med. Chem. Lett.* 23 (7), 2123–2127. doi:10.1016/j.bmcl.2013.01.118

Jiao, G. L., Yu, G. L., Wang, W., Zhao, X. L., Zhang, J. Z., and Ewart, S. H. (2012). Properties of polysaccharides in several seaweeds from atlantic Canada and their potential anti-influenza viral activities. *J. Ocean. Univ. China* 11 (2), 205–212. doi:10.1007/s11802-012-1906-x

Joseph, U., Su, Y. C. F., Vijaykrishna, D., and Smith, G. J. D. (2017). The ecology and adaptive evolution of influenza A interspecies transmission. *Influenza Other Respir. Viruses* 11 (1), 74–84. doi:10.1111/irv.12412

Karagoz, A. C., Leidenberger, M., Hahn, F., Hampel, F., Friedrich, O., Marschall, M., et al. (2019). Synthesis of new betulinic acid/betulin-derived dimers and hybrids with potent antimalarial and antiviral activities. *Bioorg. Med. Chem.* 27 (1), 110–115. doi:10.1016/j.bmc.2018.11.018

Kim, M., Kim, S. R., Park, J., Mun, S. H., Kwak, M., Ko, H. J., et al. (2022). Structure and antiviral activity of a pectic polysaccharide from the root of Sanguisorba officinalis against enterovirus 71 *in vitro*/vivo. *Carbohydr. Polym.* 281, 119057. doi:10.1016/j.carbpol.2021.119057

Kim, Y. J., Narayanan, S., and Chang, K. O. (2010). Inhibition of influenza virus replication by plant-derived isoquercetin. *Antivir. Res.* 88 (2), 227–235. doi:10.1016/j.antiviral.2010.08.016

Kong, L. B., Li, S. S., Liao, Q. J., Zhang, Y. N., Sun, R. N., Zhu, X. D., et al. (2013). Oleanolic acid and ursolic acid: Novel hepatitis C virus antivirals that inhibit NS5B activity. *Antivir. Res.* 98 (1), 44–53. doi:10.1016/j.antiviral.2013.02.003

La Regina, G., Coluccia, A., Brancale, A., Piscitelli, F., Gatti, V., Maga, G., et al. (2011). Indolylarylsulfones as HIV-1 non-nucleoside reverse transcriptase inhibitors: New cyclic substituents at indole-2-carboxamide. *J. Med. Chem.* 54 (6), 1587–1598. doi:10.1021/jm101614j

Lani, R., Hassandarvish, P., Shu, M.-H., Phoon, W. H., Chu, J. J. H., Higgs, S., et al. (2016). Antiviral activity of selected flavonoids against Chikungunya virus. *Antivir. Res.* 133, 50–61. doi:10.1016/j.antiviral.2016.07.009

Li K., K., Feng, Y. L., Cao, R, M., Chen, H., and Zhai, G, Y. (2021). Research progress on structural modification and biological activity of rutin. *Chin. Tradit. Herb. Drugs* 52 (20), 6413–6424.

Li, W., Sun, L. T., Zhao, L., Yue, X. D., and Dai, S. J. (2022). New C-9-Monoterpenoid alkaloids featuring a rare skeleton with anti-inflammatory and antiviral activities from Forsythia suspensa. *Chem. Biodivers.* 19 (1), e202100668. doi:10.1002/cbdv.202100668

Li, W., Zhao, L., Sun, L. T., Xie, Z. P., Zhang, S. M., Yue, X. D., et al. (2021). Trinorlabdane diterpenoid alkaloids featuring an unprecedented skeleton with anti-inflammatory and anti-viral activities from Forsythia suspensa. *RSC Adv.* 11 (47), 29684–29689. doi:10.1039/d1ra05760j

Li, Y., Yao, J. Y., Han, C. Y., Yang, J. X., Chaudhry, M. T., Wang, S., et al. (2016). Quercetin, inflammation and immunity. *Nutrients* 8 (3), 167. doi:10.3390/nu8030167

Li, Z. H., Cui, B., Liu, X. W., Wang, L. C., Xian, Q. J., Lu, Z. X., et al. (2020). Virucidal activity and the antiviral mechanism of acidic polysaccharides against enterovirus 71 infection *in vitro*. *Microbiol. Immunol.* 64 (3), 189–201. doi:10.1111/1348-0421.12763

Li, Z., Min, Q. X., Huang, H. J., Liu, R. X., Zhu, Y. Y., Zhu, Q. H., et al. (2018). Design, synthesis and biological evaluation of seco-A-pentacyclic triterpenoids-3, 4-lactone as potent non-nucleoside HBV inhibitors. *Bioorg. Med. Chem. Lett.* 28 (9), 1501–1506. doi:10.1016/j.bmcl.2018.03.076

Liao, Y. Y., Chen, L. Z., Li, S. M, Cui, Z. N., Lei, Z., Li, H., et al. (2019). Structure-aided optimization of 3-O-β-chacotriosyl ursolic acid as novel H5N1 entry inhibitors with high selective index. *Bioorg. Med. Chem.* 27 (18), 4048–4058. doi:10.1016/j.bmc.2019.07.028

Lin, Z. H., Liao, W. Z., and Ren, J. Y. (2016). Physicochemical characterization of a polysaccharide fraction from Platycladus orientalis (L.) Franco and its macrophage immunomodulatory and anti-hepatitis B virus activities. *J. Agric. Food Chem.* 64 (29), 5813–5823. doi:10.1021/acs.jafc.6b01387

Liu, S. S., Jiang, J. X., Huang, R., Wang, Y. T., Jiang, B. G., Zheng, K. X., et al. (2019). A new antiviral 14-nordrimane sesquiterpenoid from an endophytic fungus Phoma sp. *Phytochem. Lett.* 29, 75–78. doi:10.1016/j.phytol.2018.11.005

Liu, W. X., Feng, Y., Yu, S., Fan, Z. Q., Li, X. L., Li, J. Y., et al. (2021). The flavonoid biosynthesis network in plants. *Int. J. Mol. Sci.* 22 (23), 12824. doi:10.3390/ijms222312824

Liu, X. X., Wan, Z. J., Shi, L., and Lu, X. X. (2011). Preparation and antiherpetic activities of chemically modified polysaccharides from Polygonatum cyrtonema Hua. *Carbohydr. Polym.* 83 (2), 737–742. doi:10.1016/j.carbpol.2010.08.044

Liu, X., Zhang, X. C., Li, J., Zhou, H., Carr, M. J., Xing, W. J., et al. (2019). Effects of acetylshikonin on the infection and replication of coxsackievirus A16 *in vitro* and *in vivo*. *J. Nat. Prod.* 82 (5), 1089–1097. doi:10.1021/acs.jnatprod.8b00735

Lopes, N., Ray, S., Espada, S. F., Bomfim, W. A., Ray, B., Faccin-Galhardi, L. C., et al. (2017). Green seaweed enteromorpha compressa (chlorophyta, ulvaceae) derived sulphated polysaccharides inhibit herpes simplex virus. *Int. J. Biol. Macromol.* 102, 605–612. doi:10.1016/j.ijbiomac.2017.04.043

Lu, W. J., Yang, Z. F., Chen, J., Wang, D., and Zhang, Y. (2021). Recent advances in antiviral activities and potential mechanisms of sulfated polysaccharides. *Carbohydr. Polym.* 272, 118526. doi:10.1016/j.carbpol.2021.118526

Ma, C. M., Wu, X. H., Hattori, M., Wang, X. J., and Kano, Y. (2009). HCV protease inhibitory, cytotoxic and apoptosis-inducing effects of oleanolic acid derivatives. *J. Pharm. Pharm. Sci.* 12 (3), 243–248. doi:10.18433/J3DW2D

Ma, F. W., Kong, S. Y., Tan, H. S., Wu, R., Xia, B., Zhou, Y., et al. (2016). Structural characterization and antiviral effect of a novel polysaccharide PSP-2B from prunellae spica. *Carbohydr. Polym.* 152, 699–709. doi:10.1016/j.carbpol.2016.07.062

Macedo, N. R. P. V., Ribeiro, M. S., Villaca, R. C., Ferreira, W., Pinto, A. M., Teixeira, V. L., et al. (2012). Caulerpin as a potential antiviral drug against herpes simplex virus type 1. *Rev. Bras. Farmacogn.* 22 (4), 861–867. doi:10.1590/s0102-695x2012005000072

Mast, F. D., Navare, A. T., van der Sloot, A. M., Coulombe-Huntington, J., Rout, M. P., Baliga, N. S., et al. (2020). Crippling life support for SARS-CoV-2 and other viruses through synthetic lethality. *J. Cell Biol.* 219 (10), e202006159. doi:10.1083/jcb.202006159

Matsumoto, Y., Matsuura, T., Aoyagi, H., Matsuda, M., Hmwe, S. S., Date, T., et al. (2013). Antiviral activity of glycyrrhizin against hepatitis C virus *in vitro*. *Plos One* 8 (7), e68992. doi:10.1371/journal.pone.0068992

Meneguzzo, F., Ciriminna, R., Zabini, F., and Pagliaro, M. (2020). Review of evidence available on hesperidin-rich products as potential tools against COVID-19 and hydrodynamic cavitation-based extraction as a method of increasing their production. *Processes* 8 (5), 549. doi:10.3390/pr8050549

Meng, L. J., Guo, Q. L., Xu, C. B., Zhu, C. G., Liu, Y. F., Chen, M. H., et al. (2017b). Diglycosidic indole alkaloid derivatives from an aqueous extract of Isatis indigotica roots. *J. Asian Nat. Prod. Res.* 19 (6), 529–540. doi:10.1080/10286020.2017.1320547

Meng, L. J., Guo, Q. L., Liu, Y. F., Chen, M. H., Li, Y. H., Jiang, J. D., et al. (2017a). Indole alkaloid sulfonic acids from an aqueous extract of Isatis indigotica roots and their antiviral activity. *Acta Pharm. Sin. B* 7 (3), 334–341. doi:10.1016/j.apsb.2017.04.003

Miranda, R. d. S., de Jesus, B. d. S. M., da Silva Luiz, S. R., Viana, C. B., Aā Malafaia, C. R., Figueiredo, F. d. S., et al. (2022). Antiinflammatory activity of natural triterpenes-An overview from 2006 to 2021. *Phytotherapy Res.* 36 (4), 1459–1506. doi:10.1002/ptr.7359

Moghaddam, E., Teoh, B. T., Sam, S. S., Lani, R., Hassandarvish, P., Chik, Z., et al. (2014). Baicalin, a metabolite of baicalein with antiviral activity against Dengue virus. *Sci. Rep.* 4 (1), 5452. doi:10.1038/srep05452

Moradi, M. T., Karimi, A., Rafieian-Kopaei, M., and Fotouhi, F. (2017). *In vitro* antiviral effects of Peganum harmala seed extract and its total alkaloids against influenza virus. *Microb. Pathog.* 110, 42–49. doi:10.1016/j.micpath.2017.06.014

Mukherjee, S., Pujol, C. A., Jana, S., Damonte, E. B., Ray, B., and Ray, S. (2021). Chemically sulfated arabinoxylans from Plantago ovata seed husk: Synthesis, characterization and antiviral activity. *Carbohydr. Polym.* 256, 117555. doi:10.1016/j.carbpol.2020.117555

Muralidharan, A., Russell, M. S., Larocque, L., Gravel, C., Sauvé, S., Chen, Z., et al. (2019). Chitosan alters inactivated respiratory syncytial virus vaccine elicited immune responses without affecting lung histopathology in mice. *Vaccine* 37 (30), 4031–4039. doi:10.1016/j.vaccine.2019.06.003

Newman, D. J., and Cragg, G. M. (2016). Natural products as sources of new drugs from 1981 to 2014. *J. Nat. Prod.* 79 (3), 629–661. doi:10.1021/acs.jnatprod.5b01055

Newman, D. J., and Cragg, G. M. (2020). Natural products as sources of new drugs over the nearly four decades from 01/1981 to 09/2019. *J. Nat. Prod.* 83 (3), 770–803. doi:10.1021/acs.jnatprod.9b01285

Nguyen, T. L., Chen, J., Hu, Y. L., Wang, D. Y., Fan, Y. P., Wang, J. M., et al. (2012). *In vitro* antiviral activity of sulfated Auricularia auricula polysaccharides. *Carbohydr. Polym.* 90 (3), 1254–1258. doi:10.1016/j.carbpol.2012.06.060

Ni, G., Shen, Z. F., Lu, Y., Wang, Y. H., Tang, Y. B., Chen, R. Y., et al. (2011). Glucokinase-activating sesquinlignans from the rhizomes of Acorus tatarinowii schott. *J. Org. Chem.* 76 (7), 2056–2061. doi:10.1021/jo1022712

Nunes, P. C. G., Daumas, R. P., Sanchez-Arcila, J. C., Nogueira, R. M. R., Horta, M. A. P., and Dos Santos, F. B. (2019). 30 years of fatal Dengue cases in Brazil: A review. *BMC Public Health* 19 (1), 329. doi:10.1186/s12889-019-6641-4

Ogawa, M., Shirasago, Y., Ando, S., Shimojima, M., Saijo, M., and Fukasawa, M. (2018). Caffeic acid, a coffee-related organic acid, inhibits infection by severe fever with thrombocytopenia syndrome virus *in vitro*. *J. Infect. Chemother.* 24 (8), 597–601. doi:10.1016/j.jiac.2018.03.005

Oo, A., Rausalu, K., Merits, A., Higgs, S., Vanlandingham, D., Bakar, S. A., et al. (2018). Deciphering the potential of baicalin as an antiviral agent for Chikungunya virus infection. *Antivir. Res.* 150, 101–111. doi:10.1016/j.antiviral.2017.12.012

Owen, L., Laird, K., and Shivkumar, M. (2022). Antiviral plant-derived natural products to combat RNA viruses: Targets throughout the viral life cycle. *Lett. Appl. Microbiol.* 75, 476–499. doi:10.1111/lam.13637

Pan, Q. M., Li, Y. H., Hua, J., Huang, F. P., Wang, H. S., and Liang, D. (2015). Antiviral matrine-type Alkaloids from the rhizomes of Sophora tonkinensis. *J. Nat. Prod.* 78 (7), 1683–1688. doi:10.1021/acs.jnatprod.5b00325

Pang, J. Y., Zhao, K. J., Wang, J. B., Ma, Z. J., and Xiao, X. H. (2014). Green tea polyphenol, epigallocatechin-3-gallate, possesses the antiviral activity necessary to fight against the hepatitis B virus replication *in vitro*. *J. Zhejiang Univ. Sci. B* 15 (6), 533–539. doi:10.1631/jzus.B1300307

Pang, R., Tao, J. Y., Zhang, S. L., Zhao, L., Yue, X., Wang, Y. F., et al. (2010). *In vitro* antiviral activity of lutein against hepatitis B virus. *Phytother. Res.* 24 (11), 1627–1630. doi:10.1002/ptr.3155

Panraksa, P., Ramphan, S., Khongwichit, S., and Smith, D. R. (2017). Activity of andrographolide against Dengue virus. *Antivir. Res.* 139, 69–78. doi:10.1016/j.antiviral.2016.12.014

Parvez, M. K., Al-Dosari, M. S., Alam, P., Rehman, M., Alajmi, M. F., and Alqahtani, A. S. (2019). The anti-hepatitis B virus therapeutic potential of anthraquinones derived from aloe vera. *Phytotherapy Res.* 33 (11), 2960–2970. doi:10.1002/ptr.6471

Pasetto, S., Pardi, V., and Murata, R. M. (2014). Anti-HIV-1 activity of flavonoid myricetin on HIV-1 infection in a dual-chamber *in vitro* model. *Plos One* 9 (12), e115323. doi:10.1371/journal.pone.0115323

Patel, O. P. S., Beteck, R. M., and Legoabe, L. J. (2021). Antimalarial application of quinones: A recent update. *Eur. J. Med. Chem.* 210, 113084. doi:10.1016/j.ejmech.2020.113084

Quintana, V. M., Selisko, B., Brunetti, J. E., Eydoux, C., Guillemot, J. C., Canard, B., et al. (2020). Antiviral activity of the natural alkaloid anisomycin against Dengue and Zika viruses. *Antivir. Res.* 176, 104749. doi:10.1016/j.antiviral.2020.104749

Ratnoglik, S. L., Aoki, C., Sudarmono, P., Komoto, M., Deng, L., Shoji, I., et al. (2014). Antiviral activity of extracts from *Morinda citrifolia* leaves and chlorophyll catabolites, pheophorbide a and pyropheophorbide a, against hepatitis C virus. *Microbiol. Immunol.* 58 (3), 188–194. doi:10.1111/1348-0421.12133

Rincao, V. P., Yamamoto, K. A., Ricardo, N. M. P. S., Soares, S. A., Meirelles, L. D. P., Nozawa, C., et al. (2012). Polysaccharide and extracts from lentinula edodes: Structural features and antiviral activity. *Virol. J.* 9 (1), 37–46. doi:10.1186/1743-422x-9-37

Saha, S., Navid, M. H., Bandyopadhyay, S. S., Schnitzler, P., and Ray, B. (2012). Sulfated polysaccharides from laminaria angustata: Structural features and *in vitro* antiviral activities. *Carbohydr. Polym.* 87 (1), 123–130. doi:10.1016/j.carbpol.2011.07.026

Schnepf, N., Corvo, J., Sanson-Le Pors, M. J., and Mazeron, M. C. (2011). Antiviral activity of ganciclovir and artesunate towards human cytomegalovirus in astrocytoma cells. *Antivir. Res.* 89 (2), 186–188. doi:10.1016/j.antiviral.2010.12.002

Schutz, D., Conzelmann, C., Fois, G., Groß, R., Weil, T., Wettstein, L., et al. (2021). Carrageenan-containing over-the-counter nasal and oral sprays inhibit SARS-CoV-2 infection of airway epithelial cultures. *Am. J. Physiology-Lung Cell. Mol. Physiology* 320 (5), L750–L756. doi:10.1152/ajplung.00552.2020

Shen, J., Wang, G. F., and Zuo, J. P. (2018). Caffeic acid inhibits HCV replication via induction of IFNα antiviral response through p62-mediated Keap1/Nrf2 signaling pathway. *Antivir. Res.* 154, 166–173. doi:10.1016/j.antiviral.2018.04.008

Shohan, M., Nashibi, R., Mahmoudian-Sani, M. R., Abolnezhadian, F., Ghafourian, M., Alavi, S. M., et al. (2022). The therapeutic efficacy of quercetin in combination with antiviral drugs in hospitalized COVID-19 patients: A randomized controlled trial. *Eur. J. Pharmacol.* 914, 174615. doi:10.1016/j.ejphar.2021.174615

Si, L. L., Meng, K., Tian, Z. Y., Sun, J. Q., Li, H. Q., Zhang, Z. W., et al. (2018). Triterpenoids manipulate a broad range of virus-host fusion via wrapping the HR2 domain prevalent in viral envelopes. *Sci. Adv.* 4 (11), eaau8408. doi:10.1126/sciadv.aau8408

Song, G. P., Shen, X. T., Li, S. M., Li, Y. B., Liu, Y. P., Zheng, Y. S., et al. (2015). Structure-activity relationships of 3-O-Beta-Chacotriosyl ursolic acid derivatives as novel H5N1 entry inhibitors. *Eur. J. Med. Chem.* 93, 431–442. doi:10.1016/j.ejmech.2015.02.029

Su, M. X., Li, Y. L., Leung, K. T., Cen, Y. Z., Li, T., Chen, R. Z., et al. (2006). Antiviral activity and constituent of Ardisia chinensis Benth against coxsackie B3 virus. *Phytother. Res.* 20 (8), 634–639. doi:10.1002/ptr.1912

Sun, I. C., Chen, C. H., Kashiwada, Y., Wu, J. H., Wang, H. K., and Lee, K. H. (2002). Anti-AIDS agents 49. Synthesis, anti-HIV, and anti-fusion activities of IC9564 analogues based on betulinic acid. *J. Med. Chem.* 45 (19), 4271–4275. doi:10.1021/jm020069c

Thapa, M., Kim, Y., Desper, J., Chang, K. O., and Hua, D. H. (2012). Synthesis and antiviral activity of substituted quercetins. *Bioorg. Med. Chem. Lett.* 22 (1), 353–356. doi:10.1016/j.bmcl.2011.10.119

Thuy, T. T. T., Ly, B. M., Van, T. T. T., Van Quang, N., Tu, H. C., Zheng, Y., et al. (2015). Anti-HIV activity of fucoidans from three Brown seaweed species. *Carbohydr. Polym.* 115, 122–128. doi:10.1016/j.carbpol.2014.08.068

Tseng, C. K., Hsu, S. P., Lin, C. K., Wu, Y. H., Lee, J. C., and Young, K. C. (2017). Celastrol inhibits hepatitis C virus replication by upregulating heme oxygenase-1 via the JNK MAPK/Nrf2 pathway in human hepatoma cells. *Antivir. Res.* 146, 191–200. doi:10.1016/j.antiviral.2017.09.010

Tsypysheva, I. P., Koval'skaya, A. V., Lobov, A. N., Zarubaev, V. V., Karpinskaya, L. A., Petrenko, I. A., et al. (2013). Search for compounds with antiviral activity among synthetic (−)-Cytisine derivatives. *Chem. Nat. Compd.* 48 (6), 1042–1046. doi:10.1007/s10600-013-0460-0

Tsypysheva, I. P., Lai, H. C., Kiu, Y. T., Koval'skaya, A. V., Tsypyshev, D. O., Huang, S. H., et al. (2021). Synthesis and antiviral evaluation of cytisine derivatives against Dengue virus types 1 and 2. *Bioorg. Med. Chem. Lett.* 54, 128437. doi:10.1016/j.bmcl.2021.128437

Tuvaanjav, S., Shuqin, H., Komata, M., Ma, C. J., Kanamoto, T., Nakashima, H., et al. (2016). Isolation and antiviral activity of water-soluble *Cynomorium songaricum* Rupr. polysaccharides. *J. Asian Nat. Prod. Res.* 18 (2), 159–171. doi:10.1080/10286020.2015.1082547

Van Poelvoorde, L. A. E., Saelens, X., Thomas, I., and Roosens, N. H. (2020). Next-generation sequencing: An eye-opener for the surveillance of antiviral resistance in influenza. *Trends Biotechnol.* 38 (4), 360–367. doi:10.1016/j.tibtech.2019.09.009

Walker, P. J., Siddell, S. G., Lefkowitz, E. J., Mushegian, A. R., Adriaenssens, E. M., Alfenas-Zerbini, P., et al. (2021). Changes to virus Taxonomy and to the international code of virus classification and nomenclature ratified by the international committee on Taxonomy of viruses (2021). *Arch. Virol.* 166 (9), 2633–2648. doi:10.1007/s00705-021-05156-1

Wang, C. R., Ng, T. B., Li, L., Fang, J. C., Jiang, Y., Wen, T. Y., et al. (2011). Isolation of a polysaccharide with antiproliferative, hypoglycemic, antioxidant and HIV-1 reverse transcriptase inhibitory activities from the fruiting bodies of the abalone mushroom pleurotus abalonus. *J. Pharm. Pharmacol.* 63 (6), 825–832. doi:10.1111/j.2042-7158.2011.01274.x

Wang, L. J., Geng, C. A., Ma, Y. B., Huang, X. Y., Luo, J., Chen, H., et al. (2012). Synthesis, biological evaluation and structure-activity relationships of glycyrrhetinic acid derivatives as novel anti-hepatitis B virus agents. *Bioorg. Med. Chem. Lett.* 22 (10), 3473–3479. doi:10.1016/j.bmcl.2012.03.081

Wang, W., Zhang, P., Yu, G. L., Li, C. X., Hao, C., Qi, X., et al. (2012). Preparation and anti-influenza A virus activity of kappa-carrageenan oligosaccharide and its sulphated derivatives. *Food Chem. x.* 133 (3), 880–888. doi:10.1016/j.foodchem.2012.01.108

Wang, Y. J., Pan, K. L., Hsieh, T. C., Chang, T. Y., Lin, W. H., and Hsu, J. T. A. (2011). Diosgenin, a plant-derived sapogenin, exhibits antiviral activity *in vitro* against hepatitis C virus. *J. Nat. Prod.* 74 (4), 580–584. doi:10.1021/np100578u

Weng, J. R., Lin, C. S., Lai, H. C., Lin, Y. P., Wang, C. Y., Tsai, Y. C., et al. (2019). Antiviral activity of Sambucus formosana nakai ethanol extract and related phenolic acid constituents against human coronavirus NL63. *Virus Res.* 273, 197767. doi:10.1016/j.virusres.2019.197767

Witvrouw, M., and De Clercq, E. (1997). Sulfated polysaccharides extracted from sea algae as potential antiviral drugs. *General Pharmacol. Vasc. Syst.* 29 (4), 497–511. doi:10.1016/s0306-3623(96)00563-0

Wohlfarth, C., and Efferth, T. (2009). Natural products as promising drug candidates for the treatment of hepatitis B and C. *Acta Pharmacol. Sin.* 30 (1), 25–30. doi:10.1038/aps.2008.5

Wright, G. D. (2019). Unlocking the potential of natural products in drug discovery. *Microb. Biotechnol.* 12 (1), 55–57. doi:10.1111/1751-7915.13351

Wu, Y. J., Li, S., Li, H. X., Zhao, C. Z., Ma, H., Zhao, X. N., et al. (2016). Effect of a polysaccharide from poria cocos on humoral response in mice immunized by H1N1 influenza and HbsAg vaccines. *Int. J. Biol. Macromol.* 91, 248–257. doi:10.1016/j.ijbiomac.2016.05.046

Xi, Z., Zhang, R. Y., Yu, Z. H., and Ouyang, D. (2006). The interaction between tylophorine B and TMV RNA. *Bioorg. Med. Chem. Lett.* 16 (16), 4300–4304. doi:10.1016/j.bmcl.2006.05.059

Xu, Q. L., Xie, J. D., Xu, Z. F., Cai, Y. J., Chen, G. Y., Fu, W. Z., et al. (2021). Quercetin mitigates cardiomyocyte damage caused by viral infections by inhibiting endoplasmic reticulum stress. *Chin. J. Gerontol.* 41 (09), 1933–1936.

Yao, X., Ling, Y., Guo, S., Wu, W., He, S., Zhang, Q., et al. (2018). Tatanan A from the Acorus calamus L. Root inhibited Dengue virus proliferation and infections. *Phytomedicine* 42, 258–267. doi:10.1016/j.phymed.2018.03.018

Yildirim, A., Duran, G. G., Duran, N., Jenedi, K., Bolgul, B. S., Miraloglu, M., et al. (2016). Antiviral activity of hatay propolis against replication of herpes simplex virus type 1 and type 2. *Med. Sci. Monit.* 22, 422–430. doi:10.12659/Msm.897282

Yonekawa, M., Shimizu, M., Kaneko, A., Matsumura, J., and Takahashi, H. (2019). Suppression of R5-type of HIV-1 in CD4(+) NKT cells by V delta 1(+)T cells activated by flavonoid glycosides, hesperidin and linarin. *Sci. Rep.* 9 (1), 7506–7512. doi:10.1038/s41598-019-40587-6

Yoo, D. G., Kim, M. C., Park, M. K., Park, K. M., Quan, F. S., Song, J. M., et al. (2012). Protective effect of ginseng polysaccharides on influenza viral infection. *Plos One* 7 (3), e33678. doi:10.1371/journal.pone.0033678

Yu, D. L., Sakurai, Y., Chen, C. H., Chang, F. R., Huang, L., Kashiwada, Y., et al. (2006). Anti-AIDS agents 69. Moronic acid and other triterpene derivatives as novel potent anti-HIV agents. *J. Med. Chem.* 49 (18), 5462–5469. doi:10.1021/jm0601912

Yu, Y. J. (2017). Analysis of active ingredients and pharmacological effects of Chinese medicine honeysuckle. *Nei Mong. J. Trad. Chin. Med.* 36 (14), 131–150. doi:10.16040/j.cnki.cn15-1101.2017.14.130

Yu, Y., Zhu, C. G., Wang, S. J., Song, W. X., Yang, Y. C., and Shi, J. G. (2013). Homosecoiridoid alkaloids with amino acid units from the flower buds of *Lonicera japonica*. *J. Nat. Prod.* 76 (12), 2226–2233. doi:10.1021/np4005773

Yue, Y. Y., Li, Z. H., Li, P., Song, N. N., Li, B. Q., Lin, W., et al. (2017). Antiviral activity of a polysaccharide from laminaria japonica against enterovirus 71. *Biomed. Pharmacother.* 96, 256–262. doi:10.1016/j.biopha.2017.09.117

Zandi, K., Teoh, B. T., Sam, S. S., Wong, P. F., Mustafa, M. R., and Abu Bakar, S. (2011). Antiviral activity of four types of bioflavonoid against Dengue virus type-2. *Virol. J.* 8 (1), 560–611. doi:10.1186/1743-422x-8-560

Zeng, F. L., Xiang, Y. F., Liang, Z. R., Wang, X., Huang, D. E., Zhu, S. N., et al. (2013). Anti-hepatitis B virus effects of dehydrocheilanthifoline from corydalis saxicola. *Am. J. Chin. Med.* 41 (1), 119–130. doi:10.1142/s0192415x13500092

Zhang, J, H., Liu, W, J., and Li, H, M. (2018). Advances in activities of terpenoids in medicinal plants. *Moder. Trad. Chin. Med. Mat. Medica-World Sci. Tech.* 20 (03), 419–430.

Zhang, L., Zhang, C. J., Zhang, D. B., Wen, J., Zhao, X. W., Li, Y., et al. (2014). An unusual indole alkaloid with anti-adenovirus and anti-HSV activities from *Alstonia scholaris*. *Tetrahedron Lett.* 55 (10), 1815–1817. doi:10.1016/j.tetlet.2014.01.122

Zhang, Y., Hu, H. M., and He, C. F. (2021). An overview of anti-virus of plant essential oil. *Chin. Wild Plant Res.* 40 (07), 48–54.

Zhao, X. N., Hu, Y. L., Wang, D. Y., Guo, L. W., Yang, S. J., Fan, Y. P., et al. (2011). Optimization of sulfated modification conditions of Tremella polysaccharide and effects of modifiers on cellular infectivity of NDV. *Int. J. Biol. Macromol.* 49 (1), 44–49. doi:10.1016/j.ijbiomac.2011.03.010

Zhu, H. Y., Han, L., Shi, X. L., Wang, B. L., Huang, H., Wang, X., et al. (2015). Baicalin inhibits autophagy induced by influenza A virus H3N2. *Antivir. Res.* 113, 62–70. doi:10.1016/j.antiviral.2014.11.003

Zhu, H. Y., Lu, X. X., Ling, L. J., Li, H., Ou, Y. Y., Shi, X. L., et al. (2018). Houttuynia cordata polysaccharides ameliorate pneumonia severity and intestinal injury in mice with influenza virus infection. *J. Ethnopharmacol.* 218, 90–99. doi:10.1016/j.jep.2018.02.016

Zhu, L., Gao, T., Yang, W. H., Liu, Y. N., Liu, X., Hu, Y., et al. (2020). Ebola virus replication is regulated by the phosphorylation of viral protein VP35. *Biochem. Biophys. Res. Commun.* 521 (3), 687–692. doi:10.1016/j.bbrc.2019.10.147

# Natural products in drug discovery and development: Synthesis and medicinal perspective of leonurine

Zhaoyi Li[1†], Keyuan Chen[1†], Peter Rose[2] and Yi Zhun Zhu[1,3]*

[1]State Key Laboratory of Quality Research in Chinese Medicine, School of Pharmacy, Macau University of Science and Technology, Taipa, Macau, China, [2]School of Biosciences, University of Nottingham, Nottingham, United Kingdom, [3]Shanghai Key Laboratory of Bioactive Small Molecules, Department of Pharmacology, School of Pharmacy, Fudan University, Shanghai, China

Natural products, those molecules derived from nature, have been used by humans for thousands of years to treat ailments and diseases. More recently, these compounds have inspired chemists to use natural products as structural templates in the development of new drug molecules. One such compound is leonurine, a molecule isolated and characterized in the tissues of *Herb leonuri*. This molecule has received attention from scientists in recent years due to its potent anti-oxidant, anti-apoptotic, and anti-inflammatory properties. More recently researchers have shown leonurine to be useful in the treatment of cardiovascular and nervous system diseases. Like other natural products such as paclitaxel and artemisinin, the historical development of leonurine as a therapeutic is very interesting. Therefore, this review provided an overview of natural product discovery, through to the development of a potential new drug. Content will summarize known plant sources, the pathway used in the synthesis of leonurine, and descriptions of leonurine's pharmacological properties in mammalian systems.

## Introduction

Human civilization, across all continents, has a long history of use of natural products either in the form of plant, fungal, microbial, or animal-derived extracts, preparations, or isolated compounds. These preparations are being used in the treatment of various ailments and diseases (Ji et al., 2009). Examples of developments in this field litter the historical records in various research publications and pharmacopeias. Common examples include the18th-century description by Europeans of the discovery of aspirin in the leaves of the willow tree (*genus Salix*), having properties that reduce pain, fever, and inflammation (Ugurlucan et al., 2012). Similarly, Paclitaxel, a popular anticancer drug, that was first isolated from the bark and needles of Taxus brevifolia in 1971, and now approved by the FDA for the treatment of various types of cancer (Zhu and

Chen, 2019). Even today, natural products derived from various plants species are still a valuable source of lead compounds, and this is inspiring a generation of scientists interested in the development and design of new therapeutic drugs (Katz and Baltz, 2016). Many of these compounds have various biological activities (Dutta et al., 2019) including anti-inflammation (Azab et al., 2016), anti-cancer (Liu et al., 2020), anti-oxidation (Jaganjac et al., 2021), and anti-viral properties (Thomas et al., 2021). Here, we draw on some of these examples, and describe various success stories relating to the development of natural products as drugs. This review will cover paclitaxel, artemisinin, aspirin, and camptothecin, and we summarize the unique aspects of their developmental process. In addition, a description will be given relating to plant sources, synthetic pathways, and pharmacological activities of the natural product, leonurine. Leonurine has gained interest from scientist due to its therapeutic potential in the treatment of cardiovascular and neurological diseases.

## Extraction and separation

Plants, fungi, microorganisms, and some animal species are novel sources of natural products, and tissues form these have been exploited by researchers in their search for new therapeutics (Sen and Samanta, 2014; Beutler, 2019). Due to the diverse chemical structures and differences in stability and physicochemical properties of natural products, extraction and separation methodologies of natural products have always been a huge challenge. Indeed, difficulties in extraction procedures are a common topic of discussion in the early phases of research on natural products (Sarker and Nahar, 2012; Wang et al., 2022). This problem has led to the development of numerous forms of extraction and isolation procedures used by natural product chemists, ranging from basic solvent extraction procedures through to supercritical $CO_2$ extraction methods; each has its challenges. Historically, solvent extract procedures have been described since the 17th century. Scientists used solvent extraction techniques to isolated morphine from the milk of poppies (Brook et al., 2017), quinine from the bark of the Cinchona tree, and cocaine from coca leaves (Goldstein et al., 2009; Achan et al., 2011). In addition to extraction methods, further complexity arises when the compound of interest requires separation from other constituents present in the tissues of the natural source. For this reason, separation methods such as column chromatography have been developed, and these are often coupled to some form of screening technique to ensure the molecules of interest are present in separated fractions. For example, a biological assay or compound confirmation assessment like nuclear magnetic resonance (NMR) or mass spectroscopy (Chun-Sheng et al., 2016). Common separation methods include high performance liquid chromatography (HPLC) or more informed approaches like liquid
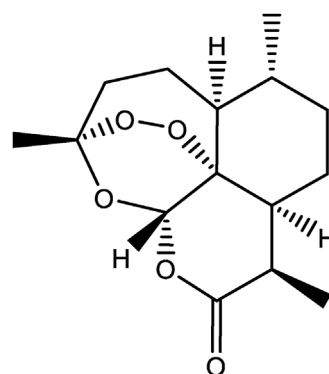


**FIGURE 1**
The chemical structures of Artemisinin.

chromatograph mass spectroscopy (LC-MS) that can be utilized to establish a picture of compound composition. For example, HPLC has been used to conduct fingerprint analysis of compounds having free radical scavenging activities in Angelica sinensis (Yang, 2013).

One of the success stories in natural product chemistry is the extraction and isolation of the antimalarial drug, artemisinin. Artemisinin is an example of a sesquiterpene lactone and was first extracted from the plant sweet wormwood (Figure 1) (A.s.r group, 1977). Isolation and characterization were conducted in the laboratory of Tu Youyou, who won the Lasker Prize in Clinical Medicine in 2011, and later the Nobel Prize for Medicine in 2015. Initial work found that extracts of *Artemisia annua* obtained by heating of plant tissues had minimal antimalarial effects. Therefore, researchers began to interrogate the earliest historical reference to *Artemisia annua* in Ge Hong's "Elbow Reserve Emergency Recipe". These records revealed a more efficient extraction method *viz. A. annua* immersed in water to obtain a juice. This method avoided heating, and yielded extracts with effective anti-malarial properties. Researchers then modified the extraction process in view of the historical information and later used low temperature extraction procedures to isolated the, active ingredients (Tu, 2016; Wang et al., 2019). Finally, the extracts were separated to obtain artemisinin and analogues allowing for further structural confirmation (White et al., 2015; Chang, 2016; Xia et al., 2020). In addition to antimalarial activity, artemisinin also has antiviral (Liu et al., 2019), antitumor (Slezáková and Ruda-Kucerova, 2017), anti-inflammatory (Zhang et al., 2021), and other pharmacological activities, and has a certain therapeutic effect on autoimmune diseases (Efferth and Oesch, 2021). This example of the isolation and characterization of artemisinin draws on the appreciation of historical and traditional knowledge. And allowed for the optimization of methods to facilitate the extraction of artemisinin now widely used in the treatment of malaria.
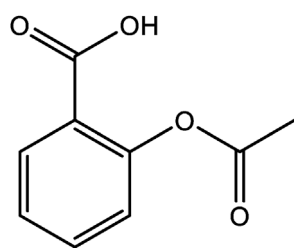
FIGURE 2
The chemical structures of Aspirin.
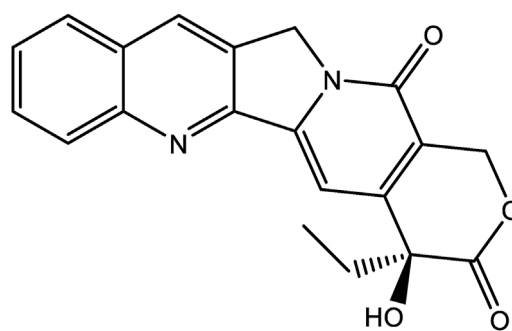


FIGURE 3
The chemical structures of Camptothecin.

Advances in analytical chemistry and organic synthetic routes, extraction and separation techniques have allowed for new approaches to be used by natural product chemistry that give higher extraction efficiency and greater yields. For example, carnosic acid and rosmarinic acid from rosemary were obtained by supercritical fluid extraction (Lefebvre et al., 2021), and brassin from *Caesalpinia sappan* was separated by high-speed countercurrent chromatography (He et al., 2020).

## Artificial synthesis and structural modification

On occasion, researchers are faced with the problem that they are unable to obtain plant tissues in large quantities for the extraction of molecules of interest or that traditional extraction approaches are not efficient enough to obtain compounds at usable levels. Therefore, by the middle of the 19th century, synthetic organic chemistry provided an alternative route to obtaining natural products, albeit *via* a synthetic chemical means. This is exemplified by the breakthrough in production of the first synthetic drug, chloral hydrate (Jones, 2011). This breakthrough spawned a new era in drug development and paved the way for the production of other biological active molecules with the capacity to produce molecules on an industrial scale (Crane and Gademann, 2016).

Aspirin, also known as acetylsalicylic acid, exerts an anti-inflammatory effect by inhibiting the production of prostaglandins and thromboxanes in mammalian cells and tissues, and is widely prescribed as an anti-inflammatory, pain relief and fever reducing medication (Vane, 1971; Montinari et al., 2019). It is one of the most widely used chemically synthesized drugs in the world (Montinari et al., 2019). Interestingly, the origin of aspirin can be traced back 3,500 years ago to the use of willow bark as an ancient pain reliever and antipyretic drug. The active ingredient salicin is now chemically synthesized (Mann, 2000; Montinari et al., 2019). Salicin and other natural derivatives offer examples of how synthetic approaches can be used to im-prove on the original

molecule. In many instances, therapeutics are developed through different structural modifications to reduce toxicity, or to improve the physicochemical traits of compounds such as poor water solubility; this affording better candidate drugs (Yao et al., 2017; Solís-Cruz et al., 2021). Chemically synthesized salicylates are known to cause nausea, stomach irritation and ringing in the ears as side effects. Therefore, to solve this problem, sodium salicylate was modified using acetyl chloride to synthesize acetylsalicylic acid, more commonly known commercially as aspirin (Figure 2) (Montinari et al., 2019; Valgimigli, 2019). This simple modification reduced some of the side-effects attributed to this compound. Aspirin was patented in the United States in 1900, and it was successfully marketed 4 years later. The use of synthetic routes of production show that this approach can have advantages over traditional methods of extraction from plant tissues. To date, asprin is the best-selling drug in the world (Montinari et al., 2019; Valgimigli, 2019), that is mainly used as an anti-platelet drug to prevent cardiovascular and cerebrovascular diseases, such as myocardial infarction, thrombosis, and cerebral apoplexy (Desborough and Keeling, 2017).

Other natural products are also worthy of mention. The quinoline alkaloid, camptothecin is highly cytotoxic and was first isolated from the bark and branches of *Camptotheca acuminata* in China (Figure 3). Camptothecin has significant antitumor properties and was approved in 1970 for the treatment of gastric cancer, bladder cancer and some leukemias (Wall et al., 1966; Chen and Liu, 1994; Khaiwa et al., 2021).

While camptothecin has a wide range of applications, it is limited due to its poor water solubility, fast hydrolysis rate, high toxicity and issues relating to drug resistance (Li et al., 2006; Li et al., 2017). In order to improve the anticancer efficacy and safety of camptothecin, a series of analogs were synthesized using structural modification (Venditto and Simanek, 2010; Khaiwa et al., 2021). On the basis of retaining the key active structure of camptothecin, chemical modifications focused on changes to key functional groups (Martino et al., 2017). For example, the

quinoline ring in the original structure can be opened to convert the molecule into a corresponding ring-opened sodium salt, so as to improve the solubility, and to aid its use in intravenous administration (Ulukan and Swaan, 2002; Martino et al., 2017). Moreover, if the modifications are made on the quinoline ring, the anti-cancer activity can be retained without increasing the cytotoxicity of the molecule. In parallel, by increasing the number of carbon chains in the quinoline ring it is possible to increases lipid solubility and stability in plasma (Liu et al., 2015). Lastly, the hydrolysis of the lactone ring *in vivo* reduces the anticancer activity of camptothecin, by reducing intramolecular hydrogen bond prevents hydrolysis from occurring (Martino et al., 2017).

To date, camptothecin has been used as a structural template for the synthesis of other derivatives namely topotecan, irinotecan and homocamptothecin respectively. Both topotecan and irinotecan have FDA-approval and are both water-soluble derivatives used in the treatment of some clinical cancers (Winterfeldt et al., 1975; Thomas et al., 2004). Topotecan (7-ethyl-10-[4-(1-piperidino)-1-piperidino] carbonyloxycamptothecin) contains a basic amine side chain, which makes it easy to form an ammonium salt and improves water solubility. Topotecan is widely used clinically to treat ovarian cancer and small lung cancer (Liu et al., 2015; Martino et al., 2017). Similarly, irinotecan (9-[(dimethylamino)methyl]-10-hydroxy-camptothecin) is a carbamate analogue of camptothecin, and has enhanced water solubility that is attributed to the presence of an alkaline side chain. Interestingly, irinotecan can be hydrolyzed into metabolites with strong anti-tumor activity *in vivo*, and this drug is currently used in the treatment of rectal cancer (Martino et al., 2017). Collectively, camptothecin is a good example of how structural modification of natural products can be used to manipulate the physicochemical properties of a molecule. On the basis of retaining the original active skeleton, through structural modification, better solubility, greater stability and enhanced anticancer activity can be achieved.

## Drug delivery

As discussed, structural modification of natural products can improve solubility, chemical stability, resistance to metabolism, and to enhance the ability of a drug to cross the blood-brain barrier (Chen et al., 2015; Yao et al., 2017). Occasionally, structural modification of target drug molecules fails to alter bioavailability or to reduce drug toxicity. In this scenario, other strategies are needed to improve and manage the delivery of drugs to cells and tissues. In the last decade, novel drug delivery systems have become popular and include various nano-carriers (Erdoğar et al., 2018; Patra et al., 2018), lipid agents (Efendy Goon et al., 2019), and transdermal delivery systems (Patil and Saraogi, 2014). At present, nanocarriers are one of the most



**FIGURE 4**
The chemical structures of Paclitaxel.
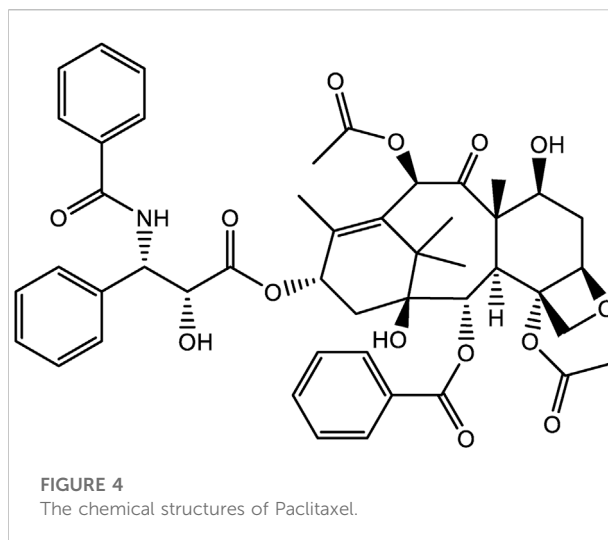
robust delivery systems used in drug research to deliver encapsulate drugs (Wong et al., 2020; Solís-Cruz et al., 2021).

The natural product, paclitaxel, is a secondary metabolite produced by the *genus Taxus*, and was first isolated from the Pacific yew in 1971 (Figure 4). Due to its strong anticancer activity, it was approved for use by the FDA in 1993 for the treatment of various cancers, such as breast cancer, Ovarian, and lung cancer (Wani et al., 1971; Cragg, 1998; Gallego-Jara et al., 2020). Unfortunately, members of the *genus Taxus* are slow growing species, with plants often taking 200 years to reach an appreciable size *viz.* 40 feet in height. At this size, following harvest, only 0.5 g of paclitaxel could be feasibly extracted from plant tissues. To place this into some context, to treat a single patient requires 2 g of paclitaxel, the equivalent of four mature yew trees. As a result, the supply of paclitaxel was greatly restricted in the early years of its clinical use (Alqahtani et al., 2019; Gallego-Jara et al., 2020). However, as patient demand for paclitaxel grew, new developments were needed to meet the growing demand for this drug. This droves research to identify alternative paclitaxel production methods, including total synthetic routes, semi-synthesis, and microbial engineering (Gallego-Jara et al., 2020). Currently, the most commonly used methods of production are semi-synthetic methods (Kumar et al., 2019).

While paclitaxel has strong anticancer activity, its use is made challenging due to its hydrophobic properties and low solubility in water (Bernabeu et al., 2017; Gallego-Jara et al., 2020). To solve this problem, polyoxyethylene castor oil, Cremphor EL (CrEL), and ethanol delivery systems are being developed as novel drug carrier systems. Other approaches are also been considered to facilitate parenteral administration and to reduce adverse reactions like severe allergic reactions (Gelderblom et al., 2001). Currently, albumin-bound paclitaxel (nab-paclitaxel) a nano-delivery approaches have been developed. Nab-paclitaxel,

FIGURE 5
The plant diagram of *Herb Leonuri*.



FIGURE 6
The chemical structures of four alkaloids from *Herb Leonuri*.
**(A)** The chemical structures of leonurine. **(B)** The chemical structures of stachydrine. **(C)** The chemical structures of betaine. **(D)** The chemical structures of trigonelline.

is a formulation that utilises nanoparticles as a carrier without the need for CrEL. Nano-particles are ap-proximately 130 nm in size, and allow for intravenous infusion (Petrelli et al., 2010). Compared with traditional paclitaxel, nab-paclitaxel has reduced side-effects that is largely attributed to the lack of CrEL. This means that higher doses of paclitaxel can be delivered with shorter infusion duration (Gradishar, 2006). In 2005, nab-paclitaxel was approved by FDA for the treatment of metastatic breast cancer (Kundranda and Niu, 2015).

Paclitaxel is a natural product with potent anti-tumor activity. In recent years, a variety of methods have been developed to replace traditional extraction protocols, that circumvent the demand for large batches of raw materials. In addition, by adopting nanotechnology delivery approaches, problems of poor water solubility, low bioavailability, and toxicity have been resolved. These advances have become important in the development of clinical first-line treatment of some cancers by delivering anti-cancer drugs in a more refined manner.

## Herb leonuri and the identification and characterization of leonurine

Stories relating to the development of other natural products are equally as fascinating as that of asprin, camptothecin, and paclitaxel. *Herb leonuri*, commonly known as "Yi-Mu-Cao", is an annual or biennial herb of the lamiaceae family. The plant is native to parts of China, Central Europe, Scandinavia, and Russia, is now naturalized in Japan, Java, Malaysia, and North America (Zhu et al., 2018). According to the Flora of China, *H. leonuri* has a squarish stem, which is clad in short trichome hairs, and is often purplish in coloration especially near the nodes. The opposite leaves have serrated margins and are palmately lobed with long petioles, basal leaves are wedge-shaped with three points while the upper left have three to five. They are slightly hairs above and greyish beneath, and flowers appear in leaf axils on the upper part of the plant and have three-lobed bracts. The calyx of each flower is bell-shaped and has five lobes, and the corolla is irregular and eight to 12 mm in length. The flowers are pink to lavender, usually with a hairy lower lip. There are four protruding stamens, two short and two long, with one pistil, and the fruit has four-chambers (Figure 5) (Wojtyniak et al., 2013).

According to the record of "Shen Nong's Materia Medica", *H. Leonuri* has a pungent taste, and is bitter. The plant is widely used to promote blood circulation, to manage and regulate menstruation, to aid hydration, reducing swelling, clearing heat, and to aid detoxifying (Miao et al., 2019). *H. Leonuri*, as its name is" a beneficial herb for mothers" (Miao et al., 2019), and is considered as a traditional herbal medicine. Other use for this plant includes the treatment of gynecological diseases, irregular menstruation, dysmenorrhea, lochia, edema, oliguria, and Sores (Li et al., 2020). Since 1990, it also has been listed in the Pharmacopoeia of the People's Republic of China, in which many kinds of traditional Chinese medicine prescription contain this plant species. To date, several active compounds have been identified in tissues and extracts of *H. leonuri* including various alkaloids, flavonoids, diterpenes, iridoid glycosides, sterols, peptides, phenylpropanoids, and phenolic

glycosides (Li et al., 2020). Alkaloids are the most important class of active ingredients in this plant, and have become the focus of much research (Zhang et al., 2018). Indeed, four alkaloids have been isolated and characterized in the tissues of this plant namely, leonurine, stachydrine, betaine, and trigonelline, respectively (Figure 6). The pharmacological effects of *H. leonuri* are mainly attributed to the presence of leonurine (Fiskum et al., 2004; Liu X. et al., 2010; Li et al., 2020), a compound present in levels equivalent to 0.02%–0.12% fresh weight (Liu et al., 2013; Huang et al., 2021).

## Isolation and purification aspects of leonurine

Leonurine was first isolated from the plant *H. Leonuri* in 1930, and other alkaloid compounds such as stachydine, betaine, and trigonelline were also isolated. There are various approaches for extracting, isolating, and purifying leonurine from the plant. As early as 1977, Yeung et al. ground and impregnated 5 L of acid methanol (0.1%, v/v) per kilogram of dried plants to obtain a methanol extract of leonurine, and then used alumina column and dextran G-25 column, eluted with a gradient of methanol to 2% acetic acid-methanol, and finally isolated 50 mg/kg of leonurine (Yeung et al., 1977). In 2004, Chao et al. reported the use of ethyl acetate in a Soxhlet extractor to decolorize H. Leonuri and ethanol ultrasonic extraction. The total alkaloids in 2 g crude drug powder accounted for 0.3%, of which stachydine accounted for 0.1–0.2% and accounted for 0.01–0.05% (Zhi et al., 2004). In 2010, Chen et al. reported a method with a high recovery rate, Chen et al. extracted 350 ml of 95% ethanol per 100 g of dry plants for 2 h each, repeated 3 times, and finally obtained 0.15 mg/g of leonurine (Chen et al., 2010). In 2012, Kuchta et al. published a high-performance liquid chromatography method. Kuchta et al. used 120 ml of boiling water to extract 6 g of the plant powder under reflux for 1 h and fixed it with a special octadecyl-bonded stationary phase and an acetonitrile/water gradient as fluidity yielded approximately 3 mg of leonurine (Kuchta et al., 2012). In 2017, Jiang et al. used a two-phase system of ethyl acetate-n-butanol-water (3:2:5) as high-speed countercurrent chromatography to obtain 68 mg of leonurine from 2.48 g of the plant crude extract, and the purity is about 96.2% (Jiang, 2017). In the same year, Cao et al. successfully developed an acidic ionic liquid ultrasonic-assisted extraction method. Cao et al. mixed 1 g of dried plants powder with 20 ml of a 1 mol/L [HMIM][HSO4] aqueous solution, ultrasonicated, and filtered, which could be extracted 0.136‰ of leonurine from plants within 30 min (Cao et al., 2018). This method not only greatly shortens the extraction time, but also reduces the use of organic reagents.

## Structural elucidation and analysis of leonurine

In the past, the traditional identification method of leonurine was to use reverse silica gel thin layer chromatography plate (60 F254) and MeOH:CH$_2$Cl$_2$:NH$_3$ 25% (8:2:3) as mobile phase, under 154 nm UV lamp, leonurine was identified with the Rf value of 0.31 (Kuchta et al., 2012). Nowadays, the identification of leonurine relies more on HPLC, MS, and NMR. Chen et al. used a Acquity UPLC BEH C18 reversed-phase column (100 mm × 2.1 mm) with 1.7 μm spherical porous particles and methanol-ammonium formate (pH = 4.0) as the mobile phase at a flow rate of 0.2 ml/min separation, the maximum absorption peak area of leonurine was detected at 277 nm. Further, under the conditions of the ESI model and typical background source pressure read by ion meter of 1.2 × 10−5 Torr, the capillary temperature of 250 ˚C, electrospray needle voltage of 4 kV, and drying gas of nitrogen, finally, leonurine was obtained with m/z of 321 and ion fragment m/z of 259, 181, and 114 (Chen et al., 2010). At the same time, Xie et al. also used an Agilent Edlipse Plus C18 (100 mm × 2.1 mm, 3.5 μm) reversed-phase column and methanol–0.1% formic acid solution (20:80, 0.2 ml/min) as the mobile phase. In positive electrospray ionization interface and multiple reaction monitoring modes, m/z 312.2→181.1 was determined to be leonurine (Xie et al., 2015). Li et al. used diphenhydramine as the internal standard on an Agilent ZORBAX Eclipse XDB-C18 column (150 mm × 4.6 mm, 5 μm) and a methanol-water mixture containing 0.1% formic acid as the mobile phase with 0.6 ml/min of flow rate was obtained at the retention time of 6.43 min. Furthermore, leonurine was also determined by m/z of 312.2→181.1 under the reaction monitoring (MRM) mode of multiple transitions for mass spectrometry analysis, which used an Agilent 1,200 series HPLC system and an Agilent 6,410 triple quadrupole mass spectrometer equipped with an electrospray ionization (ESI) source. This method detected leonurine and stachydrine in rat plasma, their lower limits of quantitation were 0.895 ng/ml and 0.287 ng/ml, respectively. The linear relationship coefficient with the calibration curve containing the internal standard exceeded 0.99 (Li et al., 2013).

## Artificial synthesis of leonurine

In a similar scenario to that described for paclitaxel, plant-derived leonurine limits its availability for use in research or in the clinical due to it occurring at low levels in plant tissues. While traditional separation and extraction methods do yield leonurine with higher purity (Deng et al., 2013; Cao et al., 2018), the amounts obtained are often low. Therefore, organic synthesis approaches are being employed to produce greater quantities of leonurine.

The synthetic route used in the production of leonurine involves the preparation of the intermediary leucine urea,
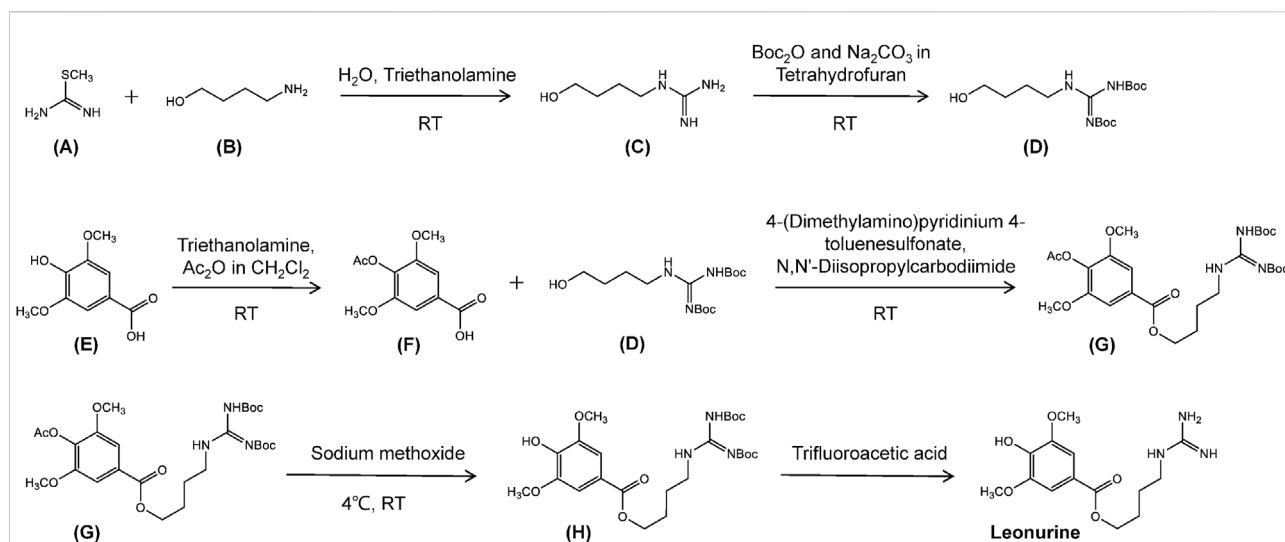
**FIGURE 7**
The chemical synthesis route of leonurine. RT, room temperature. Ac₂O, acetic anhydride. Boc, tert-butoxycarbony group. **(A)** S-methyl-isothiourea. **(B)** 4-Amino-1-butanol. **(C)** N-(4-Hydroxybutyl). **(D)** Boc-protected N-(4-Hydroxybutyl)guanidine. **(E)** Caryophyllic acide. **(F)** 4-Acetoxy-3,5-dimethoxybenzoic acid. **(G)** Boc-protected 4-[(Aminoiminomethyl)amino]butyl 4-(acetyloxy)-3,5-dimethoxybenzoate. **(H)** Boc-protected leonurine.

from succinic acid *via* the Gabriel reaction. This product is then reacted with S-methyl isothiourea sulfate to form leonurine (Cheng et al., 1979). This approach offers a simple method of production although the raw materials are rather expensive. This method has now been superseded using an optimized method developed in the laboratory of Zhu Yizhun at the University of Macau (Figure 7). The production of leonurine can now be achieved at low cost, and in high yield using S-methylisothiourea and 4-amino-1-butanol in a multistep synthesis. The compounds are protected using Boc anhydride to obtain an intermediate (D), and the phenolic hydroxyl group of caryophyllic acid acetic anhydride is used to obtain another key intermediate (F). Both (D) and (F) intermediates are further condensed to obtain a final intermediate (H), which is then deprotected under acidic conditions, to obtain leonurine (Cheng et al., 1979). This method produces large quantities of leonurine of high-purity and offers new sources of this compound for use in research or for clinical application.

## Pharmacological effects of leonurine

In mammalian models, leonurine is reported to promote blood circulation and overcome blood stasis (Miao et al., 2019), these properties are similar to the anticoagulant and anti-inflammatory effects of other traditional Chinese medicines (Deng et al., 1988). The anticoagulant effects have been reported to reduce the formation of thrombosis, reduce the

risk of cardiovascular and cerebrovascular diseases such as atherosclerosis and myocardial infarction (Poredos et al., 2020; Alkarithi et al., 2021). This aroused the authors interest in leonurine and its potential use in cardiovascular and cerebrovascular diseases (Poredos et al., 2020; Alkarithi et al., 2021; Huang et al., 2021).

Cardiovascular disease is a complex multifactorial set of conditions with high mortality rate globally (Bozkurt et al., 2021). Long-term studies have shown that extracts of mother-wort have cardioprotective effect and can improve cardiovascular diseases, such as in models of atherosclerosis, myocardial infarction, and myocardial ischemia. In parallel, studies using purified leonurine are beginning to explore the efficacy of this compound in several clinical trials for the treatment of cardiovascular diseases. Indeed, atherosclerosis is the pathological basis of most serious cardiovascular diseases such as myocardial infarction and thrombosis, coupled with dyslipidemia; a key pathogenic risk factor linked to atherosclerosis. At present, the clinical treatment of atherosclerosis is largely based on the use of statins, but several side effects occur with this class of medication *viz.* impacts on muscle and severe liver function impairment (Suguro et al., 2018; Bozkurt et al., 2021). However, in the future other alternatives derived from natural products could be developed like leonurine. Leonurine has no apparent side-effects or adverse reactions when tested in various models and is effective at reducing atherosclerotic plaque formation, and attenuating atherosclerotic lesions by modulating

inflammatory and oxidative stress pathways (Zhang et al., 2012). The pharmacological mechanism responsible for leonurine action to-ward inflammation and oxidative stress are complex are under investigation. Research by us and other groups, show that leonurine promotes cholesterol efflux by regulating the Pparγ/Lxrα signaling pathway, and attenuates the formation of atherosclerosis (Jiang et al., 2017). Moreover, leonurine not only reduced the occurrence of inflammatory response by inhibiting the activation of NF-κB (Liu et al., 2012), but also enhanced stress defenses in tissues including the activities of catalase (CAT), superoxide dismutase (SOD), glutathione peroxidase (GPx), and glutathione (GSH) levels to regulate oxidative stress (Zhang et al., 2012).

In addition to atherosclerosis, leonurine also improves myocardial infarction, an ischemic heart disease associated with cardiac damage and apoptosis. Leonurine protects cardiac function after myocardial infarction by increasing the viability of hypoxia-injured cardiomyocytes (Liu et al., 2009), by activating the PI3K/AKT/GSK3β signaling pathway (Xu et al., 2018), reducing the expression of pro-apoptotic genes including Bax and Bcl-2, and by inhibiting cell apoptosis (Liu et al., 2009). Similarly, leonurine also prevents cardiac fibrosis and cardiac fibroblast activation following myocardial infarction by regulating the Nox4-ROS pathway (Liu et al., 2013) and attenuate myocardial fibrosis after myocardial infarction by up-regulating miR-29a-3p. Combined these bioactive properties exerting cardio-protective effects in mammalian systems (Wang et al., 2021). More recently, a clinical phase I study has reported that leonurine alter the composition of intestinal microflora, and up-regulates the biosynthesis of adenosylcobalamin (AdoCbl). In turn, these actions promoted the conversion of homocysteine to methionine, reducing the levels of this proatherogenic sulfur amino acid (Liao et al., 2021).

Other research has shown leonurine to have significant therapeutic effects on diseases associated with the central nervous system including stroke, Alzheimer's dis-ease, Parkinson's disease, and depression syndrome (Huang et al., 2021). In the near future, clinical trials are being planned to assess leonurine in the treatment of central nervous system diseases. Stroke is one of the main types of cerebrovascular diseases seen in the clinic, that causes damage to brain tissues caused by cerebral ischemia and hypoxia (Kuriakose and Xiao, 2020). Research has shown that leonurine induces the antioxidant response by activating nuclear factor erythrocyte 2-related factor 2 (Nrf2), and upregulates the expression of vascular endothelial growth factor (VEGF) in neurons, astrocytes, and endothelial cells. Collectively, this prevents brain tissue ischemic injury (Xie et al., 2019). Moreover, leonurine was also shown to improve mitochondrial ultrastructure, to regulated mitochondrial function, and inhibited ATP synthesis, thereby exerting neuroprotective effects (Qi et al., 2010). Furthermore, researchers have shown that leonurine protects the integrity of



FIGURE 8
The structural modification of leonurine. **(A)** The chemical structures of leonurine-cysteine. **(B)** The chemical structures of leonurine-aspirin. **(C)** The chemical structures of leonurine-SPRC.
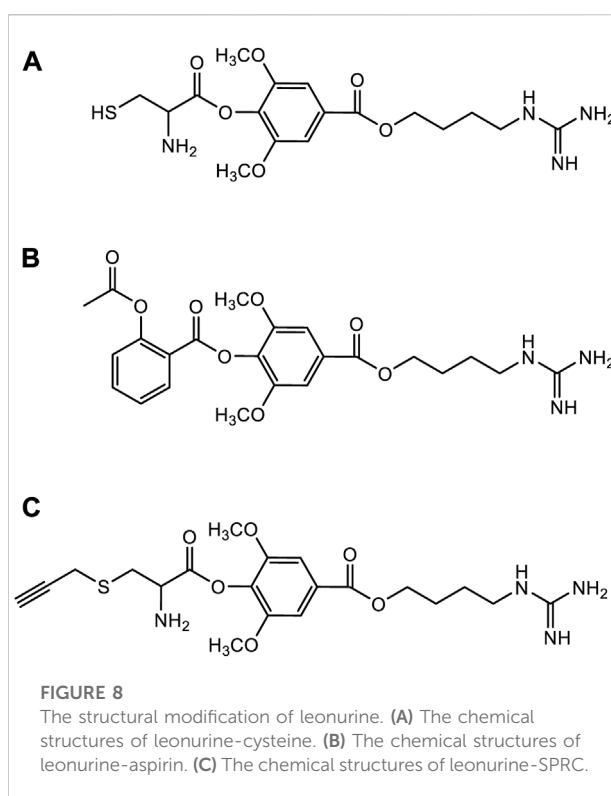
the blood-brain barrier, and prevents stroke by regulating the HDAC4/NOX4/MMP-9 pathway (Zhang et al., 2017). In other neurological conditions like Alzheimer's disease, Parkinson's disease, and depression, leonurine likely acts by inhibiting neuro-inflammation. In other neurological conditions, leonurine promotes maturation of oligodendrocytes and enhancing the myelin sheaths in models of multiple sclerosis (Jin et al., 2019), inhibits the production of pro-inflammatory cytokines including interleukin one beta as well as interleukin 6, inhibits the nuclear factor kappa B signaling pathway (Jia et al., 2017), and promotes neurite outgrowth and neurotrophic activity by modulating the GR/SGK1 signaling pathway (Jia et al., 2017), thereby exerting an antidepressant effect.

Some evidence also points to other potential therapeutuc effects in mammalian systems. Indeed, leonurine can inhibit PDZ-binding motif (TAZ) expression to regulate Treg/Th17 balance to alleviate rheumatoid arthritis (Du et al., 2020), it can inhibit PI3K/Akt/NF-κB signaling pathway to improve osteoarthritis (Yin and Lei, 2018), and improved renal fibrosis by inhibiting TGF-β and NF-κB signaling pathways (Cheng et al., 2015). Other studies show, leonurine can alleviate endometriosis by inhibiting the differentiation of regulatory T cells, providing a therapeutic approach for intractable diseases (Li et al., 2022). Taken together, this simple alkaloid appears to target multiple pathways linked to cytoprotection and inflammation in mammalian systems.

## Structure-activity relationship

Although leonurine has great cardioprotective effects and has broad development prospects as a novel cardioprotective agent, it has certain difficulties in clinical application due to its unique chemical structure such as the guanidine group (Huang et al., 2021). Therefore, several medicinal chemists have been inspired by combination drug studies to study the structural modifications and structure-activity relationships (SARs) of leonurine. A study of SARs showed that the cardioprotective effect of leonurine was essential with butanolamine and guanidine group, and that the aromatic ring was tolerant to various substituents (Luo et al., 2020). Currently, the structural modification of leonurine mainly focuses on the combination with cysteine (Liu et al., 2011), aspirin (Gao et al., 2016), or S-propargyl cysteine (SPRC) (Luo et al., 2020) (Figure 8). Based on cysteine's regulation of endogenous $H_2S$ through the cystathionine γ-lyase (CSE) pathway, Liu et al. designed a leonurine-cysteine analog conjugate. Leonurine-cysteine could modulate hydrogen sulfide production *in vivo*, enhance antioxidant activity, and have better anti-myocardial ischemia effects than leonurine (Liu et al., 2011). On the previous basis, Liu et al. further synthesized SPRC and combined leonurine and SPRC. The alkynyl group of SPRC is a strong electron-withdrawing group, and the carbon atom between the alkynyl group and the sulfur atom is more easily attacked by nucleophiles to generate cysteine, further releasing H2S. Leonurine-SPRC is also easily hydrolyze to release its bioactive substances, such as anti-oxidative stress and anti-apoptosis, and had effective cardioprotection against hypoxia-induced myocardial injury effect (Liu C. et al., 2010). Furthermore, Gao et al. designed a novel combination of leonurine-aspirin based on the antiplatelet activity of aspirin. It not only enhances antioxidant activity and protects cell membrane integrity, but also inhibits pro-inflammatory mediators for more efficient cardioprotection (Gao et al., 2016). So far, all of the novel compounds are more cardioprotective than either compound alone. Therefore, it is necessary to use leonurine as the parent nucleus to modify its structure to develop new novel drugs for cardioprotection.

## Conclusion and prospects

The current review summarizes some of the historical breakthroughs made using classical approaches to drugs discovery. In this instance, the natural products such as paclitaxel, artemisinin, aspirin, and camptothecin have been described. We also introduce, some of the work on the alkaloid, leonurine. Leonurine, is a novel natural product source, that is currently in development as a potential drug candidate. Work systematically summarized its development in recent times, including the plant origin, traditional therapeutic effects, chemical synthesis process, and rich pharmacological activities. Leonurine has attracted worldwide attention due to it having significant protective effects in the cardiovascular and neurological systems in mammals. Indeed, leonurine is now in the clinical trial stages of assessment. It is likely that this molecule, will become another example of how natural products can be exploited in modern day drug discovery programs. Hopefully, this series of stories will inspire new ideas for the development of natural products as drug candidates.

## Author contributions

ZL and KC: Writing—original draft. Peter Rose and YZ: Writing—review and editing. The article was approved for submission by all authors.

## Funding

## Acknowledgments

## Conflict of interest

The authors declare that the research was conducted in the absence of any commercial or financial relationships that could be construed as a potential conflict of interest.

## Publisher's note

All claims expressed in this article are solely those of the authors and do not necessarily represent those of their affiliated organizations, or those of the publisher, the editors and the reviewers. Any product that may be evaluated in this article, or claim that may be made by its manufacturer, is not guaranteed or endorsed by the publisher.

# References

Achan, J., Talisuna, A. O., Erhart, A., Yeka, A., Tibenderana, J. K., Baliraine, F. N., et al. (2011). Quinine, an old anti-malarial drug in a modern world: Role in the treatment of malaria. *Malar. J.* 10 (1), 1–12. doi:10.1186/1475-2875-10-144

Alkarithi, G., Duval, C., Shi, Y., Macrae, F. L., and Ariëns, R. A. (2021). Thrombus structural composition in cardiovascular disease. *Arter. Throm Vas* 41 (9), 2370–2383. doi:10.1161/ATVBAHA.120.315754

Alqahtani, F. Y., Aleanizy, F. S., El Tahir, E., Alkahtani, H. M., and AlQuadeib, B. T. (2019). Paclitaxel. *Profiles drug subst excip relat methodol* 44, 205–238. doi:10.1016/bs.podrm.2018.11.001

A.s.r group (1977). A new type of sesquiterpene lactone—Artemisinin. *Chin. Sci. Bull.* 22, 142. doi:10.1016/B978-0-12-813133-6.00003-2

Azab, A., Nassar, A., and Azab, A. N. (2016). Anti-inflammatory activity of natural products. *Molecules* 21 (10), 1321. doi:10.3390/molecules21101321

Bernabeu, E., Cagel, M., Lagomarsino, E., Moretton, M., and Chiappetta, D. A. (2017). Paclitaxel: What has been done and the challenges remain ahead. *Int. J. Pharm. X.* 526 (1-2), 474–495. doi:10.1016/j.ijpharm.2017.05.016

Beutler, J. A. (2019). Natural products as a foundation for drug discovery. *Curr. Protoc. Pharmacol.* 86 (1), e67. doi:10.1002/cpph.67

Bozkurt, B., Hershberger, R. E., Butler, J., Grady, K. L., Heidenreich, P. A., Isler, M. L., et al. (2021). 2021 ACC/AHA key data elements and definitions for heart failure: A report of the American college of cardiology/American heart association task force on clinical data standards (writing committee to develop clinical data standards for heart failure). *J. Am. Coll. Cardiol.* 14 (4), 2053–2150. doi:10.1016/j.jacc.2020.11.012

Brook, K., Bennett, J., and Desai, S. P. (2017). The chemical history of morphine: An 8000-year journey, from resin to de-novo synthesis. *J. Anesth. Hist.* 3 (2), 50–55. doi:10.1016/j.janh.2017.02.001

Cao, X., Zhu, C., Wang, L., Ye, X., Yu, Y., Mo, W., et al. (2018). Investigating acidic ionic liquid-based ultrasonic-assisted extraction of leonurine from Herba Leonuri. *Sep. Sci. Technol.* 53 (3), 481–486. doi:10.1080/01496395.2017.1385628

Chang, Z. (2016). The discovery of qinghaosu (artemisinin) as an effective anti-malaria drug: A unique China story. *Sci. China Life Sci.* 59 (1), 81–88. doi:10.1007/s11427-015-4988-z

Chen, A. Y., and Liu, L. F. (1994). Design of topoisomerase inhibitors to overcome MDR1-mediated drug resistance. *Adv. Pharmacol.* 29, 245–256. doi:10.1016/s1054-3589(08)61141-2

Chen, J., Li, W., Yao, H., and Xu, J. (2015). Insights into drug discovery from natural products through structural modification. *Fitoterapia* 103, 231–241. doi:10.1016/j.fitote.2015.04.012

Chen, Z., Wu, J. B., Liao, X. J., Yang, W., and Song, K. (2010). Development and validation of an UPLC-DAD-MS method for the determination of leonurine in Chinese motherwort (Leonurus japonicus). *J. Chromatogr. Sci.* 48 (10), 802–806. doi:10.1093/chromsci/48.10.802

Cheng, H., Bo, Y., Shen, W., Tan, J., Jia, Z., Xu, C., et al. (2015). Leonurine ameliorates kidney fibrosis via suppressing TGF-β and NF-κB signaling pathway in UUO mice. *Int. Immunopharmacol.* 25 (2), 406–415. doi:10.1016/j.intimp.2015.02.023

Cheng, K., Yip, C., Yeung, H., and Kong, Y. (1979). Leonurine, an improved synthesis. *Experientia* 35 (5), 571–572. doi:10.1007/BF01960323

Chun-Sheng, Z., Zhi-Jian, L., Ming-Liang, X., Hong-Juan, N., and Zhang, B. (2016). The spectrum-effect relationship—A rational approach to screening effective compounds, reflecting the internal quality of Chinese herbal medicine. *Chin. J. Nat. Med.* 14 (3), 177–184. doi:10.1016/S1875-5364(16)30014-0

Cragg, G. M. (1998). Paclitaxel (Taxol®): A success story with valuable lessons for natural product drug discovery and development. *Med. Res. Rev.* 18 (5), 315–331. doi:10.1002/(sici)1098-1128(199809)18:5<315:aid-med3>3.0.co;2-w

Crane, E. A., and Gademann, K. (2016). Capturing biological activity in natural product fragments by chemical synthesis. *Angew. Chem. Int. Ed.* 55 (12), 3882–3902. doi:10.1002/anie.201505863

Deng, S., Wang, T., Wu, C., Qu, L., Han, L., and Zhang, Y. (2013). Isolation and identification of constituents from Leonurus japonicus. *Chin. J. Med. Chem.* 23, 209–212.

Deng, Y., Yan, W., Chen, C., Gao, D., Yuan, Y., and Dai, D. (1988). Clinical observation on the treatment of thrombocytopenic purpura by huoxue huayu drugs. *J. Tradit. Chin. Med.* 8 (3), 173–176. doi:10.19852/j.cnki.jtcm.1988.03.005

Desborough, M. J., and Keeling, D. M. (2017). The aspirin story–from willow to wonder drug. *Br. J. Haematol.* 177 (5), 674–683. doi:10.1111/bjh.14520

Du, Y.-Y., Chen, Z.-X., Liu, M.-Y., Liu, Q.-P., Lin, C.-S., Chu, C.-Q., et al. (2020). Leonurine regulates Treg/Th17 balance to attenuate rheumatoid arthritis through inhibition of TAZ expression. *Front. Immunol.* 2305, 556526. doi:10.3389/fimmu.2020.556526

Dutta, S., Mahalanobish, S., Saha, S., Ghosh, S., and Sil, P. C. (2019). Natural products: An upcoming therapeutic approach to cancer. *Food Chem. Toxicol.* 128, 240–255. doi:10.1016/j.fct.2019.04.012

Efendy Goon, D., Sheikh Abdul Kadir, S. H., Latip, N. A., Rahim, S. A., and Mazlan, M. (2019). Palm oil in lipid-based formulations and drug delivery systems. *Biomolecules* 9 (2), 64. doi:10.3390/biom9020064

Efferth, T., and Oesch, F. (2021). The immunosuppressive activity of artemisinin-type drugs towards inflammatory and autoimmune diseases. *Med. Res. Rev.* 41 (6), 3023–3061. doi:10.1002/med.21842

Erdoğar, N., Akkın, S., and Bilensoy, E. (2018). Nanocapsules for drug delivery: An updated review of the last decade. *Recent Pat. Drug Deliv. Formul.* 12 (4), 252–266. doi:10.2174/1872211313666190123153711

Fiskum, G., Rosenthal, R. E., Vereczki, V., Martin, E., Hoffman, G. E., Chinopoulos, C., et al. (2004). Protection against ischemic brain injury by inhibition of mitochondrial oxidative stress. *J. Bioenerg. Biomembr.* 36 (4), 347–352. doi:10.1023/B:JOBB.0000041766.71376.81

Gallego-Jara, J., Lozano-Terol, G., Sola-Martínez, R. A., Cánovas-Díaz, M., and de Diego Puente, T. (2020). A compressive review about taxol®: History and future challenges. *Molecules* 25 (24), 5986. doi:10.3390/molecules25245986

Gao, H., Yang, X., Gu, X., and Zhu, Y.-Z. (2016). Synthesis and biological evaluation of the codrug of Leonurine and Aspirin as cardioprotective agents. *Bioorg. Med. Chem. Lett.* 26 (19), 4650–4654. doi:10.1016/j.bmcl.2016.08.058

Gelderblom, H., Verweij, J., Nooter, K., and Sparreboom, A. (2001). Cremophor EL: The drawbacks and advantages of vehicle selection for drug formulation. *Eur. J. Cancer* 37 (13), 1590–1598. doi:10.1016/S0959-8049(01)00171-X

Goldstein, R. A., DesLauriers, C., Burda, A., and Johnson-Arbor, K. (2009). Cocaine: History, social implications, and toxicity: A review. *Semin Diagn Pathol* 26 (1), 10–17. doi:10.1016/bs.podrm.2018.11.001

Gradishar, W. J. (2006). Albumin-bound paclitaxel: A next-generation taxane. *Expert Opin. Pharmacother.* 7 (8), 1041–1053. doi:10.1517/14656566.7.8.1041

He, W., Fan, Q., Zhou, L., Huang, F., Jiang, X., Na, Z., et al. (2020). Preparation of brazilein from Caesalpinia sappan by high performance countercurrent chromatography. *Se Pu* 38 (12), 1363–1368. doi:10.3724/SP.J.1123.2020.03016

Huang, L., Xu, D. Q., Chen, Y. Y., Yue, S. J., and Tang, Y. P. (2021). Leonurine, a potential drug for the treatment of cardiovascular system and central nervous system diseases. *Brain Behav.* 11 (2), e01995. doi:10.1002/brb3.1995

Jaganjac, M., Sredoja Tisma, V., and Zarkovic, N. (2021). Short overview of some assays for the measurement of antioxidant activity of natural products and their relevance in dermatology. *Molecules* 26 (17), 5301. doi:10.3390/molecules26175301

Ji, H. F., Li, X. J., and Zhang, H. Y. (2009). Natural products and drug discovery: Can thousands of years of ancient medical knowledge lead us to new and powerful drug combinations in the fight against cancer and dementia? *EMBO Rep.* 10 (3), 194–200. doi:10.1038/embor.2009.12

Jia, M., Li, C., Zheng, Y., Ding, X., Chen, M., Ding, J., et al. (2017). Leonurine exerts antidepressant-like effects in the chronic mild stress-induced depression model in mice by inhibiting neuroinflammation. *Int. J. Neuropsychopharmacol.* 20 (11), 886–895. doi:10.1093/ijnp/pyx062

Jiang, M.-H. (2017). *Isolation and preparation of leonurine from Leonurus japonicus by high speed countercurrent chromatography.* Zhong Cao Yao, 1778–1783. doi:10.7501/j.issn.0253-2670.2017.09.013

Jiang, T., Ren, K., Chen, Q., Li, H., Yao, R., Hu, H., et al. (2017). Leonurine prevents atherosclerosis via promoting the expression of ABCA1 and ABCG1 in a Pparγ/Lxrα signaling pathway-dependent manner. *Cell. Physiol. biochem.* 43 (4), 1703–1717. doi:10.1159/000484031

Jin, M., Li, Q., Gu, Y., Wan, B., Huang, J., Xu, X., et al. (2019). Leonurine suppresses neuroinflammation through promoting oligodendrocyte maturation. *J. Cell. Mol. Med.* 23 (2), 1470–1485. doi:10.1111/jcmm.14053

Jones, A. W. (2011). Early drug discovery and the rise of pharmaceutical chemistry. *Drug Test. Anal.* 3 (6), 337–344. doi:10.1002/dta.301

Katz, L., and Baltz, R. H. (2016). Natural product discovery: Past, present, and future. *J. Ind. Microbiol. Biotechnol.* 43 (2-3), 155–176. doi:10.1007/s10295-015-1723-5

Khaiwa, N., Maarouf, N. R., Darwish, M. H., Alhamad, D. W., Sebastian, A., Hamad, M., et al. (2021). Camptothecin's journey from discovery to WHO Essential

Medicine: Fifty years of promise. *Eur. J. Med. Chem.* 223, 113639. doi:10.1016/j.ejmech.2021.113639

Kuchta, K., Ortwein, J., and Rauwald, H. (2012). Leonurus japonicus, leonurus cardiaca, leonotis leonurus: A novel HPLC study on the occurrence and content of the pharmacologically active guanidino derivative leonurine. *Pharmazie* 67 (12), 973–979. doi:10.1691/ph.2012.1856

Kumar, P., Singh, B., Thakur, V., Thakur, A., Thakur, N., Pandey, D., et al. (2019). Hyper-production of taxol from Aspergillus fumigatus, an endophytic fungus isolated from Taxus sp. of the Northern Himalayan region. *Biotechnol. Rep. (Amst.)* 24, e00395. doi:10.1016/j.btre.2019.e00395

Kundranda, M. N., and Niu, J. (2015). Albumin-bound paclitaxel in solid tumors: Clinical development and future directions. *Drug Des. devel. Ther.* 9, 3767–3777. doi:10.2147/DDDT.S88023

Kuriakose, D., and Xiao, Z. (2020). Pathophysiology and treatment of stroke: Present status and future perspectives. *Int. J. Mol. Sci.* 21 (20), 7609. doi:10.3390/ijms21207609

Lefebvre, T., Destandau, E., and Lesellier, E. (2021). Sequential extraction of carnosic acid, rosmarinic acid and pigments (carotenoids and chlorophylls) from Rosemary by online supercritical fluid extraction-supercritical fluid chromatography. *J. Chromatogr. A* 1639, 461709. doi:10.1016/j.chroma.2020.461709

Li, B., Wu, J., and Li, X. (2013). Simultaneous determination and pharmacokinetic study of stachydrine and leonurine in rat plasma after oral administration of Herba Leonuri extract by LC–MS/MS. *J. Pharm. Biomed. Anal.* 76, 192–199. doi:10.1016/j.jpba.2012.12.029

Li, F., Jiang, T., Li, Q., and Ling, X. (2017). Camptothecin (CPT) and its derivatives are known to target topoisomerase I (Top1) as their mechanism of action: Did we miss something in CPT analogue molecular targets for treating human disease such as cancer? *Am. J. Cancer Res.* 7 (12), 2350–2394.

Li, Q.-Y., Zu, Y.-G., Shi, R.-Z., and Yao, L.-P. (2006). Review camptothecin: Current perspectives. *Curr. Med. Chem.* 13 (17), 2021–2039. doi:10.2174/092986706777585004

Li, Y.-y., Lin, Y.-k., Li, Y., Liu, X.-h., Li, D.-j., Wang, X.-l., et al. (2022). SCM-198 alleviates endometriosis by suppressing estrogen-erα mediated differentiation and function of CD4+ CD25+ regulatory T cells. *Int. J. Biol. Sci.* 18 (5), 1961–1973. doi:10.7150/ijbs.68224

Li, Y.-y., Lin, Y.-k., Liu, X.-h., Wang, L., Yu, M., Li, D.-j., et al. (2020). Leonurine: From gynecologic medicine to pleiotropic agent. *Chin. J. Integr. Med.* 26 (2), 152–160. doi:10.1007/s11655-019-3453-0

Liao, J., Suguro, R., Zhao, X., Yu, Y., Cui, Y., Zhu, Y. Z. J. C., et al. (2021). Leonurine affected homocysteine-methionine metabolism based on metabolomics and gut microbiota studies of clinical trial samples. *Clin. Transl. Med.* 11 (10), e535. doi:10.1002/ctm2.535

Liu, C., Gu, X., and Zhu, Y. Z. (2010). Synthesis and biological evaluation of novel leonurine–SPRC conjugate as cardioprotective agents. *Bioorg. Med. Chem. Lett.* 20 (23), 6942–6946. doi:10.1016/j.bmcl.2010.09.135

Liu, C., Guo, W., Shi, X., Kaium, M., Gu, X., and Zhu, Y. Z. (2011). Leonurine-cysteine analog conjugates as a new class of multifunctional anti-myocardial ischemia agent. *Eur. J. Med. Chem.* 46 (9), 3996–4009. doi:10.1016/j.ejmech.2011.05.073

Liu, X.-H., Pan, L.-L., Deng, H.-Y., Xiong, Q.-H., Wu, D., Huang, G.-Y., et al. (2013). Leonurine (SCM-198) attenuates myocardial fibrotic response via inhibition of NADPH oxidase 4. *Free Radic. Biol. Med.* 54, 93–104. doi:10.1016/j.freeradbiomed.2012.10.555

Liu, X., Cao, J., Huang, G., Zhao, Q., and Shen, J. (2019). Biological activities of artemisinin derivatives beyond malaria. *Curr. Top. Med. Chem.* 19 (3), 205–222. doi:10.2174/1568026619666190122144217

Liu, X. H., Xin, H., Hou, A. J., and Zhu, Y. Z. (2009). Protective effects of leonurine in neonatal rat hypoxic cardiomyocytes and rat infarcted heart. *Clin. Exp. Pharmacol. Physiol.* 36 (7), 696–703. doi:10.1111/j.1440-1681.2008.05135.x

Liu, X., Pan, L., Chen, P., and Zhu, Y. (2010). Leonurine improves ischemia-induced myocardial injury through antioxidative activity. *Phytomedicine* 17 (10), 753–759. doi:10.1016/j.phymed.2010.01.018

Liu, X., Pan, L., Wang, X., Gong, Q., and Zhu, Y. Z. (2012). Leonurine protects against tumor necrosis factor-α-mediated inflammation in human umbilical vein endothelial cells. *Atherosclerosis* 222 (1), 34–42. doi:10.1016/j.atherosclerosis.2011.04.027

Liu, Y. Q., Li, W. Q., Morris-Natschke, S. L., Qian, K., Yang, L., Zhu, G. X., et al. (2015). Perspectives on biologically active camptothecin derivatives. *Med. Res. Rev.* 35 (4), 753–789. doi:10.1002/med.21342

Liu, Y., Yang, S., Wang, K., Lu, J., Bao, X., Wang, R., et al. (2020). Cellular senescence and cancer: Focusing on traditional Chinese medicine and natural products. *Cell Prolif.* 53 (10), e12894. doi:10.1111/cpr.12894

Luo, S., Xu, S., Liu, J., Ma, F., and Zhu, Y. Z. (2020). Design and synthesis of novel SCM-198 analogs as cardioprotective agents: Structure-activity relationship studies and biological evaluations. *Eur. J. Med. Chem.* 200, 112469. doi:10.1016/j.ejmech.2020.112469

Mann, J. (2000). *Murder, magic, and medicine*. USA: Oxford University Press.

Martino, E., Della Volpe, S., Terribile, E., Benetti, E., Sakaj, M., Centamore, A., et al. (2017). The long story of camptothecin: From traditional medicine to drugs. *Bioorg. Med. Chem. Lett.* 27 (4), 701–707. doi:10.1016/j.bmcl.2016.12.085

Miao, L.-L., Zhou, Q.-M., Peng, C., Liu, Z.-H., and Xiong, L. (2019). Leonurus japonicus (Chinese motherwort), an excellent traditional medicine for obstetrical and gynecological diseases: A comprehensive overview. *Biomed. Pharmacother.* 117, 109060. doi:10.1016/j.biopha.2019.109060

Montinari, M. R., Minelli, S., and De Caterina, R. (2019). The first 3500 years of aspirin history from its roots–A concise summary. *Vasc. Pharmacol.* 113, 1–8. doi:10.1016/j.vph.2018.10.008

Patil, U. K., and Saraogi, R. (2014). Natural products as potential drug permeation enhancer in transdermal drug delivery system. *Arch. Dermatol. Res.* 306 (5), 419–426. doi:10.1007/s00403-014-1445-y

Patra, J. K., Das, G., Fraceto, L. F., Campos, E. V. R., Rodriguez-Torres, M. d. P., Acosta-Torres, L. S., et al. (2018). Nano based drug delivery systems: Recent developments and future prospects. *J. Nanobiotechnology* 16 (1), 71–33. doi:10.1186/s12951-018-0392-8

Petrelli, F., Borgonovo, K., and Barni, S. (2010). Targeted delivery for breast cancer therapy: The history of nanoparticle-albumin-bound paclitaxel. *Expert Opin. Pharmacother.* 11 (8), 1413–1432. doi:10.1517/14656561003796562

Poredos, P., Gregoric, I. D., and Jezovnik, M. K. (2020). Inflammation of carotid plaques and risk of cerebrovascular events. *Ann. Transl. Med.* 8 (19), 1281. doi:10.21037/atm-2020-cass-15

Qi, J., Hong, Z. Y., Xin, H., and Zhu, Y. Z. (2010). Neuroprotective effects of leonurine on ischemia/reperfusion-induced mitochondrial dysfunctions in rat cerebral cortex. *Biol. Pharm. Bull.* 33 (12), 1958–1964. doi:10.1248/bpb.33.1958

Sarker, S. D., and Nahar, L. (2012). An introduction to natural products isolation. *Methods Mol. Biol.* 864, 1–25. doi:10.1007/978-1-61779-624-1_1

Sen, T., and Samanta, S. K. (2014). Medicinal plants, human health and biodiversity: A broad review. *Adv. Biochem. Eng. Biotechnol.* 147, 59–110. doi:10.1007/10_2014_273

Slezáková, S., and Ruda-Kucerova, J. (2017). Anticancer activity of artemisinin and its derivatives. *Anticancer Res.* 37 (11), 5995–6003. doi:10.21873/anticanres.12046

Solís-Cruz, G. Y., Pérez-López, L. A., Alvarez-Roman, R., Rivas-Galindo, V. M., Silva-Mares, D. A., and Ibarra-Rivera, T. R. (2021). Nanocarriers as administration systems of natural products. *Curr. Top. Med. Chem.* 21 (26), 2365–2373. doi:10.2174/1568026621666210915121957

Suguro, R., Chen, S., Yang, D., Yang, Z., Miao, L., Wu, W., et al. (2018). Anti-hypercholesterolemic effects and a good safety profile of SCM-198 in animals: From ApoE knockout mice to rhesus monkeys. *Front. Pharmacol.* 1468, 1468. doi:10.3389/fphar.2018.01468

Thomas, C. J., Rahier, N. J., and Hecht, S. M. (2004). Camptothecin: Current perspectives. *Bioorg. Med. Chem.* 12 (7), 1585–1604. doi:10.1016/j.bmc.2003.11.036

Thomas, E., Stewart, L. E., Darley, B. A., Pham, A. M., Esteban, I., and Panda, S. S. (2021). Plant-based natural products and extracts: Potential source to develop new antiviral drug candidates. *Molecules* 26 (20), 6197. doi:10.3390/molecules26206197

Tu, Y. (2016). Artemisinin—A gift from traditional Chinese medicine to the world (Nobel lecture). *Angew. Chem. Int. Ed.* 55 (35), 10210–10226. doi:10.1002/anie.201601967

Ugurlucan, M., M Caglar, I., N Turhan Caglar, F., Ziyade, S., Karatepe, O., Yildiz, Y., et al. (2012). Aspirin: From a historical perspective. *Recent Pat. cardiovasc. Drug Discov.* 7 (1), 71–76. doi:10.2174/157489012799362377

Ulukan, H., and Swaan, P. W. (2002). Camptothecins: A review of their chemotherapeutic potential. *Drugs* 62 (14), 2039–2057. doi:10.2165/00003495-200262140-00004

Valgimigli, M. (2019). The remarkable story of a wonder drug, which now comes to an end in the primary prevention setting: Say bye-bye to aspirin. *Eur. Heart J.* 40 (7), 618–620. doi:10.1093/eurheartj/ehy872

Vane, J. R. (1971). Inhibition of prostaglandin synthesis as a mechanism of action for aspirin-like drugs. *Nat. New Biol.* 231, 232–235. doi:10.1038/newbio231232a0

Venditto, V. J., and Simanek, E. E. (2010). Cancer therapies utilizing the camptothecins: A review of the *in vivo* literature. *Mol. Pharm.* 7 (2), 307–349. doi:10.1021/mp900243b

Wall, M. E., Wani, M. C., Cook, C., Palmer, K. H., McPhail, A. a., and Sim, G. (1966). Plant antitumor agents. I. The isolation and structure of camptothecin, a novel alkaloidal leukemia and tumor inhibitor from camptotheca acuminata1, 2. *J. Am. Chem. Soc.* 88 (16), 3888–3890. doi:10.1021/ja00968a057

Wang, J., Xu, C., Wong, Y. K., Li, Y., Liao, F., Jiang, T., et al. (2019). Artemisinin, the magic drug discovered from traditional Chinese medicine. *Engineering* 5 (1), 32–39. doi:10.1016/j.eng.2018.11.011

Wang, R., Peng, L., Lv, D., Shang, F., Yan, J., Li, G., et al. (2021). Leonurine attenuates myocardial fibrosis through upregulation of miR-29a-3p in mice post-myocardial infarction. *J. Cardiovasc. Pharmacol.* 77 (2), 189–199. doi:10.1097/FJC.0000000000000957

Wang, W., Liu, Z., Liu, Y., Su, Z., and Liu, Y. (2022). Plant polypeptides: A review on extraction, isolation, bioactivities and prospects. *Int. J. Biol. Macromol.* 207, 169–178. doi:10.1016/j.ijbiomac.2022.03.009

Wani, M. C., Taylor, H. L., Wall, M. E., Coggon, P., and McPhail, A. T. J. J. o. t. A. C. S. (1971). Plant antitumor agents. VI. Isolation and structure of taxol, a novel antileukemic and antitumor agent from Taxus brevifolia. *J. Am. Chem. Soc.* 93 (9), 2325–2327. doi:10.1021/ja00738a045

White, N. J., Hien, T. T., and Nosten, F. H. (2015). A brief history of Qinghaosu. *Trends Parasitol.* 31 (12), 607–610. doi:10.1016/j.pt.2015.10.010

Winterfeldt, E., Klásek, A., Weinbergová, O., Khorlin, A.Y., and Zurayjan, S. (1975). "Approaches to camptothecin| The Pyrrolizidine Alkaloids| Advances in the Chemistry of Glycosaminides". Budapest, Hungary: Akadémiai Kiadó.

Wojtyniak, K., Szymański, M., and Matławska, I. (2013). Leonurus cardiaca L.(motherwort): A review of its phytochemistry and pharmacology. *Phytother. Res.* 27 (8), 1115–1120. doi:10.1002/ptr.4850

Wong, K. H., Lu, A., Chen, X., and Yang, Z. (2020). Natural ingredient-based polymeric nanoparticles for cancer treatment. *Molecules* 25 (16), 3620. doi:10.3390/molecules25163620

Xia, M., Liu, D., Liu, Y., and Liu, H. (2020). The therapeutic effect of artemisinin and its derivatives in kidney disease. *Front. Pharmacol.* 11, 380. doi:10.3389/fphar.2020.00380

Xie, J., Sang, L., Zhang, Y., Fang, L., and Li, Y. (2015). Determination of stachydrine and leonurine in herba leonuri and its succedaneum—herba lagopsis—With a sensitive HPLC–MS/MS method. *J. Liq. Chromatogr. Relat. Technol.* 38 (7), 810–815. doi:10.1080/10826076.2014.973965

Xie, Y. Z., Zhang, X. J., Zhang, C., Yang, Y., He, J. N., and Chen, Y. X. (2019). Protective effects of leonurine against ischemic stroke in mice by activating nuclear factor erythroid 2-related factor 2 pathway. *CNS Neurosci. Ther.* 25 (9), 1006–1017. doi:10.1111/cns.13146

Xu, L., Jiang, X., Wei, F., and Zhu, H. (2018). Leonurine protects cardiac function following acute myocardial infarction through anti-apoptosis by the PI3K/AKT/GSK3β signaling pathway. *Mol. Med. Rep.* 18 (2), 1582–1590. doi:10.3892/mmr.2018.9084

Yang, Y.-L. (2013). Spectrum-effect relationship of active fraction from Angelicae Sinensis Radix with effect of reinforcing Qi. *Zhong Cao Yao*, 3346–3351.

Yao, H., Liu, J., Xu, S., Zhu, Z., and Xu, J. (2017). The structural modification of natural products for novel drug discovery. *Expert Opin. Drug Discov.* 12 (2), 121–140. doi:10.1080/17460441.2016.1272757

Yeung, H., Kong, Y., Lay, W., and Cheng, K. (1977). The structure and biological effect of leonurine. *Planta Med.* 31 (01), 51–56. doi:10.1055/s-0028-1097489

Yin, W., and Lei, Y. (2018). Leonurine inhibits IL-1β induced inflammation in murine chondrocytes and ameliorates murine osteoarthritis. *Int. Immunopharmacol.* 65, 50–59. doi:10.1016/j.intimp.2018.08.035

Zhang, Q.-Y., Wang, Z.-J., Sun, D.-M., Wang, Y., Xu, P., Wu, W.-J., et al. (2017). Novel therapeutic effects of leonurine on ischemic stroke: New mechanisms of BBB integrity. *Oxid. Med. Cell. Longev.* 2017, 1–17. doi:10.1155/2017/7150376

Zhang, R.-h., Liu, Z.-k., Yang, D.-s., Zhang, X.-j., Sun, H.-d., and Xiao, W. L. (2018). Phytochemistry and pharmacology of the genus Leonurus: The herb to benefit the mothers and more. *Phytochemistry* 147 (147), 167–183. doi:10.1016/j.phytochem.2017.12.016

Zhang, W., Xiong, L., Chen, J., Tian, Z., Liu, J., Chen, F., et al. (2021). Artemisinin protects porcine mammary epithelial cells against lipopolysaccharide-induced inflammatory injury by regulating the NF-κB and MAPK signaling pathways. *Animals* 11 (6), 1528. doi:10.3390/ani11061528

Zhang, Y., Guo, W., Wen, Y., Xiong, Q., Liu, H., Wu, J., et al. (2012). SCM-198 attenuates early atherosclerotic lesions in hypercholesterolemic rabbits via modulation of the inflammatory and oxidative stress pathways. *Atherosclerosis* 224 (1), 43–50. doi:10.1016/j.atherosclerosis.2012.06.066

Zhi, C., Li1ling, M., and Xiu1jia, Z. (2004). Determination of stachydrine and leonurine in Herba Leonuri by ion1! pair reversed1phase high1performance liquid chromatography. *Di 1 jun yi da xue xue bao* 24, 1224. doi:10.3321/j.issn:1673-4254.2004.11.002

Zhu, L., and Chen, L. (2019). Progress in research on paclitaxel and tumor immunotherapy. *Cell. Mol. Biol. Lett.* 24 (1), 40–11. doi:10.1186/s11658-019-0164-y

Zhu, Y. Z., Wu, W., Zhu, Q., and Liu, X. (2018). Discovery of leonuri and therapeutical applications: From bench to bedside. *Pharmacol. Ther.* 188, 26–35. doi:10.1016/j.pharmthera.2018.01.006

# Acorane sesquiterpenes from the deep-sea derived *Penicillium bilaiae* fungus with anti-neuroinflammatory effects

Wenfang Zhang[1,2], Qingyu Meng[1], Jingshuai Wu[1], Wei Cheng[1], Dong Liu[1], Jian Huang[1], Aili Fan[1], Jing Xu[2]* and Wenhan Lin[1,3]*

[1]State Key Laboratory of Natural and Biomimetic Drugs, Institute of Ocean Research, Peking University, Beijing, China, [2]School of Chemical Engineering and Technology, Hainan University, Haikou, China, [3]Ningbo Institute of Marine Medicines, Peking University, Ningbo, China

Acorane-type sesquiterpenes comprise a unique class of natural products with a range of pharmaceutical effects. Genome sequencing and gene annotation, along with qRT-PCR detection, demonstrate that the deep-sea derived *Penicillium bilaiae* F-28 fungus shows potential to produce acorane sesquiterpenes. Chromatographic manipulation resulted in the isolation of 20 acorane sesquiterpenes from the large-scale fermented fungal strain. Their structures were established by the interpretation of spectroscopic data, together with X-ray diffraction, chemical conversion, and ECD data for configurational assignments. A total of 18 new sesquiterpenes, namely, bilaiaeacorenols A−R (**1−18**), were identified. Bilaiaeacorenols A and B represent structurally unique tricyclic acoranes. Compound **18** exhibited efficient reduction against NO production in LPS-induced BV-2 macrophages in a dose-dependent manner, and it abolished LPS-induced NF-κB in the nucleus of BV-2 microglial cells. In addition, marked reductions of iNOS and COX-2 in protein and mRNA levels were observed. This study extends the chemical diversity of acorane-type sesquiterpenoids and suggests that compound **18** is a promising lead for anti-neuroinflammation.

## Introduction

Acorane-type sesquiterpenes feature a spiro[4.5]decane core with an isopropyl unit at C-1 and dimethyl substitution at C-4 and C-8, which markedly differs from other types of the sesquiterpene family (Liu et al., 2015; Zhang et al., 2017; Guo et al., 2020). Hitherto, less than 30 acorane-based sesquiterpenes have been reported from plants and microorganisms. Acrorans in plants are characteristic of the volatile metabolites which play crucial roles as biocontrol and biostimulant agents and are also considered the chemotaxonomic markers of the plant (Zhang et al., 2020). Biogenetically, acrorans are synthesized from farnesyl diphosphate (FPP) as a common precursor by catalysis

TABLE 1 Inhibitory effects of 1–20 against NO production in LPS-induced BV-2 cells.

| No | IC$_{50}$ (μM) | CC$_{50}$ (μM) |
|---|---|---|
| 1 | >10 | >100 |
| 2 | 6.1 ± 2.3 | >100 |
| 3 | 5.3 ± 1.1 | >100 |
| 4 | 7.6 ± 1.2 | >100 |
| 5 | >10 | >100 |
| 6 | >10 | >100 |
| 7 | >10 | >100 |
| 8 | >10 | >100 |
| 9 | 3.5 ± 0.1 | >100 |
| 10 | >10 | >100 |
| 11 | 8.7 ± 2.1 | >100 |
| 12 | >10 | >100 |
| 13 | 0.53 ± 0.47 | >100 |
| 14 | >10 | >100 |
| 15 | 3.7 ± 0.1 | >100 |
| 16 | 7.5 ± 0.2 | >100 |
| 17 | >10 | >100 |
| 18 | 0.5 ± 1.2 | >100 |
| 19 | >10 | >100 |
| 20 | >10 | >100 |
| L-NMMA | 6.8 ± 4.2 | >100 |

L-NMMA, NG-monomethyl-L-arginine; CC, cell cytotoxicity.

using sesquiterpene synthases, of which EfCAS in the plant catalyzes the cyclization of FFP to afford a spiro[4.5]decane core such as eupho-acorenols A and B (Zhu et al., 2021). Enzymatic catalysis to generate the acorane core in fungi is also documented (Bian et al., 2018). Due to the unique molecular scaffolds, acrorans exhibit a wide range of bioactivities. Chermebilaene A and its hydrolyzed product from a marine-derived fungus show significant activity against pathogenic bacteria (Meng et al., 2020), daphneaines from a plant show inhibitory effects against nitric oxide (NO) production in lipopolysaccharide (LPS)-induced RAW 264.7 macrophages (Guo et al., 2020), and rhodocoranes possess various cytotoxic and antifungal effects (Sandargo et al., 2019).

# Experiment

## General experimental procedures

Optical rotations were recorded on an AUTOPOL III Automatic Polarimeter, and IR spectra were performed on a Thermo Nicolet Nexus 470 FT-IR spectrometer. NMR spectra were measured on a Bruker Avance-400 NMR spectrometer with TMS as the internal standard. HRESIMS data were recorded on a Bruker APEX IV 70 eV FT-MS spectrometer. ESIMS spectra were detected on a Finnigan MAT-95 mass spectrometer. Silica gel (200–300 mesh) and HF254 silica gel for used for TLC were purchased from Qingdao Marine Chemistry Co., Ltd., while Sephadex LH-20 (18–110 μm; Pharmacia Co., Ltd.) and ODS (50 μm, YMC, Milford, MA) were used for separation. HPLC was performed on an Alltech instrument (426-HPLC pump) equipped with a UV detector. X-ray data were collected on a Bruker SMART APEX-II DUO instrument. Dulbecco's modified Eagle's medium (DMEM) and fetal bovine serum (FBS) were purchased from HyClone (Waltham, United States). 3-(4,5-Dimethylthiazol-2-yl)-2,5-diphenyltetrazolium bromide (MTT) and lipopolysaccharide (LPS) (*Escherichia coli* 055: B5) were supplied by Sigma Chemical Co., (St Louis, MO, United States). Griess reagent (ExCell Bio) and primary antibodies were supplied by Cell Signaling Technology (Danvers, United States).

## Fungal material and fermentation

The fungal strain *Penicillium bilaiae* F-28 was collected from deep-sea sediment (GPS 27.90 W, 6.43 S, depth of 5,610 m) in the South Atlantic Ocean. The DNA was collected and amplified by the ITS primers (ITS4 and ITS5). The ITS sequence (773 bp) was deposited in GenBank (accession number LN901118.1). Based on the BLAST search, the fungal strain was identical to *P. bilaiae*. Then, fermentation was performed in rice (80 g for each, 120 Fernbach flasks, 500 ml) with distilled $H_2O$ (80 ml for each), which was allowed to soak overnight. Each flask was seeded with 2.0 ml of the spore inoculum ($10^7$/ml) and incubated at 25°C for 35 days. The EtOAc solvent was used for the extraction of the fermented material.

## Genome sequencing and analysis

Genome sequencing of *P. bilaiae* F-28 was detected by using an Illumina HiSeq 2000 system. The sequence was constructed on SPAdes version 3.5.0 (http://cab.spbu.ru/software/spades/), generating 160 scaffolds (ca. 36.7 Mb). Gene annotation was undertaken by Prokka (https://github.com/tseemann/prokka). Analysis of the genome sequence by anti-SMASH and correlation revealed nine isoprenoid biosyn-C1 superfamily terpenoid cyclase genes, which were then compared and annotated to the protein sequences in NCBI.

## Quantitative RT-PCR for terpenoid cyclase genes

The expression levels of nine terpenoid cyclase genes were detected by qRT-PCR. The total RNA of *P. bilaiae* F-28 in the rice culture medium was obtained. The synthesis of cDNA was

performed with the guidance of the manufacturer's instruction [1 μg of total RNA (20 μl) and TransScriptIIAll-in-One First-Strand cDNA Synthesis Super Mix (Transgene) for qPCR]. A measure of 0.4 μl of cDNA, together with the primer (10 μM) and reverse primer (10 μM), and 10 μl 2× TransStart Top Green qPCR SuperMix (Transgene) were supplied for RT-PCR in ddH$_2$O (20 μl). Optimized PCR conditions were 94°C/5 min; 40 cycles of 94°C/20 s; 54°C/20 s; and 72°C/20 s; 72°C/5 min. Then, 4 μl of 6×DNA Loading buffer was added to the PCR product, and 8 μl was taken for agarose electrophoresis detection. The bands were observed under 300 nm UV and photographed. An internal reference gene is β-actin.

## UPLC-electrospray ionization-MS/MS data and molecular networking

The EtOAc extract of the cultured fungus was analyzed on a Thermo Vanquish F UPLC system coupled with the Thermo Q Exactive HF-X mass spectrometer equipped with an electrospray ionization (ESI) source operating with positive polarity at a mass range of $m/z$ 50–500 Da. The 0.1 mg/ml MeOH solution was filtered through a 0.2-mm PTFE syringe filter (Carl Roth) and then injected (injection volume: 5.0 μl) into the system that was equipped with an Acquity UPLC HSS T3 column (high-strength silica C$_{18}$, 1.8 μm, 100 mm × 2.1 mm i. d., Waters) operating at 40°C. Separation was achieved with a binary LC solvent system using mobile phase A [99.9% H$_2$O/0.1% formic acid (ULC/MS grade)] and B [MeCN (ULC/MS grade)], pumped at a rate of 0.3 ml/min with the following gradients: 0–1 min, 100% A; 1–3 min, 100%–95% A; 3–20 min, 95%–0% A; 20–25 min, 0% A; 25–25.5, 0–100% A; and 25.5–30 min, 100% A. TIC and EIC spectra were extracted and analyzed on Thermo Xcalibur Qual Browser software. Instrumental parameters were set as follows: source voltage 3.5 kV, lens 1 voltage −10 V, capillary temperature 320°C, gate lens voltage −40 V, capillary voltage 40 V, and tube lens voltage 100 V. The CID parameters were set as follows: CE at 20% of the maximum and an activation time of 20 ms. Tandem mass spectra arising from UPLC-MS/MS were annotated in the Advanced Mass Spectral Database (https://www.mzcloud.org) and analyzed by Compound Discoverer 3.1.0.305 software. Subsequently, UPLC-MS/MS data were further analyzed using the GNPS platform (http://gnps.ucsd.edu). The MS/MS data were converted to mzXML format with MS-Convert and then uploaded on the GNPS. Parameters for molecular network generation were set as the precursor ion mass tolerance of 0. 05 Da, product ion tolerance of 0.05 Da, and removing fragment ions below 10 counts from the MS/MS spectra. Molecular networks were generated using four minimum matched peaks and a cosine score of 0.70. Edges between two nodes were kept in the network if each of the nodes appeared in each other's respective top 10 most similar nodes. The maximum size of a molecular family was set to 100, and the lowest scoring edges

were removed from molecular families until the molecular family size was below this threshold. The spectra in the network were then searched against GNPS spectral libraries. The library spectra were filtered in the same manner as the input data. All matches kept between the network spectra and library spectra were required to have a score above 0.7 and at least six matched peaks. Data were visualized by Cytoscape 3.8.0 software.

## Extraction and isolation

The fermented fungus was extracted by EtOAc (3 L × 2 L), which was concentrated under reduced pressure to obtain the residue (38 g). The EtOAc extract was partitioned between MeOH-H$_2$O (1:10) and petroleum ether (PE), and the MeOH layer was collected. The MeOH fraction (20 g) was chromatographed upon a silica gel (200–300 mesh) vacuum liquid column and eluted using CH$_2$Cl$_2$-MeOH (from 15:1 to 0:1, v/v) to collect nine fractions (F1–F9). The $^1$H NMR spectra of F3 and F5 fractions showed the resonances featured terpene analogs. F3 (0.32 g) was purified by an RP-C18 column with a mobile phase of MeOH-H$_2$O (55:45, v/v) to yield adametacorenol A (160 mg). F5 (0.85 g) was fractionated upon an RP-C18 column and eluted using MeOH-H$_2$O (1:4, v/v) to yield subfractions of F51–F56. F51 (260 mg) was subjected to a Sephadex LH-20 column and eluted with MeOH to purify compounds **8** (5.6 mg) and **16** (3.3 mg). F52 (90 mg) was fractionated using a semipreparative RP-C18 HPLC column with MeCN-H$_2$O (30:70, v/v) as a mobile phase to yield compounds **6** (1.2 mg), **5** (1.0 mg), **13** (2 mg), and **18** (1.6 mg). F53 (42 mg) followed the same protocol as for F52 on a semipreparative RP-C18 HPLC column with MeOH-H$_2$O (1:3, v/v) to obtain compounds **17** (0.8 mg), **14** (0.6 mg), **11** (1.2 mg), and **7** (1.0 mg). F54 (400 mg) was separated using a semipreparative RP-C18 HPLC column with MeCN-H$_2$O (1:1, v/v) to collect compounds **9** (1 mg), **1** (1.1 mg), **10** (0.8 mg), **4** (4 mg), **3** (2.5 mg), **15** (4 mg), adametacorenol B (0.8 mg), **12** (1.0 mg), and **2** (3.6 mg).

## Compound characterization

Bilaiaeacorenol A (**1**): colorless monoclinic crystals (acetone); mp. 106–108°; ($\alpha$) -120 ($c$ 0.1, MeOH); UV (MeOH) λ$_{max}$ 202 nm; IR (KBr) ν$_{max}$ 3,306, 2,929, and 1,456 cm$^{-1}$; $^1$H and $^{13}$C NMR data (DMSO-$d_6$), see Supplementary Tables S3, S5; HRESIMS $m/z$ 275.1623 [M + Na]$^+$ (calcd for C$_{15}$H$_{24}$O$_3$Na, 275.1623) (Supplementary Figures S1–S9); and Flack parameter: 0.00 (6).

Bilaiaeacorenol B (**2**): colorless monoclinic crystals (acetone); mp. 108–110°; ($\alpha$) -12 ($c$ 0.1, MeOH); UV (MeOH) λ$_{max}$ 200 nm; IR (KBr) ν$_{max}$ 3,348, 2,923, 1,456, and 1,374 cm$^{-1}$; $^1$H and $^{13}$C NMR data (DMSO-$d_6$), see Supplementary Tables S3, S5;

HRESIMS $m/z$ 253.1801 [M + H]$^+$ (calcd for $C_{15}H_{25}O_3$, 253.1804) (Supplementary Figures S10–S18); and Flack parameter: 0.05 (9).

Bilaiaeacorenol C (**3**): colorless oil; [α] -40 ($c$ 0.1, MeOH); UV (MeOH) $\lambda_{max}$ 200 nm; IR (KBr) $\nu_{max}$ 3,335, 2,932, and 1,679 cm$^{-1}$; $^1$H and $^{13}$C NMR data (DMSO-$d_6$), see Supplementary Tables S3, S5; and HRESIMS $m/z$ 335.1833 [M +Na]+(calcd for $C_{17}H_{28}O_5Na$, 335.1834) (Supplementary Figures S19–S27).

Bilaiaeacorenol D (**4**): colorless oil; [α] −30 ($c$ 0.1, MeOH); UV (MeOH) $\lambda_{max}$ 202 nm; IR (KBr) $\nu_{max}$ 3,360, 2,922, 1732, 1,667, 1,385, and 1,249 cm$^{-1}$; $^1$H and $^{13}$C NMR data (DMSO-$d_6$), see Supplementary Tables S3, S5; and HRESIMS $m/z$ 319.1888 [M + Na]$^+$ (calcd for $C_{17}H_{28}O_4Na$, 319.1885) (Supplementary Figures S28–S36).

Bilaiaeacorenol E (**5**): colorless oil; [α] -8 ($c$ 0.1, MeOH); UV (MeOH) $\lambda_{max}$ 202 nm; IR (KBr) $\nu_{max}$ 3358, 1,648, and 1,321 cm$^{-1}$; $^1$H and $^{13}$C NMR data (DMSO-$d_6$), see Supplementary Tables S3, S5; and HRESIMS $m/z$ 219.1749 [M–HO]+(calcd for $C_{15}H_{23}O_2$, 219.1749) (Supplementary Figures S37–S45).

Bilaiaeacorenol F (**6**): colorless oil; [α] -20 ($c$ 0.1, MeOH); UV (MeOH) $\lambda_{max}$ 201 nm; IR (KBr) $\nu_{max}$ 3,400 and 1,388 cm$^{-1}$; $^1$H and $^{13}$C NMR data (DMSO-$d_6$), see Supplementary Tables S3, S5; and HRESIMS $m/z$ 237.1852 [M + H]$^+$ (calcd for $C_{15}H_{25}O_2$, 237.1855) (Supplementary Figures S46–S54).

Bilaiaeacorenol G (**7**): colorless oil; [α] -20 ($c$ 0.1, MeOH); UV (MeOH) $\lambda_{max}$ 201 nm; IR (KBr) $\nu_{max}$ 3,312 and 1,643 cm$^{-1}$; $^1$H and $^{13}$C NMR data (DMSO-$d_6$), see Supplementary Tables S3, S5; and HRESIMS $m/z$ 275.1621 [M + Na]$^+$ (calcd for $C_{15}H_{24}O_3Na$, 275.1623) (Supplementary Figures S55–S63).

Bilaiaeacorenol H (**8**): colorless monoclinic crystals (acetone); mp. 113–115°; [α] -20 ($c$ 0.1, MeOH); UV (MeOH) $\lambda_{max}$ 201 nm; IR (KBr) $\nu_{max}$ 3,312 and 1,643 cm$^{-1}$; $^1$H and $^{13}$C NMR data (DMSO-$d_6$), see Supplementary Tables S4, S5; HRESIMS $m/z$ 275.1625 [M + Na]+(calcd for $C_{15}H_{24}O_3Na$, 275.1623) (Supplementary Figures S64–S72); and Flack parameter: 0.01 (10).

Bilaiaeacorenol I (**9**): colorless oil; [α] -40 ($c$ 0.1, MeOH); UV (MeOH) $\lambda_{max}$ 201 nm; IR (KBr) $\nu_{max}$ 3,375, 1710, 1,374, and 1,260 cm$^{-1}$; $^1$H and $^{13}$C NMR data (DMSO-$d_6$), see Supplementary Tables S4, S5; and HRESIMS $m/z$ 317.1724 [M + Na]+(calcd for $C_{17}H_{26}O_4Na$, 317.1729) (Supplementary Figures S73–S81).

Bilaiaeacorenol J (**10**): colorless oil; [α] -20 ($c$ 0.1, MeOH); UV (MeOH) $\lambda_{max}$ 201 nm; IR (KBr) $\nu_{max}$ 3,380, 2,928, 2,872, 1734, 1375, and 1247 cm$^{-1}$; $^1$H and $^{13}$C NMR data (DMSO-$d_6$), see Supplementary Tables S4, S5; and HRESIMS $m/z$ 317.1723 [M + Na]+(calcd for $C_{17}H_{26}O_4Na$, 317.1729) (Supplementary Figures S82–S90).

Bilaiaeacorenol K (**11**): colorless oil; [α] -20 ($c$ 0.1, MeOH); UV (MeOH) $\lambda_{max}$ 200 nm; IR (KBr) $\nu_{max}$ 3,365, 2,925, 2,872, 1,680, 1,456, and 1,374 cm$^{-1}$; $^1$H and $^{13}$C NMR data (DMSO-$d_6$), see Supplementary Tables S4, S5; and HRESIMS $m/z$ 253.1817 [M + H] +(calcd for $C_{15}H_{25}O_3$, 253.1804) (Supplementary Figures S91–S99).

Bilaiaeacorenol L (**12**): colorless oil; [α] -40 ($c$ 0.1, MeOH); UV (MeOH) $\lambda_{max}$ 200 nm; IR (KBr) $\nu_{max}$ 3,335, 2,932, and 1,679 cm$^{-1}$; $^1$H and $^{13}$C NMR data (DMSO-$d_6$), see Supplementary Table S6; and HRESIMS $m/z$ 253.1806 [M - H]$^-$ (calcd for $C_{15}H_{25}O_3$, 253.1804) (Supplementary Figures S100–S108).

Bilaiaeacorenol M (**13**): colorless oil; [α] +8 ($c$ 0.1, MeOH); UV (MeOH) $\lambda_{max}$ 201 nm; IR (KBr) $\nu_{max}$ 3,366, 2,931, 1732, and 1,246 cm$^{-1}$; $^1$H and $^{13}$C NMR data (DMSO-$d_6$), see Supplementary Table S6; and HRESIMS $m/z$ 335.1833 [M + Na]+(calcd for $C_{17}H_{28}O_4Na$, 335.1834) (Supplementary Figures S109–S117).

Bilaiaeacorenol N (**14**): colorless oil; [α] +12 ($c$ 0.1, MeOH); UV (MeOH) $\lambda_{max}$ 200 nm; IR (KBr) $\nu_{max}$ 3,355, 2,929, 1,679, 1,447, and 1,204 cm$^{-1}$; $^1$H and $^{13}$C NMR data (DMSO-$d_6$), see Supplementary Table S6; and HRESIMS $m/z$ 255.1959 [M +H]+(calcd for $C_{15}H_{27}O_3$, 255.1960) (Supplementary Figures S118–S126).

Bilaiaeacorenol O (**15**): colorless monoclinic crystals (acetone); mp. 108–110°; [α] +12 ($c$ 0.1, MeOH); UV (MeOH) $\lambda_{max}$ 201 nm; IR (KBr) $\nu_{max}$ 3,420, 2,924, 2,854, 1732, 1,456, and 1,247 cm$^{-1}$; $^1$H and $^{13}$C NMR data (DMSO-$d_6$), see Supplementary Tables S4, S5; HRESIMS $m/z$ 335.1833 [M + Na]$^+$ (calcd for $C_{17}H_{28}O_5Na$, 335.1834); and Flack parameter: –0.03 (11) (Supplementary Figures S127–S135).

Bilaiaeacorenol P (**16**): colorless oil; [α] +10 ($c$ 0.1, MeOH); UV (MeOH) $\lambda_{max}$ 201 nm; IR (KBr) $\nu_{max}$ 3,365, 2,924, 2,870 1,435, and 1,374 cm$^{-1}$; $^1$H and $^{13}$C NMR data (DMSO-$d_6$), see Supplementary Tables S4, S5; and HRESIMS $m/z$ 293.1723 [M + Na]+(calcd for $C_{15}H_{26}O_4Na$, 293.1729) (Supplementary Figures S136–S144).

Bilaiaeacorenol Q (**17**): colorless oil; [α] -20 ($c$ 0.1, MeOH); UV (MeOH) $\lambda_{max}$ 199 nm; IR (KBr) $\nu_{max}$ 3,420, 1,648, and 1,387 cm$^{-1}$; $^1$H and $^{13}$C NMR data (DMSO-$d_6$), see Supplementary Table S7; and HRESIMS $m/z$ 253.1801 [M + H]$^+$ (calcd for $C_{15}H_{27}O_4$, 253.1804) (Supplementary Figures S145–S153).

Bilaiaeacorenol R (**18**): colorless oil; [α] -4 ($c$ 0.1, MeOH); UV (MeOH) $\lambda_{max}$ 200 nm; IR (KBr) $\nu_{max}$ 3,354, 2,925, and 1,679 cm$^{-1}$; $^1$H and $^{13}$C NMR data (DMSO-$d_6$), see Supplementary Table S7; and HRESIMS $m/z$ 267.1592 [M -H]$^-$ (calcd for $C_{15}H_{23}O_4$, 267.1596) (Supplementary Figures S154–S162).

## Hydrolysis

Analog **9** (1.0 mg) was dissolved in 1.0 ml MeOH, and 2.4 mg $K_2CO_3$ was added to stir at room temperature overnight. Subsequently, 1.0 ml $H_2O$ was added to the MeOH solution,

which was extracted by 3 ml EtOAc. The EtOAc solution was dried under vacuum, and the hydrolyzed product was then detected by a $^1$H NMR spectrum (DMSO-$d_6$) and optical rotation. Adametacorenols A and B, and analogs **13** and **15**, respectively, were hydrolyzed in the same manner as for compound **9**.

Hydrolyzed product of compound **9**: [α] -21 (*c* 0.05, MeOH), $^1$H NMR data, see Supplementary Figure S169.

Hydrolyzed product of compound **13**: [α] +14 (*c* 0.05, MeOH), $^1$H NMR data, see Supplementary Figure S170.

Hydrolyzed product of compound **15**: [α] +16 (*c* 0.1, MeOH), $^1$H NMR data, see Supplementary Figure S171.

Hydrolyzed product of adametacorenol A: [α] -10 (*c* 0.1, MeOH), $^1$H NMR data, see Supplementary Figure S172.

Hydrolyzed product of adametacorenol B: [α] -22 (*c* 0.1, MeOH), $^1$H NMR data, see Supplementary Figure S173.

## ECD calculation

By MacroModel 10.8.011 software using the MMFF94S force field with 2.5 kcal/mol energy cutoff, mixed torsional/low-mode conformational searches were carried out by SYBYL-X 2.0. Geometry re-optimizations of the resultant conformers (ωB97X/TZVP with the PCM solvent model for MeOH) and TDDFT calculations were performed with Gaussian 09 using B3LYP, the TZVP basis set, and the same solvent model, as in the DFT optimization step at the b3lyp/6–31 + g(d) level with the solvent of MeOH. First, 30 electronic excitations involving energies, oscillator strengths, and rotational strengths (velocity) were calculated by the TDDFT methodology at the b3lyp/6–31 + g (d,p) level. ECD data were simulated by the overlapping Gaussian function, and the simulated spectra of conformers were averaged on the basis of the Boltzmann distribution theory and the relative Gibbs free energy (ΔG). The Merck molecular force field (MMFF) conformational search resulted in initial conformers, which were re-optimized at the ωB97X/TZVP PCM/MeOH level, yielding low-energy conformers over 1% Boltzmann population.

## Crystal data

Crystal data on compounds **1**, **2**, **8**, and **15** were collected with Cu Kα radiation at T = 100.01 (10) K on a Rigaku Oxford Diffraction XtaLAB Synergy four-circle diffractometer, and the data were collected, as shown in Supplementary Figures S164–S168 and Supplementary Tables S8, S38. Crystallographic data have been deposited at the Cambridge Crystallographic Data Center as supplementary publications (CCDC 2211217 for **1**, CCDC 2211219 for **2**, CCDC 2064519 for **8**, and CCDC 2211218 for **15**).

## Cell culture and cell viability assay

Murine BV-2 microglial cells were obtained from the Cell Culture Center of Institute of Basic Medical Sciences, Chinese Academy of Medical Sciences, and the cells were cultured in Dulbecco's modified Eagle's medium (Gibco) together with 10% (v/v) fetal bovine serum (HyClone) within a 5% $CO_2$ incubator at 37°C. The MTT method was utilized to detect the cytotoxicity of the compound to read the absorbance at 570 nm using a microplate spectrophotometer (Thermo Scientifics, United States).

## Measurement of nitric oxide production

In the presence or absence of LPS (1 μg/ml), murine BV-2 microglial cells were treated with compounds with different concentrations for 24 h. The same volume of Griess reagent was added to the supernatant of culture media. The Griess method was used to determine the NO levels under the absorbance at 540 nm measured using a microplate spectrophotometer (Thermo Scientifics, United States). Based on the established calibration curve of standard sodium nitrite solutions, the content of nitrite was calculated.

## Western blot

In 12-well plates, BV-2 cells were seeded to incubate with LPS (1 μg/ml) for 1 h. Each compound was incubated with BV-2 cells for 16 h. Phenylmethylsulfonyl fluoride-protease inhibitor cocktail as the cell extraction buffer was used to lyse cells. Nuclear and cytosolic extraction kits were applied for the collection of the cytosolic and nuclear extracts. Upon SDS-PAGE, proteins were purified and transferred to PVDF membranes (Millipore). After treatment with 5% (W/V) skim milk in TBST (Tris-buffered saline with 0.1% Tween 20) for 1 h, the membranes were maintained at 4°C overnight. The membrane was washed and then incubated with a secondary antibody at 20°C for 1 h. The target proteins were visualized under a chemiluminescence (ECL) detection system, and the relative optical densities were analyzed by Image Master™ 2D Elite software.

## Immunofluorescence assay

Prior to LPS induction, BV-2 cells were pretreated by the compound (2 μM) in DMSO. Cells were seeded in glass coverslips, which were then treated with cold 4% paraformaldehyde and 0.2% Triton X-100 (in PBS). Subsequently, 5% BSA (in PBS) was added to the coverslips to stay for 1 h, and cells were incubated with NF-κB p65, a primary

**FIGURE 1**
Genome characterization and molecular networks. **(A)** qRT-PCR detection of terpene genes. **(B)** GNPS-based molecular clusters.

antibody, at 4°C overnight. After adding labeled Alexa Fluor 594 (Proteintech) and the secondary antibody for 1 h, cells were stained with DAPI, and the washed coverslips were sealed. Images were detected using a fluorescence microscope (OLYMPUS IX83).

## Results and discussion

With the aim to discover chemical diversity with pharmaceutical bioactivity, a deep-sea derived fungus, *P. bilaiae* F28, was selected for chemical examination with the help of bioinformatics and chemo-informative data, which imply that this fungal strain is capable of producing diverse and novel acorane sesquiterpenes. Anti-SMASH genome sequence analysis revealed a total of nine terpene synthases (Supplementary Table S1) in the F28 strain, and qRT-PCR detection showed five terpene genes obviously expressed (Figure 1A). Gene annotation (Supplementary Table S2) revealed gene g10525 with a high homologous identity to ffsc6, a terpene cyclase for the catalysis of acorane core formation (Brock et al., 2013). These findings suggested that the F28 strain shows potential to produce acorane-related sesquiterpenes. To validate whether the terpene genes are really activated in culture conditions, an LC-MS/MS molecular

networking approach was applied to detect the chemical metabolites of the cultured fungus by the GNPS database. Based on the LC-MS/MS spectral similarity, molecular networking categorizes the chemical metabolites with similar scaffolds into clusters (Figure 1B). Analyses of MS/MS data in the nodes of clusters annotated a profile of acorane-type analogs, indicating the activation of terpene genes in the culture medium. Chromatographic separation of the EtOAc extract of the large-scale cultured fungus resulted in the isolation of 20 acorane sesquiterpenes, including 18 undescribed acoranes, namely, bilaiacorenol A–R (**1–18**) (Figure 2), along with adametacorenols A (**19**) and B (**20**). Herein, the structural determination of new sesquiterpenes and their anti-neuroinflammation are described.

## Structure elucidation of new acoranes

Bilaiacorenol A (**1**), a colorless amorphous powder, has a molecular formula of $C_{15}H_{24}O_3$, as established by HRESIMS and NMR data. Its $^{13}C$ NMR data (Supplementary Table S5) showed 15 carbon resonances, which were classified into 13 sp3 and two sp2 carbons for a double bond by the APT and HSQC data. The sp3 resonances involved three methyl, four methylene, four methine, and two nonprotonated carbons. The COSY

**FIGURE 2**
Chemical structures of bilaiaeacorenol A−R (**1−18**).



**FIGURE 3**
Key COSY and HMBC correlations of **1−3**, **5**, **8**, **11−12**, **14**, and **17−18**.

correlations from H-2 ($\delta_H$ 4.02, ddt, $J$ = 2.0, 4.8, and 10.0 Hz) to H-1 ($\delta_H$ 1.76, d, $J$ = 10.0 Hz), OH-2 ($\delta_H$ 5.12, d, $J$ = 4.8 Hz), and H$_2$-3 ($\delta_H$ 1.00, 2.43), and from H-4 ($\delta_H$ 1.73, ddq, $J$ = 4.8, 7.2, and 8.0 Hz) to H$_2$-3 and H$_3$-14 ($\delta_H$ 0.92, d, $J$ = 7.2 Hz) along with the HMBC correlations from C-5 ($\delta_C$ 40.0) to H-1, H-2, H$_2$-3, and H-4, established a 4-methyl-2-hydroxycyclopentane unit. In addition, a cyclohexene unit was elucidated by the COSY relationships between H$_2$-6 ($\delta_H$ 1.42, 1.57)/H-7 ($\delta_H$ 3.90, $J$ = 2.0, 3.2 Hz) and H-9 ($\delta_H$ 5.38 br)/H$_2$-10 ($\delta_H$ 1.87, 2.31) in association with the HMBC correlations from H$_3$-15 ($\delta_H$

1.72 brs) to C-7 ($\delta_C$ 69.2), C-8 ($\delta_C$ 135.8), and C-9 ($\delta_C$ 125.4) and from H$_2$-6 to C-5 and C-10. These findings demonstrated an acorane core in which a *spiro*-fusion of the two moieties at C-5 with a methyl location at C-8 was characterized. The substitutions of the dioxygenated isopropyl group at C-1 ($\delta_C$ 53.1) were deduced by the COSY relationship between H$_2$-12 ($\delta_H$ 3.16, 3.18) and OH-12 ($\delta_H$ 4.83, t, $J$ = 5.0 Hz) together with the HMBC correlations from H$_3$-13 ($\delta_H$ 1.12, s) to C-1, C-11 ($\delta_C$ 77.2) and C-12 ($\delta_C$ 72.5). The formation of an ether bond across C-7 ($\delta_C$ 69.2) and C-11 was evident from the HMBC correlation
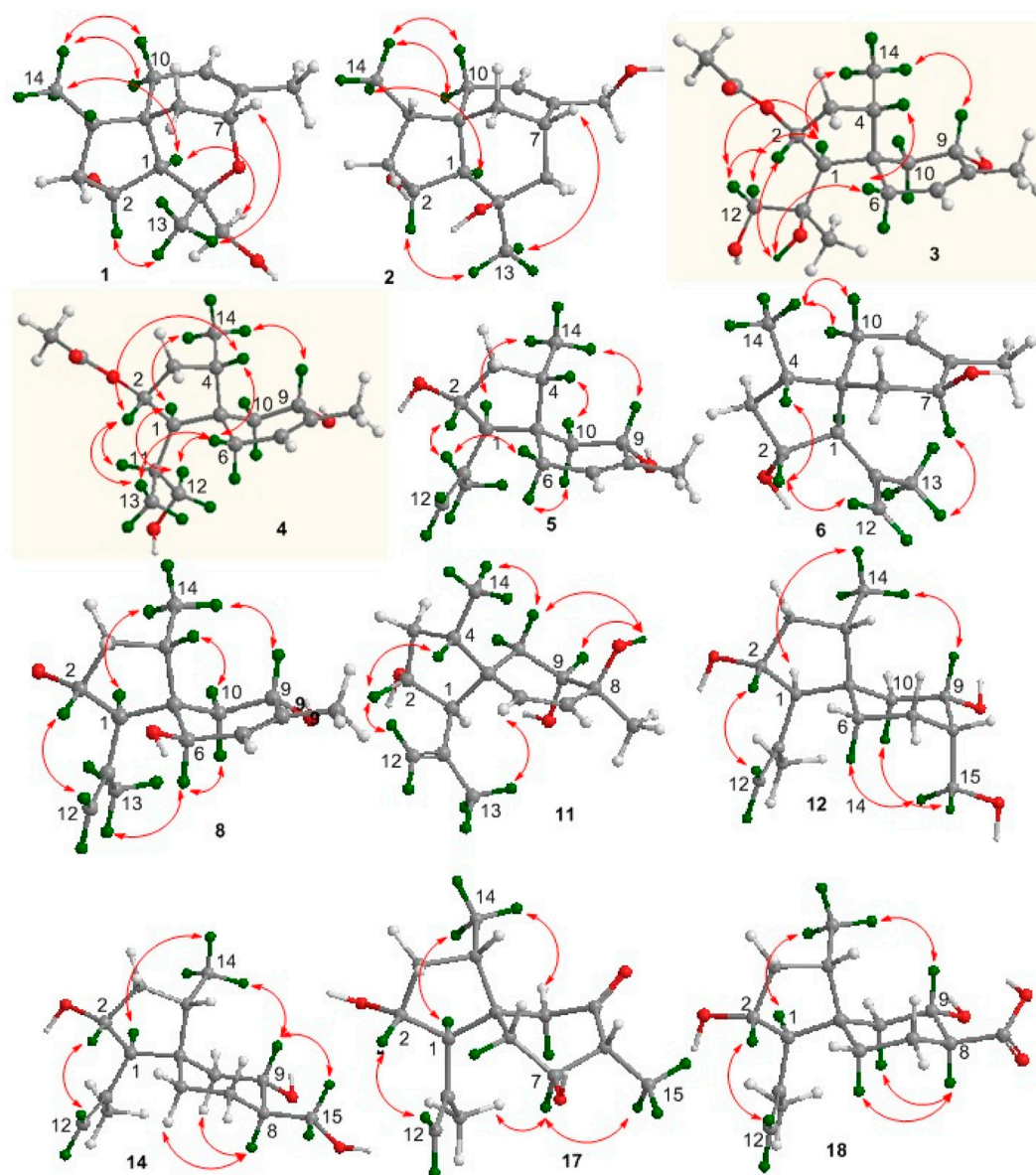
**FIGURE 4**
Key NOE correlations of **1–4**, **12**, **14**, and **17–18**.

between H-7 and C-11 (Figure 3). The NOE correlations between H-1/H$_3$-14 and H-2/H$_3$-13 suggested a cofacial relationship of H-2 with H-4, which was in the opposite face toward H-1. The NOE correlations between H$_3$-14 and H$_2$-10 established the *spiro*-chirality center C-5, for which H$_2$-10 was spatially approximated to H$_3$-14. Additional NOE correlations between H$_2$-12/H-1 and H$_3$-13/H-7 (Figure 4) established the relative configurations of C-7 and C-11, in which H$_2$-12 was spatially approximated to H-1. The X-ray diffraction data for the single crystal of **1** using the Flack parameter [0.00 (6)] assigned the absolute configurations as 1$R$, 2$R$, 4$S$, 5$S$, 7$R$, and 11$S$ (Figure 5).

Bilaiacorenol B (**2**) was obtained as a colorless amorphous crystal, and its molecular formula (C$_{15}$H$_{24}$O$_3$) was determined on the basis of the HRESIMS data. The NMR data on compound **2** (Supplementary Tables S3, S5) resembled those of **1**, and the 2D NMR data established a corane-type nucleus. The distinction was observed in the NMR data for the cyclohexene ring and the side chain at C-1 ($\delta_C$ 60.0). The connection of C-7 to C-11 ($\delta_C$ 69.4) *via* a methylene unit instead of an ether bond was demonstrated by the COSY relationship between H-7 ($\delta_H$ 2.28, ddt, $J$ = 2.0, 4.0, and 9.0 Hz) and H$_2$-12 ($\delta_H$ 1.34, 1.80), and hydroxylation at C-11 was clarified by the HMBC correlations from OH-11 ($\delta_H$ 3.91, s)
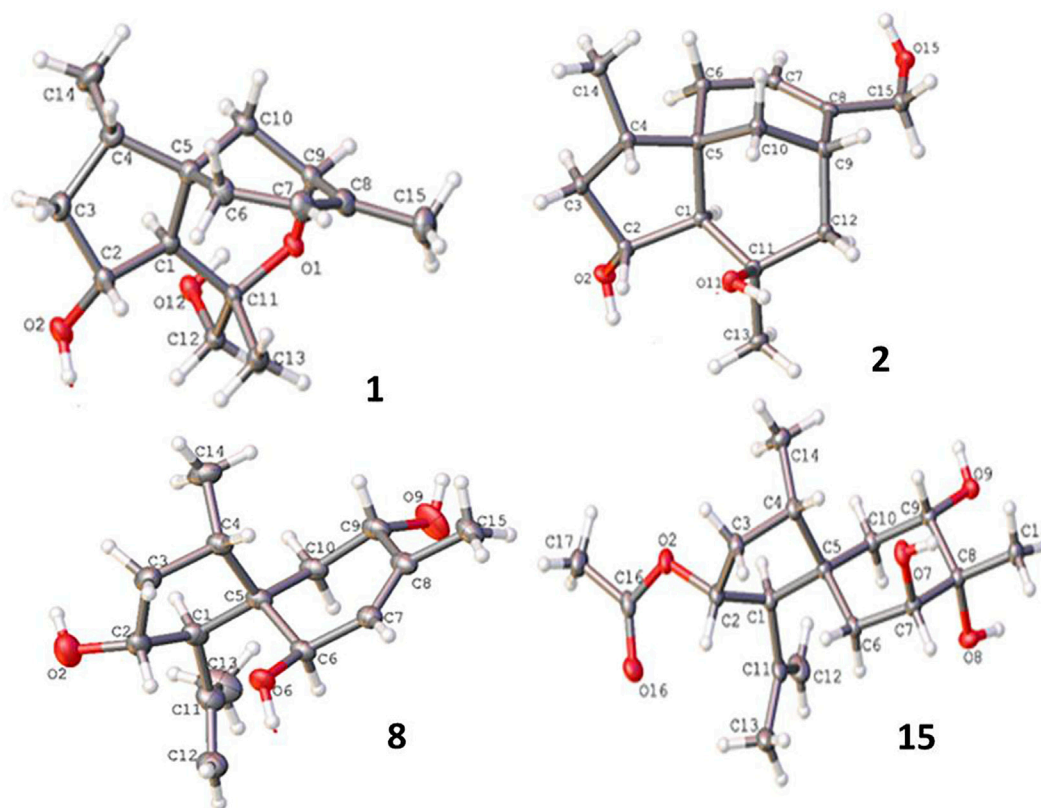
**FIGURE 5**
Structures of X-ray diffractions of **1–2**, **8**, and **15**.

to C-1, C-11 ($\delta_C$ 69.4), C-12 ($\delta_C$ 41.4), and C-13 ($\delta_C$ 30.3). In addition, a hydroxymethyl group at C-8 ($\delta_C$ 144.0) was deduced by the COSY coupling between H$_2$-15 ($\delta_H$ 3.78, 3.79) and OH-15 ($\delta_H$ 4.57, t, $J$ = 5.0 Hz) together with the HMBC correlations of H$_2$-15 to C-7 ($\delta_C$ 29.3), C-8, and C-9 ($\delta_C$ 118.3). Similar to the NOE data on **1**, the correlations from H$_3$-14 to H-1 and H$_2$-10 and between H-2 and H$_3$-13 suggested the same relative configurations at C-2 and C-4 and the *spiro*-chirality center C-5 of both compounds. The NOE correlations between OH-11/H-2 and H$_2$-12/H-1 (Figure 4) established the spatial closeness among these groups. Based on the data on a single crystal of the Cu/Kα X-ray diffraction experiment, a Flack parameter of –0.05 (9) allowed an unequivocal assignment of the 1*R*, 2*R*, 4*S*, 5*R*, 7*S*, and 11*R* configurations (Figure 5).

Bilaiacorenol C (**3**) was found to have a molecular formula of C$_{17}$H$_{28}$O$_5$, according to the HRESIMS data. Its NMR data (Supplementary Tables S3, S5) were characteristic of a corane-type sesquiterpene, related to those of compound **1**. The COSY and HMBC correlations established a planar structure, which was closely related to co-isolated adametacorenol A (Liu et al., 2015). However, the side chain at C-1 ($\delta_C$ 54.7) was assigned to a 1,2-dihydroxyisopropane moiety on the basis of the COSY

relationship between H$_2$-12 ($\delta_H$ 2.99, 3.07) and OH-12 ($\delta_H$ 4.57, t, $J$ = 5.0 Hz) in association with the HMBC correlations from H$_3$-13 ($\delta_H$ 1.21 s) and OH-11 ($\delta_H$ 4.09, s) to C-11 ($\delta_C$ 73.3) and C-12 ($\delta_C$ 69.6), and the correlations of C-1 to H$_3$-12 and OH-11. The NOE correlations between H-1 and H$_3$-14 and between H-2 and H$_2$-12 were indicative of the same relative configuration for the cyclopentane ring in both compounds **1** and **3**. Additional NOE correlations between H$_3$-14 ($\delta_H$ 0.97, d, $J$ = 7.2 Hz) and H-9 ($\delta_H$ 3.90 ddd, $J$ = 4.4, 5.0, 6.5 Hz) and between H-4 and H-6b fixed the *spiro*-form of the cyclohexene ring, in which H-9 was spatially approximated to H$_3$-14. If H-1 is arbitrarily assigned to $R^*$ configuration, the NOE correlations between H-1 and H$_2$-12, from OH-11 to H-2 and H$_2$-6, and between H$_2$-12 and H-2 (Figure 4) suggested an irrotational C$_1$-C$_{11}$ bond and 11$R^*$ configuration. The experimental ECD data were similar to those calculated for (1*R*, 2*R*, 4*S*, 5*S*, 9*S*, 11*R*)-3 (Supplementary Figure S163), suggesting the *R* configurations for C-1, C-2, and C-11, and the *S* configurations for C-4, C-5, and C-9.

The NMR and MS data (Supplementary Tables S3, S5) revealed bilaiacorenol D (**4**) to be a homolog of compound

3 with the distinction for the side chain at C-1 ($\delta_C$ 49.4). The COSY correlations from H-11 ($\delta_H$ 1.62, m) to $H_3$-13 ($\delta_H$ 0.86, d, $J$ = 7.0 Hz), H-1 ($\delta_H$ 2.00, dd, $J$ = 3.2, 9.0), and $H_2$-12 ($\delta_H$ 3.16, 3.23), and the extension of coupling between $H_2$-12 and OH-12 ($\delta_H$ 4.54, t, $J$ = 5.0 Hz) identified a hydroxylated isopropane unit at C-1. The HMBC correlations from $H_3$-13 and $H_2$-12 to C-1 and C-11 ($\delta_C$ 33.0) supported compound **4** as a 11-dehydroxylated analog of **3**. The similar NOE data on compounds **3** and **4**, such as the correlations between H-2/H-4, $H_3$-14/H-9, and $H_3$-14/H-1, suggested the same relative configurations in the backbone. The $J_{H-1/H-11}$ value (3.2 Hz) in association with the NOE correlations from $H_3$-13 to H-2 and H-6b, from $H_2$-12 to H-1 and $H_2$-6b, and between H-11 and H-2, also suggested the unrotational C-1/C-11 bond. The similar ECD data (Supplementary Figure S163) suggested that the absolute configuration of compounds **3** and **4** was identical, with the exception of C-11, which was suggested to be the $S$ configuration with the help of NOE data.

Bilaiacorenol E (**5**) was found to have a molecular formula $C_{15}H_{24}O_2$ on the basis of the HRESIMS data. Interpretation of the 2D NMR data clarified the planar structure of compound **5** to be identical to a 2-deacetylated adametacorenol A. The similar NOE data between compound 5 and adametacorenol A in association with the comparable experimental ECD data to those calculated for a model molecule of (1$R$, 2$R$, 4$S$, 5$S$, 9$S$)-**5** agreed compound 5 possessing the same absolute configuration as the known homolog. Alkaline hydrolysis of adametacorenol A derived a product whose NMR data (Supplementary Figure S172) and optical rotation were consistent with those of compound **5**, supporting the structural assignment.

Analyses of the 2D NMR and HRESIMS data assigned the planar structure of bilaiacorenol F (**6**) and compound **5** to be identical. The NOE correlations between H-1 ($\delta_H$ 2.17, d, $J$ = 5.6 Hz)/$H_3$-14 ($\delta_H$ 0.85, d, $J$ = 6.8 Hz) and $H_3$-13 ($\delta_H$ 1.64, s)/H-2 ($\delta_H$ 4.00, ddt, $J$ = 4.8, 5.6, and 10.8 Hz) suggested the same relative configuration of ring A in both compounds **5** and **6**. The distinction was attributed to the NOE interactions between rings A and B, where the NOE correlation between $H_3$-14 and $H_2$-10 ($\delta_H$ 1.87, br) and the latter protons coupling to olefinic proton H-9 ($\delta_H$ 5.34, brs) suggested the double bond shifted from C-7/C-8 of **5** to C-8/C-9 of **6**. Additional NOE correlation between $H_3$-13 and H-7 ($\delta_H$ 3.95) supported the structural assignment.

The 1D and 2D NMR data in association with the HRESIMS data identified bilaiacorenol G (**7**) as a 2-deacetylated adametacorenol B, and it was supported by the chemical conversion of adametacorenol B to compound **7** under alkaline catalysis.

Bilaiacorenol H (**8**) has a molecular formula of $C_{15}H_{24}O_3$, as established by the HRESIMS data, containing an oxygen atom more than that of compound **5**. Comparison of the NMR data (Supplementary Tables S4, S5) revealed the structure of compound **8** closely related to compound **5**, and the

cyclopentane moiety of both compounds was identical. With regard to the cyclohexene ring, two hydroxyl groups resided at C-6 and C-9, respectively, were recognized by the COSY correlations between H-6 ($\delta_H$ 3.83, brd, $J$ = 6.0 Hz)/OH-6 ($\delta_H$ 4.50, d, $J$ = 6.0 Hz) and H-9 ($\delta_H$ 3.97, ddd, $J$ = 6.0, 6.8, and 10.0 Hz)/OH-9 ($\delta_H$ 4.56, d, $J$ = 6.8 Hz) along with the HMBC correlations from OH-6 to C-5 ($\delta_C$ 52.5), C-6 ($\delta_C$ 68.9), and C-7 ($\delta_C$ 129.1) and from OH-9 to C-8 ($\delta_C$ 136.4), C-9 ($\delta_C$ 66.6), and C-10 ($\delta_C$ 39.5). These data allowed the location of a double bond at C-7/C-8. The similar NOE relationships in ring A of compounds **5** and **8** suggested the same relative configuration for the relevant protons of both compounds. Additional NOE correlations between $H_3$-14/H-9 and $H_3$-13/H-6 (Figure 4) reflected a *trans*-orientation between H-6 and H-9. The comparable experimental ECD data to those calculated for the model molecule of (1$R$, 2$R$, 4$S$, 5$R$, 6$R$, 9$S$)-**8** (Supplementary Figure S163) clarified the absolute configuration of compound **8**.

Bilaiacorenol I (**9**) was determined as a 2-acetylated analog of compound **8** based on the comparable NMR data, except for the presence of an acetyl group in compound **9**. The location of the acetyoxy group at C-2 was evident from the HMBC correlation between H-2 and the acetyl carbonyl carbon. The similar NOE correlations suggested that both compounds have the same relative configuration. The absolute configuration of compound **9** was the same as that of compound **8** based on the alkaline hydrolysis of compound **9** to produce a hydrolyzed product, whose $^1H$ NMR data (Supplementary Figure S169) and specific rotation ($[\alpha]_D^{20}$ -21) were almost identical to those of compound **8**.

The molecular formula ($C_{17}H_{26}O_4$) of bilaiacorenol J (**10**) was determined by the HRESIMS data, containing an oxygen atom more than that of adametacorenol A. Its NMR data (Supplementary Tables S4, S5) resembled those of adametacorenol A, with the only difference for the substitution at C-13. A hydroxymethylene unit to replace a methyl group of the latter was recognized by the COSY correlation between $H_2$-13 ($\delta_H$ 3.78, 3.86) and OH-13 ($\delta_H$ 4.90, t, $J$ = 5.6 Hz) together with the HMBC correlations from $H_2$-13 to the olefinic carbons C-11 ($\delta_C$ 147.4) and C-12 ($\delta_C$ 109.7), as well as C-1 ($\delta_C$ 52.7). The similar NOE interactions suggested the same relative configuration for both compound **10** and adametacorenol A. The comparable experimental ECD data with those calculated for (1$S$, 2$R$, 4$S$, 5$S$, 7$S$)-**10** reflected the same absolute configuration of both compound **10** and adametacorenol A (Supplementary Figure S163).

The molecular formula of bilaiacorenol K (**11**) was the same as that of compound **8**, as established by the HRESIMS data. A comparison of the NMR data revealed both compounds **8** and **11** share the partial structure of the cyclopentane unit. In regard to the cyclohexene unit, the olefinic coupling between H-6 ($\delta_H$ 5.28, d, $J$ = 10.0 Hz) and H-7 ($\delta_H$ 5.27, d, $J$ = 10.0 Hz) resided a double bond at C-6 ($\delta_C$
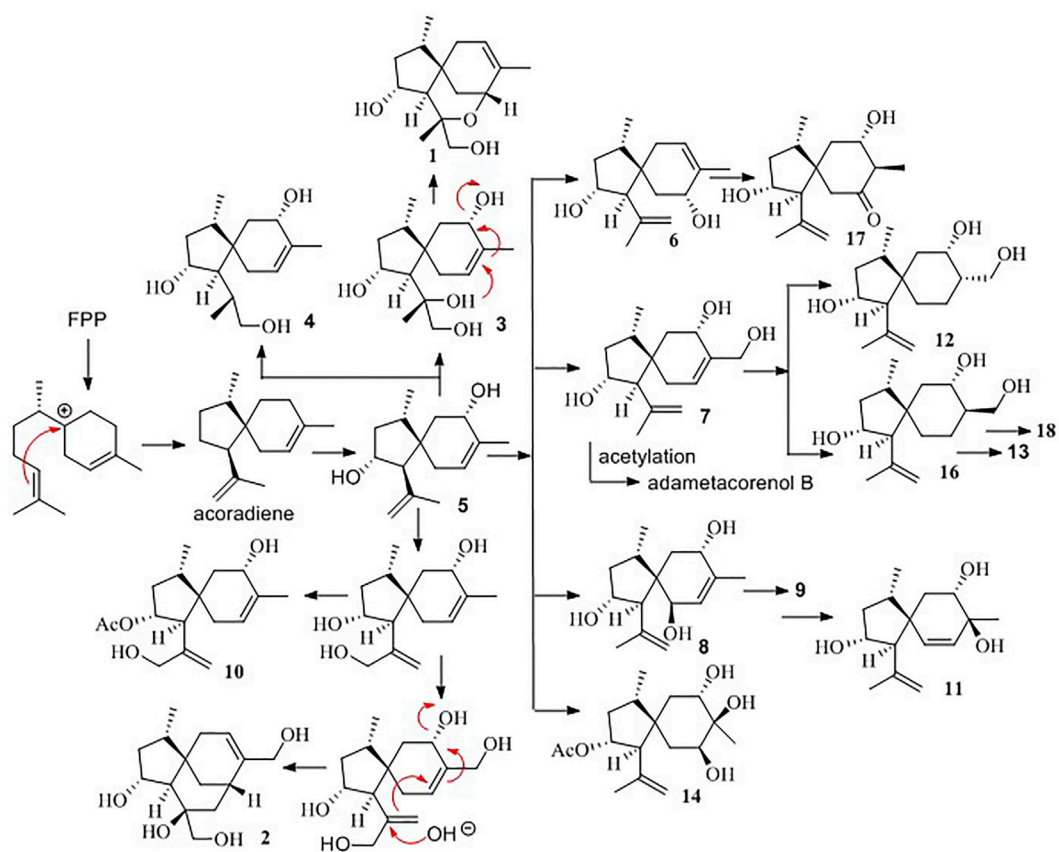
**SCHEME 1**
Biogenetic relationships of bilaiaeacorenols.
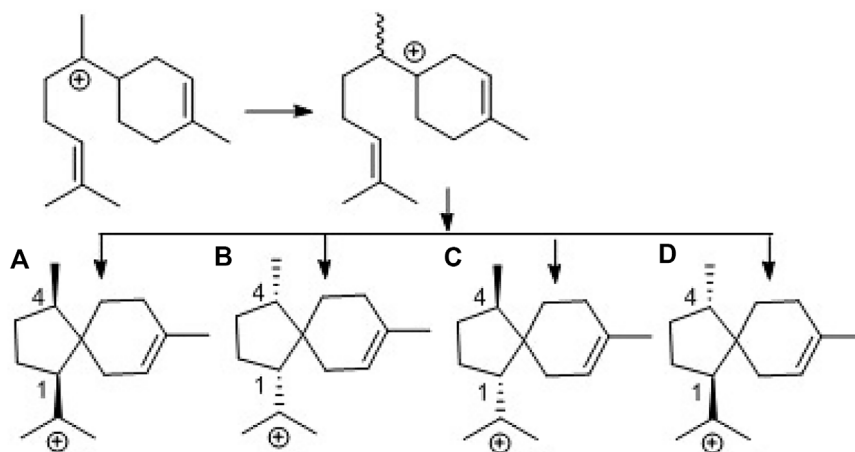


**SCHEME 2**
Biogenetic formation of the stereospecific centers of acorane cores. **(A)**: 1R,4R-form, **(B)**: 1S,4S-form, **(C)**: 1S,4R-form, **(D)**: 1R,4S-form.
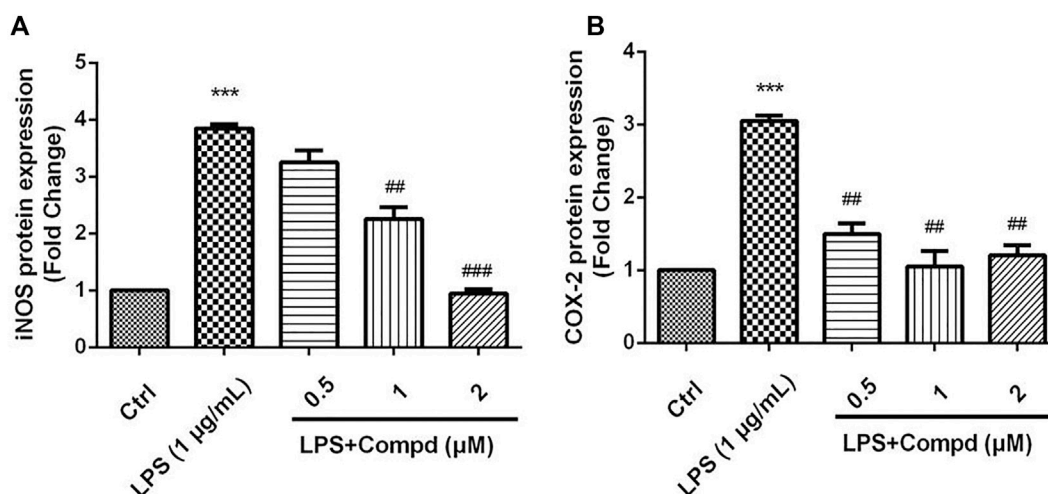
**FIGURE 6**
Analog **18** inhibited the expression of iNOS and COX-2 in LPS-induced BV-2 cells. Cells were stimulated by 1 μg/mL LPS with or without 18 for 24 h. **(A)** The protein expressions o f iNOS treated by different concentrations of 18 were determined by Western blot assay, **(B)** the expressions of COX-2 t reated by different concentrations of 18 were determined by Western blot assay. The data are represented as a mean ± S.D. from independent experiments performed in triplicate (*compared with the control, #compared with LPS, */#$p < 0.05$, **/##$p < 0.01$, and ***$p < 0.001$).
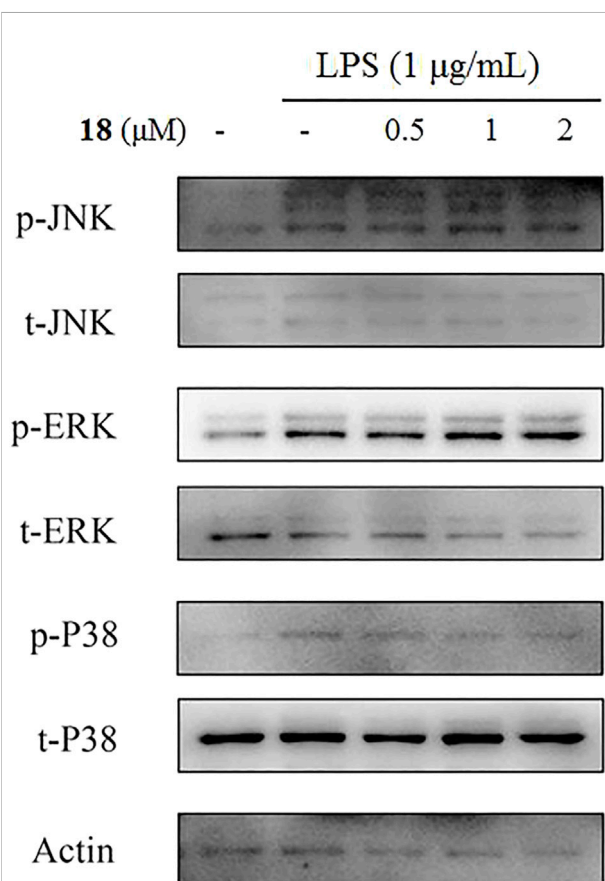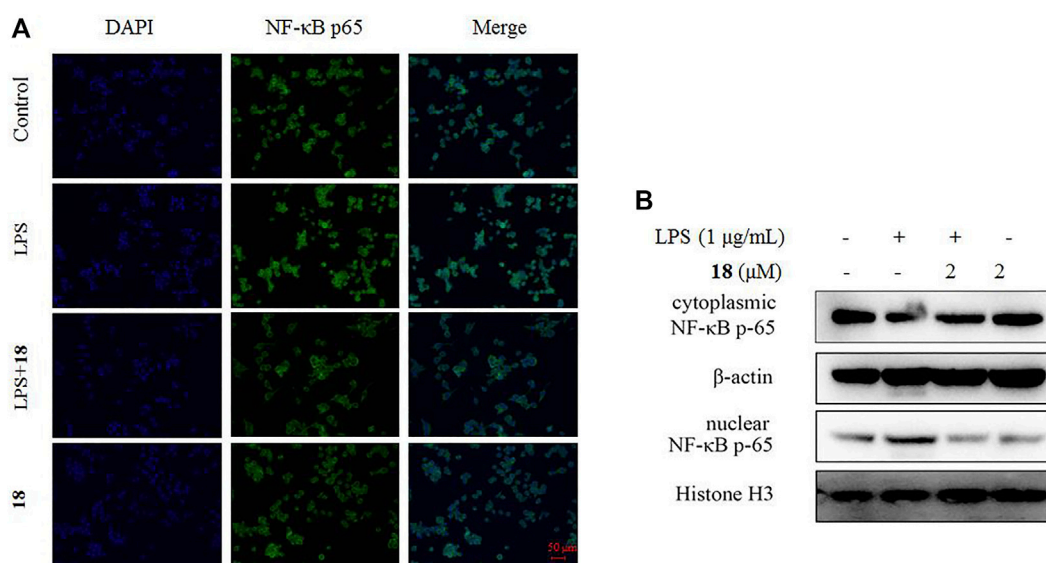


**FIGURE 7**
Ineffective analog **18** to regulate MAPK phosphorylation in LPS-stimulated BV-2 cells.

131.6)/C-7 ($\delta_C$ 133.3), and the HMBC correlations of both H$_3$-15 ($\delta_H$ 0.96, s) and OH-8 ($\delta_H$ 4.33, s) to C-7, C-8 ($\delta_C$ 71.7), and C-9 ($\delta_C$ 71.8) along with the COSY correlations from H-9 ($\delta_H$ 3.57, ddd, $J = 2.4$, 6.0, and 9.2 Hz) to H$_2$-10 ($\delta_H$ 1.43, 1.64) and OH-9 ($\delta_H$ 4.47, d, $J = 6.0$ Hz) located the hydroxyl groups at C-8 and C-9 and a methyl substitution at C-8. Thus, compound **11** is likely derived from compound **8** by hydroxyl migration from C-6 to C-8, following olefinic transformation. The NOE correlations between H-1/H$_3$-14 and H-2/H$_3$-13 suggested the same relative configuration of the cyclopentane moiety for both compounds **8** and **11**. The $J_{H-9/H-10a}$ value (9.2 Hz) was indicative of an axial orientation of H-9. The *spiro*-chirality center C-5 as the case of compound **8** was evident from the NOE correlations between H$_3$-14 and H-9 and between H$_3$-13 and H-6. The *cis*-orientation of H-9 with OH-8 was identified by their NOE interaction.

Corane-type sesquiterpenes **12–18** are structurally characteristic of a *spiro*-fusion of cyclopentane with a cyclohexane unit instead of a cyclohexene unit. The distinction was attributed to the different substitution at the backbone.

The 2D NMR data established a corane core of bilaiacorenol L (**12**). Apart from ring A, which was identical to that of compound **11**, the NMR data (Supplementary Table S6) showed two hydroxyl groups in the cyclohexane unit. The location of hydroxyl groups at C-9 ($\delta_C$ 67.5) and C-15 ($\delta_C$ 57.4) was evident from the COSY relationships between H-9 ($\delta_H$ 3.70, dt, $J = 4.0$, 10.0 Hz)/OH-9 ($\delta_H$ 5.00, d, $J = 4.0$ Hz) and H$_2$-15 ($\delta_H$ 3.29, 3.60)/OH-15 ($\delta_H$ 4.22, t, $J = 5.0$ Hz) along with the COSY correlations from H-8

**FIGURE 8**
Effect of analog **18** on the nuclear translocation of NF-κB p65 in LPS-stimulated BV-2 cells. **(A)** BV-2 cells were stimulated with LPS (1 μg/ml) in the absence or presence of analog **18** (2 μM) for 3 h, followed by detection of the NF-kB p65 subunit translocation by immunocytochemistry. NF-κB p65 is shown in green, and DNA (DAPI nuclear staining) is shown in blue. Bars: 50 μm. **(B)** BV-2 cells were stimulated with LPS (1 μg/ml) in the absence or presence of **18** (2 μM) for 3 h, and NF-kB p65 levels in the nucleus and cytoplasm were determined by Western blot. Histone H3 and β-actin were used as endogenous controls for nuclear and cytoplasmic proteins, respectively. Values represent the mean $\pm$ SD of three independent experiments (*compared with the control, #compared with LPS, */#$p < 0.05$, **/##$p < 0.01$, and ***$p < 0.001$).

($\delta_H$ 1.81, m) to H-9 and $H_2$-15. The same relative configuration of the cyclopentane unit as that of compound 11 was suggested by the similar NOE correlations of the relevant protons. A chair conformer of the cyclohexane was recognized by the $J$ values of the protons in cyclohexane. The NOE interactions from $H_2$-15 to H-6a and H-10a suggested an axial orientation of the hydroxymethylene unit. As in the case in compound **11**, the NOE correlation between $H_3$-14 and H-9 fixed the relative configuration of the *spiro*-center C-5, and H-9 was spatially approximated to $H_3$-14.

The planar structure of bilaiacorenol M (**13**) was identified as a 2-acetylated analog of compound **12** on the basis of the diagnostic 2D NMR data. The NOE data suggested the relative configuration of the cyclopentane unit to be consistent with that of compound **12**. Like the case of **12**, the NOE interaction between $H_3$-14 and H-9 identified the same *spiro*-configuration of both compounds **12** and **13**. The $J_{H-7/H-8}$ (10.0 Hz) value and the NOE correlation between $H_2$-15 and H-9 suggested a *trans* axial–axial relationship between H-8 and H-9, reflecting an equatorial orientation of $H_2$-15. This resulted in an unshielded C-15 ($\delta_C$ 63.2) of compound **13** comparing that of compound **12** ($\delta_C$ 57.4).

Diagnostic 2D NMR (Supplementary Table S6) and MS data identified bilaiacorenol N (**14**) to be a 2-deacetylated **13**, and this was confirmed by the chemical conversion of compound **13** to **14** under alkaline catalysis.

The molecular formula of bilaiacorenol O (**15**) was determined to have an oxygen atom of more than **13**, as provided by the HRESIMS data. The NMR data revealed the cyclopentane moiety of both compounds **13** and **15** to be identical. The distinction was attributed to the substitution at the cyclohexane moiety, where three hydroxyl protons were observed at OH-7 ($\delta_H$ 4.56, d, $J = 2.4$ Hz), OH-8 ($\delta_H$ 3.78, s), and OH-9 ($\delta_H$ 4.08, d, $J = 4.4$ Hz), which were clarified by the COSY relationships between H-7 ($\delta_H$ 3.53, ddd, $J = 2.4$, 3.0, and 3.6 Hz)/OH-7 and H-9 ($\delta_H$ 3.49, ddd, $J = 2.0$, 4.4, and 10.0 Hz)/OH-9. The HMBC correlations of $H_3$-15 ($\delta_H$ 1.09, s) and OH-8 to C-7 ($\delta_C$ 73.9), C-8 ($\delta_C$ 74.0), and C-9 ($\delta_C$ 70.5) further supported the hydroxyl locations. The $J_{H-9/H-10a}$ (10 Hz) value and the $J_{H7-H6}$ values (3.0, 3.6 Hz) reflected an axial H-9 and an equatorial H-7. The NOE correlation between H-9 and $H_3$-15 suggested the cofacial relationships of these groups. The remaining NOE data were similar to those of compound **13**. The single-crystal X-ray diffraction using Cu-Kα radiation (Figure 5) clarified the absolute configurations of compound 15 to be 1R, 2R, 4S, 5R, 7S, 8R, and 9S.

Bilaiacorenol P (**16**) was determined as a 2-deacetylated **15** on the basis of the NMR and MS data. Alkaline hydrolysis of compound **15** to derive compound **16** supported the structure assignment.

Bilaiacorenol Q (**17**) has a molecular formula of $C_{15}H_{24}O_3$, as established by the HRESIMS data. The 2D

NMR data provided the partial structure regarding the cyclopentane unit to be identical to that of compound **16**. The distinction was found in the cyclohexane moiety, where a ketone group at C-9 ($\delta_C$ 211.2) was evident from the HMBC correlations from H$_3$-15 ($\delta_H$ 0.93, d, $J$ = 6.0 Hz) to C-7 ($\delta_C$ 71.4), C-8 ($\delta_C$ 52.5), and C-9. The $J_{H-7/H-6a}$ and $J_{H-7/H-8}$ values (10 Hz) were characteristic of a chair conformation of the cyclohexane ring. The NOE data suggested that both compounds **17** and **16** have the same relative configuration for ring A. The NOE interaction between H$_3$-14 ($\delta_H$ 0.89, d, $J$ = 7.2 Hz) and H$_2$-10 ($\delta_H$ 2.22, 2.28) fixed the *spiro*-orientation, and the correlations of H-7 ($\delta_H$ 3.37, ddt, $J$ = 4.8, 6.0, 10.0 Hz) with H$_3$-13 ($\delta_H$ 1.69, s) and H$_3$-15 ($\delta_H$ 0.93, d, $J$ = 6.0 Hz) assigned the same face of H-7 and H$_3$-15 (Figure 4), and the former was spatially approximated to H$_3$-13.

Bilaiacorenol R (**18**) has a molecular formula of $C_{15}H_{24}O_4$, as determined by the HRESIMS data. The NMR data on compound **18** (Supplementary Table S7) resembled those of compound **14**, indicating structure similarity. The difference was attributed to the substituent at C-8, where a carboxylic group of compound **18** was found for C-15 ($\delta_C$ 176.3) due to the HMBC correlations of C-15 to H-8, H-9 and H$_2$-7. The $J_{H-7/H-8}$ (12 Hz) value and the similar NOE data suggested that both compounds **14** and **18** have the same relative configuration.

Compounds **19** and **20** were identical to adametacorenols A and B by the comparison of their spectroscopic data and the specific rotations with those reported in the literature (Liu et al., 2015). Based on the configurational assignments, the stereogenic centers in ring A regarding ring A of all analogs are conserved. This can be explained by the analogs derived from the same acorane precursor. Thus, the comparison of experimental and calculated ECD data (Supplementary Figure S163) in association with the NOE data enables to assign the absolute configurations of the amorphous analogs.

## Biogenetic postulation

Biogenetically, the bisabolyl cation, as derived from farnesyl diphosphate (FPP), is an intermediate to generate acoradiene (Citron et al., 2011), which is considered the principal component to derive an array of acorane-type sesquiterpenes *via* various oxidation and rearrangement mechanisms. 2,9-Dihydroxylation of acoradiene generates compound **5**, and further hydroxylation of compound **5** derives compounds **7** and **8**. Acetylation of compounds **5**, **7**, and **8** affords adametacorenols A and B, and compound **9**. 13-Hydroxylation of adametacorenol A derives compound **10**, but analog **6** is likely derived from 5 *via* hydroxyl migration and olefinic transformation. A similar pathway occurs for the conversion of compound **8** to **11**. Reduction of the double bond in compound 7 and adametacorenol B affords compounds **12**,

**13**, and **14**. Analogs **15** and **16** are assumed to be derived from adametacorenols A and B *via* epoxidation and hydrolysis, but analog **17** is likely derived from epoxidated 5, following oxidative epoxide cleavage. Oxidation of hydroxymethylene C-15 in compound **13** converts to **18**. Epoxidation of adametacorenol A at the side chain of ring A, following epoxide cleavage, derives 3 and 4. Analogs 1 and 2 are depicted to be derived from 11,12-epoxided 5, followed by ring fusion (Scheme 1). Since acoradiene is a fungal product isolated from our fungal strain and other organisms, it is an intermediate to derive diverse acorane analogs. Hydroxylation or oxidation at ring B is depicted to occur after the formation of the bicyclic core. The different C-5 configuration in **5** and **6** is thus raised by the hydroxylation at C-7 or C-9, respectively, rather than the induction by different fusion of the bicyclic core. The putative biogenetic relationships suggested that all isolates maintain the conserved configurations in ring A due to compound **5** as the sole precursor.

To provide evidence for the biosynthetic process of these sesquiterpenes, genome sequencing was conducted, and nine putative terpenoid synthases (TS) in different locations were annotated by anti-SMASH analysis (Supplementary Table S2). Among them, the gene *g10525* showed a high identity to *Ffsc6*, a terpene cyclase used for the synthesis of acorenols in ascomycete *Fusarium fujikuroi* (Brock et al., 2013). Using heterologous hosts to express *g10525* in *Aspergillus nidulans* A1145, a number of sesquiterpenes were detected by LC-MS/MS spectra, and a molecular ion at *m/z* 204 was consistent with that of acoradiene. These data supported that the acorane-type derivatives synthesized in *P. bilaiae* followed the similar pathways as other fungal origins reported in the literature. Notably, corane-type sesquiterpenes from different fungal species display distinct stereogenic centers regarding the cyclopentane ring. Theoretically, the cyclization of the homobisabolyl cation derives four diastereomeric acorenyl cations (Scheme 2). In *Trichoderma* strains, the intermediate B derives tricho-acorenol and relevant analogs as the main components, which are characteristic of *cis*-orientation of the substituents at C-1 and C-4 (Aoyagi et al., 2008; Citron et al., 2011; Li et al., 2011; Wu et al., 2011; Zhang et al., 2017). Eupho-acorenols from a plant are diastereoisomers of tricho-acorenol with *trans*-orientation of 1,4-substituents, as catalyzed by the sesquiterpene synthase EfTPS12 (Zhu et al., 2021). The stereogenic assembly pattern of acorane sesquiterpene from the plant *Lysionotus pauciflorus* coincides with those from *Trichoderma* fungi but in a different manner from that in the plant *Daphne genkwa* (Guo et al., 2020), which assembles the acorane skeleton through the intermediate C. A basidiomycete (mushroom)-derived acorane-type sesquiterpenoid possesses the scaffold (Sandargo et al., 2019) which is likely constructed by the intermediate A. In this work, bilaiacorenols are obviously produced from the intermediate D and are

characteristic of the 1,4-*trans*-substituted spiro [4,5]decane core. These findings suggest that the terpene cyclases from different origins play similar rules to assemble the acorane core but with a stereospecific selection of precursors, implying g10525 as a new sesquiterpene synthase. The detailed functions and catalysis mechanism require further investigation.

## Anti-neuroinflammation effects

In preliminary *in vitro* bioassay, the inhibition of lipopolysaccharide (LPS)-reduced nitric oxide (NO) production in murine BV-2 microglial cells was detected (Cheng et al., 2011; Mendes et al., 2012). Prior to the detection, the MTT method was used to test the analogs for their cytotoxic effects of analogs by counting and analyzing cell viability. All tested compounds showed no to weak cytotoxicity due to their $IC_{50}$ values more than 100 μM (Supplementary Table S2). At non-toxic concentrations (10 μM), six acorane-type analogs exhibited potent effects for the reduction of the LPS-induced NO production (Supplementary Table S2), showing higher activities than the positive control NG-monomethyl-L-arginine (L-NMMA), a nitric oxide synthase (NOS) inhibitor. Analyses of the structures related to activities suggested analogs with 2-acetylation increasing the activity in comparison with that for 2-hydroxylated counterparts, such as **8** vs. **9**, **13** vs. **14**, and **15** vs. **16**, indicating the substitution at C-2 directly affected the activity. Hydroxylation at the cyclohexane ring also affects the bioactivity, such as analogs with the triol unit (**15** and **16**) showed higher effects than those with diol and mono-hydroxylation. The most active analog **18** with a carboxylic group at C-8 showed more effects than those with the hydroxymethylene unit at C-8 (Table 1).

The inducible nitric oxide synthase (iNOS) produced the signaling molecule NO as an inflammatory factor related to neurodegenerative diseases, and iNOS regulates the NO level during neuroinflammation (Herbert et al., 2006). Western blot detection revealed that **18** decreased the iNOS and the other inflammatory mediator cyclooxygenase-2 (COX-2) levels in LPS-induced BV-2 cells (Figure 6). The MAPK and NF-kB signaling pathways are the critical transcription factors which mediate the expression of pro-inflammatory genes (Lawrence et al., 2009; DiDonato et al., 2012; Choi et al., 2019). In BV-2 microglial cells, analog **18** slightly affected the phosphorylation of c-Jun $NH_2$-terminal protein kinase (JNK), extracellular regulated protein kinases (ERK), and p38, which play key roles in the MAPK signaling pathway (Figure 7). However, the immunofluorescence and WB results revealed that **18** significantly downregulated the expression of the p65 level in the nucleus of LPS-stimulated BV-2 cells (Figure 8), suggesting the anti-neuroinflammatory effects of compound **18** related to the NF-kB signaling pathway.

## Conclusion

In this study, the bioinformatics approach in association with the molecular networking data provides an effective method to detect the metabolite patterns produced by marine-derived fungi, and a total of 18 new acorane-type sesquiterpenes are obtained from the deep-sea-derived fungus *P. bilaiae* F-28. Although the spiro[4.5] decane core of analogs from the F-28 strain is similar to that reported in the literature (Zhang et al., 2020), the distinct stereogenic centers of the analogs from this fungus to those derived from plants or the *Trichoderma* genus suggest the synthases with distinct stereospecific selections, implying a group of new synthases in this fungus. Bilaiacorenols A and B are structurally featured by the unique tricyclic acorane-type sesquiterpenes in nature. Analog **18** exhibits efficient reduction against the NO production in LPS-induced $BV_2$ macrophages in a dose-dependent manner, and it abolished LPS-induced NF-κB in the nucleus of BV-2 microglial cells, along with the inhibition of iNOS and COX-2 at cellular levels. This study extends the chemical diversity of acorane-type sesquiterpenes and demonstrates that compound **18** shows potential for the development as an anti-neuroinflammation agent after structure optimization.

## Data availability statement

The datasets presented in this study can be found in online repositories. The names of the repository/repositories and accession number(s) can be found in the article/ Supplementary Material.

## Author contributions

WZ and DL performed fungus fermentation and compound isolation; QM and JH performed the bioassays and the mode of action; JW analyzed the molecular networking data; WC and AF analyzed the bioinformatics data; JX partly helped elucidate the structures; WL elucidated the structures of new compounds and edited the manuscript.

## Funding

## Acknowledgments

## Conflict of interest

The authors declare that the research was conducted in the absence of any commercial or financial relationships that could be construed as a potential conflict of interest.

## Publisher's note

All claims expressed in this article are solely those of the authors and do not necessarily represent those of their affiliated organizations, or those of the publisher, the editors, and the reviewers. Any product that may be evaluated in this article, or claim that may be made by its manufacturer, is not guaranteed or endorsed by the publisher.

## Supplementary material

The Supplementary Material for this article can be found online at: https://www.frontiersin.org/articles/10.3389/fchem.2022.1036212/full#supplementary-material

## References

Aoyagi, A., Ito-Kobayashi, M., Ono, Y., Furukawa, Y., Takahashi, M., Muramatsu, Y., et al. (2008). Colletoic acid, a novel 11β-hydroxysteroid dehydrogenase type 1 inhibitor from *Colletotrichum gloeosporioides* SANK 21404. *J. Antibiot.* 61 (3), 136–141. doi:10.1038/ja.2008.122

Bian, G., Hou, A., Yuan, Y., Hu, B., Cheng, S., Ye, Z., et al. (2018). Metabolic engineering-based rapid characterization of a sesquiterpene cyclase and the skeletons of fusariumdiene and fusagramineol from *Fusarium graminearum*. *Org. Lett.* 20, 1626–1629. doi:10.1021/acs.orglett.8b00366

Brock, N. L., Huss, K., Tudzynski, B., and Dickschat, J. S. (2013). Genetic dissection of sesquiterpene biosynthesis by *Fusarium fujikuroi*. *ChemBioChem* 14, 311–315. doi:10.1002/cbic.201200695

Cheng, X., Zeng, Q., Ren, J., Qin, J., Zhang, S., Shen, Y., et al. (2011). Sesquiterpene lactones from Inula falconeri, a plant endemic to the Himalayas, as potential anti-inflammatory agents. *Eur. J. Med. Chem.* 46, 5408–5415. doi:10.1016/j.ejmech.2011.08.047

Choi, M. C., Jo, J., Park, J., Kang, H. K., and Park, Y. (2019). NF-κB signaling pathways in osteoarthritic cartilage destruction. *Cells* 7, e734, 8, doi:10.3390/cells8070734

Citron, C. A., Riclea, R., Brock, N. L., and Dickschat, J. S. (2011). Biosynthesis of acorane sesquiterpenes by *Trichoderma*. *RSC Adv.* 1, 290–297. doi:10.1039/c1ra00212k

DiDonato, J. A., Mercurio, F., and Karin, M. (2012). NF-κB and the link between inflammation and cancer. *Immunol. Rev.* 246, 379–400. doi:10.1111/j.1600-065x.2012.01099.x

Guo, R., Ren, Q., Tang, Y., Zhao, F., Lin, B., Huang, X., et al. (2020). Sesquiterpenoids from the roots of *Daphne genkwa* Siebold et Zucc. with potential anti-inflammatory activity. *Phytochemistry* 174, e112348. doi:10.1016/j.phytochem.2020.112348

Herbert, T., and Alexander, R. M. (2006). Adipocytokines: Mediators linking adipose tissue, inflammation and immunity. *Nat. Rev. Immunol.* 6, 772–783. doi:10.1038/nri1937

Li, G., Yang, Z., Zhao, P., Zheng, X., Luo, S., Sun, R., et al. (2011). Three new acorane sesquiterpenes from *Trichoderma* sp. YMF1.02647. *Phytochem. Lett.* 4, 86–88. doi:10.1016/j.phytol.2010.09.005

Lawrence, T. (2009). The Nuclear Factor NF-κB Pathway in Inflammation, *Cold Spring Harb. Perspect. Biol.*, 1, 6, e001651, doi:10.1101/cshperspect.a001651

Liu, Y., Li, X., Meng, L., Jiang, W., Xu, G., Huang, C., et al. (2015). Bisthiodiketopiperazines and acorane sesquiterpenes produced by the marine-derived fungus *Penicillium adametzioides* AS-53 on different culture media. *J. Nat. Prod.* 78, 1294–1299. doi:10.1021/acs.jnatprod.5b00102

Mendes, S. A. C., Mansoor, T. A., Rodrigues, A., Armas, J. B., and Ferreira, M. U. (2012). Anti-inflammatory guaiane-type sesquiterpenes from the fruits of Pittosporum undulatum. *Phytochemistry* 95, 308–314. doi:10.1016/j.phytochem.2013.06.019

Meng, L., Li, X., Li, H., and Wang, B. (2020). Chermebilaenes A and B, new bioactive meroterpenoids from co-cultures of marine-derived isolates of Penicillium bilaiae MA-267 and P. chermesinum EN-480. *Mar. Drugs* 18, e339. doi:10.3390/md18070339

Sandargo, B., Michehl, M., Praditya, D., Steinmann, E., Stadler, M., and Surup, F. (2019). Antiviral meroterpenoid rhodatin and sesquiterpenoids rhodocoranes A–E from the wrinkled peach mushroom, *Rhodotus palmatus*. *Org. Lett.* 21 (9), 3286–3289. doi:10.1021/acs.orglett.9b01017

Wu, S., Zhao, L., Chen, Y., Huang, R., Miao, C., and Wang, J. (2011). Sesquiterpenoids from the endophytic fungus *Trichoderma* sp. PR-35 of *Paeonia delavayi*. *Chem. Biodivers.* 8, 1717–1723. doi:10.1002/cbdv.201000236

Zhang, J., Yi, P., Xiong, Y., Du, C., Zhang, Y., Yuan, C., et al. (2020). A new acorane sesquiterpenes of *Lysionotus pauciflorus* maxim. *Biochem. Syst. Ecol.* 93, e104165. doi:10.1016/j.bse.2020.104165

Zhang, M., Zhao, J., Liu, J., Chen, R., Xie, K., Chen, D., et al. (2017). Neural anti-inflammatory sesquiterpenoids from the endophytic fungus *Trichoderma* sp. Xy24. *J. Asian Nat. Prod. Res.*, 19, 651–658. doi:10.1080/10286020.2016.1251908

Zhu, J., Liu, L., Wu, M., Xia, G., Lin, P., and Zi, J. (2021). Characterization of a sesquiterpene synthase catalyzing formation of cedrol and two diastereoisomers of tricho-acorenol from *Euphorbia fischeriana*. *J. Nat. Prod.* 84, 1780–1786. doi:10.1021/acs.jnatprod.1c00126

# Therapeutic potential of compounds targeting SARS-CoV-2 helicase

Matthew T. J. Halma[1,2†], Mark J. A. Wever[3,4†], Sanne Abeln[5], Didier Roche[4] and Gijs J. L. Wuite[1]*

[1]Department of Physics and Astronomy, Vrije Universiteit Amsterdam, Amsterdam, Netherlands, [2]LUMICKS B. V., Amsterdam, Netherlands, [3]DCM, University of Grenoble Alpes, Grenoble, France, [4]Edelris, Lyon, France, [5]Department of Computer Science, Vrije Universiteit Amsterdam, Amsterdam, Netherlands

The economical and societal impact of COVID-19 has made the development of vaccines and drugs to combat SARS-CoV-2 infection a priority. While the SARS-CoV-2 spike protein has been widely explored as a drug target, the SARS-CoV-2 helicase (nsp13) does not have any approved medication. The helicase shares 99.8% similarity with its SARS-CoV-1 homolog and was shown to be essential for viral replication. This review summarizes and builds on existing research on inhibitors of SARS-CoV-1 and SARS-CoV-2 helicases. Our analysis on the toxicity and specificity of these compounds, set the road going forward for the repurposing of existing drugs and the development of new SARS-CoV-2 helicase inhibitors.

KEYWORDS

SARS-CoV-2, helicase, nsp13, drug repurposing, small-molecule inhibitors, natural products, COVID-19

## 1 Introduction

The global coronavirus disease (COVID-19) pandemic is caused by severe acute respiratory syndrome coronavirus 2 (SARS-CoV-2). Coronaviruses, named after the similarity of the viral capsid on microscopy to the solar corona (Author anonymous, 1968), are widespread and can cause mild infection similar to the common cold. In fact, all four human coronaviruses: HCoV-OC43, HCoV-HKU-1, HCoV-299E, and HCoV-NL63, are endemic and continuously circulate the human population (Corman et al., 2018). Three previous coronavirus outbreaks, albeit much smaller than the COVID-19 outbreak, have been reported: SARS-CoV-1, MERS-CoV, and coronavirus HuPn-2018. Similar to COVID-19, all of these are zoonotic diseases, initially transmitted to humans *via* animal hosts (Ye et al., 2020). In contrast to previous outbreaks, COVID-19 has caused massive disruptions to the lives of virtually every person since the emergence in late 2019. As of 4 November 2022, COVID-19 has caused 6.60 million deaths globally (Ritchie et al., 2020). The significant death toll and the impact on society have resulted in large-scale campaigns to develop vaccines and antivirals to prevent and combat COVID-19.

There should be no doubt about the positive outcomes of this research effort; multiple vaccines, e.g., AstraZeneca, Moderna, Pfizer/BioNTech, have been developed and
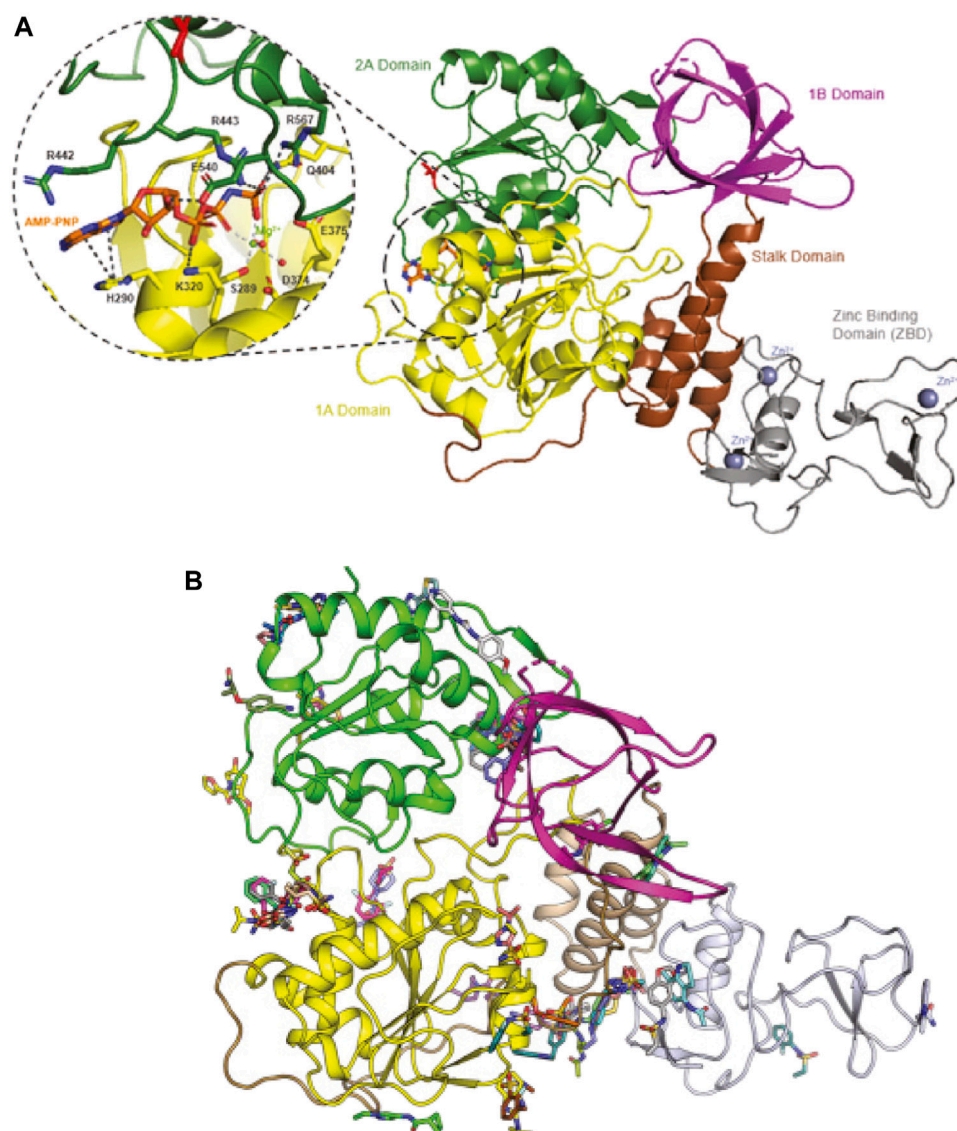
**FIGURE 1**
Binding sites of SARS-CoV-Nsp13 helicase. Panel **(A)** Structure of SARS-CoV-Nsp13 helicase (PDB ID: 7NN0) (Newman et al., 2021). V570, the single different residue from SARS Helicase (I570) is highlighted in red. The residues constituting the ATP binding site are shown in the enlarged window bound with AMP-PNP, an AMP analog. Panel **(B)** Possible binding pockets from Nsp13 fragment screening. Reproduced from Newman et al., 2021 under a Creative Commons Attribution 4.0 International License (http://creativecommons.org/licenses/by/4.0/).

deployed in many countries. The three vaccines mentioned all target the SARS-CoV-2 spike protein, either as an mRNA or inactivated adenovirus vaccine (Dai and Gao, 2021). Concerns have been raised about the emergence of vaccine-resistant SARS-CoV-2 variants, most notably the BA.4 and BA.5 omicron subvariants (Jian et al., 2022). These strains have mutations in the spike protein, and various sources report higher attack rates and infectivity for these mutants. Vaccine-produced antibodies were shown to have less neutralizing potential against omicron as compared to alpha- and delta variants

(Andrews et al., 2022). Furthermore, vaccines may be less effective or even dangerous for immunocompromised individuals (Marra et al., 2022). Moreover, certain individuals are allergic to components of vaccines (Cabanillas and Novak, 2021), and adverse events are being reported (Karlstad et al., 2022). Lastly, with the likelihood of the virus to become, and remain, endemic (Lavine et al., 2021), and given the range of confirmed animal reservoirs of SARS-CoV-2 infection (Prince et al., 2021), a variety of strategies to combat SARS-CoV-2 infection are required.

## 1.1 Current antivirals

In the early days of the pandemic, there were no approved antiviral compounds against SARS-CoV-2 (World Health Organization, 2020). This changed in October 2020, when remdesivir (brand name: Veklury; Gilead Sciences) was granted emergency use authorization (EUA) by the US Food and Drug Administration (FDA) for treatment of hospitalized patients (World Health Organization 2020). Remdesivir was the only approved medicine until the EUA of molnupiravir (Merck and Ridgeback) and paxlovid (Pfizer) in December 2021 (U.S. Food and Drug Administration, 2021).

The approved drugs have different mechanisms of action; remdesivir, a nucleotide analogue, acts by stalling SARS-CoV-2 RNA-dependent RNA polymerase (RdRp) (Kokic et al., 2021). Remdesivir exhibited conflicting impact in studies, showing improvement in time to recovery in the initial study cited during authorization (Beigel et al., 2020), but later studies showed either no statistically significant effect (Wang et al., 2020), or a statistically significant but clinically minor effect (Spinner et al., 2020). Concerns over renal toxicity (Gérard et al., 2021; Wu et al., 2022), as well as a cardiac safety signal (Rafaniello et al., 2021) challenge the safety of the drug. The second drug under EUA, molnupiravir, was approved based on a study showing a reduction in hospitalization and death (Jayk Bernal et al., 2022). Molnupiravir, in addition to remdesivir, targets RNA-dependent RNA polymerase and increases the frequency of mutations during SARS-CoV-2 replication (Kabinger et al., 2021). Concerningly, it has also been shown to induce mutations in mammalian cells (Zhou et al., 2021). The mechanism of action of molnupiravir is concerning as it has a possibility of driving new variants (Kabinger et al., 2021; Hashemian et al., 2022), as a result, its use is cautioned by the World Health Organization (World Health Organization, 2022). The third approved antiviral, paxlovid acts as a 3CL protease inhibitor. 3CL protease is necessary for viral replication (Marzi et al., 2022). Paxlovid displays a reasonable safety profile, although patients often report a "paxlovid rebound" where there is a resurgence of symptoms, often worse than the initial bout (Charness et al., 2022). Moreover, drug-drug interactions have been shown to cause adverse events (Burki, 2022). Drug resistance is also a concern, as mutations have been characterized which drastically reduce the effectiveness of paxlovid (Zhou et al., 2022).

Depending on the drug target, medication is tailored for different stages in infection. Different proteins can be targeted for therapy depending on the stage of infection. Compounds targeting the spike protein will inhibit entry of SARS-CoV-2 into cells, whereas compounds targeting RNA-dependent RNA polymerase will inhibit the replication process, but will not prevent entry into the cell. Therefore, depending on the clinical course, certain compounds can be used at different stages of infection. The helicase, being a replication protein, is active in

unwinding the RNA secondary structure so that it can be either replicated by RNA-dependent RNA polymerase or translated by the host ribosome.

## 1.2 Drug repurposing

Responding to emerging and pandemic viral illnesses requires a multifaceted approach, one strategy is drug repurposing. Drug repurposing is the use of approved drugs for novel targets and diseases. First, finding a useful medication amongst already existing drugs obviates the need to create novel drugs, thus saving time in disease response. Moreover, the side-effects of marketed drugs, having undergone clinical trials and prescribed use, are extensively researched and documented. Lastly, the manufacturing process is already known, and needs only to be scaled. Drug repurposing has previously found success, for example in sildenafil, an angina medication, that was successfully repurposed for erectile dysfunction as Viagra® (Pushpakom et al., 2019).

One example of a successfully repurposed and widely available medication for treatment of COVID-19 is fluvoxamine, a well-tolerated and selective serotonin reuptake inhibitor. Fluvoxamine is commonly used as an antidepressant (Sukhatme et al., 2021). It has been shown to reduce hospitalization in a large-scale randomized control trial (Reis et al., 2022). Being a repurposed drug, fluvoxamine, which was first approved by the FDA in 1994 (trade name: Luvox), has the advantage of decades of safety data surrounding its use. Unlike molnupiravir and paxlovid where a treatment course costs approximately 700 and 500 USD, respectively (Goswami et al., 2022; Morrison Ponce et al., 2022), fluvoxamine is accessible at 4 USD per course (Wang et al., 2021). Remdesivir is also expensive at over 2000 USD per 5-day treatment course (Carta and Conversano, 2021). The price and availability of drugs is an important consideration, especially considering that developing nations have far lower vaccination rates than developed nations (Bollyky et al., 2020). As of 25 July 2022, 73.2% of EU citizens have completed a full course with an EU-approved vaccine[1] and 55.0% have received at least one booster shot (Ritchie et al., 2020). For comparison, in Africa 42.7% of individuals have been vaccinated and only 2.5% have received at least one booster shot (Ritchie et al., 2020).

Finally, other concerns shape the adoption of a particular pharmacological compound in response to a global pandemic; these include intellectual property concerns, current and future availability, distribution, and (un)known side-effects. Ultimately,

---

1   i.e., Two doses of Moderna MRNA-1273, two doses of Pfizer-BioNTech BNT162B2, two doses of Oxford-AstraZeneca ChAdOx1 or a single dose of Johnson & Johnson Ad26.COV2.S.

an effective treatment of COVID-19 is preferred, that is widely available, inexpensive and without significant toxicity.

## 1.3 SARS-CoV-2 helicase (nsp13)

Drug repurposing is mostly a phenotypic approach, meaning that protein target and mechanism of action are often unknown. In contrast, target-based approaches seek to first identify protein targets (chemical biology) and to subsequently develop small-molecule inhibitors (medicinal chemistry) for the target. In principle, every SARS-CoV-2 protein can be considered a target, but it is preferable to target essential and/or conserved proteins. A previous review has already reviewed and postulated the main drug targets for COVID-19 (Gil et al., 2020), while this report focuses on the helicase of SARS-CoV-2. The SARS-CoV-2 nsp13 gene encodes a molecular motor, which is a $5'$ to $3'$-translocating helicase, belonging to superfamily 1B. Helicases act on (deoxy)-ribonucleic acid substrates and are fueled by (deoxy)-nucleotide triphosphates (Figure 1A). The primary functions of helicases are in DNA repair, replication, recombination, and transcription.

Nsp13 is one of the most conserved genes in the SARS-CoV-2 genome, having one of the lowest mutation rates of any of the essential SARS-CoV-2 proteins (Martin et al., 2021; Newman et al., 2021). The SARS-CoV-2 helicase differs from the SARS-CoV-1 helicase by only one amino acid residue, i.e., V570 in SARS-CoV-2 helicase (Figure 1A, highlighted in red) compared to I570 in SARS-CoV-1 helicase, allowing drugs discovered for SARS-CoV-1 to potentially be re-used. Potential binding pockets of Nsp13 were explored *via* crystallographic fragment screening (Figure 1B), presenting a starting point for structure-based drug discovery (Newman et al., 2021). Moreover, the helicase plays a critical role in replication of the viral genome (Jia et al., 2019). The combination of these two argues for the functional importance of SARS-CoV-2 helicase and makes it an attractive target for the development of antivirals. This is also evidenced by an upcoming CACHE challenge[2] that aims to discover new molecules that target SARS-CoV-2 helicase.

The viral helicase is not a new target in drug discovery, for example the helicases of herpes simplex virus and hepatitis C virus have been targeted, as reviewed by Shadrick et al. (Shadrick et al., 2013). More recent reports feature the helicases of polyomaviruses, Zika virus, and MERS-CoV (Bonafoux et al., 2016; Kumar et al., 2020; Zaher et al., 2020; Mehyar et al., 2021b). Additionally, human helicases have also attracted research interest, and inhibitors for DDX and BLM, among others, have been reported (Datta and Brosh, 2018). This approach aims to use small molecule inhibitors to sensitize cancer cells to chemotherapy and DNA-damaging agents and/or to utilize

specific tumor backgrounds for hypersensitization of tumors to pharmacological inhibition, a concept which is known as synthetic lethality (Datta and Brosh, 2018).

## 2 Main considerations

### 2.1 Target stability

As previously mentioned, SARS-CoV-2 helicase is among the most conserved proteins in the SARS-CoV-2 genome (Martin et al., 2021; Newman et al., 2021). Throughout the pandemic, it has remained largely stable. Phylogenetic evidence demonstrates increasing negative, i.e., purifying, selection over time, making it a stable target (Figure 2A). The development of drug resistance is an issue that undermines many treatments, most notably anti-biotics. Under the selection pressure of a drug treatment, the target protein can mutate such that the compound no longer binds (Richman, 1994; Menéndez-Arias and Richman, 2014). It was evaluated whether the mutations observed through genomic surveillance of COVID-19 cases (Kumari et al., 2022) altered the initial protein sequence (Newman et al., 2021). For a drug to retain effectiveness over time, the major mutations would not alter binding affinity of the drug compounds, thus maintaining drug effectiveness against mutations. Possibly, conservation of structure may enable production of pan-beta coronaviral inhibitors to guard against future zoonotic coronaviral outbreaks (Li et al., 2021; Munshi et al., 2022). This possibility is supported by the low level of nsp13 genetic variation within beta-coronaviruses, as demonstrated by the phylogenetic tree shown in Figure 2B.

The technique used here to identify mutations is exploratory, in that the predicted energetic shift was used as a proxy for conformational change. It has been assessed whether there are any changes likely to significantly impact the structural conformation of SARS-CoV-2 helicase. If a mutation was near a binding site and significantly shifted the energetic stability of the protein, it is likely that the mutation alters compound binding. Selection was determined using the toolkit made from the GISAID database[3], for all SARS-CoV-2 genomes up to 2 January 2022. In Figure 2C, site selection in terms of fixed-effects likelihood (FEL) (Kosakovsky Pond and Frost, 2005) is displayed (blue and red stem plots), FEL is a measure of selection pressure in phylogenetic trees and is calculated by comparing the expected number of non-synonymous mutations with the actual observed rate. In short, observing a higher than expected frequency of non-synonymous mutations suggests positive selection, *i.e.*, evolutionary pressure for the protein to change. Observing fewer than expected non-synonymous mutations is

---

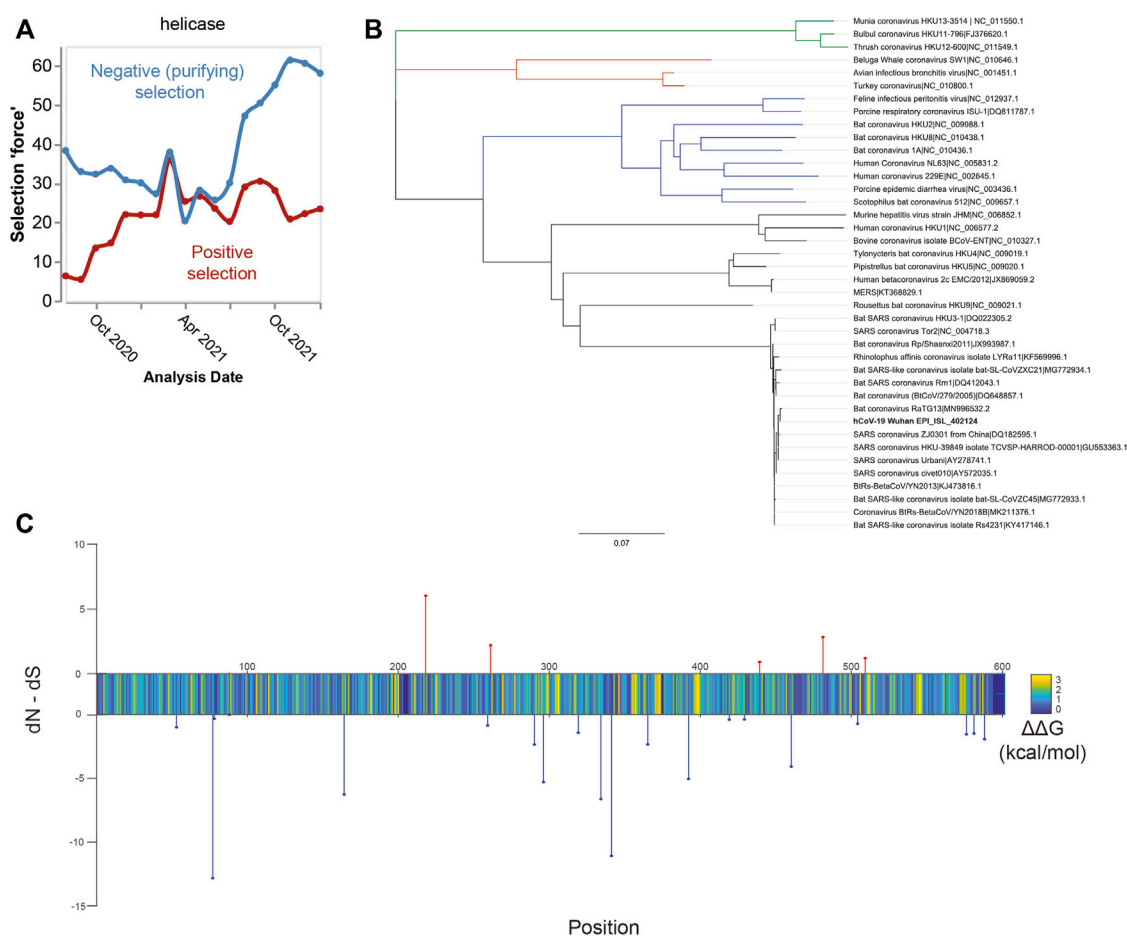2  https://cache-challenge.org/competitions/competition-2.

3  https://observablehq,com/@spond/revised-sars-cov-2-analytics-page.

**FIGURE 2**
Suitability of the nsp13 protein as a drug target. Panel **(A)** Time course of selection pressures on SARS-CoV-2 helicase from August 2020 to January 2022. Blue lines show the extent of negative selection, defined as the number of sites under negative selection normalized by kilobase of gene length and the internal tree length. Red lines how the positive selection force, defined as the number of positively selected sites with the same normalization. Over the time history, more sites show negative (purifying) selection, suggesting evolutionary stability. Panel **(B)** Phylogenetic tree of the coronavirus family based on nsp13 protein sequences. Legend: alpha-CoV (blue), beta-CoV (black), delta-CoV (red), and gamma-CoV (green). Within the beta-CoVs, there is high nsp13 conservation shown by the short tree lengths. Given the low variance amongst this clade, it may be possible that a SARS-CoV-2 nsp13 inhibitor also inhibits the other clade members. Panel **(C)** Energetics and selection on residues in SARS-CoV-2 nsp13 helicase. Stem plots show positive (red) or negative (blue) selection, expressed as FEL rate. Color plot shows the average energetic change in kcal/mol of all mutations at the site.

evidence of negative purifying selection, whereby mutants are not likely to survive and reproduce.

Additionally, a color plot depicts the average change in energetic stability of the protein resulting from the set of possible mutations at that site (Kwasigroch et al., 2002). Most mutations result in a slight destabilization of the helicase protein, suggesting a high level of structural optimization. While this makes it less likely that the protein will develop a drug resistant mutation, it is not certain. Residues where mutations have a destabilizing effect are more likely to alter the helicase structure, which affects the binding of compounds. The limitation of this approach is the lack of experimental data to support the generated model. Our assessment shows potentially worrisome loci for future drug resistance, where there is a confluence of positive

selection and an energetically destabilizing impact (upward stems in Figure 2C). These sites should be monitored for development of drug resistance and ideally a drug will either act on a different location, or the destabilization is significant enough to render the protein non-functional.

## 2.2 Current inhibitors: *In vitro*, *in vivo* and *in silico* assessment

Having established the validity of the helicase as a drug target, multiple methods can be applied for the discovery of inhibitors. *In silico* screening is experimentally less intense, requiring mostly

computational power. This methodology requires the availability of an X-ray or cryo-EM structures. The crystal structure for SARS-CoV-1 helicase was solved in 2019 (Jia et al., 2019), whereas for SARS-CoV-2 helicase structural information was first published in 2021 (Newman et al., 2021). Earlier *in silico* research made use of homology models based on either SARS-CoV-1 or MERS-CoV helicase to perform molecular modelling studies. Orthogonal to *in silico*, is *in vitro*, the screening of compounds directly on the protein of interest. This methodology can be low- (1–100), medium- (100–10.000) or high- (>10.000) throughput, depending on the equipment used and assay deployed. The most common *in vitro* assay performed for helicases is an ATP-turnover assay, there is, however, a high risk for false positives, e.g., aggregators or DNA-binders, when running these experiments (McGovern et al., 2003; Acker and Auld, 2014). Another common *in vitro* assay for helicase activity is to measure the unwound fraction by using a DNA construct with a double stranded region formed by an annealed oligonucleotide. If the helicase is active, it will separate the oligonucleotide from the construct, and a lighter band will show up on the gel. Form the intensity of this band, the unwound fraction and subsequent helicase activity can be calculated (Kim and Seo, 2009).

## 2.2.1 SARS-CoV-1 helicase

The first reports of compounds with SARS-CoV-1 helicase activity date back to 2005, when Tanner et al., described a group of adamantane-derived bananins (1-4, Supplementary Table S1, Supplementary Figure S1) with low micromolar ATPase and helicase inhibitor activities (Tanner et al., 2005). These pyridoxal-conjugated trioxa-adamantanes were shown to be non-competitive inhibitors by DNA- and ATP-competition assays and did not exhibit inhibitory activity on *E. coli* DnaB helicase. To the best of our knowledge, compounds 1-4 have not been further investigated. Structurally different Ranitidine Bismuth Citrate (5, Supplementary Table S1) inhibits ATPase and DNA-duplex unwinding activity, $IC_{50}$ = 0.3 and 0.6 μM, respectively (Yang et al., 2007b). Compound 5 is the most potent from a series of bismuth complexes (Yang et al., 2007a), whose mechanism of action involves the displacement of Zinc ions from the ATP-binding site (Yuan et al., 2020). Furthermore, flavonoids have been shown to inhibit SARS-CoV-1 helicase. Myricetin (6), baicalein (7), quercetin (8), and scutellarein (9) all are natural products that inhibit helicase and/or ATPase activity in the low micromolar range (Lee et al., 2009b; Yu et al., 2012; Keum et al., 2013). Flavonoids have been ascribed many potential health benefits, including antineoplastic and antiviral. However, there have also been multiple reports characterizing flavonoids as false positives and protein aggregators in biological assays. Myricetin (6) has been reported to inhibit many other targets including *E. coli* DnaB helicase and DNA polymerase (Griep et al., 2007). The activity of flavonoids on SARS-CoV-1 helicase has further been validated by the design and synthesis of compounds 10–15 (Lee et al., 2009b; Kim et al., 2011). There is still a

requirement for further experimentation to investigate the inhibition and selectivity of flavonoids and synthetic analogues thereof on SARS-CoV-1 helicase. Aryl di-keto acids are derived from flavonoids, and were also shown to inhibit SARS-CoV-1 helicase and various other targets, *e.g.,* hepatitis C virus RNA polymerase (Lee et al., 2009a). Lastly, four compounds (17–20) have been published but there was no information on related compounds. SSYA-10–001 (18) has additionally been reported as an inhibitor of hepatitis C virus RNA polymerase and MERS-CoV helicase (Adedeji et al., 2012, 2014).

## 2.2.2 SARS-CoV-2 helicase

The first reports on inhibitors of SARS-CoV-2 helicase were compounds that have previously been investigated for SARS-CoV-1 helicase, namely bismuth complexes (5, 21–24) (Supplementary Table S2, Supplementary Figure S2). Ranitidine Bismuth Citrate (5) was validated with sub-micromolar helicase and ATPase $IC_{50}$'s (Yuan et al., 2020) and exhibited greater activity compared to Bismuth (III) tetraphenylpoprhyrinate (23) and Bismuth (III) tetra-4-pyridiylporphyrinate (24). Moreover, 5 relieved virus-associated pneumonia in a golden Syrian hamster model. Disulfiram (25) and Ebselen (26) (Supplementary Table S2) are other Zinc-ejector drugs that have been validated on SARS-CoV-2 helicase (Chen et al., 2021).

White et al. have identified a hit list of 368 FDA-approved drugs, from which cepharanthine (27), $IC_{50}$ = 400 μM and lumacaftor (28), $IC_{50}$ = 300 μM) were confirmed in an ATPase assay (White et al., 2020). Cepharanthine (27) has previously been reported as a SARS-CoV-1 inhibitor, however at the time the target enzyme was not known (Zhang et al., 2005). Vapreotide (29), grazoprevir (30) and simeprevir (31) are other FDA-approved drugs discovered by phenotypic screening that inhibit SARS-CoV-2 helicase *in vitro*. Their activities were confirmed by a DNA-unwinding activity assay with $IC_{50}$ values of ≈10, ≈2.5, and ≈1.25 μM, respectively (Muturi et al., 2022). All three compounds have also been reported as virtual hits (Borgio et al., 2020; Gurung, 2020). Furthermore, a high-throughput screening of five thousand known pharmaceuticals by Zeng et al., mentions the inhibitory activity of FPA124 (32), $IC_{50}$ = 8.5 μM) and suramin (33, $IC_{50}$ = 0.94 μM). These hits were confirmed by a fluorescence resonance energy transfer (FRET) based helicase assay in the presence of Tween-20. Tween-20 is a non-ionic detergent that stops potential colloid formation. Both compounds still inhibited helicase activity in this assay at $IC_{50}$ = 8.4 μM and 1.1 μM, respectively, and viral inhibition was confirmed *in vivo* on Vero E6 cells (Zeng et al., 2021). SARS-CoV-1 inhibitors myricetin (6) and SSYA-100–01 (18) were used as a comparison in these experiments and were confirmed to be active on SARS-CoV-2 helicase. Research from the EXSCALATE4COV (E4C)[4] project on a natural product library once more confirmed the activity of SSYA-

---

4   www.exscalate4cov.eu.

**TABLE 1 the nine most promising SARS-CoV-2 helicase inhibitors for further development and drug repurposing.**

| Name (#) | Classification | Reference |
|---|---|---|
| Bananin (**4**) | synthetic product | Tanner et al. (2005) |
| Ranitidine Bismuth Citrate (**5**) | pharmaceutical drug | Yang et al. (2007b) |
| | | Yuan et al. (2020) |
| Myricetin (**6**) | natural product | Yu et al. (2012) |
| | | Zeng et al. (2021) |
| | | Corona et al. (2022) |
| SSYA10-001 (**18**) | synthetic product | Adedeji et al. (2012) |
| | | Zeng et al. (2021) |
| | | Corona et al. (2022) |
| Disulfiram (**25**) | pharmaceutical drug | Chen et al. (2021) |
| Vapreotide (**29**) | pharmaceutical drug | Borgio et al. (2020) |
| | | Muturi et al. (2022) |
| Grazoprevir (**30**) | pharmaceutical drug | Gurung (2020) |
| | | Muturi et al. (2022) |
| FPA124 (**32**) | synthetic product | Zeng et al. (2021) |
| Epirubicin HCl (**38**) | natural product | Mehyar et al. (2021b) |

100–01 (**18**) and identified five flavonoids with low micromolar activity: myricetin (**6**), quercetin (**8**), kaempferol (**34**), flavanone (**35**), and licoflavone C (**36**) (Corona et al., 2022). Moreover, Mehyar et al. (2021a) report on the repurposing of sulphoxide- and sulphone-containing FDA-approved compounds. Zafirlukast (**37**) was the only compound with inhibitory activity, interestingly **37** was also reported by Zeng et al., 2021), but was not selected for further analysis (Zeng et al., 2021). Mehyar et al. (2021a) also report SARS-CoV-2 helicase inhibitory activity for five previously identified MERS-CoV helicase inhibitors (**37**–**42**). Lastly, Newman et al. identified 65 fragments by crystallographic fragment screening. Although there were no inhibitory values published for these fragments, the crystal structures show binding in the ATP binding site as well as the RNA/DNA-entry tunnel. These crystal structures have been made publicly available and can be seen as a starting point for fragment growing (Newman et al., 2021). More recently, Romeo *et al.* identified multiple inhibitors with predicted binding to the RNA/DNA-entry tunnel *in vitro.* (Romeo et al., 2022).

Although *in vitro* and *in vivo* assays are the gold standard for hit validation, virtual screening allows for rapid identification of 'virtual' hits. The screening of ultra-large chemical spaces *in silico* has greatly increased the possibilities of modern drug discovery (Warr et al., 2022), but biological assays are still required to validate these hits. Not all laboratories, however, have the means to perform *in vitro* assays, thus making molecular modeling a more accessible method for initial target investigation. The SARS-CoV-2 helicase has been screened, virtually, in many instances (Supplementary Table S3). From our analysis it was observed that most publications have performed virtual screening on commercially available drugs (Balasubramaniam and Schmookler Reis 2020; Borgio et al., 2020; Gurung 2020; Iftikhar et al., 2020; Ugurel et al., 2020;

Abidi et al., 2021; Sundar et al., 2021; Alanazi et al., 2022; Azmoodeh et al., 2022) or natural products (Kousar et al., 2020; Naik et al., 2020; Ahmad et al., 2021; James et al., 2021; Vivek-Ananth et al., 2021; Bhargavi et al., 2022; Hossain et al., 2022; Samdani et al., 2022). Other published works make use of fragments (Freidel and Armen, 2021) or publicly available compound libraries (Mirza and Froeyen, 2020; García et al., 2021; El Hassab et al., 2022; Pitsillou et al., 2022). It is recognized that multi-targeted approaches are often carried out, most notably including RNA-dependent RNA polymerase and 3CL protease, to have dual-target SARS-CoV-2 inhibitors. The best scoring helicase inhibitors resulting from *in silico* approach, and without *in vitro* data, are shown in Supplementary Table S3. One particularly large study performed ultra-large virtual screening of one billion molecules on fifteen SARS-CoV-2 proteins, for each target the top 1,000 and top one million (0.1%) are publicly available online[5] (Gorgulla et al., 2021). All publications mentioned in this paragraph, however, lack the biological validation that is required to confirm activity. The occurrence of false positives in virtual screening is still high and results do often not translate to *in vitro* assays, as was recently shown by Cerón-Carrasco (Cerón-Carrasco, 2022). Thus, it remains critical to validate 'virtual' hits and to refrain from the use of thereof in determining structure-activity relationships.

## 2.3 Toxicity analysis

The potential side-effects of any treatment are a concern for medical practitioners when making a choice of which therapy to implement. Certainly, drugs with minimal off-target toxicity are preferred. While toxicity information exists for some compounds in the included tables, many have limited application as treatments and therefore little associated data on side-effects. Toxicity prediction applies machine learning to chemical structures with known toxicity tests on model organisms. Based on chemical similarities, the toxicity of untested compounds can be predicted. Toxicity prediction is a useful tool for evaluating potential harmful side-effects before taking the drug through costly pre-clinical and clinical trials.

It was not possible to use the same assay or toxicity prediction for all compounds. Individual studies often use different assays and thus report different values. Additionally, the toxicity prediction software was not always successful, and therefore several different tools were used: the Quantitative Structure-Activity Relationship (QSAR) toolbox, developed by the Organization for Economic Cooperation and Development (OECD) (Dimitrov et al., 2016); the Toxicity Estimation Software Tool (TEST) software developed by the US Environmental Protection Agency (US-EPA) (Martin et al., 2008); and the lazar toxicity prediction web server (Maunz

---

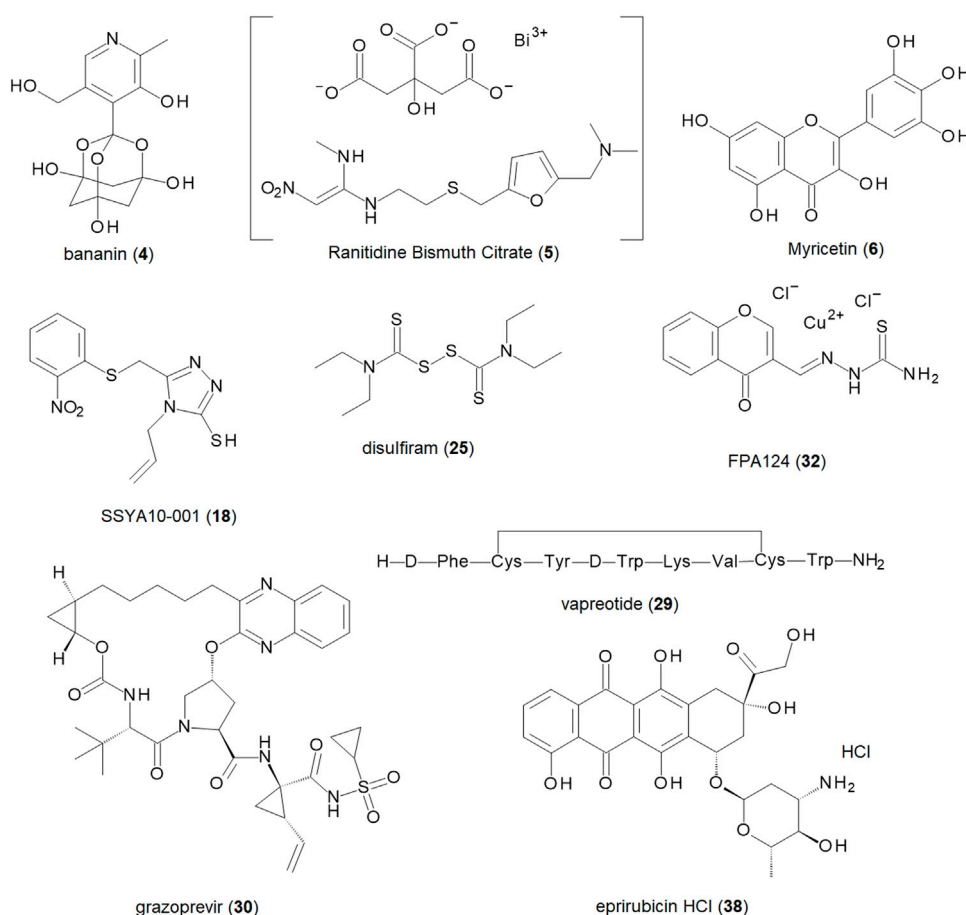5 See: https://vf4covid19.hms.harvard.edu/.

**FIGURE 3**
Structures of the nine most promising SARS-CoV-2 helicase inhibitors for further development and drug repurposing.

et al., 2013). For some compounds, particularly pharmaceutical drugs, toxicity data was accessible from public documents for their approval by either the FDA or the European Medicines Agency. Many of the natural products included have long histories of use in food as well as herbal medicines (Wang and Yang, 2020, 2021; Yang and Wang, 2021; Wang et al., 2022). Many are found in common foods and show strong association with positive health outcomes (Kumar and Pandey, 2013), including possible antiviral and antineoplastic (Rodriguez-García et al., 2019) properties. Since these products have been consumed for millennia, it is unlikely that they exhibit toxicity, although this may of course be different when the active compound becomes highly concentrated. The retrieved experimental toxicities and/or the predicted toxicity values for every compound are provided in Supplementary Tables S1,S2,S3 for the reader's consideration. For most assays, acute toxicity values were reported, this certainly has its drawbacks, as compounds may exhibit toxicity at much lower doses. These toxicities should not be overly interpreted, since the effective $IC_{50}$

doses of compounds differ, it is more beneficial to take a selective ratio against a toxicity endpoint.

## 3 Discussion

In Supplementary Tables S1,S2,S3, the source information of SARS-CoV-2 inhibitors is found, referring to where the compound can be extracted, synthesized or otherwise procured. Three categories are presented: Natural Products (NP), Synthetic Products (SP) and Pharmaceutical Drugs (PD). Natural products need only be extracted from their source organism, typically a plant; pharmaceutical drugs are approved molecules for the treatment of diseases, though some may be off-market. Synthetic products are typically only produced in very specific contexts, typically a research study. For natural products, the source organism(s) are indicated, whereas for pharmaceutical drugs the tradename and manufacturers are mentioned.

Contrary to natural products and pharmaceutical drugs, synthetic products often do not yet have a known toxicity profile.

From the compounds in Supplementary Tables S1,S2, the nine most promising compounds for further development are shown in Table 1 and Figure 3. They have been determined based on inhibitory activity, number of orthogonal assays and structural diversity. The first compound, bananin, was discovered, along with several other related compounds, to inhibit the helicase of SARS-CoV-1 (Tanner et al., 2005). As such, it presents a scaffold on which lead optimization can be performed. Two other synthetic products, SSYA10-001 and FPA124, offer promising scaffolds to develop into pharmaceutical drugs, should they have a reasonable biodistribution and safety profile. Ranitidine Bismuth Citrate (RBC) is a promising compound showing inhibition in helicase unwinding assays, as well as *in vivo* activity in a Syrian hamster model (Yuan et al., 2020). RBC has a higher level of validation than the other compounds, and its previous use as a pharmaceutical (TRITEC, GlaxoSmithKline) make it a promising drug for repurposing. Other pharmaceutical drugs for potential repurposing are disulfiram, vapreotide and grazoprevir. These are distinct enough that they can be developed as independent scaffolds. Among the natural products, myricetin, has the lowest $IC_{50}$ (0.41 µM) of flavonoid compounds against SARS-CoV-2 (Supplementary Table S2). Its safety, wide use, and availability make it a promising compound for development. Another natural product, Epirubicin HCl, is included for its low $IC_{50}$ (0.31 µM), while still being distinct enough from myricetin to develop it as a distinct scaffold.

This review summarizes and builds on the work on discovery of therapeutics targeting SARS-CoV-2 helicase, a vital replication protein. We demonstrate that this protein is highly conserved and resistant to drug-inactivating mutations. Additionally, the high degree of conservation within the coronavirus family, and particularly the beta-coronavirus clade, make coronaviral helicases attractive targets for future coronaviral outbreaks.

We have aimed to provide a complete overview of drugs, natural products, and synthetic products targeting the SARS-CoV-2 helicase, at several levels of discovery. A broad range of compounds either computationally predicted to bind to the target or with higher levels of validation, such as *in vitro* or even *in vivo* assays, have been covered. Furthermore, a summary of clinical trials for COVID-19 that involve these compounds can be found as Supplementary Table S4. Toxicity information on compounds was provided and predicted for those with absent literature values.

Overall, SARS-CoV-2 helicase is an attractive drug target for COVID-19. The potential of immune escape of future SARS-CoV-2 strains from the immunity imparted by the current vaccination program motivates the development of backup treatment options (Harvey et al., 2021; Lazarevic et al., 2021). Finally, while vaccines are a preventive measure, there is still a need for acute therapeutic interventions, for which there is currently a paucity of options. Both targeting the SARS-CoV-2 helicase by drug repurposing or new drug discovery may provide acute interventions for COVID-19 in the future.

## Data availability statement

The original contributions presented in the study are included in the article/Supplementary Material, further inquiries can be directed to the corresponding author.

## Author contributions

MH conceptualized the idea and proof outline. MH wrote the target stability and toxicity sections. MW wrote the current inhibitors section. MH and MW wrote the manuscript with input from all authors. All authors contributed to the article and approved the submitted version.

## Funding

## Acknowledgments

## Conflict of interest

The authors declare that the research was conducted in the absence of any commercial or financial relationships that could be construed as a potential conflict of interest.

## Publisher's note

All claims expressed in this article are solely those of the authors and do not necessarily represent those of their affiliated organizations, or those of the publisher, the editors and the reviewers. Any product that may be evaluated in this article, or claim that may be made by its manufacturer, is not guaranteed or endorsed by the publisher.

## Supplementary material

The Supplementary Material for this article can be found online at: https://www.frontiersin.org/articles/10.3389/fchem.2022.1062352/full#supplementary-material

# References

Abidi, S. H., Almansour, N. M., Amerzhanov, D., Allemailem, K. S., Rafaqat, W., Ibrahim, M. A. A., et al. (2021). Repurposing potential of posaconazole and grazoprevir as inhibitors of SARS-CoV-2 helicase. *Sci. Rep.* 11, 10290. doi:10.1038/s41598-021-89724-0

Acker, M. G., and Auld, D. S. (2014). Considerations for the design and reporting of enzyme assays in high-throughput screening applications. *Perspect. Sci. (Neth.)* 1, 56–73. doi:10.1016/j.pisc.2013.12.001

Adedeji, A. O., Singh, K., Calcaterra, N. E., DeDiego, M. L., Enjuanes, L., Weiss, S., et al. (2012). Severe acute respiratory syndrome coronavirus replication inhibitor that interferes with the nucleic acid unwinding of the viral helicase. *Antimicrob. Agents Chemother.* 56, 4718–4728. doi:10.1128/AAC.00957-12

Adedeji, A. O., Singh, K., Kassim, A., Coleman, C. M., Elliott, R., Weiss, S. R., et al. (2014). Evaluation of SSYA10-001 as a replication inhibitor of severe acute respiratory syndrome, mouse hepatitis, and Middle East respiratory syndrome coronaviruses. *Antimicrob. Agents Chemother.* 58, 4894–4898. doi:10.1128/AAC.02994-14

Ahmad, S., Waheed, Y., Ismail, S., Bhatti, S., Abbasi, S. W., and Muhammad, K. (2021). Structure-based virtual screening identifies multiple stable binding sites at the RecA domains of SARS-CoV-2 helicase enzyme. *Molecules* 26, 1446. doi:10.3390/molecules26051446

Alanazi, K. M., Farah, M. A., and Hor, Y.-Y. (2022). Multi-targeted approaches and drug repurposing reveal possible SARS-CoV-2 inhibitors. *Vaccines* 10, 24. doi:10.3390/vaccines10010024

Andrews, N., Stowe, J., Kirsebom, F., Toffa, S., Rickeard, T., Gallagher, E., et al. (2022). Covid-19 vaccine effectiveness against the omicron (B.1.1.529) variant. *N. Engl. J. Med.* 386, 1532–1546. doi:10.1056/NEJMoa2119451

Author anonymous (1968). Virology: Coronaviruses. *Nature* 220, 650. doi:10.1038/220650b0

Azmoodeh, S. K., Tsigelny, I. F., and Kouznetsova, V. L. (2022). Potential SARS-CoV-2 nonstructural proteins inhibitors: Drugs repurposing with drug-target networks and deep learning. *Front. Biosci. (Landmark Ed.)* 27, 113. doi:10.31083/j.fbl2704113

Balasubramaniam, M., and Shmookler Reis, R. (2020). Computational target-based drug repurposing of elbasvir, an antiviral drug predicted to bind multiple SARS-CoV-2 proteins. *ChemRxiv.* preprintAvailable at:. doi:10.26434/chemrxiv.12084822

Beigel, J. H., Tomashek, K. M., Dodd, L. E., Mehta, A. K., Zingman, B. S., Kalil, A. C., et al. (2020). Remdesivir for the treatment of covid-19 — final report. *N. Engl. J. Med.* 383, 1813–1826. doi:10.1056/NEJMoa2007764

Bhargavi, S., Madhan Shankar, S. R., and Jemmy, C. H. (2022). *In silico* and *in vitro* studies on inhibitors for SARS-CoV-2 non-structural proteins with dual herbal combination of Withania somnifera with five rasayana herbs. *J. Biomol. Struct. Dyn.* 8, 1–16. doi:10.1080/07391102.2022.2046642

Bollyky, T. J., Gostin, L. O., and Hamburg, M. A. (2020). The equitable distribution of COVID-19 therapeutics and vaccines. *JAMA* 323, 2462–2463. doi:10.1001/jama.2020.6641

Bonafoux, D., Nanthakumar, S., Bandarage, U. K., Memmott, C., Lowe, D., Aronov, A. M., et al. (2016). Fragment-based discovery of dual JC virus and BK virus helicase inhibitors. *J. Med. Chem.* 59, 7138–7151. doi:10.1021/acs.jmedchem.6b00486

Borgio, J. F., Alsuwat, H. S., Otaibi, W. M. A., Ibrahim, A. M., Almandil, N. B., Asoom, L. I. A., et al. (2020). State-of-the-art tools unveil potent drug targets amongst clinically approved drugs to inhibit helicase in SARS-CoV-2. *Arch. Med. Sci.* 16, 508–518. doi:10.5114/aoms.2020.94567

Burki, T. K. (2022). The role of antiviral treatment in the COVID-19 pandemic. *Lancet Respir. Med.* 10, e18. doi:10.1016/S2213-2600(22)00011-X

Cabanillas, B., and Novak, N. (2021). Allergy to COVID-19 vaccines: A current update. *Allergol. Int.* 70, 313–318. doi:10.1016/j.alit.2021.04.003

Carta, A., and Conversano, C. (2021). Cost utility analysis of Remdesivir and Dexamethasone treatment for hospitalised COVID-19 patients - a hypothetical study. *BMC Health Serv. Res.* 21, 986. doi:10.1186/s12913-021-06998-w

Cerón-Carrasco, J. P. (2022). When virtual screening yields inactive drugs: Dealing with false theoretical friends. *ChemMedChem* 17, e202200278. doi:10.1002/cmdc.202200278

Charness, M., Gupta, K., Stack, G., Strymish, J., Adams, E., Lindy, D., et al. (2022). Rapid relapse of symptomatic omicron SARS-CoV-2 infection following early suppression with nirmatrelvir/ritonavir. *Res. Square.* preprintAvailable at:. doi:10.21203/rs.3.rs-1588371/v2

Chen, T., Fei, C.-Y., Chen, Y.-P., Sargsyan, K., Chang, C.-P., Yuan, H. S., et al. (2021). Synergistic inhibition of SARS-CoV-2 replication using disulfiram/ebselen

and remdesivir. *ACS Pharmacol. Transl. Sci.* 4, 898–907. doi:10.1021/acsptsci.1c00022

Corman, V. M., Muth, D., Niemeyer, D., and Drosten, C. (2018). Hosts and sources of endemic human coronaviruses. *Adv. Virus Res.* 100, 163–188. doi:10.1016/bs.aivir.2018.01.001

Corona, A., Wycisk, K., Talarico, C., Manelfi, C., Milia, J., Cannalire, R., et al. (2022). Natural compounds inhibit SARS-CoV-2 nsp13 unwinding and ATPase enzyme activities. *ACS Pharmacol. Transl. Sci.* 5, 226–239. doi:10.1021/acsptsci.1c00253

Dai, L., and Gao, G. F. (2021). Viral targets for vaccines against COVID-19. *Nat. Rev. Immunol.* 21, 73–82. doi:10.1038/s41577-020-00480-0

Datta, A., and Brosh, R. M. (2018). New insights into DNA helicases as druggable targets for cancer therapy. *Front. Mol. Biosci.* 5, 59. doi:10.3389/fmolb.2018.00059

Dimitrov, S. D., Diderich, R., Sobanski, T., Pavlov, T. S., Chankov, G. V., Chapkanov, A. S., et al. (2016). QSAR Toolbox - workflow and major functionalities. *Sar. QSAR Environ. Res.* 27, 203–219. doi:10.1080/1062936X.2015.1136680

El Hassab, M. A., Eldehna, W. M., Al-Rashood, S. T., Alharbi, A., Eskandrani, R. O., Alkahtani, H. M., et al. (2022). Multi-stage structure-based virtual screening approach towards identification of potential SARS-CoV-2 NSP13 helicase inhibitors. *J. Enzyme Inhib. Med. Chem.* 37, 563–572. doi:10.1080/14756366.2021.2022659

Freidel, M. R., and Armen, R. S. (2021). Mapping major SARS-CoV-2 drug targets and assessment of druggability using computational fragment screening: Identification of an allosteric small-molecule binding site on the Nsp13 helicase. *PLOS ONE* 16, e0246181. doi:10.1371/journal.pone.0246181

García, R., Hussain, A., Koduru, P., Atis, M., Wilson, K., Park, J. Y., et al. (2021). Identification of potential antiviral compounds against SARS-CoV-2 structural and non structural protein targets: A pharmacoinformatics study of the cas COVID-19 dataset. *Comput. Biol. Med.* 133, 104364. doi:10.1016/j.compbiomed.2021.104364

Gérard, A. O., Laurain, A., Fresse, A., Parassol, N., Muzzone, M., Rocher, F., et al. (2021). Remdesivir and acute renal failure: A potential safety signal from disproportionality analysis of the WHO safety database. *Clin. Pharmacol. Ther.* 109, 1021–1024. doi:10.1002/cpt.2145

Gil, C., Ginex, T., Maestro, I., Nozal, V., Barrado-Gil, L., Cuesta-Geijo, M. Á., et al. (2020). COVID-19: Drug targets and potential treatments. *J. Med. Chem.* 63, 12359–12386. doi:10.1021/acs.jmedchem.0c00606

Gorgulla, C., Padmanabha Das, K. M., Leigh, K. E., Cespugli, M., Fischer, P. D., Wang, Z.-F., et al. (2021). A multi-pronged approach targeting SARS-CoV-2 proteins using ultra-large virtual screening. *iScience* 24, 102021. doi:10.1016/j.isci.2020.102021

Goswami, H., Alsumali, A., Jiang, Y., Schindler, M., Duke, E. R., Cohen, J., et al. (2022). Cost-effectiveness analysis of molnupiravir versus best supportive care for the treatment of outpatient COVID-19 in adults in the US. *Pharmacoeconomics* 40, 699–714. doi:10.1007/s40273-022-01168-0

Griep, M. A., Blood, S., Larson, M. A., Koepsell, S. A., and Hinrichs, S. H. (2007). Myricetin inhibits *Escherichia coli* DnaB helicase but not primase. *Bioorg. Med. Chem.* 15, 7203–7208. doi:10.1016/j.bmc.2007.07.057

Gurung, A. B. (2020). *In silico* structure modelling of SARS-CoV-2 Nsp13 helicase and Nsp14 and repurposing of FDA approved antiviral drugs as dual inhibitors. *Gene Rep.* 21, 100860. doi:10.1016/j.genrep.2020.100860

Harvey, W. T., Carabelli, A. M., Jackson, B., Gupta, R. K., Thomson, E. C., Harrison, E. M., et al. (2021). SARS-CoV-2 variants, spike mutations and immune escape. *Nat. Rev. Microbiol.* 19, 409–424. doi:10.1038/s41579-021-00573-0

Hashemian, S. M. R., Pourhanifeh, M. H., Hamblin, M. R., Shahrzad, M. K., and Mirzaei, H. (2022). RdRp inhibitors and COVID-19: Is molnupiravir a good option? *Biomed. Pharmacother.* 146, 112517. doi:10.1016/j.biopha.2021.112517

Hossain, R., Sarkar, C., Hassan, S. M. H., Khan, R. A., Arman, M., Ray, P., et al. (2022). *In silico* screening of natural products as potential inhibitors of SARS-CoV-2 using molecular docking simulation. *Chin. J. Integr. Med.* 28, 249–256. doi:10.1007/s11655-021-3504-5

Iftikhar, H., Ali, H. N., Farooq, S., Naveed, H., and Shahzad-ul-Hussan, S. (2020). Identification of potential inhibitors of three key enzymes of SARS-CoV2 using computational approach. *Comput. Biol. Med.* 122, 103848. doi:10.1016/j.compbiomed.2020.103848

James, J. P., Jyothi, D., and Priya, S. (2021). *In silico* screening of phytoconstituents with antiviral activities against SARS-COV-2 main protease, Nsp12 polymerase, and Nsp13 helicase proteins. *Lett. Drug Des. Discov.* 18, 841–857. doi:10.2174/1570180818666210317162502

Jayk Bernal, A., Gomes da Silva, M. M., Musungaie, D. B., Kovalchuk, E., Gonzalez, A., Delos Reyes, V., et al. (2022). Molnupiravir for oral treatment of covid-19 in nonhospitalized patients. *N. Engl. J. Med.* 386, 509–520. doi:10.1056/NEJMoa2116044

Jia, Z., Yan, L., Ren, Z., Wu, L., Wang, J., Guo, J., et al. (2019). Delicate structural coordination of the severe acute respiratory syndrome coronavirus Nsp13 upon ATP hydrolysis. *Nucleic Acids Res.* 47, 6538–6550. doi:10.1093/nar/gkz409

Jian, F., Yu, Y., Song, W., Yisimayi, A., Yu, L., Gao, Y., et al. (2022). Further humoral immunity evasion of emerging SARS-CoV-2 BA.4 and BA.5 subvariants. *Lancet Infect. Dis.* 22, 1535–1537. doi:10.1016/S1473-3099(22)00642-9

Kabinger, F., Stiller, C., Schmitzová, J., Dienemann, C., Kokic, G., Hillen, H. S., et al. (2021). Mechanism of molnupiravir-induced SARS-CoV-2 mutagenesis. *Nat. Struct. Mol. Biol.* 28, 740–746. doi:10.1038/s41594-021-00651-0

Karlstad, Ø., Hovi, P., Husby, A., Härkänen, T., Selmer, R. M., Pihlström, N., et al. (2022). SARS-CoV-2 vaccination and myocarditis in a nordic cohort study of 23 million residents. *JAMA Cardiol.* 7, 600–612. doi:10.1001/jamacardio.2022.0583

Keum, Y. S., Lee, J. M., Yu, M. S., Chin, Y. W., and Jeong, Y. J. (2013). Inhibition of SARS coronavirus helicase by baicalein. *Bull. Korean Chem. Soc.* 34, 3187–3188. doi:10.5012/bkcs.2013.34.11.3187

Kim, J.-H., and Seo, Y.-S. (2009). *in Vitroassays for studying helicase activities DNA replication: Methods and protocols methods in molecular biology.* Editors S. Vengrova and J. Z. Dalgaard (Totowa, NJ: Humana Press), 361–379. doi:10.1007/978-1-60327-815-7_20

Kim, M. K., Yu, M.-S., Park, H. R., Kim, K. B., Lee, C., Cho, S. Y., et al. (2011). 2, 6-Bis-arylmethyloxy-5-hydroxychromones with antiviral activity against both hepatitis C virus (HCV) and SARS-associated coronavirus (SCV). *Eur. J. Med. Chem.* 46, 5698–5704. doi:10.1016/j.ejmech.2011.09.005

Kokic, G., Hillen, H. S., Tegunov, D., Dienemann, C., Seitz, F., Schmitzova, J., et al. (2021). Mechanism of SARS-CoV-2 polymerase stalling by remdesivir. *Nat. Commun.* 12, 279. doi:10.1038/s41467-020-20542-0

Kosakovsky Pond, S. L., and Frost, S. D. W. (2005). Not so different after all: A comparison of methods for detecting amino acid sites under selection. *Mol. Biol. Evol.* 22, 1208–1222. doi:10.1093/molbev/msi105

Kousar, K., Majeed, A., Yasmin, F., Hussain, W., and Rasool, N. (2020). Phytochemicals from selective plants have promising potential against SARS-CoV-2: Investigation and corroboration through molecular docking, MD simulations, and quantum computations. *Biomed. Res. Int.* 2020, 1–15. doi:10.1155/2020/6237160

Kumar, R., Verma, H., Singhvi, N., Sood, U., Gupta, V., Singh, M., et al. (2020). Comparative genomic analysis of rapidly evolving SARS-CoV-2 reveals mosaic pattern of phylogeographical distribution. *mSystems* 5, e00505-e00520. doi:10.1128/mSystems.00505-20

Kumar, S., and Pandey, A. K. (2013). Chemistry and biological activities of flavonoids: An overview. *Sci. World J.* 2013, 1–16. doi:10.1155/2013/162750

Kumari, D., Kumari, N., Kumar, S., Sinha, P. K., Shahi, S. K., Biswas, N. R., et al. (2022). Identification and characterization of novel mutants of Nsp13 protein among Indian SARS-CoV-2 isolates. *Open Bioinforma. J.* 15, e187503622202100. doi:10.2174/18750362-v15-e2202100

Kwasigroch, J. M., Gilis, D., Dehouck, Y., and Rooman, M. (2002). PoPMuSiC, rationally designing point mutations in protein structures. *Bioinformatics* 18, 1701–1702. doi:10.1093/bioinformatics/18.12.1701

Lavine, J. S., Bjornstad, O. N., and Antia, R. (2021). Immunological characteristics govern the transition of COVID-19 to endemicity. *Science* 371, 741–745. doi:10.1126/science.abe6522

Lazarevic, I., Pravica, V., Miljanovic, D., and Cupic, M. (2021). Immune evasion of SARS-CoV-2 emerging variants: What have we learnt so far? *Viruses* 13, 1192. doi:10.3390/v13071192

Lee, C., Lee, J. M., Lee, N.-R., Jin, B.-S., Jang, K. J., Kim, D.-E., et al. (2009a). Aryl diketoacids (ADK) selectively inhibit duplex DNA-unwinding activity of SARS coronavirus NTPase/helicase. *Bioorg. Med. Chem. Lett.* 19, 1636–1638. doi:10.1016/j.bmcl.2009.02.010

Lee, C., Lee, J. M., Lee, N.-R., Kim, D.-E., Jeong, Y.-J., and Chong, Y. (2009b). Investigation of the pharmacophore space of Severe Acute Respiratory Syndrome coronavirus (SARS-CoV) NTPase/helicase by dihydroxychromone derivatives. *Bioorg. Med. Chem. Lett.* 19, 4538–4541. doi:10.1016/j.bmcl.2009.07.009

Li, X., Zhang, L., Chen, S., Ouyang, H., and Ren, L. (2021). Possible targets of pan-coronavirus antiviral strategies for emerging or Re-emerging coronaviruses. *Microorganisms* 9, 1479. doi:10.3390/microorganisms9071479

Marra, A. R., Kobayashi, T., Suzuki, H., Alsuhaibani, M., Tofaneto, B. M., Bariani, L. M., et al. (2022). Short-term effectiveness of COVID-19 vaccines in immunocompromised patients: A systematic literature review and meta-analysis. *J. Infect.* 84, 297–310. doi:10.1016/j.jinf.2021.12.035

Martin, R., Li, J., Parvangada, A., Perry, J., Cihlar, T., Mo, H., et al. (2021). Genetic conservation of SARS-CoV-2 RNA replication complex in globally circulating isolates and recently emerged variants from humans and minks suggests minimal pre-existing resistance to remdesivir. *Antivir. Res.* 188, 105033. doi:10.1016/j.antiviral.2021.105033

Martin, T. M., Harten, P., Venkatapathy, R., Das, S., and Young, D. M. (2008). A hierarchical clustering methodology for the estimation of toxicity. *Toxicol. Mech. Methods* 18, 251–266. doi:10.1080/15376510701857353

Marzi, M., Vakil, M. K., Bahmanyar, M., and Zarenezhad, E. (2022). Paxlovid: Mechanism of action, synthesis, and in silico study. *Biomed. Res. Int.* 2022, 1–16. doi:10.1155/2022/7341493

Maunz, A., Gütlein, M., Rautenberg, M., Vorgrimmler, D., Gebele, D., and Helma, C. (2013). lazar: a modular predictive toxicology framework. *Front. Pharmacol.* 4, 38. doi:10.3389/fphar.2013.00038

McGovern, S. L., Helfand, B. T., Feng, B., and Shoichet, B. K. (2003). A specific mechanism of nonspecific inhibition. *J. Med. Chem.* 46, 4265–4272. doi:10.1021/jm030266r

Mehyar, N., Mashhour, A., Islam, I., Alhadrami, H. A., Tolah, A. M., Alghanem, B., et al. (2021a). Discovery of Zafirlukast as a novel SARS-CoV-2 helicase inhibitor using *in silico* modelling and a FRET-based assay. *Sar. QSAR Environ. Res.* 32, 963–983. doi:10.1080/1062936X.2021.1993995

Mehyar, N., Mashhour, A., Islam, I., Gul, S., Adedeji, A. O., Askar, A. S., et al. (2021b). Using *in silico* modelling and FRET-based assays in the discovery of novel FDA-approved drugs as inhibitors of MERS-CoV helicase. *Sar. QSAR Environ. Res.* 32, 51–70. doi:10.1080/1062936X.2020.1857437

Menéndez-Arias, L., and Richman, D. D. (2014). Editorial overview: Antivirals and resistance: Advances and challenges ahead. *Curr. Opin. Virol.* 8, iv. vii. doi:10.1016/j.coviro.2014.08.002

Mirza, M. U., and Froeyen, M. (2020). Structural elucidation of SARS-CoV-2 vital proteins: Computational methods reveal potential drug candidates against main protease, Nsp12 polymerase and Nsp13 helicase. *J. Pharm. Anal.* 10, 320–328. doi:10.1016/j.jpha.2020.04.008

Morrison Ponce, D., Kitchen, L. K., and Devlin, J. J. (2022). Cost–benefit analysis of novel antiviral ritonavir in the active duty U.S. Military population. *Mil. Med.* 187, 274–275. doi:10.1093/milmed/usab552

Munshi, S., Neupane, K., Ileperuma, S. M., Halma, M. T. J., Kelly, J. A., Halpern, C. F., et al. (2022). Identifying inhibitors of -1 programmed ribosomal frameshifting in a broad spectrum of coronaviruses. *Viruses* 14, 177. doi:10.3390/v14020177

Muturi, E., Hong, W., Li, J., Yang, W., He, J., Wei, H., et al. (2022). Effects of simeprevir on the replication of SARS-CoV-2 *in vitro* and in transgenic hACE2 mice. *Int. J. Antimicrob. Agents* 59, 106499. doi:10.1016/j.ijantimicag.2021.106499

Naik, B., Gupta, N., Ojha, R., Singh, S., Prajapati, V. K., and Prusty, D. (2020). High throughput virtual screening reveals SARS-CoV-2 multi-target binding natural compounds to lead instant therapy for COVID-19 treatment. *Int. J. Biol. Macromol.* 160, 1–17. doi:10.1016/j.ijbiomac.2020.05.184

Newman, J. A., Douangamath, A., Yadzani, S., Yosaatmadja, Y., Aimon, A., Brandão-Neto, J., et al. (2021). Structure, mechanism and crystallographic fragment screening of the SARS-CoV-2 NSP13 helicase. *Nat. Commun.* 12, 4848. doi:10.1038/s41467-021-25166-6

Pitsillou, E., Liang, J., Hung, A., and Karagiannis, T. C. (2022). The SARS-CoV-2 helicase as a target for antiviral therapy: Identification of potential small molecule inhibitors by *in silico* modelling. *J. Mol. Graph. Model.* 114, 108193. doi:10.1016/j.jmgm.2022.108193

Prince, T., Smith, S. L., Radford, A. D., Solomon, T., Hughes, G. L., and Patterson, E. I. (2021). SARS-CoV-2 infections in animals: Reservoirs for reverse zoonosis and models for study. *Viruses* 13, 494. doi:10.3390/v13030494

Pushpakom, S., Iorio, F., Eyers, P. A., Escott, K. J., Hopper, S., Wells, A., et al. (2019). Drug repurposing: Progress, challenges and recommendations. *Nat. Rev. Drug Discov.* 18, 41–58. doi:10.1038/nrd.2018.168

Rafaniello, C., Ferrajolo, C., Sullo, M. G., Gaio, M., Zinzi, A., Scavone, C., et al. (2021). Cardiac events potentially associated to remdesivir: An analysis from the European spontaneous adverse event reporting system. *Pharm. (Basel)* 14, 611. doi:10.3390/ph14070611

Reis, G., Moreira-Silva, E. A., dos, S., Silva, D. C. M., Thabane, L., Milagres, A. C., et al. (2022). Effect of early treatment with fluvoxamine on risk of emergency care and hospitalisation among patients with COVID-19: The TOGETHER randomised, platform clinical trial. *Lancet Glob. Health* 10, e42–e51. doi:10.1016/S2214-109X(21)00448-4

Richman, D. D. (1994). Drug resistance in viruses. *Trends Microbiol.* 2, 401–407. doi:10.1016/0966-842X(94)90619-X

Ritchie, H., Mathieu, E., Rodés-Guirao, L., Appel, C., Giattino, C., Ortiz-Ospina, E., et al. (2020). Coronavirus pandemic (COVID-19). Our World in Data Available at: https://ourworldindata.org/covid-deaths (Accessed November 4, 2022).

Rodríguez-García, C., Sánchez-Quesada, C., and Gaforio, J. J. (2019). Dietary flavonoids as cancer chemopreventive agents: An updated review of human studies. *Antioxidants (Basel)* 8, 137. doi:10.3390/antiox8050137

Romeo, I., Ambrosio, F. A., Costa, G., Corona, A., Alkhatib, M., Salpini, R., et al. (2022). Targeting SARS-CoV-2 Nsp13 helicase and assessment of druggability pockets: Identification of two potent inhibitors by a multi-site in silico drug repurposing approach. *Molecules* 27, 7522. doi:10.3390/molecules27217522

Samdani, N., Morshed, N., Reza, R., Asaduzzaman, M., and Islam, A. B. M. K. (2022). Targeting SARS-CoV-2 non-structural protein 13 via helicase-inhibitor-repurposing and non-structural protein 16 through pharmacophore-based screening. *Mol. Divers.*, 1–19. doi:10.1007/s11030-022-10468-8

Shadrick, W. R., Ndjomou, J., Kolli, R., Mukherjee, S., Hanson, A. M., and Frick, D. N. (2013). Discovering new medicines targeting helicases: Challenges and recent progress. *SLAS Discov.* 18, 761–781. doi:10.1177/1087057113482586

Spinner, C. D., Gottlieb, R. L., Criner, G. J., Arribas López, J. R., Cattelan, A. M., Soriano Viladomiu, A., et al. (2020). Effect of remdesivir vs standard care on clinical status at 11 Days in patients with moderate COVID-19: A randomized clinical trial. *JAMA* 324, 1048–1057. doi:10.1001/jama.2020.16349

Sukhatme, V. P., Reiersen, A. M., Vayttaden, S. J., and Sukhatme, V. V. (2021). Fluvoxamine: A review of its mechanism of action and its role in COVID-19. *Front. Pharmacol.* 12, 652688. doi:10.3389/fphar.2021.652688

Sundar, S., Thangamani, L., Piramanayagam, S., Rahul, C. N., Aiswarya, N., Sekar, K., et al. (2021). Screening of FDA-approved compound library identifies potential small-molecule inhibitors of SARS-CoV-2 non-structural proteins NSP1, NSP4, NSP6 and NSP13: Molecular modeling and molecular dynamics studies. *J. Proteins Proteom.* 12, 161–175. doi:10.1007/s42485-021-00067-w

Tanner, J. A., Zheng, B.-J., Zhou, J., Watt, R. M., Jiang, J.-Q., Wong, K.-L., et al. (2005). The adamantane-derived bananins are potent inhibitors of the helicase activities and replication of SARS coronavirus. *Chem. Biol.* 12, 303–311. doi:10.1016/j.chembiol.2005.01.006

Ugurel, O. M., Mutlu, O., Sariyer, E., Kocer, S., Ugurel, E., Inci, T. G., et al. (2020). Evaluation of the potency of FDA-approved drugs on wild type and mutant SARS-CoV-2 helicase (Nsp13). *Int. J. Biol. Macromol.* 163, 1687–1696. doi:10.1016/j.ijbiomac.2020.09.138

U.S. Food and Drug Administration (2021). FDA authorizes first two oral antivirals for treatment of COVID-19. Available at: https://content.govdelivery.com/accounts/USFDA/bulletins/30221ce (Accessed July 25, 2022).

Vivek-Ananth, R. P., Krishnaswamy, S., and Samal, A. (2021). Potential phytochemical inhibitors of SARS-CoV-2 helicase Nsp13: A molecular docking and dynamic simulation study. *Mol. Divers.* 26, 429–442. doi:10.1007/s11030-021-10251-1

Wang, J., Levi, J., Ellis, L., and Hill, A. (2021). Minimum manufacturing costs, national prices and estimated global availability of new repurposed therapies for COVID-19. *MedRxiv [preprint]*, doi:10.1101/2021.06.01.21258147

Wang, Y., Zhang, D., Du, G., Du, R., Zhao, J., Jin, Y., et al. (2020). Remdesivir in adults with severe COVID-19: A randomised, double-blind, placebo-controlled, multicentre trial. *Lancet* 395, 1569–1578. doi:10.1016/S0140-6736(20)31022-9

Wang, Z., Wang, N., Yang, L., and Song, X. (2022). Bioactive natural products in COVID-19 therapy. *Front. Pharmacol.* 13, 926507. doi:10.3389/fphar.2022.926507

Wang, Z., and Yang, L. (2021). Chinese herbal medicine: Fighting SARS-CoV-2 infection on all fronts. *J. Ethnopharmacol.* 270, 113869. doi:10.1016/j.jep.2021.113869

Wang, Z., and Yang, L. (2020). Turning the tide: Natural products and natural-product-inspired chemicals as potential counters to SARS-CoV-2 infection. *Front. Pharmacol.* 11, 1013. doi:10.3389/fphar.2020.01013

Warr, W. A., Nicklaus, M. C., Nicolaou, C. A., and Rarey, M. (2022). Exploration of ultralarge compound collections for drug discovery. *J. Chem. Inf. Model.* 62, 2021–2034. doi:10.1021/acs.jcim.2c00224

White, M. A., Lin, W., and Cheng, X. (2020). Discovery of COVID-19 inhibitors targeting the SARS-CoV-2 Nsp13 helicase. *J. Phys. Chem. Lett.* 11, 9144–9151. doi:10.1021/acs.jpclett.0c02421

World Health Organization (2020). Off-label use of medicines for COVID-19. Scientific brief. Available at: https://paho-covid-prod.atmire.com/handle/20.500.12663/973 (Accessed July 25, 2022).31

World Health Organization (2022). Therapeutics and COVID-19: Living guideline. Available at: https://www.who.int/publications/i/item/WHO-2019-nCoV-therapeutics-2022.4 (Accessed July 25, 2022).

Wu, B., Luo, M., Wu, F., He, Z., Li, Y., and Xu, T. (2022). Acute kidney injury associated with remdesivir: A comprehensive pharmacovigilance analysis of COVID-19 reports in faers. *Front. Pharmacol.* 13, 692828. doi:10.3389/fphar.2022.692828

Yang, L., and Wang, Z. (2021). Natural products, alone or in combination with FDA-approved drugs, to treat COVID-19 and lung cancer. *Biomedicines* 9, 689. doi:10.3390/biomedicines9060689

Yang, N., Tanner, J. A., Wang, Z., Huang, J.-D., Zheng, B.-J., Zhu, N., et al. (2007a). Inhibition of SARS coronavirus helicase by bismuth complexes. *Chem. Commun.* 42, 4413–4415. doi:10.1039/B709515E

Yang, N., Tanner, J. A., Zheng, B.-J., Watt, R. M., He, M.-L., Lu, L.-Y., et al. (2007b). Bismuth complexes inhibit the SARS coronavirus. *Angew. Chem. Int. Ed.* 46, 6464–6468. doi:10.1002/anie.200701021

Ye, Z.-W., Yuan, S., Yuen, K.-S., Fung, S.-Y., Chan, C.-P., and Jin, D.-Y. (2020). Zoonotic origins of human coronaviruses. *Int. J. Biol. Sci.* 16, 1686–1697. doi:10.7150/ijbs.45472

Yu, M.-S., Lee, J., Lee, J. M., Kim, Y., Chin, Y.-W., Jee, J.-G., et al. (2012). Identification of myricetin and scutellarein as novel chemical inhibitors of the SARS coronavirus helicase, nsP13. *Bioorg. Med. Chem. Lett.* 22, 4049–4054. doi:10.1016/j.bmcl.2012.04.081

Yuan, S., Wang, R., Chan, J. F.-W., Zhang, A. J., Cheng, T., Chik, K. K.-H., et al. (2020). Metallodrug ranitidine bismuth citrate suppresses SARS-CoV-2 replication and relieves virus-associated pneumonia in Syrian hamsters. *Nat. Microbiol.* 5, 1439–1448. doi:10.1038/s41564-020-00802-x

Zaher, N. H., Mostafa, M. I., and Altaher, A. Y. (2020). Design, synthesis and molecular docking of novel triazole derivatives as potential CoV helicase inhibitors. *Acta Pharm.* 70, 145–159. doi:10.2478/acph-2020-0024

Zeng, J., Weissmann, F., Bertolin, A. P., Posse, V., Canal, B., Ulferts, R., et al. (2021). Identifying SARS-CoV-2 antiviral compounds by screening for small molecule inhibitors of nsp13 helicase. *Biochem. J.* 478, 2405–2423. doi:10.1042/BCJ20210201

Zhang, C., Wang, Y., Liu, X., Lu, J.-H., Qian, C., Wan, Z., et al. (2005). Antiviral activity of cepharanthine against severe acute respiratory syndrome coronavirus *in vitro*. *Chin. Med. J. (Engl.)* 118, 493–496.

Zhou, S., Hill, C. S., Sarkar, S., Tse, L. V., Woodburn, B. M. D., Schinazi, R. F., et al. (2021). β-d-N4-hydroxycytidine inhibits SARS-CoV-2 through lethal mutagenesis but is also mutagenic to mammalian cells. *J. Infect. Dis.* 224, 415–419. doi:10.1093/infdis/jiab247

Zhou, Y., Gammeltoft, K. A., Ryberg, L. A., Pham, L. V., Fahnøe, U., Binderup, A., et al. (2022). Nirmatrelvir resistant SARS-CoV-2 variants with high fitness *in vitro*. *BioRxiv*. preprint. doi:10.1101/2022.06.06.494921

# Combined chemical transformation and biological transformation of artemisinin: A facile approach to diverse artemisinin derivatives

Xinna Gao[1,2], Yue Bai[1], Peng Sun[1], Huimin Gao[1], Lan Yang[1], Dong Zhang[1], Yifan Zhao[1] and Yue Ma[1]*

[1]Artemisinin Research Center, Institute of Chinese Meteria Medica, China Academy of Chinese Medical Sciences, Beijing, China, [2]School of Graduate Students, Tianjin University of Traditional Chinese Medicine, Tianjin, China

**Introduction:** Artemisinin (**1**) is a milestone compound in malaria treatment, and it exhibits a broad scope of bioactivities. Herein, sequential chemo-reduction and biotransformation of artemisinin were undertaken to obtain a series of artemisinin derivatives.

**Methods:** First, 10-deoxyartemisinin (**2**) and 9-ene-10-deoxyartemisinin (**3**) were synthesized after simple handling with boron trifluoride/diethyl ether and sodium borohydride. Then, biotransformation of 10-deoxyartemisinin was conducted with *Cunninghamella echinulata* CGMCC 3.4879 and *Cunninghamella elegans* CGMCC 3.4832, and the transformed products were separated and identified. The antimalarial activity of these products was tested *in vitro* against *Plasmodium falciparum* 3D7.

**Results:** Fifteen metabolites (**4–18**), including seven novel compounds, were isolated and identified after cultivation. Compounds **2**, **3**, **13**, **15**, **16**, and **18** displayed moderate-to-good antimalarial activity, with a half-maximal inhibitory concentration ranging from 6 to 223 nM.

**Discussion:** This work explored the combination of chemical and biological transformation to develop a co-environmental, efficient, and cost-efficiency synthetic methodology and applied it to synthesize novel derivatives of artemisinin. The association of the two strategies will hopefully provide an abundant source for the development of novel drugs with bioactivities.

KEYWORDS

artemisinin, microbial transformation, *Cunninghamella* genus, anti-malarial activity, bioactive metabolites

## 1 Introduction

Artemisinin (also named qinghaosu, ART) is a legendary antimalarial agent. It was discovered from *Artemisia annua* L. by Tu et al. (1981) in 1972. In the last 50 years, millions of people suffering from malaria have been saved by artemisinin or its derivatives. Artemisinin-based combination therapy (ACT) is a recommended first-line treatment for malaria by the World Health Organization (especially for chloroquine-resistant malaria) (World Health Organization, 2021).

In recent years, parasite clearance for some patients in the Great Mekong Area and parts of Africa has been reported to be delayed after treatment with artesunate for 3 days (Uwimana et al., 2020). According to clinical studies, parasites can be cleared through 7-day treatment of artesunate, but the aforementioned delayed clearance has increased the anxiety about the possibility of resistance to artemisinin (Wang et al., 2019). To prevent the consequences of unpredictable drug resistance, there is an urgent need to explore antimalarial agents, including novel derivatives of artemisinin or other new chemical skeletons.

Microorganism-mediated modification of natural products and bioactive molecules is an efficient route for drug development (Cao et al., 2015). The abundant enzymes found in microorganisms enable hydroxylation, oxidation, reduction, and coupling reactions, with excellent chemo-, regio-, and even stereo-selectivities (Asha and Vidyavathi, 2009). In recent years, numerous microbial-based transformations of artemisinin have been attempted and various microbiological strains have been applied, including those of the genera *Aspergillus*, *Streptomyces*, *Penicillium*, and *Cunninghamella* (Parshikov et al., 2004a; Liu et al., 2006; Goswami et al., 2010; Ponnapalli et al., 2018). However, the number of compounds converted in a single transformation has been modest. In the latest research, four compounds from artemisinin were converted by *Aspergillus niger* in 2022 (Luo et al., 2022). Comparatively, plentiful metabolites were reported in this work.

Our research team has been engaged in the optimization of artemisinin (**1**) for the development of antimalarial drugs. In recent years, we have prepared a series of artemisinin derivatives through fungal-mediated transformations (Bai et al., 2019; Ma et al., 2019; Bai et al., 2021; Zhao et al., 2021). The labile lactone structure of artemisinin is widely perceived to contribute to diminishing the stability of the entire molecule. Herein, the lactone was reduced to methylene to offer 10-deoxyartemisinin (**2**), accompanied by a byproduct: 9-ene-10-deoxyartemisinin (**3**). The 10-deoxyartemisinin was modified by *Cunninghamella* species to obtain structurally divergent metabolites. The antimalarial activity of these generated products against *P. falciparum* (*Pf.*) 3D7 was examined to obtain potential lead compounds for drug development.

# 2 Materials and methods

## 2.1 General experimental procedures

$^{1}$H (600 MHz), $^{13}$C (150 MHz), and two-dimensional nuclear magnetic resonance (2D-NMR) spectroscopy were undertaken on a spectrometer (AV 600; Bruker, Billerica, MA, United States) with tetramethylsilane as an internal reference. Chemical shifts ($\delta$) are given in ppm. Coupling constants (J) are given in hertz. X-ray diffraction was carried out using a diffractometer (D8 Venture; Bruker) with Cu K$\alpha$ radiation. Column chromatography was performed with a silica flash column (330 g; Qingdao Marine Chemical Group, Qingdao, China), silica gel (200–300 mesh; Qingdao Marine Chemical Group), and a Chromatorex (FujiSilysia Chemicals, Kasugai, Japan) system. Analytical thin-layer chromatography was carried out on pre-coated silica-gel GF$_{254}$ plates (Qingdao Marine Chemical Group). Water was prepared using a Milli-Q™ system operating at 18.2 MΩ (Millipore, Bedford, MA, United States). Unless stated otherwise, all chemicals were obtained from commercially available sources and were used without further purification.

## 2.2 Synthesis of 10-deoxyartemisinin and 9-ene-10-deoxyartemisinin

Artemisinin (99% by high-performance liquid chromatography (HPLC); batch number, C00120160) was purchased from Kunming Pharmaceutical Group (Kunming, China). Under an inert atmosphere, a solution of artemisinin (2 g) and boron trifluoride/diethyl ether (BF$_3$/Et$_2$O) (26.4 mL) in dry tetrahydrofuran (THF; 30 mL) at 0 °C was added dropwise to an ice-cooled solution of sodium tetrahydroborate (NaBH$_4$; 0.6 g) in dry THF (30 mL). The reaction was carried out for 3 h at 0°C and then heated to reflux for 15 min. The synthetic route is shown in Figure 1. After cooling to room temperature, the reaction mixture was extracted thrice with ether (1:1, *v/v*). The combined organic phase was washed with saturated sodium chloride and dried over anhydrous sodium sulfate (NaSO$_4$). The solvent was removed after evaporation *in vacuo* to obtain the crude product. The latter was purified by silica-gel column chromatography. The target product, 10-deoxyartemisinin (**2**, yield 50%), and the byproduct, 9-ene-10-deoxyartemisinin (**3**, yield 22%), were obtained with petroleum ether–ethyl acetate as the eluent. High-resolution-electrospray ionization-mass spectrometry (HR-ESI-MS) and $^{1}$H-NMR and $^{13}$C-NMR spectroscopy were used to identify structures. The NMR data of 10-deoxoartemisinin and 9-ene-10-deoxyartemisinin are shown in Table 1 and Table 2. The synthesis scheme is shown in Figure 1.

## 2.3 Preparative biotransformation, extraction, and isolation of metabolites

*C. echinulata* CGMCC 3.4879 and *C. elegans* CGMCC 3.4832 were obtained from the China General Microbiological Culture Collection Center (Beijing, China). Culture was conducted in a medium comprising sabouraud dextrose broth (20 g/L), peptone (10 g/L), and sucrose (15 g/L). Two-stage fermentation was carried out. The substrate (10-deoxyartemisinin) was dissolved in methanol (25 mg/mL) and added to each flask after the second fermentation to reach a final concentration of 0.5 mg/mL. Cultures were incubated at 28 °C and agitated at 180 rpm/min for 14 days. Then, they were filtered and extracted thrice with ethyl acetate at an equal volume. The extract was dried with anhydrous Na$_2$SO$_4$ and concentrated under a vacuum at 45 °C to provide a residue.

The residue from *C. echinulata* CGMCC 3.4879 was subjected to a silica-gel column chromatography by elution with petroleum ether/ethyl acetate to provide six subfractions (Fr.1–Fr.6). Fractions 1, 2, and 4 were separated by Chromatorex silica-gel column chromatography with petroleum ether/ethyl acetate to obtain compound **12** (200 mg), compound **9** (9 mg), and compound **13** (250 mg), respectively. Fraction 3 was purified by recrystallization from ethyl acetate to provide compound **11** (120 mg). Fractions 5 and 6 were purified by semi-preparative normal-phase HPLC (methanol/water) to gain compound **14** (7 mg) and compounds **4–6** (34, 12, and 6 mg), respectively.

The residue from *C. elegans* CGMCC 3.4832 was subjected to silica-gel column chromatography by elution with petroleum ether/ethyl acetate to provide seven fractions (Fr.1–Fr.7). Fractions 1, 5, and 7 were separated by Chromatorex silica-gel column chromatography with petroleum ether/ethyl acetate to afford compound **17** (50 mg), compound **18** (154 mg), and
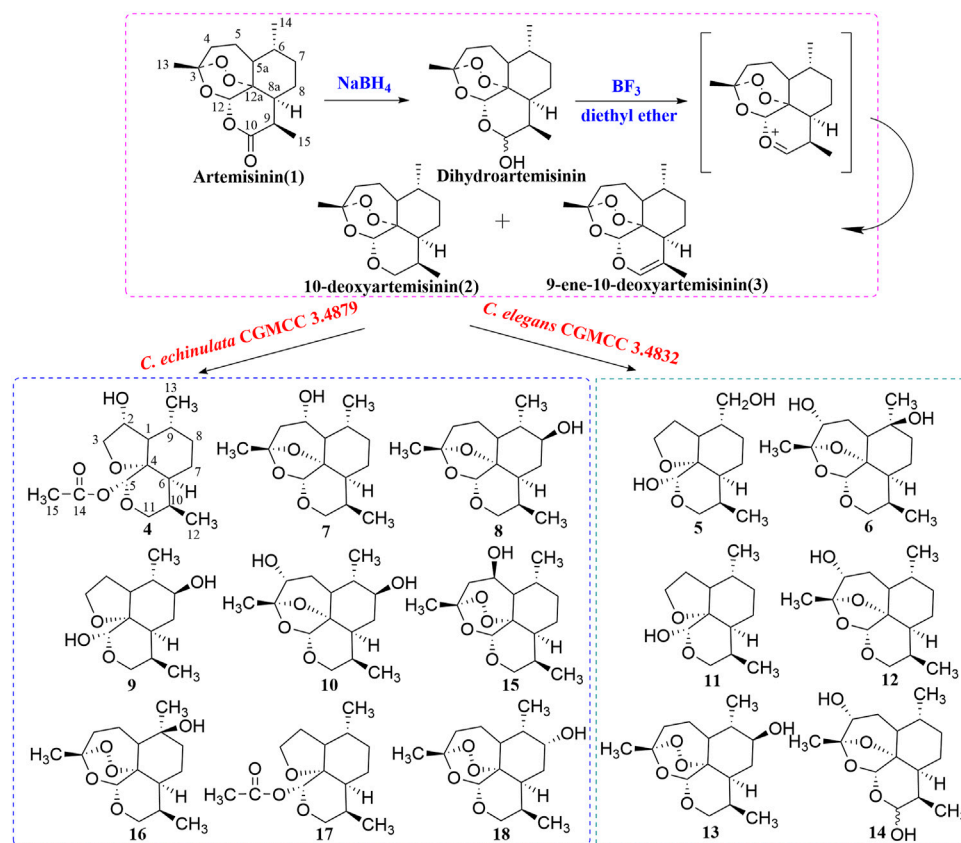
**FIGURE 1**
Synthesis route of 10-deoxyartemisinin and its metabolites by *C. elegans* and *C. echinulata*.

compound **9** (5 mg), respectively. Fraction 3 was separated by reverse-phase $C_{18}$ column chromatography with methanol/water to obtain compound **15** (10 mg). Fraction 4 was separated by Chromatorex silica-gel column chromatography with petroleum ether/ethyl acetate with additional reverse-phase $C_{18}$ column chromatography to obtain compound **7** (10 mg), compound **8** (4 mg), compound **16** (20 mg), and compound **10** (100 mg).

## 2.4 Identification of compounds

10-Deoxyartemisinin (**2**) (Jung et al., 1990): White acicular crystals (ethyl acetate). HR-ESI-MS *m/z* 291.1624 [M + Na]$^+$ (calcd for $C_{15}H_{24}O_4$, 268.1675). $^{13}$C-NMR data are shown in Table 1. $^1$H-NMR data are shown in Table 2.

9-ene-10-Deoxyartemisinin (**3**) (Xie et al., 2001): White powder (ethyl acetate). HR-ESI-MS *m/z* 289.1425 [M + Na]$^+$ (calcd for $C_{15}H_{22}O_4$, 266.1518). $^{13}$C-NMR data are shown in Table 1. $^1$H-NMR data are shown in Table 2.

2α-Hydroxy-5α-acetoxy-artemethin-ll (**4**): Colorless, transparent, columnar crystals (ethyl acetate). HR-ESI-MS *m/z* 307.1520 [M + Na]$^+$ (calcd for $C_{15}H_{24}O_5$, 284.1624). Crystal data: $C_{15}H_{24}O_5$, M = 284.34, monoclinic system, crystal size is 0.47 mm$^3$ × 0.40 mm$^3$ × 0.39 mm$^3$, a = 13.2788 (6) Å, b = 14.9910 (7) Å, c = 15.8479 (8) Å; α = β = γ = 90.00°, V = 3154.7 (3) Å3, space group P2$_1$2$_1$2$_1$ (NO. 19), T = 273.15 K, Z = 8, Z′ = 2, μ (Cu Kα) = 0.089 mm$^{-1}$, wavelength/Å = 0.71073, R1 = 0.1017, wR (F$_2$) =

0.1283. Flack parameter: 0.2 (2). Crystallographic data of compound 4 have been deposited to CCDC (www.ccdc.cam.ac.uk/, number = CCDC 2218207). The structure of a single crystal is shown in Figure 2. $^{13}$C-NMR data are shown in Table 1. $^1$H-NMR data are shown in Table 4.

5α,13-Dihydroxy-artemethin-ll (**5**): Colorless, transparent, columnar crystals (petroleum ether and acetone). HR-ESI-MS *m/z* 265.1415 [M + Na]$^+$ (calcd for $C_{13}H_{22}O_4$, 242.1518). Crystal data: $C_{13}H_{22}O_4$, M = 242.30, monoclinic system, crystal size is 0.47 mm$^3$ × 0.40 mm$^3$ × 0.39 mm$^3$, a = 6.1074 (3) Å, b = 15.6846 (7) Å, c = 6.7830 (3) Å; α = γ = 90°, V = 634.54 (5) Å3, space group P2$_1$ (NO. 4), T = 273.15 K, Z = 2, μ (Cu Kα) = 0.092 mm$^{-1}$, wavelength/Å = 0.71073, R1 = 0.0319 [I > 2σ (I)], wR (F$_2$) = 0.0875. Flack parameter: 0.2 (2). Crystallographic data of compound 5 have been deposited to CCDC (www.ccdc.cam.ac.uk/, number = CCDC 2218208). The structure of a single crystal is shown in Figure 2. $^{13}$C-NMR data are shown in Table 1. $^1$H-NMR data are shown in Table 4.

4α,6β-Dihydroxy-1-deoxy-10-deoxoartemisinin (**6**): White powder (ethyl acetate). HR-ESI-MS 307.1549 [M + Na]$^+$ (calcd for $C_{15}H_{24}O_5$, 284.1624). $^{13}$C-NMR data are shown in Table 1. $^1$H-NMR data are shown in Table 2.

5α-Hydroxy-1-deoxy-10-deoxoartemisinin (**7**): White powder (ethyl acetate). HR-ESI-MS 269.1756 [M + H]$^+$ (calcd for $C_{15}H_{24}O_4$, 268.1675). $^{13}$C-NMR data are shown in Table 1. $^1$H-NMR data are shown in Table 2.

7β-Hydroxy-1-deoxy-10-deoxoartemisinin (**8**): Yellow powder (ethyl acetate). HR-ESI-MS 269.1754 [M + H]$^+$ (calcd for $C_{15}H_{24}O_4$, 268.1675). $^{13}$C-NMR data are shown in Table 1. $^1$H-NMR data are shown in Table 2.

**TABLE 1 ¹³C-NMR spectral data (δ) for compounds 2–18.**

| No. | 2 δC | 3 δC | 4 δC | 5 δC | 6 δC | 7 δC | 8 δC | 9 δC | 10 δC | 11 δC | 12 δC | 13 δC | 14 δC | 15 δC | 16 δC | 17 δC | 18 δC |
|---|---|---|---|---|---|---|---|---|---|---|---|---|---|---|---|---|---|
| 1 | | | 61.8 | 50.7 | | | | 54.5 | | 56.2 | | | | | | 55.6 | |
| 2 | | | 75.7 | 26.3 | | | | 28.2 | | 27.4 | | | | | | 27.7 | |
| 3 | 104.2 | 104.1 | 73.5 | 68.6 | 106.4 | 105.0 | 106.5 | 71.1 | 107.5 | 69.3 | 107.3 | 104.2 | 108.1 | 102.4 | 104.0 | 68.7 | 104.2 |
| 4 | 36.3 | 36.3 | 82.0 | 80.3 | 69.1 | 44.3 | 33.1 | 81.9 | 69.2 | 81.2 | 69.8 | 36.0 | 69.6 | 46.3 | 35.9 | 80.4 | 36.3 |
| 5 | 24.8 | 24.4 | 92.5 | 93.5 | 39.3 | 68.0 | 21.0 | 95.8 | 30.3 | 94.5 | 30.3 | 24.6 | 30.3 | 69.3 | 29.8 | 92.8 | 24.6 |
| 5a | 52.2 | 51.4 | | | 42.5 | 53.1 | 42.3 | | 42.0 | | 41.8 | 49.6 | 41.1 | 59.4 | 53.4 | | 44.3 |
| 6 | 37.3 | 36.7 | 47.3 | 45.9 | 70.3 | 34.6 | 41.5 | 46.6 | 37.7 | 46.8 | 35.0 | 42.5 | 35.0 | 36.9 | 72.4 | 47.1 | 40.7 |
| 7 | 34.0 | 34.1 | 20.9 | 19.7 | 24.8 | 34.4 | 73.8 | 31.7 | 74.6 | 21.0 | 34.3 | 73.9 | 34.2 | 34.9 | 39.5 | 21.0 | 70.0 |
| 8 | 20.7 | 29.5 | 35.6 | 37.1 | 17.8 | 23.0 | 32.1 | 78.1 | 32.8 | 35.4 | 23.7 | 27.6 | 22.8 | 20.6 | 16.7 | | 28.0 |
| 8a | 44.9 | 44.2 | | | 39.6 | 39.0 | 36.8 | | 39.3 | | 39.8 | 44.1 | 41.6 | 44.7 | 45.1 | 35.3 | 37.6 |
| 9 | 28.0 | 107.7 | 30.2 | 28.5 | 26.1 | 25.4 | 25.1 | 38.7 | 26.1 | 30.4 | 26.4 | 29.9 | 33.7 | 27.8 | 28.3 | 30.4 | 27.3 |
| 10 | 66.2 | 135.3 | 28.9 | 28.8 | 63.4 | 63.3 | 63.3 | 31.1 | 64.4 | 29.8 | 64.6 | 66.1 | 96.7 | 66.2 | 66.4 | 29.6 | 66.1 |
| 11 | | | 67.9 | 66.0 | | | | 67.9 | | 66.9 | | | | | | 67.7 | |
| 12 | 92.1 | 89.4 | 12.5 | 11.8 | 94.9 | 95.2 | 94.9 | 13.1 | 95.3 | 12.8 | 95.5 | 91.8 | 95.4 | 91.7 | 93.2 | 12.7 | 91.6 |
| 12a | 80.8 | 79.1 | | | 82.7 | 81.6 | 80.7 | | 82.4 | | 83.2 | 80.0 | 83.1 | 80.1 | 81.3 | | 80.5 |
| 13 | 26.1 | 16.3 | 19.8 | 65.8 | 19.8 | 22.7 | 22.9 | 17.1 | 20.5 | 20.5 | 20.6 | 26.0 | 20.8 | 25.9 | 26.1 | 20.6 | 26.1 |
| 14 | 20.3 | 20.5 | 169.0 | | 27.7 | 20.8 | 13.3 | | 15.9 | | 18.7 | 15.4 | 18.6 | 21.3 | 19.6 | 169.2 | 16.5 |
| 15 | 13.1 | 25.9 | 21.6 | | 14.0 | 15.8 | 15.3 | | 14.2 | | 16.3 | 13.1 | 14.6 | 13.0 | 13.2 | 21.6 | 13.0 |

**TABLE 2** ¹H-NMR spectral data ($\delta$) for compounds **2**, **3**, **6–8**, and **10**.

| No. | 2 $\delta_H$ ($J$ in Hz) | 3 $\delta_H$ ($J$ in Hz) | 6 $\delta_H$ ($J$ in Hz) | 7 $\delta_H$ ($J$ in Hz) | 8 $\delta_H$ ($J$ in Hz) | 10 $\delta_H$ ($J$ in Hz) |
|---|---|---|---|---|---|---|
| 4 | | | 3.61–3.55 (m) | 2.22 (m) | 1.65 (dd, $J$ = 13.5, 5.7 Hz) | 3.56 (dd, $J$ = 9.9, 2.5 Hz) |
| | | | | 1.45 (d, $J$ = 3.5 Hz) | 1.54–1.47 (m) | |
| 5 | | | 1.71–1.63 (m) | 3.78 (m) | 1.81–1.73 (m) | |
| | | | 1.45 (m) | | 1.37–1.24 (m) | |
| 5a | | | 1.60 (m) | 1.12 (d, $J$ = 6.5 Hz) | 1.20 (m) | |
| 6 | | | | 1.45 (d, $J$ = 3.5 Hz) | 1.12 (m) | |
| 7 | | | 1.71–1.63 (m) 2.02 (m) | | 3.18 (m, $J$ = 10.4, 3,9 Hz) | |
| 8 | | | 1.93–1.84 (m) | 1.72 (m) | 1.37–1.24 (m) | |
| | | | 1.71–1.63 (m) | 1.30 (m) | 1.97 (m) | |
| 8a | | | 1.93–1.84 (m) | 1.87 (m) | 1.97 (m) | 2.02 (m) |
| 9 | 2.57 (m) | | 2.33–2.25 (m) | 2.22 (m) | 2.23 (m, $J$ = 7.1, 12.3 Hz) | 2.32 (m) |
| 10 | 3.66 (dd, $J$ = 12.0, 6.0 Hz) | 6.08 (d, $J$ = 1.9 Hz) | 3.30 (dd, $J$ = 11.6, 7.5 Hz) | 3.86 (dd, $J$ = 11.5, 7.2 Hz) | 3.85 (dd, $J$ = 11.5, 6.6 Hz) | 3.86 (dd, $J$ = 11.6, 6.3 Hz) |
| | 3.38 (t, $J$ = 12.0 Hz) | | 3.67 (dd, $J$ = 11.6, 5.5 Hz) | 3.21 (dd $J$ = 11.5, 4.4 Hz) | 3.25 (dd, $J$ = 11.6, 5.0 Hz) | 3.34 (dd, $J$ = 11.7, 5.6 Hz) |
| 12 | 5.13 (s) | 5.60 (s) | 5.67 (s) | 5.08 (s) | 5.20 (s) | 5.21 (s) |
| 13 | 1.36 (s) | 1.48 (s) | 1.50 (s) | 1.47 (s) | 1.46 (s) | 1.56 (s) |
| 14 | 0.89 (d, $J$ = 6.4 Hz) | 0.88 (d, $J$ = 6.4 Hz) | 1.13 (s) | 1.12 (d, $J$ = 6.5 Hz) | 0.96 (d, $J$ = 6.2 Hz) | 1.00 (d, $J$ = 6.4 Hz) |
| 15 | 0.71 (d, $J$ = 7.2 Hz) | 1.26 (s) | 0.82 (d, $J$ = 7.4 Hz) | 0.86 (d, $J$ = 7.4 Hz) | 0.86 (d, $J$ = 7.4 Hz) | 0.91 (d, $J$ = 7.4 Hz) |

5α,8β-Dihydroxy-artemethin-ll (**9**): Colorless, transparent, needle crystals (ethyl acetate). HR-ESI-MS *m/z* 265.1416 [M + H]⁺ (calcd for $C_{13}H_{22}O_4$, 242.1518). Crystal data: $C_{13}H_{22}O_4$, M = 242.31, triclinic system, crystal size is 0.38 mm³ × 0.11 mm³ × 0.08 mm³, a = 9.5815 (4) Å, b = 10.7290 (5) Å, c = 13.8292 (3) Å; α = 79.138 (3)°, β = 72.174 (3)°, γ = 75.565 (3)°, V = 1300.94 (9) Å3, space group P₁ (NO. 1), T = 111.6 (3) K, Z = 4, μ (Cu Kα) = 0.738 mm⁻¹, R1 = 0.0436 (all data), wR ($F_2$) = 0.1088. Flack parameter: 0.06 (11). Crystallographic data of compound 9 have been deposited to CCDC (www.ccdc.cam.ac.uk/, number = CCDC 2218214). The structure of a single crystal is shown in Figure 2. ¹³C-NMR data are shown in Table 1. ¹H-NMR data are shown in Table 4.

3α,7β-Dihydroxy-1-deoxy-10-deoxoartemisinin (**10**): Colorless, transparent, columnar crystals (ethyl acetate and acetone). HR-ESI-MS *m/z* 285.1690 [M + Na]⁺ (calcd for $C_{15}H_{24}O_5$, 284.1624). Crystal data: $C_{15}H_{24}O_5$, M = 283.94, triclinic system, crystal size is 0.46 mm³ × 0.31 mm³ × 0.27 mm³, a = 9.3731 (18) Å, b = 12.574 (3) Å, c = 15.842 (3) Å; α = 85.623 (6)°, β = 81.953 (6)°, γ = 89.302 (7)°, V = 89.302 (7) Å3, space group P₁ (NO. 1), T = 273.15 K, Z = 5, Z' = 5 μ (Cu Kα) = 0.095 mm⁻¹, wavelength/Å = 0.71073, R1 = 0.0463 [I > 2σ (I)], wR ($F_2$) = 0.1078. Flack parameter: −0.05 (19). Crystallographic data of compound 10 have been deposited to CCDC (www.ccdc.cam.ac.uk/, number = CCDC 2218210). The structure of a single crystal is shown in Figure 2. ¹³C-NMR data are shown in Table 1. ¹H-NMR data are shown in Table 2.

5α-Hydroxy-artemethin-ll (**11**) (Gaur et al., 2014): White powder (ethyl acetate). HR-ESI-MS *m/z* 249.1467 [M + Na]⁺ (calcd for $C_{13}H_{22}O_3$, 226.1569). ¹³C-NMR data are shown in Table 1. ¹H-NMR data are shown in Table 4.

4α-Hydroxy-1-deoxy-10-deoxoartemisinin (**12**) (Parshikov et al., 2004b): White powder (ethyl acetate). HR-ESIMS *m/z* 269.1741 [M + H]⁺ (calcd for $C_{15}H_{24}O_4$, 268.1675). ¹³C-NMR data are shown in Table 1. ¹H-NMR data are shown in Table 3.

7β-Hydroxy-10-deoxoartemisinin (**13**) (Parshikov et al., 2004a): White powder (ethyl acetate). HR-ESI-MS 307.1521 [M + Na]⁺(calcd for $C_{15}H_{24}O_5$, 284.1624). ¹³C-NMR data are shown in Table 1. ¹H-NMR data are shown in Table 3.

4α-Hydroxy-1-deoxydihydroartemisinin (**14**) (Lee et al., 1990): Colorless, transparent, columnar crystals (ethyl acetate). HR-ESI-MS *m/z* 307.1526 [M + Na]⁺ (calcd for $C_{15}H_{24}O_5$, 284.1624). Crystal data: $C_{15}H_{24}O_5$, M = 284.34, monoclinic system, crystal size is 0.25 mm³ × 0.21 mm³ × 0.13 mm³, a = 5.7937 (4) Å, b = 8.5070 (4) Å, c = 29.3066 (17) Å; α = β = γ = 90°, V = 1444.43 (15) Å3, space group P2₁2₁2₁ (NO. 19), T = 294.0 K, Z = 4, μ (Cu Kα) = 0.097 mm⁻¹, wavelength/Å = 0.71073, R1 = 0.0585, wR ($F_2$) = 0.1157. Flack parameter: 0.0 (12). Crystallographic data of compound 14 have been deposited to CCDC (www.ccdc.cam.ac.uk/. number = CCDC 2218211). The structure of a single crystal is shown in Figure 2. ¹³C-NMR data are shown in Table 1. ¹H-NMR data are shown in Table 3.

5β-Hydroxy-10-deoxoartemisinin (**15**) (Parshikov et al., 2004b): White powder (ethyl acetate). HR-ESI-MS 307.1519 [M + Na]⁺ (calcd for $C_{15}H_{24}O_5$, 284.1624). ¹³C-NMR data are shown in Table 1. ¹H-NMR data are shown in Table 3.

6β-Hydroxy-10-deoxoartemisinin (**16**) (Medeiros et al., 2002): Colorless, transparent, columnar crystals (ethyl acetate). HR-ESI-MS *m/z* 307.1522 [M + Na]⁺ (calcd for $C_{15}H_{24}O_5$, 284.1624). Crystal data: $C_{15}H_{24}O_5$, M = 284.34, monoclinic system, crystal size is 0.24 mm³ × 0.21 mm³ × 0.10 mm³, a = 7.1619 (10) Å, b = 12.1265 (17) Å, c = 16.910 (2) Å; α = β = γ = 90.00°, V = 1468.6 (3) Å3, space group P2₁2₁2₁ (NO. 19), T = 273.15 K, Z = 4, Z' = 1, μ (Cu Kα) = 0.095 mm⁻¹, R1 = 0.0469 [I > 2σ (I)], wR ($F_2$) = 0.1142. Flack parameter: −0.2 (4). Crystallographic data of compound 16 have been deposited to CCDC (www.ccdc.cam.ac.uk/, number = CCDC
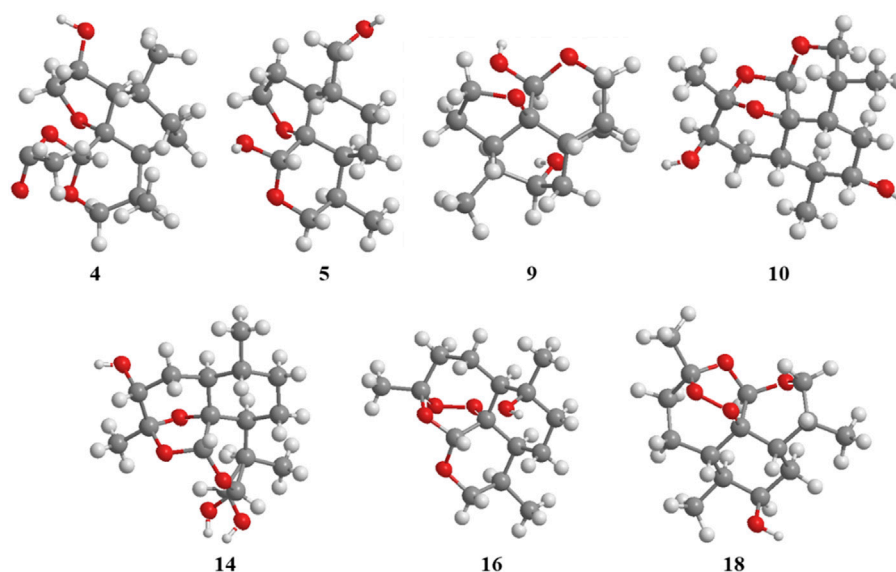
**FIGURE 2**
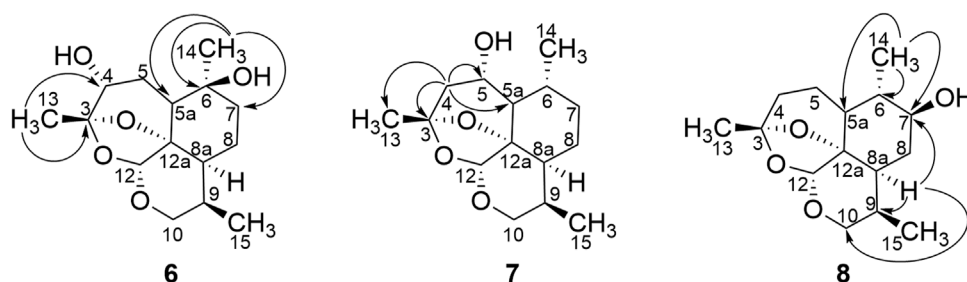ORTEP drawing of the X-ray structures of compounds 4, 5, 9, 10, 14, 16, and 18.



**FIGURE 3**
HMBC correlations for compounds 6, 7, and 8.

2218212). The structure of a single crystal is shown in Figure 2. $^{13}$C-NMR data are shown in Table 1. $^{1}$H-NMR data are shown in Table 3.

5α-Acetoxy-artemethin-ll (**17**) (Khalifa et al., 1995): Colorless, transparent, oily substance (ethyl acetate). HR-ESI-MS $m/z$ 291.1573 [M + Na]$^+$ (calcd for $C_{15}H_{24}O_4$, 268.1675). $^{13}$C-NMR data are shown in Table 1. $^{1}$H-NMR data are shown in Table 4.

7α-Hydroxy-10-deoxoartemisinin (**18**) (Khalifa et al., 1995): Colorless, transparent, columnar crystals (ethyl acetate). HR-ESI-MS $m/z$ 307.1520 [M + Na]$^+$ (calcd for $C_{15}H_{24}O_5$, 284.1624). Crystal data: $C_{15}H_{24}O_5$, M = 284.34, triclinic system, crystal size is 0.46 mm$^3$ × 0.31 mm$^3$ × 0.27 mm$^3$, a = 10.2388 (17) Å, b = 14.937 (3) Å, c = 9.8826 (17) Å; α = 94.230 (6)°, β = 101.038 (6)°, γ = 90.123 (5)°, V = 1479.2 (4) Å3, space group P1 (NO. 1), T = 293 (2) K, Z = 4, $\mu$ (Cu Kα) = 0.095 mm$^{-1}$, R1 = 0.1021 [I > 2σ (I)], wR (F2) = 0.2594. Flack parameter: −0.3 (15). Crystallographic data of compound 18 have been deposited to CCDC (www.ccdc.cam.ac.uk/, number = CCDC 2218213). The structure of a single crystal is shown in Figure 2. $^{13}$C-NMR data are shown in Table 1. $^{1}$H-NMR data are shown in Table 3.

## 2.5 Evaluation of antimalarial activity *in vitro*

*Pf*. 3D7 strains were obtained from Professor Chenqijun (Institute of Zoonosis, Jilin University, Jilin, China). *Pf*. 3D7 strains were grown under a gas mixture (5% CO$_2$, 5% O$_2$, and 90% N$_2$). Human erythrocytes were grown at 2% hematocrit. Synchronization was carried out by treatment with 5% D-sorbitol when most parasites were in the "ring" stage. All compounds were prepared in dimethyl sulfoxide and diluted serially in culture medium (100 μL) across the columns of a 96-well tissue-culture plate. Artemisinin was used as a positive control drug. Then, 100 μL of a parasite suspension (1% ring-infected erythrocytes at 4% hematocrit) was added to each well. The plate was incubated under the gas mixture for 72 h at 37 °C. After incubation, 100 μL of lysis buffer (Tris-Cl (1 M), EDTA (0.5 M), 10% saponin, 0.08% Triton X-100, pH 7.5, SYBR™ Green 1, at the recommended dilution of the manufacturer) was added to each well. The plate was agitated for 1.5 h, and fluorescence was measured at an excitation wavelength of 485 nm and emission wavelength of 530 nm. The half-maximal inhibitory concentration (IC$_{50}$) was used to evaluate the anti-malarial action of all compounds.

**TABLE 3** ¹H-NMR spectral data (δ) for compounds 12–16 and 18.

| No. | 12 $\delta_H$ (J in Hz) | 13 $\delta_H$ (J in Hz) | 14 $\delta_H$ (J in Hz) | 15 $\delta_H$ (J in Hz) | 16 $\delta_H$ (J in Hz) | 18 $\delta_H$ (J in Hz) |
|---|---|---|---|---|---|---|
| 4 | 3.31 (dd, J = 11.6, 5.1 Hz) | 2.36 (m) | | | | 2.43 (m) |
| | | 2.05 (m) | | | | |
| 5 | 1.88 (m) | | | 3.94 (q, J = 7.9 Hz) | | |
| 5a | | | | 1.27 (dd, J = 11.3, 8.0 Hz) | | |
| 6 | 1.27–1.17 (m) | | | 1.58 (m) | | |
| 7 | 1.75 (m) | 3.26 (td, J = 10.7, 4.4 Hz) | | | | 3.88–3.84 (m) |
| | 1.02 (m) | | | | | |
| 8 | 1.88 (m) | 1.87 (m) | | | | 1.88–1.76 (m) |
| | 1.34–1.27 (m) | | | | | |
| 8a | 1.97 (d, J = 10.3 Hz) | 1.64–1.57 (m) | | 1.64 (m) | | 2.13–2.02 (m) |
| 9 | 2.33–2.25 (m) | 2.62 (m) | 2.46 (m) | 2.63 (m) | 2.64 (m) | 2.71 (m) |
| 10 | 3.89 (dd, J = 11.5, 6.6 Hz) | 3.73 (dd, J = 11.8, 3.6 Hz) | 5.32 (s) | 3.70 (dd, J = 11.7, 4.2 Hz) | 3.75 (dd, J = 11.6, 4.0 Hz) | 3.78 (dd, J = 11.8, 5.0 Hz) |
| | 3.31 (dd, J = 11.6, 5.1 Hz) | 3.44 (t, J = 11.8 Hz) | | 3.44 (t, J = 11.8 Hz) | 3.48 (t, J = 11.7 Hz) | 3.45 (t, J = 11.8 Hz) |
| 12 | 5.18 (s) | 5.22 (s) | | 5.14 (s) | 5.61 (s) | 5.20 (s) |
| 13 | 1.56 (s) | 1.41 (s) | 1.54 (s) | 1.41 (s) | 1.46 (s) | 1.45 (s) |
| 14 | 0.91 (d, J = 7.4 Hz) | 1.06 (d, J = 6.0 Hz) | 0.96 (d, J = 7.5 Hz) | 1.13 (d, J = 6.6 Hz) | 1.30 (s) | 1.08 (d, J = 6.8 Hz) |
| 15 | 0.87 (d, J = 6.4 Hz) | 0.78 (d, J = 7.2 Hz) | 0.88 (d, J = 6.4 Hz) | 0.76 (d, J = 7.2 Hz) | 0.82 (d, J = 7.2 Hz) | 0.80 (d, J = 7.2 Hz) |

**TABLE 4** ¹H-NMR spectral data (δ) for compounds 4, 5, 9, 11, and 17.

| No. | 4 $\delta_H$ (J in Hz) | 5 $\delta_H$ (J in Hz) | 9 $\delta_H$ (J in Hz) | 11 $\delta_H$ (J in Hz) | 17 $\delta_H$ (J in Hz) |
|---|---|---|---|---|---|
| 1 | | | 1.36 (m) | | 1.33 (m) |
| 2 | 3.52 (t, J = 11.9 Hz) | 2.20 (m) | | 1.84 (m) | 1.96–1.89 (m) |
| | | 2.12–1.90 (m) | | 2.18 (m) | |
| 3 | 4.54–4.51 (m) | 4.15–4.10 (m) | 4.18 (t, J = 8.4 Hz) | 3.84 (m) | 3.91 (q, J = 8.0 Hz) |
| | | 3.82 (m) | 3.84 ( q, J = 7.7 Hz) | 4.17 (m) | 4.27–4.22 (m, 1H) |
| 5 | 5.92 (s) | 4.95 (d, J = 8.0 Hz) | 5.10 (s) | 4.99 (d, J = 8.3 Hz) | 5.97 (s) |
| 6 | 1.71 (m) | | 1.75 (m) | | |
| 7 | 1.96–1.86 (m) | | 1.58 (m) | 1.40–2.00 (m) | |
| | | | 1.92–1.85 (m) | 1.66 (m) | |
| 8 | | 0.89 (d, J = 6.6 Hz) | 3.24 (dd, J = 10.3, 5.8 Hz) | 0.86 (m) | 1.96–1.89 (m) |
| | | 1.85–1.79 (m) | | 1.87 (m) | |
| 9 | | 2.60 (d, J = 8.3 Hz) | 1.58 (m) | 1.70–1.75 (m) | 1.52 (m) |
| 10 | 2.49–2.43 (m) | 2.38–2.32 (m) | 2.23 (m) | 2.36 (m) | 2.45 (m, J = 11.9, 5.0 Hz) |
| 11 | 3.72 (dd, J = 11.7, 5.1 Hz) | 3.62 (m) | 3.58 (dd, J = 11.7, 5.1 Hz) | 3.43 (d, J = 11.5 Hz) | 3.52 (t, J = 11.8 Hz) |
| | 3.59 (dd, J = 8.1, 4.8 Hz) | 3.41 (t, J = 11.7 Hz) | 3.42 (t, J = 11.8 Hz, 1H) | 3.64 (m) | 3.70 (dd, J = 11.6, 5.2 Hz) |
| 12 | 0.78 (d, J = 7.1 Hz) | 0.71 (d, J = 7.1 Hz) | 0.76 (d, J = 7.1 Hz) | 0.73 (d, J = 7.2 Hz) | 0.76 (d, J = 7.1 Hz) |
| 13 | 1.06 (d, J = 6.4 Hz) | | 1.03 (d, J = 6.3 Hz) | 0.94 (d, J = 6.5 Hz) | 0.91 (d, J = 6.4 Hz) |
| 15 | 2.14 (s) | | | | |

# 3 Results

## 3.1 Structural elucidation

The two chemically synthesized derivatives, 10-deoxyartemisinin (**2**) and 9-ene-10-deoxyartemisinin (**3**), were obtained following reduction, dehydration, and a second reduction from artemisinin. In addition, 10-deoxyartemisinin (**2**) was employed as the substrate for microbial transformation with *C. elegans* CGMCC 3.4832 and *C. echinulata* CGMCC 3.4879.

Seven new metabolites and eight known metabolites were isolated and characterized unambiguously by various spectroscopy methods (Figure 1). The biotransformation products were identified to be 2$\alpha$-hydroxy-5$\alpha$-acetoxy-artemethin-ll (**4**), 5$\alpha$,13-dihydroxy-artemethin-ll (**5**), 4$\alpha$,6$\beta$-dihydroxy-1-deoxy-10-deoxoartemisinin (**6**), 5$\alpha$-hydroxy-1-deoxy-10-deoxoartemisinin (**7**), 7$\beta$-hydroxy-1-deoxy-10-deoxoartemisinin (**8**), 5$\alpha$,8$\beta$-dihydroxy-artemethin-ll (**9**), and 4$\alpha$,7$\beta$-dihydroxy-1-deoxy-10-deoxoartemisinin (**10**). The known compounds were determined to be 5$\alpha$-hydroxy-artemethin-ll (**11**), 4$\alpha$-hydroxy-1-deoxy-10-deoxoartemisinin (**12**), 7$\beta$-hydroxy-10-deoxoartemisinin (**13**), 4$\alpha$-hydroxy-1-deoxydihydroartemisinin (**14**), 5$\beta$-hydroxy-10-deoxoartemisinin (**15**), 6$\beta$-hydroxy-10-deoxoartemisinin (**16**), 5$\alpha$-acetoxy-artemethin-ll (**17**), and 7$\alpha$-hydroxy-10-deoxoartemisinin (**18**).

Metabolite **4** had a molecular formula of $C_{15}H_{24}O_5$, as deduced from HR-ESI-MS $m/z$ of 307.1520 $[M + Na]^+$. $^{13}C$-NMR data suggested one hydroxy carbon signal ($\delta_C$ 75.7) instead of an alkane carbon signal. The hydroxy group was at C-2 on the basis of the data for 5$\alpha$-acetoxy-artemethin-II (Khalifa et al., 1995). The structure was confirmed by X-ray crystallography. The structure of a single crystal is shown in Figure 2. Thus, metabolite 4 was identified as 2$\alpha$-hydroxy-5$\alpha$-acetoxy-artemethin-ll.

Metabolite **5** had a molecular formula of $C_{13}H_{22}O_4$, as deduced from its HR-ESI-MS $m/z$ of 265.1415 $[M + Na]^+$. $^1H$-NMR spectra showed $-CH_3$ ($\delta_H$ 0.95, 3H) to be substituted by $-CH_2OH$ ($\delta_H$ 0.94, 2H). $^{13}C$-NMR spectra showed that $\delta_C$ 20.5 (C-13) shifted to $\delta_C$ 65.8 compared with 5$\alpha$-hydroxy-artemethin-II (Gaur et al., 2014). Thus, the hydroxy group was at C-13. The structure was confirmed by X-ray crystallography. The structure of a single crystal is shown in Figure 2. Thus, metabolite 5 was identified as 5$\alpha$,13-dihydroxy-artemethin-ll.

Metabolite **6** had a molecular formula of $C_{15}H_{24}O_5$, as deduced from its HR-ESI-MS $m/z$ of 307.1549 $[M + Na]^+$. $^{13}C$-NMR (150 MHz, $CDCl_3$) and distortionless enhancement by polarization transfer (DEPT) spectroscopy showed 15 carbon signals: three methyl, four methylene, five methine, and three quaternary carbon atoms. The low-field shift of C-3 ($\delta_C$ 106.4) together with C-12 ($\delta_C$ 94.9) and C-12a ($\delta_C$ 82.7) compared with those of **2** implied deoxidation of an endoperoxide bridge. Compared with 4$\alpha$-hydroxy-1-deoxy-10-deoxoartemisinin (Parshikov et al., 2004a), a quaternary carbon signal $\delta_C$ 70.3 was found in place of a tertiary carbon signal. Together with a mass shift of 16 Da, the aforementioned information implied one more hydroxy group than that in 4$\alpha$-hydroxy-1-deoxy-10-deoxoartemisinin. Heteronuclear multiple-bond coherence (HMBC) correlation from the methoxy proton ($\delta_H$ 1.13, H-14) to the quaternary carbon ($\delta_C$ 70.3, C-6) confirmed a hydroxyl group at C-6. HMBC correlation for metabolite 6 is shown in Figure 3. Thus, metabolite **6** was identified as 4$\alpha$,6$\beta$-dihydroxy-1-deoxy-10-deoxoartemisinin.

Metabolite **7** had a molecular formula of $C_{15}H_{24}O_4$, as determined by HR-ESI-MS at $m/z$ of 269.1756 $[M + H]^+$. $^{13}C$-NMR (150 MHz,
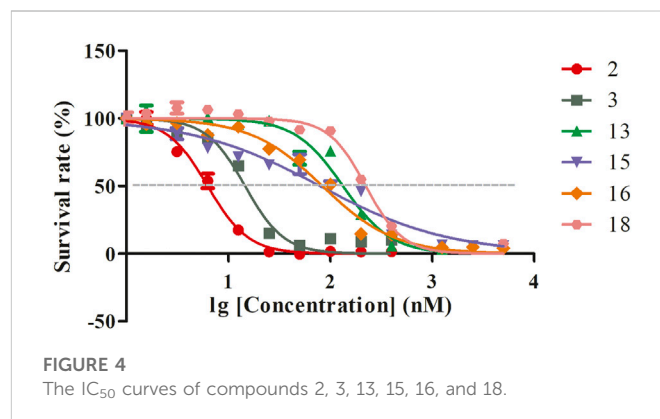


**FIGURE 4**
The IC$_{50}$ curves of compounds 2, 3, 13, 15, 16, and 18.

$CDCl_3$), and DEPT spectroscopy showed three methyl carbon signals ($\delta$ 22.7, 20.7, and 15.8), four methylene signals ($\delta$ 63.3, 44.3, 34.4, and 23.0), six tertiary carbon signals ($\delta$ 95.2, 67.9, 54.1, 39.0, 34.6, and 25.4), and two quaternary carbon signals ($\delta$ 105.0 and 81.7). Compared with 4$\alpha$-hydroxy-1-deoxy-10-deoxoartemisinin (Parshikov et al., 2004b), metabolite **7** was indicated to be a monohydroxy of 1,10-deoxy-artemisinin. $^1H$-NMR spectroscopy (600 MHz, $CDCl_3$) showed three methyl hydrogen signals: $\delta_H$ 1.47 (s, 3 H, H-13), 1.12 (d, J = 6.5 Hz, 3 H, H-14), and .86 (d, J = 7.4 Hz, 3 H, H-15), which implied that the hydroxyl group may be present at positions 5, 7, or 8. Based on HMBC spectroscopy, $\delta_H$ 2.22 (m, 1H, H-4$\alpha$) and $\delta_H$ 1.45 (d, 1H, J = 3.5 Hz, H-4$\beta$) were remotely correlated to $\delta_C$ 105.0 (C-3), $\delta_C$ 15.8 (C-13), $\delta_C$ 53.1 (C-5a), and $\delta_C$ 67.9, and the hydroxyl group was suggested to be located at C-5. HMBC correlation for metabolite **7** is shown in Figure 3. Given the characterized hydroxylation C-5 of artemisinin, the structure of metabolite **7** was identified as 5$\alpha$-hydroxy-1-deoxy-10-deoxoartemisinin.

Metabolite **8** had a molecular formula of $C_{15}H_{24}O_4$, as deduced from its HR-ESI-MS $m/z$ of 269.1754 $[M + H]^+$. $^{13}C$-NMR (150 MHz, $CDCl_3$), and DEPT spectroscopy showed three methyl signals ($\delta$ 22.9, 15.3, and 13.3), four methylene signals ($\delta$ 63.3, 33.1, 32.1, and 21.0), six tertiary carbon signals ($\delta$ 94.9, 73.8, 42.3, 41.5, 36.8, and 25.1), and two quaternary carbon atoms. Compared with $^{13}C$-NMR spectroscopy of 1-deoxy-10-deoxoartemisinin, $\delta_C$ 73.8 was predicted to be a hydroxyl carbon signal. Metabolite **8** was suggested to be hydroxyl 1-deoxy-10-deoxoartemisinin. HMBC spectroscopy showed a correlation from $\delta_H$ 0.96 (d, J = 6.2 Hz, 3H, H-14) to $\delta_C$ 42.3 (C-5a), $\delta_C$ 41.50 (C-6), and $\delta_C$ 73.8, and a correlation from $\delta_H$ 2.02–1.92 (m, 1 H, H-8a) to $\delta_C$ 25.1 (C-9), $\delta_C$ 63.3 (C-10), $\delta_C$ 32.1 (C-8), and $\delta_C$ 73.8. Thus, the hydroxyl group was suggested to be positioned at C-7. HMBC correlation for metabolite **8** is shown in Figure 3. Based on the distinction between 7$\alpha$ ($\delta_C$ 73.5) and 7$\beta$ ($\delta_C$ 68.7) hydroxylated chemical-shift deviation of artemisinin C-7 ($\delta_C$ 33.6), metabolite **8** was finally identified as 7$\beta$-hydroxy-1-deoxy-10-deoxoartemisinin.

Metabolite **9** had a molecular formula of $C_{13}H_{22}O_4$, as deduced from its HR-ESI-MS $m/z$ of 265.1416 $[M + H]^+$. $^{13}C$-NMR spectroscopy showed one more hydroxy carbon signal ($\delta_C$ 78.1) than that for 5$\alpha$-hydroxy-artemethin-II. Combined with its molecular formula, metabolite **9** was predicted to be hydroxylated 5$\alpha$-hydroxy-artemethin-II. The $^1H$-NMR spectrum showed a hydrogen signal $\delta_H$ 3.24 (dd, J = 10.3, 5.8 Hz, 1H), which indicated that the hydroxy group was at position C-8. The structure of metabolite **9** was confirmed by X-ray crystallography. The structure

of a single crystal is shown in Figure 2. Thus, metabolite **9** was identified as 5α,8β-dihydroxy-artemethin-II.

Metabolite **10** had a molecular formula of $C_{15}H_{24}O_5$, as deduced from its HR-ESI-MS *m/z* of 285.1690 [M + Na]$^+$. $^{13}$C-NMR spectroscopy indicated that metabolite **10** was a two hydroxy of 1-deoxy-10-deoxyartemisinin, of which hydroxy carbon signals were at $\delta_C$ 69.2 and $\delta_C$ 74.6. Compared with 4α-hydroxy-1-deoxy-10-deoxyartemisinin, $^1$H-NMR spectroscopy indicated that the hydroxy groups were located at C-4 and C-7. Finally, the structure of metabolite **10** was confirmed by X-ray crystallography. The structure of a single crystal is shown in Figure 2. Thus, metabolite **10** was identified as 4α,7β-dihydroxy-1-deoxy-10-deoxyartemisinin.

## 3.2 Antimalarial activity *in vitro*

The positive control drug (artemisinin) exhibited *in vitro* antimalarial activity against *Pf.* 3D7, with an IC$_{50}$ (50% inhibition concentration) value of 11 nM. The *in vitro* antimalarial activity against *Pf.* 3D7 of compounds **2**, **3**, **13**, **15**, **16**, and **18** was indicated by IC$_{50}$ values (nM) of 6, 15, 133, 79, 84, and 223 (Figure 4). The other compounds did not show activity against *Pf.* 3D7.

## 4 Discussion

Artemisinin is an unusual sesquiterpene lactone possessing an endoperoxide moiety. The sesquiterpene lactone endoperoxide structure of artemisinin is the pharmacophore characteristic element. The partial resistance of artemisinin refers to a delay in the clearance of malaria parasites from the bloodstream following treatment with ACT. This class of compounds with parent nucleus structures is characterized by a relatively complex metabolic process *in vivo*, which was considered to be partly responsible for the drug resistance phenomenon by some perspectives. Exploring the associated hydroxylation derivatives, especially hydroxylation, which is highly similar to the *in vivo* disposal process of artemisinin, is an effective approach to discover novel agents with higher activities.

Structural modification of artemisinin to improve its solubility, stability, and bioavailability has been a research "hotspot" in medicinal chemistry since its discovery. In recent years, the need for novel antimalarial drugs to prevent unpredictable drug tolerance has been urgent. 10-Deoxyartemisinin was first synthesized by Jung in 1989, and it was shown to be more stable in gastric acid and more efficacious than artemisinin. The synthesis of 10-deoxyartemisinin has been previously examined in detail, and in this work the reaction conditions were optimized, including temperature, duration, and solvent. As a result, a direct one-step reduction of the carbonyl function of artemisinin into 10-deoxyartemisinin was successfully achieved by NaBH$_4$ in the presence of BF$_3$/Et$_2$O, with a yield of 50%. Moreover, 9-ene-10-deoxyartemisinin was isolated as a by-product, and it demonstrated similar antimalarial activity to that of artemisinin. Subsequently, 10-deoxyartemisinin was chosen as the substrate for microbial transformation.

*Cunninghamella* species are commonly used models for microbial transformation. Numerous research studies have confirmed that *Cunninghamella* functioned with outstanding hydroxylation ability, which was responsible for the cytochrome P450 activity of fungus (Wang et al., 2000; Asha and Vidyavathi, 2009). In addition, some

research studies found that the cytochrome P450 in *Cunninghamella* species belongs to the CYP5I family, and the role of these enzymes was confirmed as the function of CYP3A4 enzyme in mammal metabolism (Dube et al., 2016). Thus, *Cunninghamella* was also employed to transform xenobiotics for the simulation of phase I (oxidative) and phase II (conjugative) metabolism (Zhang et al., 1996). In this work, two strains were chosen based on our previous study on the biotransformation of artemisinin (Ma et al., 2019) and dihydroartemisinin (unpublished data). The activity evaluation of the microbial transformation products showed that the antimalarial activity of the C-5 hydroxylated product was better than others. Though metabolites **13** and **18** were both hydroxylated products at the C-7 position, the antimalarial activity of the β-OH product exhibited two times better efficiency than the α-OH product. Unfortunately, hydroxylated products at C-5, C-6, and C-7 positions of 10-deoxyartemisinin led to attenuated antimalarial activities. Nevertheless, hydroxylation could improve the solubility of the compound, while also providing the possibility for further functionalization. Derivatives with a reduced peroxide bridge exhibited negligible antimalarial activity, a finding that is in accordance with previous reports (O'Neill et al., 2010). The synergistic effect of these products on malarial treatment and other bioactivities needs to be further studied.

## 5 Conclusion

In summary, seventeen artemisinin derivatives, including seven novel compounds (**4–10**) and ten known compounds, were isolated and identified through combined chemical and biological transformation. This protocol provided a highly efficient and divergent translation strategy for artemisinin. The pharmacological activities of the generated products were evaluated, and some derivatives displayed good antimalarial activity, which inspired us to conduct a comprehensive druggability study. The novel products with divergent structural moieties provided promising candidates for further bio-evaluation and drug development.

## Data availability statement

The data presented in the study are deposited in the article/Supplementary Material. The crystallographic data presented in the study are deposited in www.ccdc.cam.ac.uk/, accession numbers CCDC 2218207 (M4), 2218208 (M5), 2218214 (M9), 2218210 (10), 2218211 (14), 2218212 (M16), 2218213 (M18).

## Author contributions

Conceptualization and methodology: YM; investigation and original draft preparation: XG and YB; data analysis: DZ; software: YZ; writing—review: PS and HG; and funding acquisition: LY. All authors read and agreed to the published version of the manuscript.

## Funding

## Conflict of interest

The authors declare that the research was conducted in the
absence of any commercial or financial relationships that could be
construed as a potential conflict of interest.

## Publisher's note

All claims expressed in this article are solely those of the authors
and do not necessarily represent those of their affiliated organizations,
or those of the publisher, the editors, and the reviewers. Any product
that may be evaluated in this article, or claim that may be made by its
manufacturer, is not guaranteed or endorsed by the publisher.

## Supplementary material

The Supplementary Material for this article can be found online at:
https://www.frontiersin.org/articles/10.3389/fchem.2022.1089290/
full#supplementary-material

## References

Asha, S., and Vidyavathi, M. (2009). *Cunninghamella*-a microbial model for drug metabolism studies-a review. *Biotechnol. Adv.* 27 (1), 16–29. doi:10.1016/j.biotechadv.2008.07.005

Bai, Y., Zhang, D., Sun, P., Zhao, Y. F., Chang, X. Q., Ma, Y., et al. (2019). Evaluation of microbial transformation of 10-Deoxyartemisinin by UPLC-ESI-Q-TOF-MS^E. *Molecules* 24 (21), 3874. doi:10.3390/molecules24213874

Bai, Y., Zhao, Y. F., Gao, X. N., Zhang, D., Ma, Y., Yang, L., et al. (2021). A novel antimalarial metabolite in erythrocyte from the hydroxylation of dihydroartemisinin by *Cunninghamella elegans*. *Front. Chem.* 10, 850133. doi:10.3389/fchem.2022.850133

Cao, H., Chen, X., Jassbi, A. R., Xiao, J., and Kumar, M. S. (2015). Microbial biotransformation of bioactive flavonoids Biotransformation of bromhexine by Cunninghamella elegans, C. echinulata and C. blakesleeana. *Biotechnol. Adv.Braz. J. Microbiol.* 3348 (12), 214259–223267. doi:10.1016/j.bjm.2016.11.003

Dube, A. K., and Kumar, M. S. (2016). Biotransformation of bromhexine by *Cunninghamella elegans, C. echinulata* and *C. blakesleeana*. *Braz. J. Microbiol.* 48 (2), 259–267. doi:10.1016/j.bjm.2016.11.003

Gaur, R., Patel, S., Verma, R. K., Mathur, A., and Bhakuni, R. S. (2014). Biotransformation of Artemisinin derivatives by *glycyrrhiza glabra, lavandula officinalis*, and *panax quinquefolium*. *Med. Chem. Res.* 23, 1202–1206. doi:10.1007/s00044-013-0726-x

Goswami, A., Saikia, P., Barua, N., Bordoloi, M., Yadav, A., Bora, T., et al. (2010). Biotransformation of artemisinin using soil microbe: Direct C-acetoxylation of artemisinin at C-9 by *Penicillium simplissimum*. *Bioorg. Med. Chem. Lett.* 20, 359–361. doi:10.1016/j.bmcl.2009.10.097

Jung, M., Li, X., Bustos, D. A., ElSohly, H. N., McChesney, J. D., and Milhous, W. K. (1990). Synthesis and antimalarial activity of (+)- Deoxoartemisinin. *J. Med. Chem.* 33, 1516–1518. doi:10.1021/jm00167a036

Khalifa, S. I., Baker, J. K., Jung, M., Mcchesney, J. D., and Hufford, C. D. (1995). Microbial and mammalian metabolism studies on the semisynthetic antimalarial, Deoxoartemisinin. *Pharm. Res.* 12, 1493–1498. doi:10.1023/a:1016239505506

Lee, I. S., Elsohly, H. N., and Hufford, C. D. (1990). Microbial metabolism studies of the antimalarial drug arteether. *Pharm. Res.* 7, 199–203. doi:10.1023/a:1015845306124

Liu, J. H., Chen, Y. G., Yu, B. Y., and Chen, Y. J. (2006). A novel ketone derivative of Artemisinin biotransformed by *Streptomyces griseus* ATCC 13273. *Bioorg. Med. Chem. Lett.* 16, 1909–1912. doi:10.1016/j.bmcl.2005.12.076

Luo, J., Mobley, R., Woodfine, S., Drijfhout, F., Horrocks, P., Ren, X. D., et al. (2022). Biotransformation of Artemisinin to a novel derivative via ring rearrangement by *Aspergillus niger*. *Appl. Microbiol. Biot.* 106 (7), 2433–2444. doi:10.1007/s00253-022-11888-0

Ma, Y., Sun, P., Zhao, Y., Wang, K., Chang, X., Bai, Y., et al. (2019). A microbial transformation model for simulating mammal metabolism of artemisinin. *Molecules* 24 (2), 315. doi:10.3390/molecules24020315

Medeiros, S. F., Avery, M. A., Avery, B., Leite, S., and Williamson, J. S. (2002). Biotransformation of 10-deoxoartemisinin to its 7β-hydroxy derivative by *Mucor ramannianus*. *Biotechnol. Lett.* 24, 937–941. doi:10.1023/A:1015516929682

O'Neill, P., Barton, V., and Ward, S. (2010). The molecular mechanism of action of artemisinin-the debate continues. *Molecules* 15, 1705–1721. doi:10.3390/molecules15031705

Parshikov, I. A., Muraleedharan, K. M., Avery, M. A., and Williamson, J. S. (2004a). Transformation of artemisinin by *Cunninghamella elegans*. *Appl. Microbiol. Biot.* 64 (6), 782–786. doi:10.1007/s00253-003-1524-z

Parshikov, I. A., Muraleedharan, K. M., Miriyala, B., Avery, M. A., and Williamson, J. S. (2004b). Hydroxylation of 10-deoxoartemisinin by *Cunninghamella elegans*. *Nat. Prod.* 67, 1595–1597. doi:10.1021/np040089c

Ponnapalli, M. G., Suea, M. B., Sudhakar, R., Govindarajalu, G., and Sijwali, P. S. (2018). Biotransformation of artemisinin to 14-hydroxydeoxyartemisinin: C-14 hydroxylation by *Aspergillus flavus*. *J. Agric. Food. Chem.* 66 (40), 10490–10495. doi:10.1021/acs.jafc.8b03573

Tu, Y. Y., Ni, M. Y., Zhong, Y. R., Li, L. N., Cui, S. L., Zhang, M. Q., et al. (1981). Studies on the constituents of *Artemisia annua* L. *Acta. Pharm. Sin. B* 16 (5), 366. doi:10.16438/j.0513-4870.1981.05.008

Uwimana, A., Legrand, E., Stokes, B. H., Ndikumana, J. L. M., Warsame, M., Umulisa, N., et al. (2020). Emergence and clonal expansion of *in vitro* Artemisinin-resistant *Plasmodium falciparum* kelch13 R561H mutant parasites in Rwanda. *Nat. Med.* 26 (10), 1602–1608. doi:10.1038/s41591-020-1005-2

Wang, J. G., Xu, C., Liao, F. L., Jiang, T., Krishna, S., and Tu, Y. (2019). A temporizing solution to "artemisinin resistance. *New. Engl. J. Med.* 380 (22), 2087–2089. doi:10.1056/NEJMp1901233

Wang, R., Cao, W., Khan, A., Khan, A., and Cerniglia, C. (2000). Cloning, sequencing, and expression in *Escherichia coli* of a cytochrome P450 gene from *Cunninghamella elegans*. *Fems. Microbiol. Lett.* 188, 55–61. doi:10.1111/j.1574-6968.2000.tb09168.x

World Health Organization (2021). *World malaria report 2021*, Available at: https://apps.who.int/iris/handle/10665/350147.

Xie, X. T., Zheng, P., Zhang, G. Y., and Yang, M. (2001). Isolation and identification of new components in mother liquor of synthetic Dihydroartemisinin methyl ether. *Chin. Traditional Herb. Drugs* 32, 388.

Zhang, D., Yang, Y., Leakey, J., and Cerniglia, C. (1996). Phase I and phase II enzymes produced by *Cunninghamella elegans* for the metabolism of xenobiotics. *Fems. Microbiol. Lett.* 138, 221–226. doi:10.1111/j.1574-6968.1996.tb08161.x

Zhao, Y., Sun, P., Ma, Y., Chang, X., Chen, X., Ji, X., et al. (2021). Metabolite profiling of dihydroartemisinin in blood of plasmodium-infected and healthy mice using UPLC-Q-TOF-MS^E. *Front. Pharmacol.* 11, 614159. doi:10.3389/fphar.2020.614159

# Recent updates in click and computational chemistry for drug discovery and development

Jiang Hong Cai[1†], Xuan Zhe Zhu[1†], Peng Yue Guo[2], Peter Rose[3], Xiao Tong Liu[1], Xia Liu[2] and Yi Zhun Zhu[1,4]*

[1]State Key Laboratory of Quality Research in Chinese Medicine, School of Pharmacy, Macau University of Science and Technology, Taipa, Macau, China, [2]Department of Clinical Pharmacy, School of Pharmacy, Second Military University, Shanghai, China, [3]School of Biosciences, University of Nottingham, Nottingham, United Kingdom, [4]Shanghai Key Laboratory of Bioactive Small Molecules, Department of Pharmacology, School of Pharmacy, Fudan University, Shanghai, China

Drug discovery is a costly and time-consuming process with a very high failure rate. Recently, click chemistry and computer-aided drug design (CADD) represent popular areas for new drug development. Herein, we summarized the recent updates in click and computational chemistry for drug discovery and development including clicking to effectively synthesize druggable candidates, synthesis and modification of natural products, targeted delivery systems, and computer-aided drug discovery for target identification, seeking out and optimizing lead compounds, ADMET prediction as well as compounds synthesis, hopefully, inspires new ideas for novel drug development in the future.

KEYWORDS

click chemistry, computational chemistry, CADD, druggable candidates, drug development

## Introduction

Click chemistry, an efficient chemo-selective synthesis method for coupling molecular fragments under mild reaction conditions, mainly includes Cu-catalyzed azide-alkyne cycloaddition reaction (CuAAC), strain-promoted azide-alkyne cycloaddition reaction (SPAAC), thiol-ene reaction, inverse electron demand Diels–Alder reaction (IEDDA), hydrazone click chemistry and the newly emerging sulfur fluoride exchange (SuFEx) reaction, has been a hot research topic in the field of chemistry since it was first reported in 2001 (Zhang et al., 2021a; Ashe, 2022). Computer-aided drug design (CADD) has attracted a lot of attention for its potential to accelerate and reduce the cost of the drug development process (Wu et al., 2020). In addition, natural products provide a variety of lead compounds and novel drugs, are worthy of further development. Furthermore, early and late-stage development of new drugs may be slowed down by problems such as poor target selectivity or side effects, toxicity, resistance, inappropriate physicochemical and pharmacokinetic properties. Therefore, we summarized the recent applications of click and computational chemistry in drug development such as click to effectively synthesize druggable candidates, synthesis and modification of natural products, targeted delivery systems including hydrogels, nanoparticles (NPs), carbon nanotubes (CNT), etc, and computer-aided drug discovery including molecular docking and molecular dynamics to identify target, virtual screening (VS.) and pharmacophore to found and optimize lead compounds, ADMET prediction as well as compounds synthesis, which are making a splash in new drug development, hopefully, providing new insights for the discovery of new drug from click and computational chemistry.

GRAPHICAL ABSTRACT
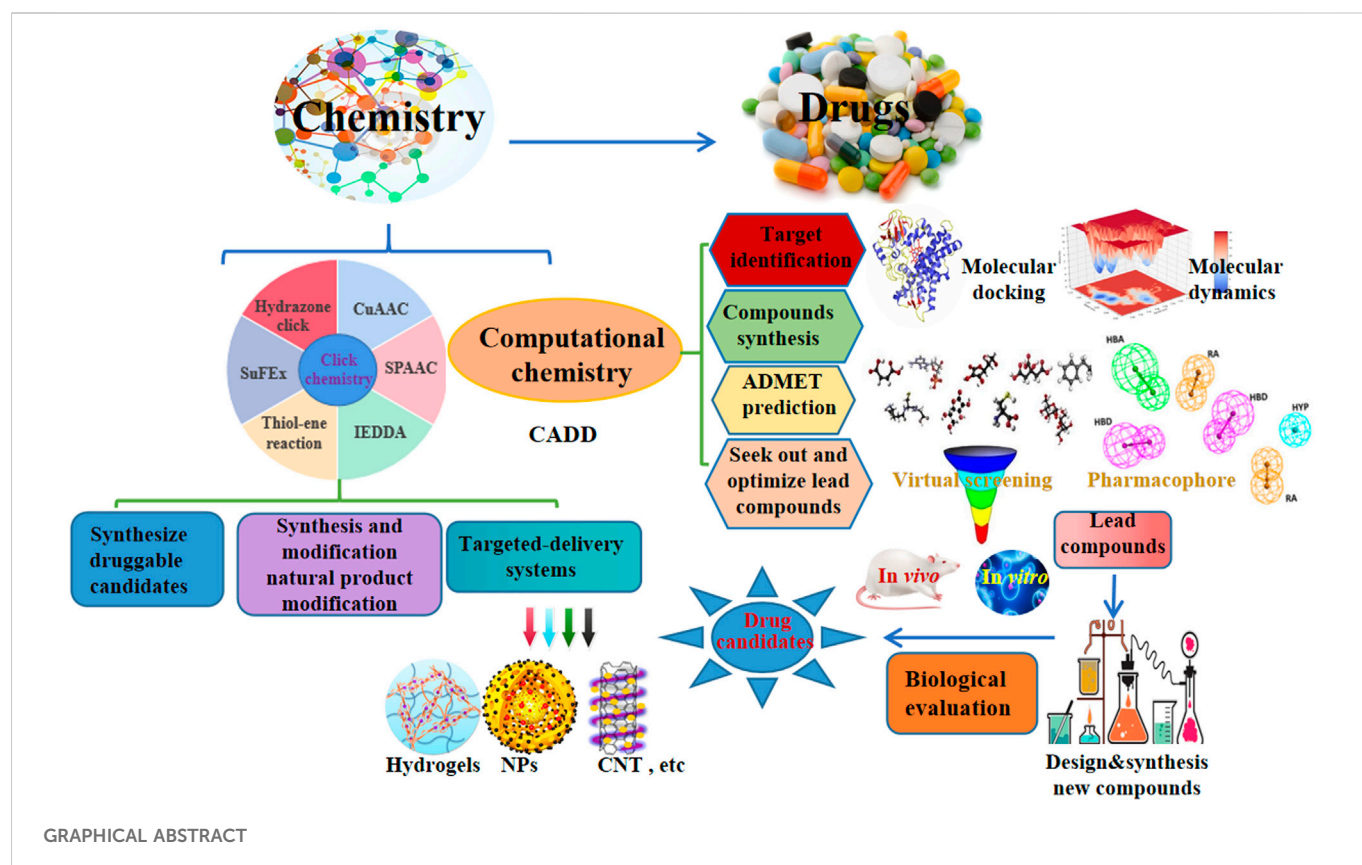
# Click chemistry

## Click to efficiently synthesize druggable candidates

The transformation of the active compound skeleton is a magic weapon for researchers to break through patent restrictions and improve the activity of compounds in the development of new drugs. Copper-catalyzed 1,3-dipolar cycloaddition (CuAAC) to form 1,2,3-triazoles is the most popular reaction in click chemistry. Recently, 1,2,3-triazole backbones with hydrogen bonds, moderate dipole moments and enhanced water solubility had been widely used to generate drug candidates of anti-tumor (Brown et al., 2022; Elganzory et al., 2022; Mohammed et al., 2022; Oekchuae et al., 2022; Oliveira et al., 2022; Mironov et al., 2023), anti-seizure (Bhattacherjee et al., 2022), anti-diabetic (Dhameja et al., 2022), anti-parasitic (Aljohani et al., 2022), anti-bacterial (Daher et al., 2022; Mokariya et al., 2022; Nsira et al., 2022) and anti-viral (Kutkat et al., 2022; Tatarinov et al., 2022) via CuAAC click chemistry (Figure 1A).

## Synthesis and modification of natural products

Natural products have provide abundant resources for drug discovery. Recently, click chemistry had been adopted for synthesis and modification of natural products, for instances, SPAAC was used to modularly generate Bcl-xL inhibitor (Brauer et al., 2022), adjust PEG chain length and targeting moiety to further improve half-life as

well as targeting IL-4 to arthritic joint (Figure 1B) (Spieler et al., 2020). It was reported that poly (globalide-co-ε-caprolactone) could be functionalized with N-acetylcysteine side chains via thiol-ene reaction (Guindani et al., 2019). Furthermore, IEDDA could be used to introduce aromatic heterocycles (Figure 1C) (Xu et al., 2020) and triazines (Zhang et al., 2021b). Similarly, the synthetic efficiency of biosynthesis of anti-fungal drug candidate Ilicicolin H increased $3 \times 10^5$ times via IEDDA (Figure 1D) (Zhang et al., 2019). Moreover, 5-fluorouracil-coumarin conjugation (Figure 1E) as anti-cancer drug candidate (ópez et al., 2022) and pH responsive doxorubicin delivery polymers nano-particles (Wallat et al., 2018) for treatment of breast and ovarian cancer were generated by modification of natural products via CuAAC. In addition, quercetin-gold quantum dots for adenocarcinoma treatment (Pansare et al., 2022) and chondroitin sulfate-multiarmed PEG hydrogels for skin tissue engineering (Sousa et al., 2022) had been developed by modification of natural products (Figure 1F).

## Targeted delivery systems

Existing drugs may have dis-advantages such as low selectivity, long synthetic routes, poor stability and side effects, thence the development of targeted delivery systems make great sense. Recently click-generated hydrogels had broad applications in the fields of anti-tumor (Ali et al., 2022; Bonardd et al., 2022), wound repair (Basurto et al., 2022) and long term regeneration therapy (Jang et al., 2021) via IEDDA, CuAAC,thiol-ene reaction, and SuFEx, respectively. Biomimetic stiffening of cell-laden hydrogels via sequential thiol-ene and hydrazone click reactions (Chang et al.,
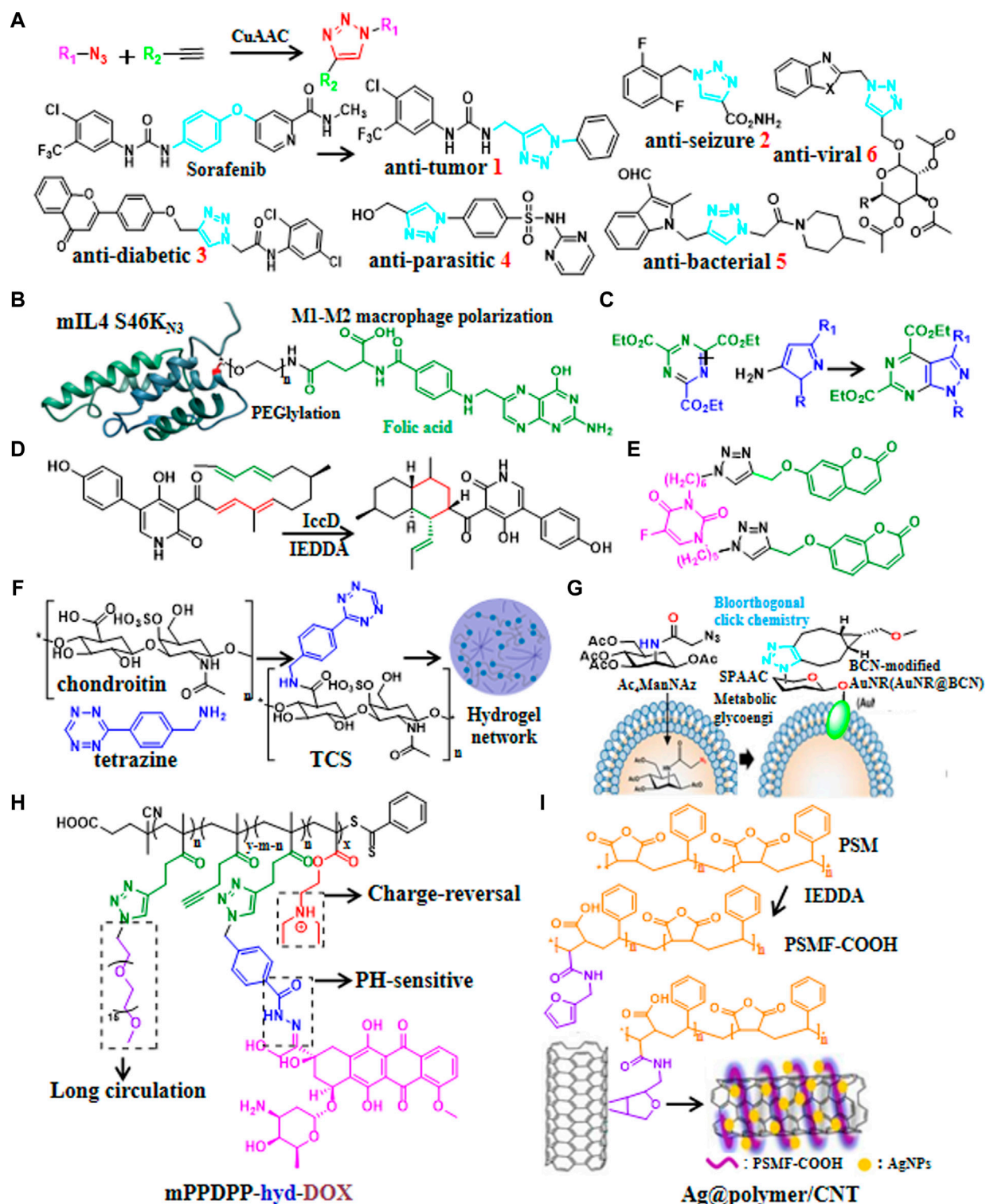
**FIGURE 1**
Recent updates in click chemistry for drug discovery and development. **(A)** Reaction formula of CuAAC and some recent applications of CuAAC for developing drug candidates containing 1,2,3-triazoles ring. **(B)** An example of natural product modification to improve half-life and target IL-4 to arthritic joint via SPAAC. **(C)** An example of introduction aromatic heterocycles via IEDDA. **(D)** An example of efficient synthesis of natural products via IEDDA. **(E)** An example of the generation of anti-cancer drug candidate by modification of the natural product coumarin via CuAAC. **(F)** Catalyst-free click chemistry to generate chondroitin sulfate-multiarmed PEG hydrogels for skin tissue engineering. **(G)** An example of the generation of MSCs-mediated deep tumor delivery of gold nanorod for anti-tumor therapy via SPAAC. **(H)** An example of polymer nanomicelle platform for cancer treatment via CuAAC. **(I)** An example of the generation of silver nanoparticle-supported polymer-encapsulated carbon nanotubes (CNTs) via IEDDA for nonenzymatic glucose sensing and antimicrobial activity applications.
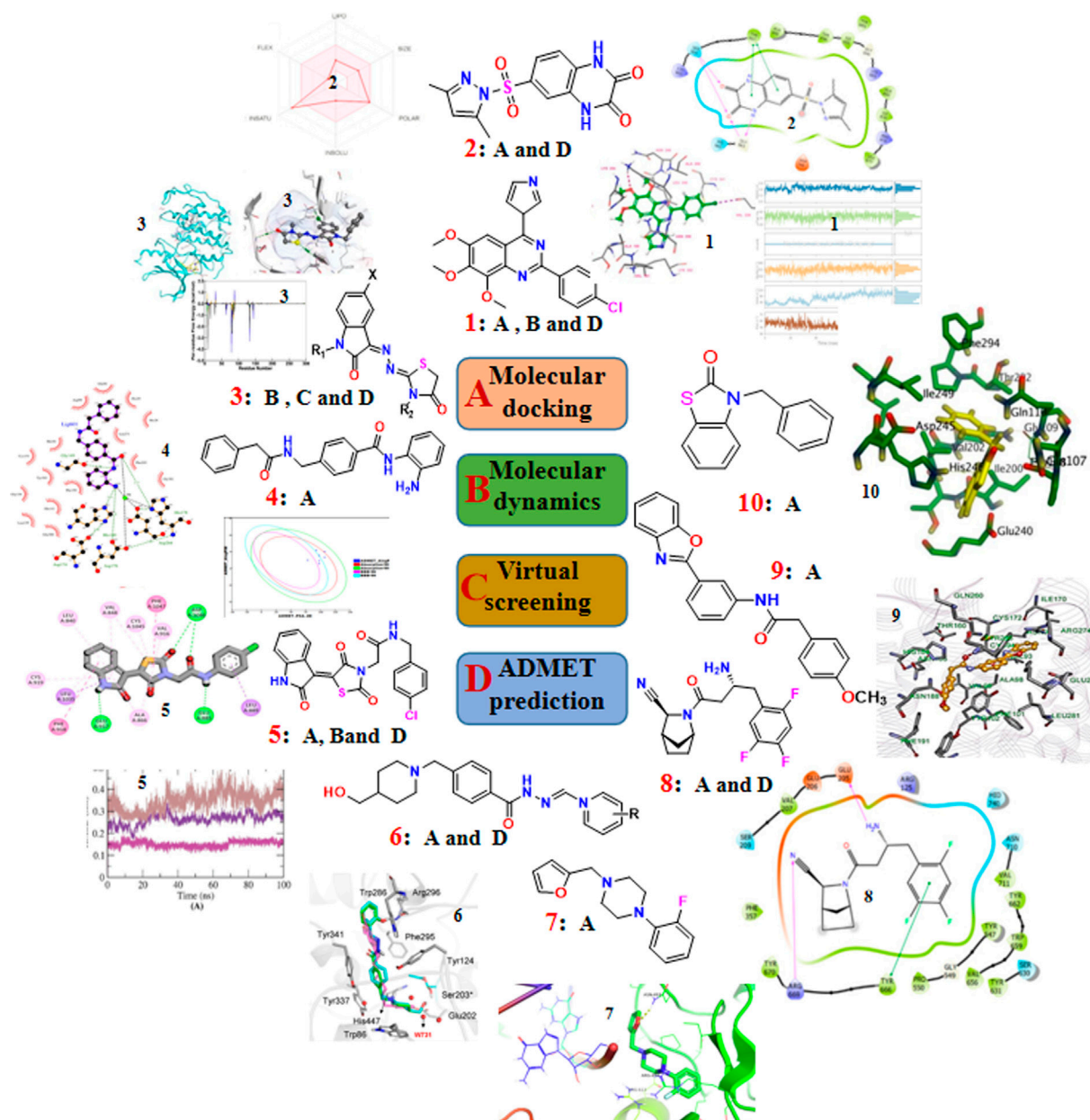
**FIGURE 2**
The recent updates of computational chemistry in target identification, lead compound discovery and ADMET prediction for drug development.

2021). Furthermore, nanoscale covalent organic frameworks (COFs) (Guan et al., 2022), Nisin-shelled nanoemulsion (Hashad et al., 2022), and MSCs-mediated deep tumor delivery of gold nanorod (Figure 1G) (Yun et al., 2022) had been synthesized for anti-tumor therapy *via* thiol-ene reactions, SPAAC, and SPAAC, respectively. Moreover, pH-sensitive polysaccharide-gold nanorod conjugate (Hou et al., 2019) and polymer nanomicelle platform (Figure 1H) (Liao et al., 2021) were reported to treat cancers *via* hydrazone click reaction and CuAAC, respectively. In addition, silver nanoparticle-supported polymer-wrapped carbon nanotubes (CNT) (Cao et al., 2022) for non-enzymatic glucose sensing and antimicrobial applications (Figure 1I), COF-based nanoreactors for click-activated pro-drug delivery and precise anti-vascular therapy (Wang et al., 2022) had been synthesized *via* IEDDA, these click chemistry-based targeting strategies may find widespread application in drug delivery in the future.

# Computational chemistry in drug discovery

To effectively and efficiently design and develop new drugs, computational methods had been applied for drug design including target identification, seeking out and optimizing lead compounds prediction of pharmacokinetic and toxicological properties as well as compound synthesis by molecular docking and molecular dynamics, virtual screening, pharmacophore and ADMET prediction. Novel quinazoline derivative **1** as tubulin

polymerization inhibitor (Dwivedi et al., 2022), PARP-1 inhibitor **2** (Syam et al., 2022), CDK2 inhibitor **3** (Qayed et al., 2022), HDAC-1-3 inhibitor **4** (Cheshmazar et al., 2022), VEGFR-2 inhibitor **5** (Taghour et al., 2022) were identified for cancer therapies. Furthermore, AChE inhibitor **6** (Macedo Vaz et al., 2022) for treatment of Alzheimer's disease and Mtb RNAP inhibitor **7** (Mekonnen Sanka et al., 2022) for antitubercular and antimicrobial treatment were deserve further study. Moreover, a lead compound **8** of DDP4 inhibitor (Maslov et al., 2022) and acetamide derivative **9** (Zhou et al., 2022) as P2Y14R antagonist were considered as drug candidates for treating type 2 diabetes and gout, respectively. Additionally, potential SARS-CoV-2 main protease inhibitor **10** (Dong et al., 2023) and carbazole alkaloids from Murraya koenigii (Wadanambi et al., 2023) were identified as a promising drug candidates for inhibiting coronavirus infection. Surprisingly, it had been reported a computationally guided asymmetric total synthesis of resveratrol dimers, which possessed a wide range of biological activities such as antioxidant, anti-tumor and cardiovascular activities (Nakajima et al., 2022), suggesting that computationally guided organic synthesis may be a powerful strategy to advance the chemistry of natural products (Figure 2).

## Conclusion and prospects

In the review, we summarized recent updates in click chemistry for drug discovery and development, including chemical click synthesis of druggable candidates, synthesis and modification of natural products, targeted delivery systems. In addition, we introduced updated computational chemistry in drug discovery for target identification, discovery and optimization of lead compounds, compounds synthesis and prediction of pharmacokinetic and toxicological properties. Click chemistry is a very powerful tool in drug discovery, in which the synthesis of 1,2,3-triazole ring as a pharmacophore, bioisostere *via* CuAAC has great potential in the drug design for a variety of diseases, however, 1,2,3-triazole ring itself is not a commonly used pharmacophore, and it is rare in marketed drugs, indicating that the use of 1,2,3-triazole as drug molecules still has certain limitations. Furthermore, the CuAAC reaction introduces copper species into biological systems and organisms, leading to potential toxicity issues while many Cu chelation sites may inhibit catalyst activity. Moreover, Copper-free cycloaddition SPAAC reaction and IEDDA reaction have their own issues: for example, they are susceptible to side reactions with nucleophilic residues (e.g., thiol residues in glutathione), and the reactive (electrophilic) nature of the requisite cyclic alkynes/alkenes may result in poor regiospecificity. Although computer molecular docking and molecular dynamics have important applications for target identification, however, the protein used for molecular

docking may have a huge unknown difference from the protein in the pathological state due to site mutation. Additionally, computational chemistry needs to be combined with more biological activity test and mechanism exploration. In a word, although click and computational chemistry have shortcomings, which still hold a great and unnegligible potential for drug discovery and development, hopefully, this review can stimulate new ideas for the development of drugs with high selectivity, low toxicity, good stability and their clinical application in the near future.

## Author contributions

JC and XZ: Writing-original draft. XL and YZ: proof-reading and editing. XTL and others: data collection, the article was approved for submission by all authors.

## Funding

## Acknowledgments

## Conflict of interest

The authors declared that the research was conducted in the absence of any commercial or financial relationships that could be construed as a potential conflict of interest.

## Publisher's note

All claims expressed in this article are solely those of the authors and do not necessarily represent those of their affiliated organizations, or those of the publisher, the editors and the reviewers. Any product that may be evaluated in this article, or claim that may be made by its manufacturer, is not guaranteed or endorsed by the publisher.

## References

Ali, I., Gulfam, M., Jo, S. H., Seo, J. W., Rizwan, A., Park, S. H., et al. (2022). Reduction-responsive and bioorthogonal carboxymethyl cellulose based soft hydrogels cross-linked via IEDDA click chemistry for cancer therapy application. *Int. J. Biol. Macromol.* 219, 109–120. doi:10.1016/j.ijbiomac.2022.07.229

Aljohani, F. S., Rezki, N., Aouad, M. R., Elwakil, B. H., Hagar, M., Sheta, E., et al. (2022). Synthesis, characterization and nanoformulation of novel sulfonamide-1,2,3-triazole molecular conjugates as potent antiparasitic agents. *Int. J. Mol. Sci.* 23 (8), 4241. doi:10.3390/ijms23084241

Ashe, K. (2022). Chemistry just a click away. *Nat. Chem.* 14 (12), 1341. doi:10.1038/s41557-022-01108-7

Basurto, I. M., Passipieri, J. A., Gardner, G. M., Smith, K. K., Amacher, A. R., Hansrisuk, A. I., et al. (2022). Photoreactive hydrogel stiffness influences volumetric muscle loss repair. *Tissue Eng. Part A* 28 (7-8), 312–329. doi:10.1089/ten.TEA.2021.0137

Bhattacherjee, D., Kovalev, I. S., Kopchuk, D. S., Rahman, M., Santra, S., Zyryanov, G. V., et al. (2022). Mechanochemical approach towards multi-functionalized 1,2,3-triazoles and

anti-seizure drug rufinamide analogs using copper beads. *Molecules* 27 (22), 7784. doi:10.3390/molecules27227784

Bonardd, S., Maiti, B., Grijalvo, S., Rodriguez, J., Enshaei, H., Kortaberria, G., et al. (2022). Biomass-derived isosorbide-based thermoresponsive hydrogel for drug delivery. *Soft Matter* 18 (26), 4963–4972. doi:10.1039/d2sm00623e

Brauer, J., Mötzing, M., Gröst, C., Hoffmann, R., and Berg, T. (2022). Templated generation of a bcl-xL inhibitor by isomer-free SPAAC based on azacyclonon-5-yne. *Chemistry* 28 (66), e202202259. doi:10.1002/chem.202202259

Brown, T., Cao, M., and Zheng, Y. G. (2022). Synthesis and activity of triazole-adenosine analogs as protein arginine methyltransferase 5 inhibitors. *Molecules* 27 (12), 3779. doi:10.3390/molecules27123779

Cao, X. T., Ngan Tran, T. Q., Ngo, D. H., Tai, D. C., and Kumar, S. (2022). Click-chemistry-mediated synthesis of silver nanoparticle-supported polymer-wrapped carbon nanotubes: Glucose sensor and antibacterial material. *ACS Omega* 7 (42), 37095–37102. doi:10.1021/acsomega.2c02832

Chang, C. Y., Johnson, H. C., Babb, O., Fishel, M. L., and Lin, C. C. (2021). Biomimetic stiffening of cell-laden hydrogels via sequential thiol-ene and hydrazone click reactions. *Acta Biomater.* 130, 161–171. doi:10.1016/j.actbio.2021.05.054

Cheshmazar, N., Hemmati, S., Hamzeh-Mivehroud, M., Sokouti, B., Zessin, M., Schutkowski, M., et al. (2022). Development of new inhibitors of HDAC1-3 enzymes aided by in silico design strategies. *J. Chem. Inf. Model* 62 (10), 2387–2397. doi:10.1021/acs.jcim.1c01557

Daher, S. S., Lee, M., Jin, X., Teijaro, C. N., Barnett, P. R., Freundlich, J. S., et al. (2022). Alternative approaches utilizing click chemistry to develop next-generation analogs of solithromycin. *Eur. J. Med. Chem.* 233, 114213. doi:10.1016/j.ejmech.2022.114213

Dhameja, M., Kumar, H., Kurella, S., Uma, A., and Gupta, P. (2022). Flavone-1,2,3-triazole derivatives as potential α-glucosidase inhibitors: Synthesis, enzyme inhibition, kinetic analysis and molecular docking study. *Bioorg Chem.* 127, 106028. doi:10.1016/j.bioorg.2022.106028

Dong, J., Varbanov, M., Philippot, S., Vreken, F., Zeng, W. B., and Blay, V. (2023). Ligand-based discovery of coronavirus main protease inhibitors using MACAW molecular embeddings. *J. Enzyme Inhib. Med. Chem.* 38 (1), 24–35. doi:10.1080/14756366.2022.2132486

Dwivedi, A. R., Rawat, S. S., Kumar, V., Kumar, N., Anand, P., Yadav, R. P., et al. (2022). Synthesis and screening of novel 4-N-heterocyclic-2-aryl-6,7,8-trimethoxyquinazolines as antiproliferative and tubulin polymerization inhibitors. *Bioorg Med. Chem.* 72, 116976. doi:10.1016/j.bmc.2022.116976

Elganzory, H. H., Alminderej, F. M., El-Bayaa, M. N., Awad, H. M., Nossier, E. S., and El-Sayed, W. A. (2022). Design, synthesis, anticancer activity and molecular docking of new 1,2,3-triazole-based glycosides bearing 1,3,4-thiadiazolyl, indolyl and arylacetamide scaffolds. *Molecules* 27 (20), 6960. doi:10.3390/molecules27206960

Guan, Q., Zhou, L. L., Zhou, W., and Dong, Y. B. (2022). A vinyl-decorated covalent organic framework for ferroptotic cancer therapy via visible-light-triggered cysteine depletion. *J. Mater Chem. B* 10 (43), 8894–8909. doi:10.1039/d2tb01815b

Guindani, C., Dozoretz, P., Araújo, P. H. H., Ferreira, S. R. S., and de Oliveira, D. (2019). N-acetylcysteine side-chain functionalization of poly(globalide-co-ε-caprolactone) through thiol-ene reaction. *Mater Sci. Eng. C Mater Biol. Appl.* 94, 477–483. doi:10.1016/j.msec.2018.09.060

Hashad, R. A., Singla, R., Kaur Bhangu, S., Jap, E., Zhu, H., Peleg, A. Y., et al. (2022). Chemoenzymatic surface decoration of Nisin-shelled nanoemulsions: Novel targeted drug-nanocarriers for cancer applications. *Ultrason. Sonochem* 90, 106183. doi:10.1016/j.ultsonch.2022.106183

Hou, G., Qian, J., Xu, W., Sun, T., Wang, Y., Wang, J., et al. (2019). A novel pH-sensitive targeting polysaccharide-gold nanorod conjugate for combined photothermal-chemotherapy of breast cancer. *Carbohydr. Polym.* 212, 334–344. doi:10.1016/j.carbpol.2019.02.045

Jang, K. J., Lee, W. S., Park, S., Han, J., Kim, J. E., Kim, B. M., et al. (2021). Sulfur(VI) fluoride exchange (SuFEx)-Mediated synthesis of the chitosan-PEG conjugate and its supramolecular hydrogels for protein delivery. *Nanomater. (Basel)* 11 (2), 318. doi:10.3390/nano11020318

Kutkat, O., Kandeil, A., Moatasim, Y., Elshaier, Y. A. M. M., El-Sayed, W. A., Gaballah, S. T., et al. (2022). *In vitro* and *in vivo* antiviral studies of new heteroannulated 1,2,3-triazole glycosides targeting the neuraminidase of influenza A viruses. *Pharm. (Basel)* 15 (3), 351. doi:10.3390/ph15030351

Liao, J., Peng, H., Liu, C., Li, D., Yin, Y., Lu, B., et al. (2021). Dual pH-responsive-charge-reversal micelle platform for enhanced anticancer therapy. *Mater Sci. Eng. C Mater Biol. Appl.* 118, 111527. doi:10.1016/j.msec.2020.111527

Macedo Vaz, S., de Freitas Silva, M., Dos Reis Rosa Franco, G., Jorge R. Guimaraes, M., Motta R. da Silva, F., Goncalves Castro, N., et al. (2022). Synthesis and biological evaluation of 4-hydroxy-methylpiperidinyl-N-benzyl-acylarylhydrazone hybrids designed as novel multifunctional drug candidates for Alzheimer's disease. *Bioorg Med. Chem.* 71, 116952. doi:10.1016/j.bmc.2022.116952

Maslov, I. O., Zinevich, T. V., Kirichenko, O. G., Trukhan, M. V., Shorshnev, S. V., Tuaeva, N. O., et al. (2022). Design, synthesis and biological evaluation of neogliptin, a novel 2-azabicyclo[2.2.1]heptane-based inhibitor of dipeptidyl peptidase-4 (DPP-4). *Pharm. (Basel)* 15 (3), 273. doi:10.3390/ph15030273

Mekonnen Sanka, B., Mamo Tadesse, D., Teju Bedada, E., Mengesha, E. T., and Babu, G. N. (2022). Design, synthesis, biological screening and molecular docking studies of novel multifunctional 1,4-di (aryl/heteroaryl) substituted piperazine derivatives as potential antitubercular and antimicrobial agents. *Bioorg Chem.* 119, 105568. doi:10.1016/j.bioorg.2021.105568

Mironov, M. E., Rybalova, T. V., Pokrovskii, M. A., Emaminia, F., Gandalipov, E. R., Pokrovskii, A. J., et al. (2023). Synthesis of fully functionalized spirostanic 1,2,3-triazoles by the three component reaction of diosgenin azides with acetophenones and aryl aldehydes and their biological evaluation as antiproliferative agents. *Steroids* 190, 109133. doi:10.1016/j.steroids.2022.109133

Mohammed, H. H. H., Abd El-Hafeez, A. A., Ebeid, K., Mekkawy, A. I., Abourehab, M. A. S., Wafa, E. I., et al. (2022). New 1,2,3-triazole linked ciprofloxacin-chalcones induce DNA damage by inhibiting human topoisomerase I& II and tubulin polymerization. *J. Enzyme Inhib. Med. Chem.* 37 (1), 1346–1363. doi:10.1080/14756366.2022.2072308

Mokariya, J. A., Kalola, A. G., Prasad, P., and Patel, M. P. (2022). Simultaneous ultrasound- and microwave-assisted one-pot 'click' synthesis of 3-formyl-indole clubbed 1,2,3-triazole derivatives and their biological evaluation. *Mol. Divers* 26 (2), 963–979. doi:10.1007/s11030-021-10212-8

Nakajima, M., Adachi, Y., and Nemoto, T. (2022). Computation-guided asymmetric total syntheses of resveratrol dimers [published correction appears in Nat Commun. 2022 Apr 27;13(1):2418. *Nat. Commun.* 13 (1), 152. doi:10.1038/s41467-021-27546-4

Nsira, A., Mtiraoui, H., Chniti, S., Al-Ghulikah, H., Gharbi, R., and Msaddek, M. (2022). Regioselective one-pot synthesis, biological activity and molecular docking studies of novel conjugates N-(p-Aryltriazolyl)-1,5-benzodiazepin-2-ones as potent antibacterial and antifungal agents. *Molecules* 27 (13), 4015. doi:10.3390/molecules27134015

Oekchuae, S., Sirirak, J., Charoensuksai, P., Wongprayoon, P., Chuaypen, N., Boonsombat, J., et al. (2022). The design and synthesis of a new series of 1,2,3-triazole-cored structures tethering aryl urea and their highly selective cytotoxicity toward HepG2. *Pharm. (Basel)* 15 (5), 504. doi:10.3390/ph15050504

Oliveira, A., Moura, S., Pimentel, L., Neto, J., Dantas, R., Silva-Jr, F., et al. (2022). New imatinib derivatives with antiproliferative activity against A549 and K562 cancer cells. *Molecules* 27 (3), 750. doi:10.3390/molecules27030750

ópez, S., Gracia, I., Plaza-Pedroche, R., Rodriguez, J. F., Perez-Ortiz, J. M., Rodriguez-Lopez, J., et al. (2022). *In vitro* antioxidant and pancreatic anticancer activity of novel 5-fluorouracil-coumarin conjugates. *Pharmaceutics* 14 (10), 2152. doi:10.3390/pharmaceutics14102152

Pansare, A. V., Pansare, P. V., Shedge, A. A., Pansare, S. V., Patil, V. R., Terrasi, G. P., et al. (2022). Click gold quantum dots biosynthesis with conjugation of quercetin for adenocarcinoma exertion. *RSC Adv.* 12 (29), 18425–18430. doi:10.1039/d2ra02529a

Qayed, W. S., Hassan, M. A., El-Sayed, W. M., Rogério A Silva, J., and Aboul-Fadl, T. (2022). Novel azine linked hybrids of 2-indolinone and thiazolodinone scaffolds as CDK2 inhibitors with potential anticancer activity: *In silico* design, synthesis, biological, molecular dynamics and binding free energy studies. *Bioorg Chem.* 126, 105884. doi:10.1016/j.bioorg.2022.105884

Sousa, G. F., Afewerki, S., Dittz, D., Santos, F. E. P., Gontijo, D. O., Scalzo, S. R. A., et al. (2022). Catalyst-free click chemistry for engineering chondroitin sulfate-multiarmed PEG hydrogels for skin tissue engineering. *J. Funct. Biomater.* 13 (2), 45. doi:10.3390/jfb13020045

Spieler, V., Ludwig, M. G., Dawson, J., Tigani, B., Littlewood-Evans, A., Safina, C., et al. (2020). Targeting interleukin-4 to the arthritic joint. *J. Control Release* 326, 172–180. doi:10.1016/j.jconrel.2020.07.005

Syam, Y. M., Anwar, M. M., Abd El-Karim, S. S., Elokely, K. M., and Abdelwahed, S. H. (2022). New quinoxaline-based derivatives as PARP-1 inhibitors: Design, synthesis, antiproliferative, and computational studies. *Molecules* 27 (15), 4924. doi:10.3390/molecules27154924

Taghour, M. S., Elkady, H., Eldehna, W. M., El-Deeb, N., Kenawy, A. M., Elkaeed, E. B., et al. (2022). Design, synthesis, anti-proliferative evaluation, docking, and MD simulations studies of new thiazolidine-2,4-diones targeting VEGFR-2 and apoptosis pathway. *PLoS One* 17 (9), e0272362. doi:10.1371/journal.pone.0272362

Tatarinov, D. A., Garifullin, B. F., Belenok, M. G., Andreeva, O. V., Strobykina, I. Y., Shepelina, A. V., et al. (2022). The first 5'-phosphorylated 1,2,3-triazolyl nucleoside analogues with uracil and quinazoline-2,4-dione moieties: A synthesis and antiviral evaluation. *Molecules* 27 (19), 6214. doi:10.3390/molecules27196214

Wadanambi, P. M., Jayathilaka, N., and Seneviratne, K. N. (2023). A computational study of carbazole alkaloids from Murraya koenigii as potential SARS-CoV-2 main protease inhibitors. *Appl. Biochem. Biotechnol.* 195 (1), 573–596. doi:10.1007/s12010-022-04138-6

Wallat, J. D., Harrison, J. K., and Pokorski, J. K. (2018). pH responsive doxorubicin delivery by fluorous polymers for cancer treatment. *Mol. Pharm.* 15 (8), 2954–2962. doi:10.1021/acs.molpharmaceut.7b01046

Wang, P., Li, M., Zhou, F., Yang, Y., Yin, X., Zhang, X. B., et al. (2022). COF-based nanoreactors for click-activated prodrug delivery and precise anti-vascular therapy. *Chem. Commun. (Camb)* 58 (79), 11107–11110. doi:10.1039/d2cc03931a

Wu, F., Zhou, Y., Li, L., Shen, X., Chen, G., Wang, X., et al. (2020). Computational approaches in preclinical studies on drug discovery and development. *Front. Chem.* 8, 726. doi:10.3389/fchem.2020.00726

Xu, G., Bai, X., and Dang, Q. (2020). Aromatic heterocycles as productive dienophiles in the inverse electron-demand diels-alder reactions of 1,3,5-triazines. *Acc. Chem. Res.* 53 (4), 773–781. doi:10.1021/acs.accounts.9b00604

Yun, W. S., Shim, M. K., Lim, S., Song, S., Kim, J., Yang, S., et al. (2022). Mesenchymal stem cell-mediated deep tumor delivery of gold nanorod for photothermal therapy. *Nanomater. (Basel).* 12 (19), 3410. doi:10.3390/nano12193410

Zhang, F. G., Chen, Z., Tang, X., and Ma, J. A. (2021). Triazines: Syntheses and inverse electron-demand diels-alder reactions. *Chem. Rev.* 121 (23), 14555–14593. doi:10.1021/acs.chemrev.1c00611

Zhang, X., Zhang, S., Zhao, S., Wang, X., Liu, B., and Xu, H. (2021). Click chemistry in natural product modification. *Front. Chem.* 9, 774977. doi:10.3389/fchem.2021.774977

Zhang, Z., Jamieson, C. S., Zhao, Y. L., Li, D., Ohashi, M., Houk, K. N., et al. (2019). Enzyme-catalyzed inverse-electron demand diels–alder reaction in the biosynthesis of antifungal Ilicicolin H. *J. Am. Chem. Soc.* 141 (14), 5659–5663. doi:10.1021/jacs.9b02204

Zhou, M., Wang, W., Wang, Z., Wang, Y., Zhu, Y., Lin, Z., et al. (2022). Discovery and computational studies of 2-phenyl-benzoxazole acetamide derivatives as promising P2Y14R antagonists with anti-gout potential. *Eur. J. Med. Chem.* 227, 113933. doi:10.1016/j.ejmech.2021.113933

frontiers | Frontiers in Chemistry

*CORRESPONDENCE
Caijuan Zheng,
✉ caijuan2002@163.com

†These authors have contributed equally
to this work

# Toad venom-derived bufadienolides and their therapeutic application in prostate cancers: Current status and future directions

Qingmei Ye[1,2†], Xin Zhou[3†], Fangxuan Han[2] and Caijuan Zheng[1]*

[1]Key Laboratory of Tropical Medicinal Resource Chemistry of Ministry of Education, Key Laboratory of Tropical Medicinal Plant Chemistry of Hainan Province, College of Chemistry and Chemical Engineering, Hainan Normal University, Haikou, Hainan, China, [2]Hainan General Hospital & Hainan Affiliated Hospital of Hainan Medical University, Haikou, Hainan, China, [3]The Fifth People's Hospital of Hainan Province & Affiliated Dermatology Hospital of Hainan Medical University, Haikou, Hainan, China

Cancer is the second leading cause of death worldwide. Specially, the high incidence rate and prevalence of drug resistance have rendered prostate cancer (PCa) a great threat to men's health. Novel modalities with different structures or mechanisms are in urgent need to overcome these two challenges. Traditional Chinese medicine toad venom-derived agents (TVAs) have shown to possess versatile bioactivities in treating certain diseases including PCa. In this work, we attempted to have an overview of bufadienolides, the major bioactive components in TVAs, in the treatment of PCa in the past decade, including their derivatives developed by medicinal chemists to antagonize certain drawbacks of bufadienolides such as innate toxic effect to normal cells. Generally, bufadienolides can effectively induce apoptosis and suppress PCa cells in-vitro and in-vivo, majorly mediated by regulating certain microRNAs/long non-coding RNAs, or by modulating key pro-survival and pro-metastasis players in PCa. Importantly, critical obstacles and challenges using TVAs will be discussed and possible solutions and future perspectives will also be presented in this review. Further in-depth studies are clearly needed to decipher the mechanisms, e.g., targets and pathways, toxic effects and fully reveal their application. The information collected in this work may help evoke more effects in developing bufadienolides as therapeutic agents in PCa.

KEYWORDS

toad venom-derived bufadienolides, therapeutic application, prostate cancers, current status, future directions

## 1 Introduction

The quality of life of cancer patients have been improved significantly due to the progress of application of new technologies, including drug development, especially precision medicine. Targeted therapies and the cutting-edge immunotherapies have reached a new paradigm for cancer treatment, which work together with renovated surgery and radiotherapy, etc., to markedly improve treatment outcomes. However, there are still many challenges in treating certain types of cancer including prostate cancer (PCa)
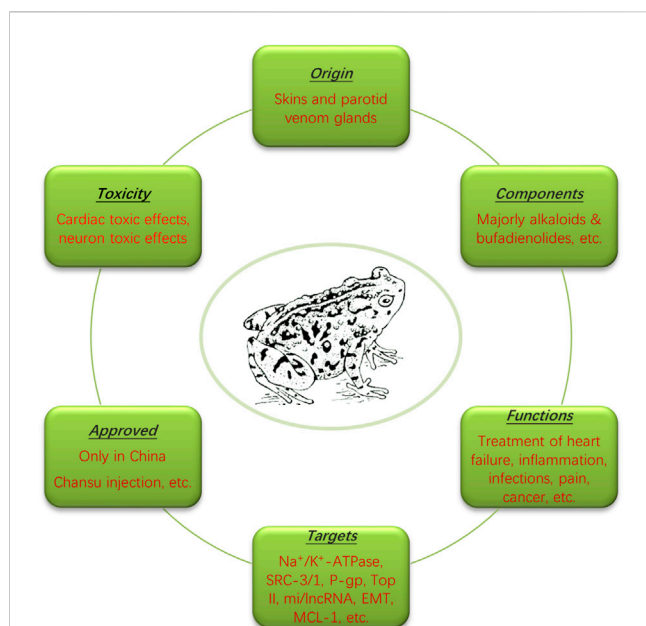
FIGURE 1
The origin, components, functions, toxicity and mechanisms of toad venom. Originated from the skin and auricular glands of Chinese toad, toad venom contains mostly alkaloids and bufadienolides, functioning to treat heart disease, inflammation, infection, pain and cancer through regulating Na$^+$/K$^+$-ATPase, SRC-3 and -1, etc. Drugs containing toad venom are only approved in China.

which has two unique characteristics. The first one is the high prevalence since it's one of the leading cancers in men and one of the leading causes of deaths among men worldwide (Gomella, 2017; Schatten, 2018; Zhang et al., 2022a). The second characteristic is the high incidence of drug resistance, since more than 90% of PCa will eventually develop resistance to androgen-depredation therapy (ADT), termed as castration-resistant PCa (CRPC), and later second resistance to subsequent chemotherapies (Armstrong and Gao, 2015; Cohen et al., 2021; Liotti et al., 2021; Morel et al., 2021; Ji et al., 2022; Peery et al., 2022). It's known that various factors contribute to the development of drug resistance in PCa, such as the alteration/mutation of androgen receptor (AR) or oncogenes, metabolism adaptation, overexpression of ATP-binding cassette (ABC) transporters, apoptosis resistance, enhanced DNA repair and cellular defensive systems against toxic inducers, etc. (Peery et al., 2017; Wang et al., 2020a; de Leeuw et al., 2020; Messina et al., 2020; Peery et al., 2020; Yang et al., 2020; Do and Webster, 2021; Filon et al., 2022). Thus, structurally and mechanistically renovated agents that can effectively suppress PCa and/or less likely develop resistance are in urgent need.

Toad venom, also named as Chan-Su, is a traditional Chinese medicine that has shown therapeutic efficacies in clinic (mainly in China) and has been widely used for the treatment of cancer, cardiovascular diseases, pain, and inflammation/inflammatory diseases as shown in Figure 1 (Gao et al., 2017; Li et al., 2021a; Xu et al., 2021; Zheng et al., 2022). Originally derived from the skin and auricular glands of Chinese toad, toad venom is used to repel toad's natural enemies primarily, working as a protective agent. Known for the toxic effects to cause cardiac arrhythmia, toad venom-derived agents (TVAs) usually work as an inhibitor of

Na$^+$/K$^+$-ATPase and a regulator of calcium homeostasis, which leads to seizure and coma, etc., thereby causing toxic effects (Chen and Kovarikova, 1967; Bick et al., 2002; Lopez-Lopez et al., 2008). In addition to toxic effects, however, toad venom has therapeutic effects that can be applied to treat certain diseases. Till now, due to its strict export ban to other countries by state law, drugs that contain toad venom are only approved for clinical use in China, such as Chansu injection, Liu Shen Wan, Xin Bao Wan, Chan-Su Wan, Hua-Chan Wan (made of isolated cinobufagin in toad venom), Kyushin, Zuo Xiang Bao Xin Wan, etc. (Morishita et al., 1992). In addition to Chinese Chan-Su in the application of cancer treatments, toad venom from other species has also been reported, including Indian toad venom (Gomes et al., 2011), although they have not been fully studied for its application.

In this review, we focused on the applications of bufadienolides, especially those isolated pure compounds in TVAs, in treating PCa in the past 10 years. While it is true that not too many studies have been published as of December 2022, and that the research and application of TVAs in cancer treatment are still at its early stage, the information collected could certainly serve as a base for their further exploration in PCa treatment.

## 2 Bufadienolides in toad venom and their therapeutic implication in cancers

In total, several dozens of different components were identified and characterized in toad venom (Zhang et al., 2005; Wang et al., 2018a; Cao et al., 2019). Their pharmacological effects can be majorly attributed to alkaloids (Dai et al., 2018a; Dong et al., 2022) and bufadienolides which share steroids scaffold in common (Qu et al., 2012). Both alkaloids and bufadienolides are among the most prominent and most-studied compounds in toad venom. Growing studies have confirmed that both alkaloids and bufadienolides can work in treating cardiovascular diseases and cancers (Chen et al., 2020). Our special and major interest in this review falls in these bufadienolides (Figure 2).

There are several prominent members that are categorized as bufadienolides (Figure 2) (Cunha-Filho et al., 2010; Zhang et al., 2014), including Bufalin, (3β,14-dihydroxy-5β-bufa-20,22-dienolide, shown as compound 1) (Zhang et al., 2020a), bufatalin [(3β,14,16β-Trihydroxy-5β-bufa-20,22-dienolide) 16-acetate, shown as compound 2] (Zhang et al., 2022b), cinobufagin, (3β-Hydroxy-14,15β-epoxy-5β-bufa-20,22-dienolid-16β-yl acetate, shown as 3) (Toma et al., 1987), resibufogenin [(3β,5β,15β)-14,15-epoxy-3-hydroxy-bufa-20,22-dienolide, shown as 4] (Yang et al., 2021a), and arenobufagin [(3β,5β,11α)-3,11,14-Trihydroxy-12-oxobufa-20,22-dienolide, shown as 5] (Zhang et al., 2013). These compounds are structurally related, and specially, all of them can be regarded as bufalin's derivatives, with minor differences at certain position, which are shown and highlighted in Figure 2. It appears that TVAs have broad-spectrum anticancer potential (Liu et al., 2019; Niu et al., 2021; Jia et al., 2022). Research has indicated that they, either by single use or as a mixture when combined with other agents, are effective in treating acute myeloid leukemia (Hirasaki et al., 2022), lung cancer (Xie et al., 2018; Li et al., 2021b; Meng et al., 2021), colorectal cancer (Li et al., 2019; Bai et al., 2021; Meng et al., 2021), liver cancer (Zhang et al., 2012; Zhao et al., 2019; Zhang et al.,
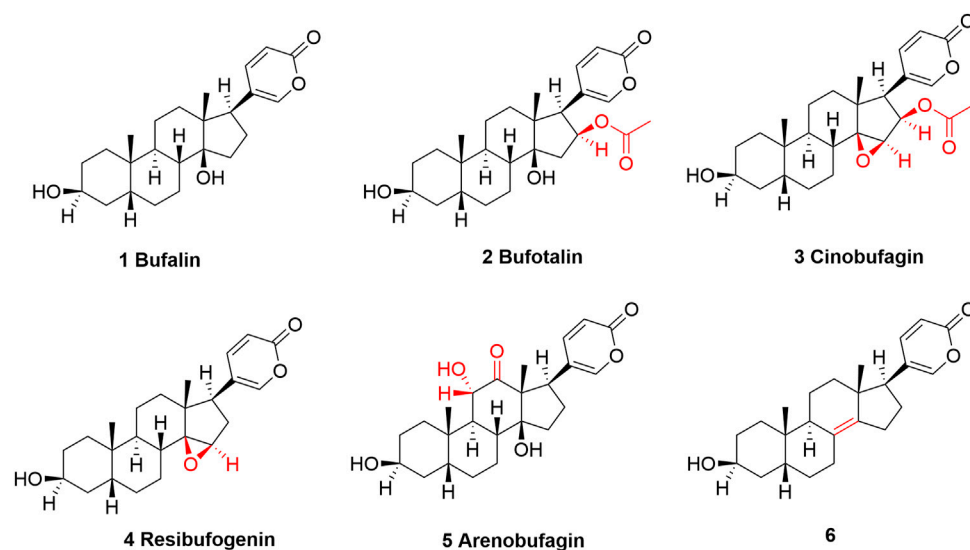
**FIGURE 2**
The structures of bufalin and its derivatives found in toad venom which show cancer-suppressing effects. Structurally, bufalin can be regarded as a parent compound, and all other TVAs are modified on bufalin at different positions. The structural differences are highlighted in red.

2020b; Yang et al., 2021b), breast cancer (Zhu et al., 2018), oral cancer (Jo et al., 2021), gastric cancer (Xiong et al., 2019), Ehrlich ascites carcinoma (Giri et al., 2018), melanoma (Pan et al., 2019; Zhang et al., 2020c; Kim et al., 2020), nasopharyngeal carcinoma (Pan et al., 2020; Hou et al., 2022), osteosarcoma (Cao et al., 2017; Dai et al., 2018b; Zhang et al., 2019a), cholangiocarcinoma (Ren et al., 2019), myeloma (Baek et al., 2015), etc.

# 3 Therapeutic application of bufadienolides in PCa

## 3.1 Mono-therapy of TVAs in PCa

Bufalin is one of the most intensively studied compounds among all TVAs (Wang et al., 2018b; Lan et al., 2019; Soumoy et al., 2022). A study by Zhang et al. (2018) showed that bufalin worked as an anticancer agent *via* a p53-mediated mechanism in PCa cells both *in-vitro* and *in-vivo*. In p53-mutant DU145 cells and p53-wild type LNCaP cells, bufalin (5–100 nM, 48 h) treatment could upregulate the expression of cleaved poly (ADP-ribose) polymerase (PARP), and downregulate steroid receptor co-activator 1/3 (SRC1/3), AR and prostate specific antigen (PSA). This study showed that bufalin increased p53 expression in LNCaP cells, but decreased p53 in DU145 cells, however, cleaved PARP or p53 was not observed in p53-null PC-3 cells although inhibited proliferation was identified, suggesting a p53-mediated efficacy (Zhang et al., 2018). The microarray detection of certain mRNA levels indicated that in LNCaP cells, bufalin treatment increased p53 and its transcriptional target P21CIP1, as well as mRNAs related to cellular stress and DNA damage response, and certain senescence-associated genes, such as *CYR61/CCNI*, *CTGF/CCN2* and *CDKN1A*, which were then been validated by the subsequent assays of cell cycle distribution (sub $G_{0/1}$) and the presence of

senescence-like phenotype (Zhang et al., 2018). The knockdown of p53 could attenuate bufalin-induced apoptosis as indicated by the decreased level of cleaved PARP. Finally, in the *in-vivo* model of LNCaP xenograft, bufalin (1.5 mg/kg body weight, IP, daily) for 9 weeks inhibited tumor growth, resulting in a 67% decrease as compared to untreated group, without affecting body weight significantly which might suggest a safe profile. More importantly, in bufalin-treated tumors, phospho-p53 was increased, confirming the on-target effect and a network of bufalin with p53 (Zhang et al., 2018).

A recent study by Zhang et al. (2019) found that bufalin can alter the expression of both microRNAs (miRNAs) and long non-coding RNAs (lncRNAs) that are critical for PCa (Zhang et al., 2019b). In CRPC DU145 and PC-3 cells, bufalin suppressed the cell viability in a dose-dependent manner, with an $IC_{50}$ value of 0.89 and 1.28 μM, respectively. At lower than the corresponding $IC_{50}$ (to be more specific, at half of the corresponding $IC_{50}$), bufalin could significantly reduce the migration and invasion of DU145 and PC-3 cells as confirmed by the wound healing assay and transwell assay. The authors screened lncRNA alteration after bufalin treatment (0.1–5 μM) using a lncRNA microarray, and they identified that HOX transcript antisense RNA (HOTAIR) was one of the mostly reduced (Zhang et al., 2019b). HOTAIR targets and inhibits miR-520b as confirmed by RNA immunoprecipitation assay; meanwhile, miR-520b can negatively regulate the expression of fibroblast growth factor receptor 1 protein (FGFR1) which plays a pivotal role in PCa progression and metastasis (Yang et al., 2013; Wang et al., 2019). The authors also investigated and confirmed the positive correlation of HOTAIR and FGFR1 with PCa bone metastasis, and that the overexpression of HOTAIR could reverse bufalin-induced cancer-suppressing effects. Thus, this study indicated that bufalin can inhibit PCa proliferation, migration and invasion *via* regulating the HOTAIR-miR520b-FGFR1 loop (Zhang et al., 2019b).

MiRNA-181, composed with subunits miRNA-181a and b, targets apoptosis-associated proteins such as Bcl-2 family members, functioning as a tumor suppressor (Liu et al., 2017; Pei et al., 2020). Zhai et al. (2013) found that in bufalin (10 µM, 24 h)-treated PC-3 cells, miRNA-181a, but not the others such as miRNA-10b, −17, 18a, 20a, 21, −106, −155, −221 and −372, was markedly upregulated (5-fold), which was later confirmed to be a dose-dependent manner (1, 10 and 15 µM) (Zhai et al., 2013). In PC-3 cells, bufalin (15 µM) significantly decreased the expression of Bcl-2, an anti-apoptotic protein, accompanied with caspase-3 protein activation (via testing the level of cleaved caspase-3), which is essential in promoting apoptosis (Kesavardhana et al., 2020). At the same time, the rescue experiments showed that bufalin-induced apoptosis and caspase-3 proteins activation can be partially reversed by miR-181a inhibitor co-treatment (100 nM), validating the targeted effects of bufalin toward miR-181a (Zhai et al., 2013).

Structurally, bufalin is a hydrophobic compound that may encounter poor absorption and bioavailability (Shao et al., 2021). Thus, Liu and Huang (2016) constructed an amphiphilic targeting brush-type copolymers that can deliver bufalin to CRPC cells, which exhibited controlled drug release and higher anticancer capability than free bufalin both in-vitro and in-vivo (Liu and Huang, 2016). This constructed BUF-loaded micellar nanoparticle BUF-NP-(G3-C12) was found to have an $IC_{50}$ value of 8.0 ng/mL, which was lower than that of free bufalin (which was 13.3 ng/mL) in CRPC DU145 cells; and consistent results were also observed in inducing apoptosis. In DU145 xenograft model, when used by intravenous injection iv) at an equivalent 1.0 mg bufalin/kg, BUF-NP-(G3-C12) showed significantly higher tumor-inhibiting effects than that of free bufalin. Importantly, it didn't change body weight as compared to vehicle control, suggesting its safety (Liu and Huang, 2016). Further evaluation is clearly needed to develop it as a drug candidate for PCa.

Chen et al. (2017) reported that arenobufagin, among five bufadienolides including cinobufotalin, bufarenogin, 19-oxocinobufotalin and 19-hydroxybufalin, showed the highest potency in suppressing the progress of epithelial-mesenchymal transition (EMT) in PC-3 cells, leading to decreased ability of migration and invasion (Chen et al., 2017). Arenobufagin (8 nM) time-dependently (24, 36 and 48 h) downregulated EMT markers in PC-3 cells, including slug, zinc finger E-box binding homeobox 1 (ZEB1), snail, N-cadherin, vimentin and Twist1 as confirmed by the Western bolt experiment. In addition, β-catenin was reduced at both mRNA and expression levels by arenobufagin, which then lead to the downregulation of its downstream genes including *Met*, *LEF*, *TCF*, *c-Myc* and *cyclin D1*. These effects can be reversed by β-catenin overexpression, suggesting the network of arenobufagin with β-catenin. Arenobufagin (1 mg/kg) reduced tumor growth without altering the body weight or causing harms to major organs including heart, liver, spleen, lung and kidney. In the *in-vivo* PC-3 cells pulmonary metastases model, arenobufagin markedly reduced the number and size of tumor metastatic foci in lung tissues, suggesting its dual role in preventing tumor growth and metastasis, warranting further study (Chen et al., 2017).

Niu et al. (2018) reported the anticancer effects and the mode of action of another TVA, cinobufagin, in CRPC PC-3 cells. Cinobufagin could significantly suppress PC-3 cells proliferation, with an approximately $IC_{50}$ of 100 nM (24 h) or 50 nM (48 h), suggesting a dose- and time-dependent manner. When tested in colony formation, cinobufagin possessed a much lower $IC_{50}$ (slightly lower than 5 nM). Mechanistically, cinobufagin induced apoptosis of PC-3 cells *via* down-regulating anti-apoptotic MCL-1 protein (Niu and Qin, 2018). Cinobufagin appears to be much more potent than bufalin, which has an $IC_{50}$ of 1.28 µM in PC-3 cells.

## 3.2 Combinational therapy of TVAs in PCa

In addition to its role in working alone to suppress PCa, TVA bufalin has also been found to work as a chemo-sensitizer when combined with other conventional therapeutics.

Bufalin was identified as a possible DNA topoisomerase II (Top II) inhibitor (Hashimoto et al., 1997; Pastor and Cortes, 2003). Previous *in-vitro* studies showed that sequential administration of different Top isomer inhibitors exhibited improved outcomes as compared to simultaneous administration, suggesting a feasible combinational strategy (Cho and Cho-Chung, 2003; Griffith and Kemp, 2003). Recently, Gu and Zhang (2021) investigated the combination of low-dose (0.4–0.8 mg/kg) bufalin with hydroxycamptothecin, a Top I inhibitor (Gu and Zhang, 2021). In this study, CRPC DU145 cells xenograft model in nude mice were constructed and treated by hydroxycamptothecin (2 mg/kg) combined with 0.4 mg/kg, 0.6 mg/kg or 0.8 mg/kg bufalin, respectively. The results showed that among all treatments, the combination of hydroxycamptothecin with 0.6 mg/kg bufalin showed the strongest tumor-reducing effect (93% inhibition) than the other two combinations or monotherapy, bufalin at 1 mg/kg (~30% inhibition) or hydroxycamptothecin at 2 mg/kg (58% inhibition), without altering body weight significantly (Gu and Zhang, 2021). This combination, named as H6B, induced significantly higher apoptosis but reduced proliferating cell nuclear antigen (PCNA) proteins in the tumors than the other treatments as confirmed by the TUNEL assay and immunohistochemistry, respectively. Western blot assay showed that H6B increased pro-apoptotic proteins such as Bax, p53 and programmed cell death protein 4 (PDCD4); whereas it decreased anti-apoptotic proteins such as Bcl-XL and p-AKT (Gu and Zhang, 2021). While this study presented a possible combinational treatment that was safe and can be further validated in other models and even in humans, it remains unclear if H6B inhibit Top I/II in the treated tumor tissue.

## 4 Other therapeutic implication of TVAs in PCa

Growing evidence has suggested that TVAs may have other therapeutic application in treating PCa.

Firstly, both cinobufagin and bufalin could inhibit P-glycoprotein (P-gp, also named as ABCB1 or multidrug resistance mutation 1, MDR1) (Yuan et al., 2017; Madugula and Neerati, 2020; Zhan et al., 2020; Neerati and Munigadapa, 2022).

Since P-gp plays an essential role, and sometime the leading role in inducing anticancer drug of both conventional and targeted therapies resistance *via* transporting them out of cancer cells (Robey et al., 2018; Wang et al., 2020b; Feng et al., 2020; Thomas and Tampe, 2020; Wang et al., 2021), cinobufagin and bufalin may likely have potentials in sensitizing certain conventional chemotherapeutics that are substrates of P-gp. In addition, as all of these bufadienolides possess the same pharmacophore which indicates that they may have similar bioactivities, it is reasonable to predict that other TVAs (in addition to cinobufagin and bufalin) may also impact P-gp and may have synergistic/sensitizing effects in PCa treatment when used by combination (Wu et al., 2020a; Gao et al., 2020; Chen et al., 2021), warranting further exploration. Furthermore, it's also worth studying whether TVAs impact other members of ABC transporters. Thus, a broader screening and validation is necessary to explore their full potential.

Secondly, TVAs can induce cytochrome P450 3A in the pharmacokinetic (PK) study (Jiang et al., 2012; Dai et al., 2019), suggesting that they may affect other drugs metabolism and requiring a real-time monitor of PK profiles when used by combination.

Thirdly, since TVAs could alleviate cancer-related pain, it is meaningful in trying optimal combinational strategies with certain anticancer drugs (Xu et al., 2019).

Furthermore, there are several bufalin-derived TVAs that show better inhibitory effect in PCa cells than bufalin, including compound 6 (Figure 2), a de-hydroxyl bufalin, showed higher AR binding affinity but lower inhibition on the $Na^+/K^+$-ATPase, which may suggest a higher cytotoxic effect to PCa cells but lower toxic effect to heart, warranting further evaluation (Tian et al., 2014).

While several TVAs derivatives also exhibited promising anticancer effects in PCa and other cancer types (Yuan et al., 2014; Meng et al., 2021; Sampath et al., 2022), their application remains to be fully exploited. It's also noteworthy that except for bufalin, arenobufagin, and cinobufagin, very few studies of bufotalin and resibufogenin in PCa have been reported in the past decade.

# 5 Toxic and potential adverse effects of TVAs

One of the major challenges in using TVAs is the toxic effect, which may significantly cripple their application potential in PCa. Thus, the toxic effects and the associated mechanism are discussed briefly.

## 5.1 Cardiac toxic effects *via* regulating $Na^+/K^+$-ATPase

Several TVAs have been confirmed to induce cardiac toxicity. Resibufogenin (0.2 mg/kg, iv) could significantly increase heart burden as indicated by contractile force in rabbit, cat and dog, leading to delayed afterdepolarization and triggered arrhythmias (Xie et al., 2001). These effects were partially mediated by its disturbance of $Na^+/K^+$-ATPase which caused calcium ($Ca^+$) overload (Xie et al., 2001). Similarly, in human cardiomyocytes model, bufalin (30–300 nM) showed a biphasic effect on the contractility, which was strengthening contractility, accelerating

conduction, and increasing beating rate at the earlier stage, while in the opposite when at the later stage (Li et al., 2020).

## 5.2 Neuron toxicity due to inhibit voltage-gated potassium channels

TVAs are known to cause neuron toxicity as reported previously (Brubacher et al., 1999; Dasgupta, 2003; Ma et al., 2007). In addition to the inhibition of $Na^+/K^+$-ATPase, in rat hippocampal neurons (Wang et al., 2014a), both resibufogenin and cinobufagin could also inhibit outward delayed rectifier potassium current (Hao et al., 2011), which may work together to induce toxicity in neuron system. However, we believe that more studies are needed to reveal the doses or concentrations on inducing human neuron cells related toxicity.

## 5.3 Drug-drug interactions due to the inhibition of human cytochrome P450 3A4 (CYP3A4)

A study by Li et al. (2009) found that bufalin had an inhibitory toward recombinant human CYP3A4 *in vitro*, with an $IC_{50}$ of 14.52 μM, leading to increased elimination half-time, peak plasma level of midazolam (a substrate of CYP3A4) in the rat model. Thus, when being used with combination, adverse effects due to CYP3A4 inhibition of TVAs should be monitored and prevented.

## 5.4 The narrow therapeutic window

It's known that in mouse model the median lethal dose ($LD_{50}$) of bufalin in nude mice is 2.2 mg/kg (Tu et al., 2000), which is pretty close to the doses of achieving therapeutic effects of tumor inhibition (normally not more than 1 mg/kg), suggesting a very narrow therapeutic window, and that the accumulative TVAs may further worsen certain toxic effects. Thus, when being tested in humans, a close monitor of serum concentration is necessary.

# 6 Discussion and future perspectives

Cancers have become a great burden to modern people due to high prevalence and high cost in treatment and care (Desai et al., 2021; Wells, 2021). Cancer-related deaths rank the second among all deaths caused by different diseases (Siegel et al., 2022). As our major research interest, PCa stands out for three reasons, the most diagnosed cancer in men, the second most cancer deaths in men globally, and extremely high rate of drug resistance (Wade and Kyprianou, 2018). Currently, effective therapeutic strategies for PCa include surgery, cytotoxic chemotherapy agents, AR inhibitors, PARP inhibitors, and radiopharmaceuticals, etc. (Do and Webster, 2021). Unfortunately, the vast majority of PCa patients will develop acquired resistance to most of these therapeutic agents (Moreira-Silva et al., 2022).

Toad venom is a traditional Chinese medicine that has been applied (mostly used by certain extraction/mixture in combination with other drugs) in clinic for hundreds of years in China (Li et al., 2021a). It should be mentioned that all the approved drugs contain the extraction

TABLE 1 Key facts of bufadienolides in the treatment of PCa (as of August 2022).

| TVAs | Mechanisms/Targets | Effects | Ref |
|---|---|---|---|
| Bufalin | Suppressing p53 | Reducing tumor growth (1.5 mg/kg, IP) | Zhang et al. (2018) |
|  | Regulating HOTAIR | Inhibiting PCa cells metastasis | Zhang et al. (2019b) |
|  | Regulating miRNA181a/apoptotic proteins | Inducing PC-3 apoptosis | Zhai et al. (2013) |
|  | Un-defined | Inhibiting DU145 cells *in-vitro* and *in-vivo* | Liu and Huang (2016) |
|  | Inhibiting Top II and inducing apoptosis | Sensitizing hydroxycamptothecin | Gu and Zhang (2021) |
| Arenobufagin | Down-regulating EMT | Inhibiting PC-3 metastasis *in-vivo* | Chen et al. (2017) |
| Cinobufagin | Down-regulating MCL-1 | Killing PC-3 cells | Niu and Qin (2018) |
|  | Inhibiting P-gp | Sensitizing drugs that are P-gp substrates | Griffith and Kemp (2003) |

Note: HOTAIR, HOX, transcript antisense RNA; EMT, epithelial-mesenchymal transition; P-gp, P-glycoprotein.

of toad venom but not the isolated active components such as these discussed bufadienolides in this review. For example, while Chansu injection, an approved drug in China for infective diseases, has been evaluated for its potential in cancer treatment, its effectiveness and safety among cancer patients are yet to be proved (Jia et al., 2022). A clinical study, published in 2016 in stage III-IV patients of non-Hodgkin lymphoma, showed that the combination of Chansu injection with EOAP (etoposide, vincristine, cytosine arabinoside and prednisone) failed to improve the therapeutic effect when compared to EOAP group (Niu et al., 2016). Another clinical evaluation showed that while Chansu injection might enhance the treatment effects of certain anticancer agents (Ma et al., 2018), we believe that further broader clinical trials are still needed to validate the efficacy.

It's assumed that bufadienolides have several advantages over those approved drugs, because 1) bufadienolides are new therapeutic agents with distinct structures, and laboratory studies have suggested that PCa cells are sensitive to them. Thus, it's likely that PCa cells may not be able to quickly develop resistance. 2) The above mentioned approved drugs are all single-targeted agents, which can be antagonized by adaptation of PCa cells. Bufadienolides are known for multi-targeted compounds, rendering them hard to develop resistance by PCa cells. 3) Reports have shown that P-gp can induce resistance of some PCa drugs including docetaxel (Kato et al., 2015), PARP inhibitor talazoparib (Naito et al., 2021; Teyssonneau et al., 2022), etc. As P-gp is one of bufadienolides' targets, thus, to reverse or achieve sensitizing effects, it's reasonable to use combinational regimens, including combination composed with approved drugs in PCa. However, cautions remain since 1) the efficacy and safety of pure isolated bufadienolides in human is unknown; 2) bufadienolides may have intensive drug-drug interactions as they have interactions with cytochrome P450 3A (Jiang et al., 2012; Dai et al., 2019); and 3) it's unclear of the exact targets.

Though these components have been extensively studied in the past decade, none of them have been approved. The application of TVAs in PCa is still at early stage but is attracting more attentions recently.

## 6.1 Summary of TVAs in PCa

The above literature review has summarized the application of TVAs in PCa (Table 1; Figure 3). Generally, TVAs could suppress

PCa cells proliferation *via* inducing apoptosis and regulating certain miRNAs and lncRNAs; meanwhile, they also show activity in reducing PCa cells migration and invasion *in-vitro* and *in-vivo* through negatively regulating critical players involved in metastasis. It's known that bufalin targets steroid receptor coactivators SRC-3 and SRC-1 (Wang et al., 2014b), while growing evidence suggests that bufalin is a multi-targeting or multi-functional agent, especially in the treatment of cancers.

By far, except for bufalin that has been extensively studied, the therapeutic applications of other TVAs in PCa are yet to be fully revealed. While we suspect that since they all share a very similar scaffold, there may be limited differences of the underlying mechanisms, requiring further validations.

It also comes to our notice that TVAs have been approved and/or under active clinical evaluations only in China. Currently, combinational therapies of using some of TVAs are also actively tested in clinical trials, such as the combination of thalidomide with cinobufagin to treat lung cancer cachexia (Xie et al., 2018). Other TVAs-related clinical trial was either conducted more than 10 years ago (Meng et al., 2009), or using formulations made of toad venom extraction rather than isolated single component (Meng et al., 2012; Wu et al., 2020b; Tan et al., 2021). Since both the active components (major and minor) and the associated mechanisms remain largely elusive, thus, these formulations will likely meet many obstacles to be approved in other countries outside China due to different new drugs regulations. More studies using corresponding isolated pure compounds are in urgent need to support their further evaluation in humans.

## 6.2 Future perspectives

While the anticancer of TVAs in PCa can be confirmed in lab (*in-vitro* and *in-vivo*), much more works are needed before they can be eventually applied in patients worldwide. The authors propose that six future directions are worth trying.

(1) Rational design of TVAs derivatives or analogs *via* the assistance of computer-aided drug design (CADD). These structures of bufadienolides can serve as leading compounds that may undergo structural modification for improved target-binding and anticancer effects. By far, this research area is extremely
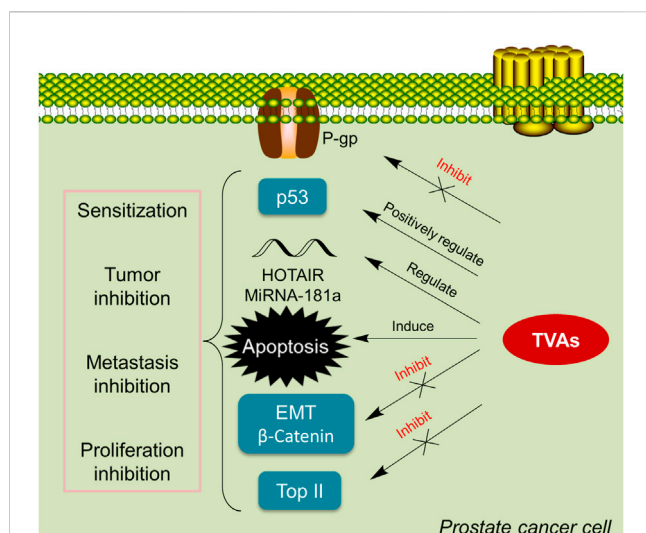
**FIGURE 3**
TVAs suppress cancer growth *via* various pathways. TVAs appear to be able to suppress P-gp, activate p53, and regulate critical players in EMT, inhibit Top II and modulate certain mi/lncRNA, leading to PCa cells apoptosis which thereby suppressing cancer progression.

undeveloped. Very few studies have been published, and most of them are focusing on the modification of hydroxyl groups at different positions (Sampath et al., 2022). Further and varied structural modification at other positions and functional groups are necessary.

(2) In-depth pharmacological/mechanistic study for target(s) identification and verification. While bufadienolides appear to regulating multifaceted signal pathways and targets in PCa, it remains elusive regarding the decisive factor. Proteomics study and gene sequence after TVAs treatment along with the associated pharmacological and validation studies is required.

(3) Following the pharmacological/mechanistic study, toxicological mechanisms, beside their inhibition on $Na^+/K^+$-ATPase or other ion channels, are needed. In addition, it is also possible that certain metabolites of TVAs may contribute to toxic effects, requiring further validation.

(4) PK study. The PK study can answer the time-course of the absorption, distribution, metabolism and elimination, as well as toxicity of bufadienolides, which may offer solutions for the doses and frequency of administration in PCa patients. Unfortunately, there is no PK data using isolated TVAs in humans. Recently in 2019, a PK study using bufalin in rats were published (Wei et al., 2019). It is shown that bufalin (10 mg/kg, oral administration) reached the peak serum concentration (14.722 ± 4.681 ng/mL) after only 15 min, which had a half time of 5.7 ± 3.06 h (Wei et al., 2019). Bufalin could quickly undergo metabolism into more than nine different metabolites. This study provided very useful information of using bufalin in rats, which may help to design and develop protocols in monitoring metabolism of TVAs in humans. In addition, these identified metabolites may help to reveal potential pharmacological effects as well as toxic effects in humans.

(5) More *in-vivo* models validation of bufadienolides in PCa. In addition to *in-vitro* models, *in-vivo* models including patient-

derived xenograft models are warranted. Furthermore, due to its innate toxic effects, the combinational regimens of low-dose bufadienolides with certain conventional chemotherapeutics will be promising.

(6) Deciphering associated resistance reasons and developing combinational strategy. Drug resistance is a major obstacle in PCa treatment (Do and Webster, 2021; Zhao et al., 2021). While we suspect that PCa cells may not develop resistance to bufadienolides easily, it's largely unknown when and how, as well as the resistance rate and resistant mechanisms. For the full application and indications, more studies are needed to reveal resistant reasons.

Finally, more clinical trials in PCa are necessary to test the efficacies of TVAs including their pharmaceutical formulations.

# 7 Conclusion

PCa, due to its high incidence rate and prevalence of drug resistance, is one of the leading threats to men's health. Chinese traditional medicine toad venom and TVAs have emerged as promising therapeutic agents in PCa, which have been validated by cell- and animal-based models. Further in-depth studies are also clearly needed for the underlying mechanisms, toxicology, and for exploring combinational therapies in PCa.

# Author contributions

QY designed and wrote the draft; XZ, FH, and CZ revised this review. QY and CZ finalized the manuscript. All authors read and approved the final manuscript.

# Funding

# Conflict of interest

The authors declare that the research was conducted in the absence of any commercial or financial relationships that could be construed as a potential conflict of interest.

# Publisher's note

# References

Armstrong, C. M., and Gao, A. C. (2015). Drug resistance in castration resistant prostate cancer: Resistance mechanisms and emerging treatment strategies. *Am. J. Clin. Exp. Urol.* 3, 64–76.

Baek, S. H., Kim, C., Lee, J. H., Nam, D., Lee, J., Lee, S. G., et al. (2015). Cinobufagin exerts anti-proliferative and pro-apoptotic effects through the modulation ROS-mediated MAPKs signaling pathway. *Immunopharm Immunot* 37, 265–273. doi:10.3109/08923973.2015.1027916

Bai, Y., Wang, X., Cai, M., Ma, C., Xiang, Y., Hu, W., et al. (2021). Cinobufagin suppresses colorectal cancer growth via STAT3 pathway inhibition. *Am. J. Cancer Res.* 11, 200–214.

Bick, R. J., Poindexter, B. J., Sweney, R. R., and Dasgupta, A. (2002). Effects of chan su, a traditional Chinese medicine, on the calcium transients of isolated cardiomyocytes: Cardiotoxicity due to more than Na, K-ATPase blocking. *Life Sci.* 72, 699–709. doi:10.1016/s0024-3205(02)02302-0

Brubacher, J. R., Lachmanen, D., Ravikumar, P. R., and Hoffman, R. S. (1999). Efficacy of digoxin specific Fab fragments (Digibind®) in the treatment of toad venom poisoning. *Toxicon* 37, 931–942. doi:10.1016/s0041-0101(98)00224-4

Cao, Y., Wu, J., Pan, H., and Wang, L. (2019). Chemical profile and multicomponent quantitative analysis for the quality evaluation of toad venom from different origins. *Molecules* 24, 3595. doi:10.3390/molecules24193595

Cao, Y., Yu, L., Dai, G., Zhang, S., Zhang, Z., Gao, T., et al. (2017). Cinobufagin induces apoptosis of osteosarcoma cells through inactivation of Notch signaling. *Eur. J. Pharmacol.* 794, 77–84. doi:10.1016/j.ejphar.2016.11.016

Chen, K. K., and Kovarikova, A. (1967). Pharmacology and toxicology of toad venom. *J. Pharm. Sci-Us* 56, 1535–1541. doi:10.1002/jps.2600561202

Chen, L., Mai, W., Chen, M., Hu, J., Zhuo, Z., Lei, X., et al. (2017). Arenobufagin inhibits prostate cancer epithelial-mesenchymal transition and metastasis by down-regulating beta-catenin. *Pharmacol. Res.* 123, 130–142. doi:10.1016/j.phrs.2017.07.009

Chen, X. Y., Wang, J. Q., Yang, Y., Li, J., and Chen, Z. S. (2021). Natural product as substrates of ABC transporters: A review. *Recent Pat. Anti-Canc* 16, 222–238. doi:10.2174/1574892816666210218220943

Chen, Y. L., Dai, Y. H., Wang, A. D., Zhou, Z. Y., Lei, M., Liu, J., et al. (2020). Two new indole alkaloids from toad venom of *Bufo bufo* gargarizans. *Molecules* 25, 4511. doi:10.3390/molecules25194511

Cho, Y. S., and Cho-Chung, Y. S. (2003). Antisense protein kinase A RIalpha acts synergistically with hydroxycamptothecin to inhibit growth and induce apoptosis in human cancer cells: Molecular basis for combinatorial therapy. *Clin. Cancer Res.* 9, 1171–1178.

Cohen, L., Livney, Y. D., and Assaraf, Y. G. (2021). Targeted nanomedicine modalities for prostate cancer treatment. *Drug Resist Update* 56, 100762. doi:10.1016/j.drup.2021.100762

Cunha-Filho, G. A., Resck, I. S., Cavalcanti, B. C., Pessoa, C. O., Moraes, M. O., Ferreira, J. R., et al. (2010). Cytotoxic profile of natural and some modified bufadienolides from toad Rhinella schneideri parotoid gland secretion. *Toxicon* 56, 339–348. doi:10.1016/j.toxicon.2010.03.021

Dai, G., Zheng, D., Guo, W., Yang, J., and Cheng, A. Y. (2018). Cinobufagin induces apoptosis in osteosarcoma cells via the mitochondria-mediated apoptotic pathway. *Cell Physiol. Biochem.* 46, 1134–1147. doi:10.1159/000488842

Dai, Y. H., Wang, A. D., Chen, Y. L., Xia, M. Y., Shao, X. Y., Liu, D. C., et al. (2018). A new indole alkaloid from the traditional Chinese medicine Chansu. *J. Asian Nat. Prod. Res.* 20, 581–585. doi:10.1080/10286020.2017.1339697

Dai, Z. R., Ning, J., Sun, G. B., Wang, P., Zhang, F., Ma, H. Y., et al. (2019). Cytochrome P450 3A enzymes are key contributors for hepatic metabolism of bufotalin, a natural constitute in Chinese medicine Chansu. *Front. Pharmacol.* 10, 52. doi:10.3389/fphar.2019.00052

Dasgupta, A. (2003). Review of abnormal laboratory test results and toxic effects due to use of herbal medicines. *Am. J. Clin. Pathol.* 120, 127–137. doi:10.1309/p024k7vrddpjctvn

de Leeuw, R., Cao, Q., and Lam, H. M. (2020). Editorial: Response and resistance in castration-resistant prostate cancer. *Front. Oncol.* 10, 607298. doi:10.3389/fonc.2020.607298

Desai, A., Kuderer, N. M., and Lyman, G. H. (2021). Aligning cancer clinical trials with cancer burden: Need for greater global leadership, resources, and vision. *JAMA Oncol.* 7, 357–358. doi:10.1001/jamaoncol.2020.7293

Do, P. C., and Webster, R. M. (2021). The prostate cancer drug market. *Nat. Rev. Drug Discov.* 20, 663–664. doi:10.1038/d41573-021-00111-w

Dong, Q., Liu, L., Yuan, Y., Turdu, G., Mirzaakhmedov, S., Aisa, H. A., et al. (2022). Two new polyamine alkaloids from the *Bufo viridis* toad venom. *Nat. Prod. Res.* 2022, 1–5. doi:10.1080/14786419.2022.2086545

Feng, W., Zhang, M., Wu, Z. X., Wang, J. Q., Dong, X. D., Yang, Y., et al. (2020). Erdafitinib antagonizes ABCB1-mediated multidrug resistance in cancer cells. *Front. Oncol.* 10, 955. doi:10.3389/fonc.2020.00955

Filon, M. J., Gillette, A. A., Yang, B., Khemees, T. A., Skala, M. C., and Jarrard, D. F. (2022). Prostate cancer cells demonstrate unique metabolism and substrate adaptability acutely after androgen deprivation therapy. *Prostate* 82, 1547–1557. doi:10.1002/pros.24428

Gao, F., Wang, X., Li, Z., Zhou, A., Tiffany-Castiglioni, E., Xie, L., et al. (2017). Identification of anti-tumor components from toad venom. *Oncol. Lett.* 14, 15–22. doi:10.3892/ol.2017.6160

Gao, H. L., Gupta, P., Cui, Q., Ashar, Y. V., Wu, Z. X., Zeng, L., et al. (2020). Sapitinib reverses anticancer drug resistance in colon cancer cells overexpressing the ABCB1 transporter. *Front. Oncol.* 10, 574861. doi:10.3389/fonc.2020.574861

Giri, B., Dey, S., and Gomes, A. (2018). Indian toad (*Bufo melanostictus*, Schneider) skin extract induces apoptosis and shows cytotoxic effect on Ehrlich ascites carcinoma (EAC) cells. *J. Drug Deliv. Ther.* 8, 303–312. doi:10.22270/jddt.v8i5.1873

Gomella, L. G. (2017). Prostate cancer statistics: Anything you want them to Be. *Can. J. Urol.* 24, 8603–8604.

Gomes, A., Giri, B., Alam, A., Mukherjee, S., Bhattacharjee, P., and Gomes, A. (2011). Anticancer activity of a low immunogenic protein toxin (BMP1) from Indian toad (*Bufo melanostictus*, Schneider) skin extract. *Toxicon* 58, 85–92. doi:10.1016/j.toxicon.2011.05.008

Griffith, T. S., and Kemp, T. J. (2003). The topoisomerase I inhibitor topotecan increases the sensitivity of prostate tumor cells to TRAIL/Apo-2L-induced apoptosis. *Cancer Chemoth Pharm.* 52, 175–184. doi:10.1007/s00280-003-0656-2

Gu, R., and Zhang, Q. (2021). Effects of low-dose bufalin combined with hydroxycamptothecin on human castration-resistant prostate cancer xenografts in nude mice. *Exp. Ther. Med.* 22, 1015. doi:10.3892/etm.2021.10447

Hao, S., Bao, Y. M., An, L. J., Cheng, W., Zhao, R. G., Bi, J., et al. (2011). Effects of Resibufogenin and Cinobufagin on voltage-gated potassium channels in primary cultures of rat hippocampal neurons. *Toxicol Vitro* 25, 1644–1653. doi:10.1016/j.tiv.2011.07.001

Hashimoto, S., Jing, Y., Kawazoe, N., Masuda, Y., Nakajo, S., Yoshida, T., et al. (1997). Bufalin reduces the level of topoisomerase II in human leukemia cells and affects the cytotoxicity of anticancer drugs. *Leuk. Res.* 21, 875–883. doi:10.1016/s0145-2126(97)00061-1

Hirasaki, Y., Okabe, A., Fukuyo, M., Rahmutulla, B., Mano, Y., Seki, M., et al. (2022). Cinobufagin inhibits proliferation of acute myeloid leukaemia cells by repressing c-Myc pathway-associated genes. *Chem-Biol Interact.* 360, 109936. doi:10.1016/j.cbi.2022.109936

Hou, R., Liu, X., Yang, H., Deng, S., Cheng, C., Liu, J., et al. (2022). Chemically synthesized cinobufagin suppresses nasopharyngeal carcinoma metastasis by inducing ENKUR to stabilize p53 expression. *Cancer Lett.* 531, 57–70. doi:10.1016/j.canlet.2022.01.025

Ji, X., Liu, K., Li, Q., Shen, Q., Han, F., Ye, Q., et al. (2022). A mini-review of flavone isomers apigenin and genistein in prostate cancer treatment. *Front. Pharmacol.* 13, 851589. doi:10.3389/fphar.2022.851589

Jia, J., Li, J., Zheng, Q., and Li, D. (2022). A research update on the antitumor effects of active components of Chinese medicine ChanSu. *Front. Oncol.* 12, 1014637. doi:10.3389/fonc.2022.1014637

Jiang, B., Cai, F., Gao, S., Meng, L., Liang, F., Dai, X., et al. (2012). Induction of cytochrome P450 3A by shexiang baoxin pill and its main components. *Chem-Biol Interact.* 195, 105–113. doi:10.1016/j.cbi.2011.12.001

Jo, S., Yang, E., Lee, Y., Jeon, D., and Namkung, W. (2021). Cinobufagin exerts anticancer activity in oral squamous cell carcinoma cells through downregulation of ANO1. *Int. J. Mol. Sci.* 22, 12037. doi:10.3390/ijms222112037

Kato, T., Mizutani, K., Kameyama, K., Kawakami, K., Fujita, Y., Nakane, K., et al. (2015). Serum exosomal P-glycoprotein is a potential marker to diagnose docetaxel resistance and select a taxoid for patients with prostate cancer. *Urol. Oncol-Semin Ori* 33, 385.e15–385.e20. doi:10.1016/j.urolonc.2015.04.019

Kesavardhana, S., Malireddi, R., and Kanneganti, T. D. (2020). Caspases in cell death, inflammation, and pyroptosis. *Annu. Rev. Immunol.* 38, 567–595. doi:10.1146/annurev-immunol-073119-095439

Kim, G. H., Fang, X. Q., Lim, W. J., Park, J., Kang, T. B., Kim, J. H., et al. (2020). Cinobufagin suppresses melanoma cell growth by inhibiting LEF1. *Int. J. Mol. Sci.* 21, 6706. doi:10.3390/ijms21186706

Lan, Y. L., Lou, J. C., Jiang, X. W., Wang, X., Xing, J. S., Li, S., et al. (2019). A research update on the anticancer effects of bufalin and its derivatives. *Oncol. Lett.* 17, 3635–3640. doi:10.3892/ol.2019.10062

Li, F. J., Hu, J. H., Ren, X., Zhou, C. M., Liu, Q., and Zhang, Y. Q. (2021). Toad venom: A comprehensive review of chemical constituents, anticancer activities, and mechanisms. *Arch. Pharm.* 354, e2100060. doi:10.1002/ardp.202100060

Li, H. Y., Xu, W., Zhang, X., Zhang, W. D., and Hu, L. W. (2009). Bufalin inhibits CYP3A4 activity *in vitro* and *in vivo*. *Acta Pharmacol. Sin.* 30, 646–652. doi:10.1038/aps.2009.42

Li, J., Zhang, Z., Deng, H., and Zheng, Z. (2021). Cinobufagin-loaded and folic acid-modified polydopamine nanomedicine combined with photothermal therapy for the treatment of lung cancer. *Front. Chem.* 9, 637754. doi:10.3389/fchem.2021.637754

Li, M., Wang, X. J., Zhao, Q., Wang, J. X., Xing, H. Y., Zhang, Y. Z., et al. (2020). Bufalin-induced cardiotoxicity: New findings into mechanisms. *Chin. J. Nat. Med.* 18, 550–560. doi:10.1016/s1875-5364(20)30065-0

Li, X., Chen, C., Dai, Y., Huang, C., Han, Q., Jing, L., et al. (2019). Cinobufagin suppresses colorectal cancer angiogenesis by disrupting the endothelial mammalian target of rapamycin/hypoxia-inducible factor 1α axis. *Cancer Sci.* 110, 1724–1734. doi:10.1111/cas.13988

Liotti, A., La Civita, E., Cennamo, M., Crocetto, F., Ferro, M., Guadagno, E., et al. (2021). Periprostatic adipose tissue promotes prostate cancer resistance to docetaxel by paracrine IGF-1 upregulation of TUBB2B beta-tubulin isoform. *Prostate* 81, 407–417. doi:10.1002/pros.24117

Liu, H., Zhang, Z., and Li, Q. (2017). DR5 but not miRNA-181 or miRNA-211 is involved in ER stress-mediated apoptosis induced by palmitate in islet beta cells. *Int. J. Clin. Exp. Patho* 10, 7692–7698.

Liu, J. S., Deng, L. J., Tian, H. Y., Ruan, Z. X., Cao, H. H., Ye, W. C., et al. (2019). Anti-tumor effects and 3D-quantitative structure-activity relationship analysis of bufadienolides from toad venom. *Fitoterapia* 134, 362–371. doi:10.1016/j.fitote.2019.03.006

Liu, T., and Huang, Q. (2016). Biodegradable brush-type copolymer modified with targeting peptide as a nanoscopic platform for targeting drug delivery to treat castration-resistant prostate cancer. *Int. J. Pharm.* 511, 1002–1011. doi:10.1016/j.ijpharm.2016.08.017

Lopez-Lopez, J. M., Sanabria, M. R., and de Prada, S. J. (2008). Ocular toxicity caused by toad venom. *Cornea* 27, 236–237. doi:10.1097/ico.0b013e31815b8317

Ma, F., Zhang, L., and Wang, H. (2018). Clinical evaluation of the combination of Chansu injection with targeted therapy in NSCLC. *Dr.* 3, 76–77.

Ma, H. Y., Kou, J. P., Wang, J. R., and Yu, B. Y. (2007). Evaluation of the anti-inflammatory and analgesic activities of Liu-Shen-Wan and its individual fractions. *J. Ethnopharmacol.* 112, 108–114. doi:10.1016/j.jep.2007.02.008

Madugula, N. K., and Neerati, P. (2020). Influence of toad parotid gland secretion from Indian toad (*Bufo melanostictus*) in diabetic rats: An experimental evidence of P-glycoprotein inhibition. *J. Pharm. Res. Int.* 32, 125–135. doi:10.9734/jpri/2020/v32i2030736

Meng, L., Li, S., Kong, Q., Wang, M., Zhang, X., Zhu, X., et al. (2021). Two new 19-hydroxy bufadienolides with cytotoxic activity from the skins of Bufo melanosticus. *Nat. Prod. Res.* 35, 4894–4900. doi:10.1080/14786419.2020.1741582

Meng, Z., Garrett, C. R., Shen, Y., Liu, L., Yang, P., Huo, Y., et al. (2012). Prospective randomised evaluation of traditional Chinese medicine combined with chemotherapy: A randomised phase II study of wild toad extract plus gemcitabine in patients with advanced pancreatic adenocarcinomas. *Brit J. Cancer* 107, 411–416. doi:10.1038/bjc.2012.283

Meng, Z., Yang, P., Shen, Y., Bei, W., Zhang, Y., Ge, Y., et al. (2009). Pilot study of huachansu in patients with hepatocellular carcinoma, nonsmall-cell lung cancer, or pancreatic cancer. *Cancer-Am Cancer Soc.* 115, 5309–5318. doi:10.1002/cncr.24602

Messina, C., Cattrini, C., Soldato, D., Vallome, G., Caffo, O., Castro, E., et al. (2020). BRCA mutations in prostate cancer: Prognostic and predictive implications. *J. Oncol.* 2020, 1–7. doi:10.1155/2020/4986365

Moreira-Silva, F., Henrique, R., and Jeronimo, C. (2022). From therapy resistance to targeted therapies in prostate cancer. *Front. Oncol.* 12, 877379. doi:10.3389/fonc.2022.877379

Morel, K. L., Hamid, A. A., Clohessy, J. G., Pandell, N., Ellis, L., and Sweeney, C. J. (2021). NF-κB blockade with oral administration of dimethylaminoparthenolide (DMAPT), delays prostate cancer resistance to androgen receptor (AR) inhibition and inhibits AR variants. *Mol. Cancer Res.* 19, 1137–1145. doi:10.1158/1541-7786.mcr-21-0099

Morishita, S., Shoji, M., Oguni, Y., Ito, C., Higuchi, M., and Sakanashi, M. (1992). Pharmacological actions of "kyushin," a drug containing toad venom: Cardiotonic and arrhythmogenic effects, and excitatory effect on respiration. *Am. J. Chin. Med.* 20, 245–256. doi:10.1142/s0192415x92000254

Naito, Y., Kuboki, Y., Ikeda, M., Harano, K., Matsubara, N., Toyoizumi, S., et al. (2021). Safety, pharmacokinetics, and preliminary efficacy of the PARP inhibitor talazoparib in Japanese patients with advanced solid tumors: Phase 1 study. *Invest. New Drug* 39, 1568–1576. doi:10.1007/s10637-021-01120-7

Neerati, P., and Munigadapa, S. (2022). Novel indole derivative as the first P-glycoprotein inhibitor from the skin of Indian toad <i&gt;(*Bufo melanostictus*) </i&gt;. *Turk J. Pharm. Sci.* 19, 63–69. doi:10.4274/tjps.galenos.2021.47417

Niu, J., Wang, J., Zhang, Q., Zou, Z., and Ding, Y. (2021). Cinobufagin-induced DNA damage response activates G2/M checkpoint and apoptosis to cause selective cytotoxicity in cancer cells. *Cancer Cell Int.* 21, 446. doi:10.1186/s12935-021-02150-0

Niu, T., and Qin, G. (2018). The inhibitory effects of cinobufagin on the *in vitro* proliferation of human castration-resistant prostate cancer PC3 cells. *J. Beijing Univ. Traditional Chin. Med.* 41, 1019–1024.

Niu, Y., Shi, J., Wang, G., and Yang, J. (2016). The combination of Chansu injection with EOAP in stage III-IV non-Hodgkin lymphoma. *Leuk. Lymphoma* 25, 224–227.

Pan, Z., Luo, Y., Xia, Y., Zhang, X., Qin, Y., Liu, W., et al. (2020). Cinobufagin induces cell cycle arrest at the S phase and promotes apoptosis in nasopharyngeal carcinoma cells. *Biomed. Pharmacother.* 122, 109763. doi:10.1016/j.biopha.2019.109763

Pan, Z., Zhang, X., Yu, P., Chen, X., Lu, P., Li, M., et al. (2019). Cinobufagin induces cell cycle arrest at the G2/M phase and promotes apoptosis in malignant melanoma cells. *Front. Oncol.* 9, 853. doi:10.3389/fonc.2019.00853

Pastor, N., and Cortes, F. (2003). Bufalin influences the repair of X-ray-induced DNA breaks in Chinese hamster cells. *Dna Repair* 2, 1353–1360. doi:10.1016/j.dnarep.2003.08.001

Peery, R., Cui, Q., Kyei-Baffour, K., Josephraj, S., Huang, C., Dong, Z., et al. (2022). A novel survivin dimerization inhibitor without a labile hydrazone linker induces spontaneous apoptosis and synergizes with docetaxel in prostate cancer cells. *Bioorgan Med. Chem.* 65, 116761. doi:10.1016/j.bmc.2022.116761

Peery, R., Kyei-Baffour, K., Dong, Z., Liu, J., de Andrade, H. P., Dai, M., et al. (2020). Synthesis and identification of a novel lead targeting survivin dimerization for proteasome-dependent degradation. *J. Med. Chem.* 63, 7243–7251. doi:10.1021/acs.jmedchem.0c00475

Peery, R. C., Liu, J. Y., and Zhang, J. T. (2017). Targeting survivin for therapeutic discovery: Past, present, and future promises. *Drug Discov. Today* 22, 1466–1477. doi:10.1016/j.drudis.2017.05.009

Pei, Y. F., He, Y., Hu, L. Z., Zhou, B., Xu, H. Y., and Liu, X. Q. (2020). The crosstalk between lncRNA-SNHG7/miRNA-181/cbx7 modulates malignant character in lung adenocarcinoma. *Am. J. Pathol.* 190, 1343–1354. doi:10.1016/j.ajpath.2020.02.011

Qu, T., Gao, H. M., Chen, L. M., Wang, Z. M., Zhang, Q. W., and Cheng, Y. Y. (2012). Content of indole alkaloids and bufadienolides contained in toad medicines. *Zhongguo Zhong Yao Za Zhi* 37, 3086–3091.

Ren, J., Wang, S., Jin, L., Ma, F., Zhou, D., and Cai, Q. (2019). Cinobufagin inhibits tumor growth by inducing apoptosis through Notch signaling pathways in human cholangiocarcinoma. *Transl. Cancer Res.* 8, 2461–2469. doi:10.21037/tcr.2019.10.06

Robey, R. W., Pluchino, K. M., Hall, M. D., Fojo, A. T., Bates, S. E., and Gottesman, M. M. (2018). Revisiting the role of ABC transporters in multidrug-resistant cancer. *Nat. Rev. Cancer* 18, 452–464. doi:10.1038/s41568-018-0005-8

Sampath, V., Horesh, N., Sasi, B., Zannadeh, H., Pogodin, I., Singh, S. V., et al. (2022). Synthesis and biological evaluation of novel bufalin derivatives. *Int. J. Mol. Sci.* 23, 4007. doi:10.3390/ijms23074007

Schatten, H. (2018). Brief overview of prostate cancer statistics, grading, diagnosis and treatment strategies. *Adv. Exp. Med. Biol.* 1095, 1–14. doi:10.1007/978-3-319-95693-0_1

Shao, H., Li, B., Li, H., Gao, L., Zhang, C., Sheng, H., et al. (2021). Novel strategies for solubility and bioavailability enhancement of bufadienolides. *Molecules* 27, 51. doi:10.3390/molecules27010051

Siegel, R. L., Miller, K. D., Fuchs, H. E., and Jemal, A. (2022). Cancer statistics, 2022. *Ca-Cancer J. Clin.* 72, 7–33. doi:10.3322/caac.21708

Soumoy, L., Ghanem, G. E., Saussez, S., and Journe, F. (2022). Bufalin for an innovative therapeutic approach against cancer. *Pharmacol. Res.* 184, 106442. doi:10.1016/j.phrs.2022.106442

Tan, X., Liang, X., Xi, J., Guo, S., Meng, M., Chen, X., et al. (2021). Clinical efficacy and safety of huachansu injection combination with platinum-based chemotherapy for advanced non-small cell lung cancer: A systematic review and meta-analysis of randomized controlled trials. *Medicine* 100, e27161. doi:10.1097/md.0000000000027161

Teyssonneau, D., Thiery-Vuillemin, A., Dariane, C., Barret, E., Beauval, J. B., Brureau, L., et al. (2022). PARP inhibitors as monotherapy in daily practice for advanced prostate cancers. *J. Clin. Med.* 11, 1734. doi:10.3390/jcm11061734

Thomas, C., and Tampe, R. (2020). Structural and mechanistic principles of ABC transporters. *Annu. Rev. Biochem.* 89, 605–636. doi:10.1146/annurev-biochem-011520-105201

Tian, H. Y., Yuan, X. F., Jin, L., Li, J., Luo, C., Ye, W. C., et al. (2014). A bufadienolide derived androgen receptor antagonist with inhibitory activities against prostate cancer cells. *Chem-Biol Interact.* 207, 16–22. doi:10.1016/j.cbi.2013.10.020

Toma, S., Morishita, S., Kuronuma, K., Mishima, Y., Hirai, Y., and Kawakami, M. (1987). Metabolism and pharmacokinetics of cinobufagin. *Xenobiotica* 17, 1195–1202. doi:10.3109/00498258709167411

Tu, S. P., Zhong, J., Tan, J. H., Jiang, X. H., Qiao, M. M., Wu, Y. X., et al. (2000). Induction of apoptosis by arsenic trioxide and hydroxy camptothecin in gastriccancer cells *in vitro*. *World J. Gastroentero* 6, 532–539. doi:10.3748/wjg.v6.i4.532

Wade, C. A., and Kyprianou, N. (2018). Profiling prostate cancer therapeutic resistance. *Int. J. Mol. Sci.* 19, 904. doi:10.3390/ijms19030904

Wang, C., Liu, Z., Ke, Y., and Wang, F. (2019). Intrinsic FGFR2 and ectopic FGFR1 signaling in the prostate and prostate cancer. *Front. Genet.* 10, 12. doi:10.3389/fgene.2019.00012

Wang, J., Wang, J. Q., Cai, C. Y., Cui, Q., Yang, Y., Wu, Z. X., et al. (2020). Reversal effect of ALK inhibitor NVP-TAE684 on ABCG2-overexpressing cancer cells. *Front. Oncol.* 10, 228. doi:10.3389/fonc.2020.00228

Wang, J., Xia, Y., Zuo, Q., and Chen, T. (2018). Molecular mechanisms underlying the antimetastatic activity of bufalin. *Mol. Clin. Oncol.* 8, 631–636. doi:10.3892/mco.2018.1591

Wang, J. Q., Teng, Q. X., Lei, Z. N., Ji, N., Cui, Q., Fu, H., et al. (2020). Reversal of cancer multidrug resistance (MDR) mediated by ATP-binding cassette transporter G2 (ABCG2) by AZ-628, a RAF kinase inhibitor. *Front. Cell Dev. Biol.* 8, 601400. doi:10.3389/fcell.2020.601400

Wang, J. Q., Wu, Z. X., Yang, Y., Teng, Q. X., Li, Y. D., Lei, Z. N., et al. (2021). ATP-binding cassette (ABC) transporters in cancer: A review of recent updates. *J. Evid-Based Med.* 14, 232–256. doi:10.1111/jebm.12434

Wang, P. F., Fang, Y. G., Li, Z. Y., Chen, L. M., Wang, Z. M., Zou, Z. M., et al. (2018). Study on quality control method of toad venom based on characteristic chromatogram and QAMS. *Zhongguo Zhong Yao Za Zhi* 43, 2863–2871. doi:10.19540/j.cnki.cjcmm.2018.0088

Wang, Y., Lonard, D. M., Yu, Y., Chow, D. C., Palzkill, T. G., Wang, J., et al. (2014). Bufalin is a potent small-molecule inhibitor of the steroid receptor coactivators SRC-3 and SRC-1. *Cancer Res.* 74, 1506–1517. doi:10.1158/0008-5472.can-13-2939

Wang, Z. J., Sun, L., and Heinbockel, T. (2014). Resibufogenin and cinobufagin activate central neurons through an ouabain-like action. *Plos One* 9, e113272. doi:10.1371/journal.pone.0113272

Wei, W., Yu, Y., Wang, X., Yang, L., Zhang, H., Ji, H., et al. (2019). Simultaneous determination of bufalin and its nine metabolites in rat plasma for characterization of metabolic profiles and pharmacokinetic study by LC(-)MS/MS. *Molecules* 24, 1662. doi:10.3390/molecules24091662

Wells, J. M. (2021). Cancer burden, finance, and health-care systems. *Lancet Oncol.* 22, 13–14. doi:10.1016/s1470-2045(20)30681-1

Wu, J., Zhang, D., Ni, M., Xue, J., Wang, K., Duan, X., et al. (2020). Effectiveness of huachansu injection combined with chemotherapy for treatment of gastric cancer in China: A systematic review and meta-analysis. *J. Tradit. Chin. Med.* 40, 749–757. doi:10.19852/j.cnki.jtcm.2020.05.004

Wu, Z. X., Yang, Y., Wang, J. Q., Zhou, W. M., Chen, J., Fu, Y. G., et al. (2020). Elevated ABCB1 expression confers acquired resistance to aurora kinase inhibitor GSK-1070916 in cancer cells. *Front. Pharmacol.* 11, 615824. doi:10.3389/fphar.2020.615824

Xie, J. T., Dey, L., Wu, J. A., Lowell, T. K., and Yuan, C. S. (2001). Cardiac toxicity of resibufogenin: Electrophysiological evidence. *Acta Pharmacol. Sin.* 22, 289–297.

Xie, M., Chen, X., Qin, S., Bao, Y., Bu, K., and Lu, Y. (2018). Clinical study on thalidomide combined with cinobufagin to treat lung cancer cachexia. *J. Cancer Res. Ther.* 14, 226–232. doi:10.4103/0973-1482.188436

Xiong, X., Lu, B., Tian, Q., Zhang, H., Wu, M., Guo, H., et al. (2019). Inhibition of autophagy enhances cinobufagininduced apoptosis in gastric cancer. *Oncol. Rep.* 41, 492–500. doi:10.3892/or.2018.6837

Xu, D., Wang, J., Chen, W., Yang, X., Zhou, J., Ma, H., et al. (2021). Evaluation of analgesic and anti-inflammatory actions of indolealkylamines from toad venom in mice using lipidomics and molecular docking. *J. Ethnopharmacol.* 269, 113677. doi:10.1016/j.jep.2020.113677

Xu, L. S., Feng, Q. L., Zhang, X. P., Wang, Y. G., and Yao, M. (2019). Study on analgesic effect and mechanism of cinobufagin on rats with bone cancer pain. *Zhonghua Yi Xue Za Zhi* 99, 1307–1311. doi:10.3760/cma.j.issn.0376-2491.2019.17.007

Yang, A. L., Wu, Q., Hu, Z. D., Wang, S. P., Tao, Y. F., Wang, A. M., et al. (2021). A network pharmacology approach to investigate the anticancer mechanism of cinobufagin against hepatocellular carcinoma via downregulation of EGFR-CDK2 signaling. *Toxicol. Appl. Pharm.* 431, 115739. doi:10.1016/j.taap.2021.115739

Yang, F., Zhang, Y., Ressler, S. J., Ittmann, M. M., Ayala, G. E., Dang, T. D., et al. (2013). FGFR1 is essential for prostate cancer progression and metastasis. *Cancer Res.* 73, 3716–3724. doi:10.1158/0008-5472.can-12-3274

Yang, T., Jiang, Y. X., Wu, Y., Lu, D., Huang, R., Wang, L. L., et al. (2021). Resibufogenin suppresses triple-negative breast cancer angiogenesis by blocking VEGFR2-mediated signaling pathway. *Front. Pharmacol.* 12, 682735. doi:10.3389/fphar.2021.682735

Yang, Y., Ji, N., Cai, C. Y., Wang, J. Q., Lei, Z. N., Teng, Q. X., et al. (2020). Modulating the function of ABCB1: *In vitro* and *in vivo* characterization of sitravatinib, a tyrosine kinase inhibitor. *Cancer Commun.* 40, 285–300. doi:10.1002/cac2.12040

Yuan, X. F., Tian, H. Y., Li, J., Jin, L., Jiang, S. T., Liu, K. W., et al. (2014). Synthesis of bufalin derivatives with inhibitory activity against prostate cancer cells. *Nat. Prod. Res.* 28, 843–847. doi:10.1080/14786419.2014.881363

Yuan, Z., Shi, X., Qiu, Y., Jia, T., Yuan, X., Zou, Y., et al. (2017). Reversal of P-gp-mediated multidrug resistance in colon cancer by cinobufagin. *Oncol. Rep.* 37, 1815–1825. doi:10.3892/or.2017.5410

Zhai, X. F., Fang, F. F., Liu, Q., Meng, Y. B., Guo, Y. Y., and Chen, Z. (2013). MiR-181a contributes to bufalin-induced apoptosis in PC-3 prostate cancer cells. *Bmc Complem Altern. M.* 13, 325. doi:10.1186/1472-6882-13-325

Zhan, Y., Qiu, Y., Wang, H., Wang, Z., Xu, J., Fan, G., et al. (2020). Bufalin reverses multidrug resistance by regulating stemness through the CD133/nuclear factor-κB/MDR1 pathway in colorectal cancer. *Cancer Sci.* 111, 1619–1630. doi:10.1111/cas.14345

Zhang, C., Chao, F., Wang, S., Han, D., and Chen, G. (2022). Cell-free DNA as a promising diagnostic biomarker in prostate cancer: A systematic review and meta-analysis. *J. Oncol.* 2022, 1505087. doi:10.1155/2022/1505087

Zhang, C., Ma, K., and Li, W. Y. (2019). <p&gt;Cinobufagin suppresses the characteristics of osteosarcoma cancer cells by inhibiting the IL-6-OPN-STAT3 pathway</p&gt;. *Drug Des. Devel Ther.* 13, 4075–4090. doi:10.2147/dddt.s224312

Zhang, D. M., Liu, J. S., Deng, L. J., Chen, M. F., Yiu, A., Cao, H. H., et al. (2013). Arenobufagin, a natural bufadienolide from toad venom, induces apoptosis and autophagy in human hepatocellular carcinoma cells through inhibition of PI3K/Akt/mTOR pathway. *Carcinogenesis* 34, 1331–1342. doi:10.1093/carcin/bgt060

Zhang, D. M., Liu, J. S., Tang, M. K., Yiu, A., Cao, H. H., Jiang, L., et al. 2012). Bufotalin from Venenum Bufonis inhibits growth of multidrug resistant HepG2 cells through G2/M cell cycle arrest and apoptosis. *Eur. J. Pharmacol.* 692, 19–28. doi:10.1016/j.ejphar.2012.06.045

Zhang, J., Hong, Y., Xie, P., Chen, Y., Jiang, L., Yang, Z., et al. (2020). Spatial lipidomics reveals anticancer mechanisms of bufalin in combination with cinobufagin in tumor-bearing mice. *Front. Pharmacol.* 11, 593815. doi:10.3389/fphar.2020.593815

Zhang, J. J., Zhou, X. H., Zhou, Y., Wang, Y. G., Qian, B. Z., He, A. N., et al. (2019). Bufalin suppresses the migration and invasion of prostate cancer cells through HOTAIR, the sponge of miR-520b. *Acta Pharmacol. Sin.* 40, 1228–1236. doi:10.1038/s41401-019-0234-8

Zhang, L., Huang, X., Guo, T., Wang, H., Fan, H., and Fang, L. (2020). Study of cinobufagin as a promising anticancer agent in uveal melanoma through intrinsic apoptosis pathway. *Front. Oncol.* 10, 325. doi:10.3389/fonc.2020.00325

Zhang, P., Cui, Z., Liu, Y., Wang, D., Liu, N., and Yoshikawa, M. (2005). Quality evaluation of traditional Chinese drug toad venom from different origins through a simultaneous determination of bufogenins and indole alkaloids by HPLC. *Chem. Pharm. Bull.* 53, 1582–1586. doi:10.1248/cpb.53.1582

Zhang, P. W., Jiang, R. W., Ye, W. C., and Tian, H. Y. (2014). Bufadienolides from venom of *Bufo bufo* gargarizans. *Zhongguo Zhong Yao Za Zhi* 39, 841–845.

Zhang, W., Jiang, B., Liu, Y., Xu, L., and Wan, M. (2022). Bufotalin induces ferroptosis in non-small cell lung cancer cells by facilitating the ubiquitination and degradation of GPX4. *Free Radic. Bio Med.* 180, 75–84. doi:10.1016/j.freeradbiomed.2022.01.009

Zhang, X., Zhao, X., Liu, K., Che, Y., Qiu, X., Qu, Y., et al. (2020). Bufalin: A systematic review of research hotspots and antitumor mechanisms by text mining and bioinformatics. *Am. J. Chin. Med.* 48, 1633–1650. doi:10.1142/s0192415x20500810

Zhang, Y., Dong, Y., Melkus, M. W., Yin, S., Tang, S. N., Jiang, P., et al. (2018). Role of P53-senescence induction in suppression of LNCaP prostate cancer growth by cardiotonic compound bufalin. *Mol. Cancer Ther.* 17, 2341–2352. doi:10.1158/1535-7163.mct-17-1296

Zhao, L., Fu, L., Xu, Z., Fan, R., Xu, R., Fu, R., et al. (2019). The anticancer effects of cinobufagin on hepatocellular carcinoma Huh7 cells are associated with activation of the p73 signaling pathway. *Mol. Med. Rep.* 19, 4119–4128. doi:10.3892/mmr.2019.10108

Zhao, R., Ma, X., Bai, L., Li, X., Mamouni, K., Yang, Y., et al. (2021). Overcoming prostate cancer drug resistance with a novel organosilicon small molecule. *Neoplasia* 23, 1261–1274. doi:10.1016/j.neo.2021.11.006

Zheng, Y., Deng, L., Cao, H., Xu, N., Zhang, D., Tian, H., et al. (2022). Screening of bufadienolides from toad venom identifies gammabufotalin as a potential anti-inflammatory agent. *Planta Med.* 88, 43–52. doi:10.1055/a-1248-2626

Zhu, L., Chen, Y., Wei, C., Yang, X., Cheng, J., Yang, Z., et al. (2018). Anti-proliferative and pro-apoptotic effects of cinobufagin on human breast cancer MCF-7 cells and its molecular mechanism. *Nat. Prod. Res.* 32, 493–497. doi:10.1080/14786419.2017.1315575

# Investigation of preclinical pharmacokinetics of *N*-demethylsinomenine, a potential novel analgesic candidate, using an UPLC-MS/MS quantification method

Lulu Yu[1†], Xunjia Qian[1†], Yiheng Feng[1], Yujian Yin[1], Xiao-Dan Zhang[1], Qianqian Wei[1], Liyun Wang[1], Weiwei Rong[1,2], Jie-Jia Li[3], Jun-Xu Li[1]* and Qing Zhu[1,2]*

[1]School of Pharmacy, Nantong University, Nantong, Jiangsu, China, [2]Provincial Key Laboratory of Inflammation and Molecular Drug Target, Nantong, Jiangsu, China, [3]Center for Neural Developmental and Degenerative Research of Nantong University, Institute for Translational Neuroscience, Affiliated Hospital 2 of Nantong University, Nantong, Jiangsu, China

**N-** Demethylsinomenine (NDSM), the *in vivo* demethylated metabolite of sinomenine, has exhibited antinociceptive efficacy against various pain models and may become a novel drug candidate for pain management. However, no reported analytical method for quantification of **N-** Demethylsinomenine in a biological matrix is currently available, and the pharmacokinetic properties of **N-** Demethylsinomenine are unknown. In the present study, an ultra-high performance liquid chromatography with tandem mass spectrometry (UPLC-MS/MS) method for quantification of **N-** Demethylsinomenine in rat plasma was developed and utilized to examine the preclinical pharmacokinetic profiles of **N-** Demethylsinomenine. The liquid-liquid extraction using ethyl acetate as the extractant was selected to treat rat plasma samples. The mixture of 25% aqueous phase (0.35% acetic acid-10 mM ammonium acetate buffer) and 75% organic phase (acetonitrile) was chosen as the mobile phases flowing on a ZORBAX C18 column to perform the chromatographic separation. After a 6-min rapid elution, NDSM and its internal standard (IS), metronidazole, were separated successfully. The ion pairs of 316/239 and 172/128 were captured for detecting **N-** Demethylsinomenine and IS, respectively, using multiple reaction monitoring (MRM) under a positive electrospray ionization (ESI) mode in this mass spectrometry analysis. The standard curve met linear requirements within the concentration range from 3 to 1000 ng/mL, and the lower limit of quantification (LLOQ) was 3 ng/mL. The method was evaluated regarding precision, accuracy, recovery, matrix effect, and stability, and all the results met the criteria presented in the guidelines for validation of biological analysis method. Then the pharmacokinetic profiles of **N-** Demethylsinomenine in rat plasma were characterized using this validated UPLC-MS/MS method. **N-** Demethylsinomenine exhibited the feature of linear pharmacokinetics after intravenous (*i.v.*) or intragastric (*i.g.*) administration in rats. After *i. v.* bolus at three dosage levels (0.5, 1, and 2 mg/kg), **N-** Demethylsinomenine showed the profiles of rapid elimination with mean half-life ($T_{1/2Z}$) of 1.55–1.73 h, and extensive tissue distribution with volume of distribution ($V_Z$) of 5.62–8.07 L/kg. After *i. g.*

administration at three dosage levels (10, 20, and 40 mg/kg), **N-**Demethylsinomenine showed the consistent peak time ($T_{max}$) of 3 h and the mean absolute bioavailability of **N-** Demethylsinomenine was 30.46%. These pharmacokinetics findings will aid in future drug development decisions of **N-**Demethylsinomenine as a potential candidate for pain analgesia.

# 1 Introduction

Chronic pain usually refers to pain that persists or relapses for more than 3 months (Treede et al., 2019), which affects the physical and psychological health of patients in their daily life (Attal et al., 2018). Conventional oral analgesics are often chosen as the primary treatment for their fast action, low cost, and relative safety (Hylands-White et al., 2017). Although there are many analgesics available for clinical use, they all have some shortcomings such as limited efficacy or unexpected effects. Non-steroidal anti-inflammatory drugs (NSAIDs) are usually used as a starting medicine in treating pain, but they have limited efficacy against neuropathic pain and have a range of adverse effects related to the gastrointestinal, renal, and cardiovascular systems (Harirforoosh et al., 2013). Opioids are the most effective analgesics, but their broad unexpected effects can be serious and even lethal (Szigethy et al., 2018). Therefore, there is an urgent clinical need to discover new and effective analgesics with fewer side effects for the control of pain.

Traditional Chinese medicine (TCM) has a long history of human use and medicinal plants have been the sources of many successful modern medicines. Modern research on TCM has mostly focused on extracting and studying the pharmacology and mechanisms of ingredient compounds in TCM. Previous studies have found that sinomenine, a morphinan alkaloid, has significant analgesic properties in multiple chronic pain models (Zhao et al., 2012; Gao et al., 2013; Gao et al., 2014; Pertovaara, 2014; Zhu et al., 2016). However, clinical use of sinomenine is limited by its unexpected effects such as allergic and gastrointestinal reactions caused by strong histamine release and sedative effects (Zhang et al., 2018). *N*-Demethylsinomenine (NDSM), the demethylated derivative of sinomenine, is one of the bioactive ingredients of traditional Chinese herb *Sinomenium acutum*, and also an active metabolite of sinomenine (Cheng et al., 2007; Yi et al., 2012). Previous studies in our laboratory have shown that NDSM has analgesic effects against postoperative pain (Ou et al., 2018) and chronic pain (Zhou et al., 2021) without a sinomenine-like peripheral allergic reaction, and its sedative effect is far less than sinomenine (see Supplementary Figure S1 and Supplementary Table S1), suggesting that NDSM may be more advantageous than sinomenine for pain management.

Given the importance of pharmacokinetic profiling in preclinical drug development (Singh, 2006; Zheng et al., 2022), we aimed to continue our research into NDSM by extending the understanding of its pharmacokinetic profiles to rats. In the present study, a fast, accurate, and sensitive ultra-high performance liquid chromatography with tandem mass spectrometry (UPLC-MS/MS) method was established and certified to quantitatively detect NDSM in rat plasma. This method was utilized to investigate pharmacokinetics of NDSM after successful intravenous or oral administration.

# 2 Materials and methods

## 2.1 Chemicals and reagents

NDSM (purity >98.0% by HPLC purity analysis) was synthesized in-house and confirmed by NMR spectroscopy, which conformed to a previous report (Cheng et al., 2007). The internal standard (IS) metronidazole (purity >98.0%) was purchased from Beijing InnoChem Science and Technology Co., Ltd. (Beijing, China). Methanol and acetonitrile provided by Tedia (Fairfield, OH, United States) meet the requirements for mass spectrometry analysis. Chromatographic grade acetic acid, ammonium acetate, and ethyl acetate were purchased from Aldrich-Sigma (St Louis, MO, United States of America). Deionized water was provided by a Milli-Q ultrapure water preparation system (Millipore, MA, United States). Other reagents were all analytical grades.

## 2.2 Animals

Male and female Sprague-Dawley rats, weighing 200–250 g, were obtained from the Laboratory Animal Center of Nantong University (Nantong, China). Animals were acclimated under a controlled environment including humidity between 50%–70%, temperature of 25℃, and a 12-h light/dark cycle. All rats were subjected to overnight fasting with free access to water prior to the experiments. The animal protocols were approved by the Institution for Animal Care and Use Committee of Nantong University and followed the United States National Institutes of Health Guide for the Care and Use of Laboratory Animals (eighth edition).

## 2.3 Instruments and UPLC-MS/MS conditions

The UPLC-MS/MS system comprised an Agilent 1290 series UPLC system (Agilent Technologies, CA, United States) and a SCIEX 5500 QTrap triple quadrupole/linear ion trap hybrid mass spectrometer outfitted with an electrospray ionization (ESI) source (Applied Biosystems/MDS Sciex, ON, Canada). Equipment control, data, and analysis were acquired and manipulated by the Analyst 1.6.2 software (Applied Biosystems/MDS Sciex, ON, Canada).

Chromatography was conducted on an Agilent Eclipse XDB-C18 column (5 μm, 4.6 × 150 mm) attached to a guard column,

Agilent Eclipse XDB-C18 (5 μm, 4.6 × 12.5 mm). The temperature of the chromatographic column was kept at 30°C, and a 6-min isocratic elution program was conducted under aqueous phase A (10 mM ammonium acetate containing 0.35% acetic acid) and organic phase B (acetonitrile): 0–6 min (75% B). The flow rate was set as 0.3 mL/min, and 2 μL of analyte was injected into the analysis system. Mass spectrometry under ESI positive ion mode was conducted under the settings optimized as follows: nitrogen as the nebulizer gas, gas ion source 1 (50 psi), gas ion source 2 (50 psi), source temperature (350°C), and ion spray voltage (4000 V). Collision energy (CE), declustering potential (DP), collision exit potential (CXP), and entrance potential (EP) were optimized at 27, 160, 12, and 10 V for NDSM and 19, 103, 9, and 10 V for IS, respectively.

Quantitative detection was conducted based on multiple reaction monitoring (MRM) mode with parent-daughter ion transitions of m/z 316→239 for NDSM and m/z 172→128 for IS, respectively.

## 2.4 Standard solution and quality control (QC) samples

Stock solutions of NDSM (1 mg/mL) and IS (1 mg/mL) were prepared accurately in methanol and stored at −20°C. The standard working solutions (0.03, 0.1, 0.3, 1, 3, and 10 μg/mL) and QC solutions (0.06, 0.6, and 8 μg/mL) were acquired by serially diluting the stock solution of NDSM in methanol. The plasma standard samples (3, 10, 30, 100, 300, and 1000 ng/mL) used for the calibration curve were prepared by mixing 90 μL of blank rat plasma and 10 μL of standard working solutions. QC samples (6, 60, and 800 ng/mL, respectively) were prepared in the same way. The IS working solution was prepared in methanol to yield an ultimate concentration of 30 ng/mL.

## 2.5 Sample preparation

Ethyl acetate was selected as the extractant for liquid-liquid extraction (LLE). First, 100 μL of plasma samples spiked with 10 μL of IS working solution and 10 μL of 1M NaOH were vortexed for 1 min to mix. Subsequently, 1000 μL of ethyl acetate were added in two batches, each swirled for 8 min, followed by being centrifuged at 10,000 rpm for 10 min. The supernatant was transferred into a new centrifuge tube and then dried under nitrogen stream with water bath at 30°C. The residue was redissolved with 110 μL of 75% acetonitrile/water and then was centrifuged (12,000 rpm for 12 min) again. Finally, 80 μL of the supernatant was moved into an autosampler vial for analysis.

## 2.6 Method validation

To demonstrate the rationality of the UPLC-MS/MS method, the sensitivity, specificity, linearity, precision and accuracy, matrix effects, extraction recovery, and stability of NDSM in rat plasma were validated following the regulations and standards outlined by the Food and Drug Administration (FDA) in the United States (Kadian et al., 2016).

### 2.6.1 Specificity and sensitivity

The chromatograms of mixed blank plasma from six different healthy rats and six replicated standard plasma samples at the lower limit of quantification (LLOQ) spiked with IS (at final concentration of 30 ng/mL) was compared to assess the specificity and sensitivity of this method. In addition, the *in vivo* plasma samples after an oral dosage of NDSM (20 mg/kg) were also detected to assess whether this method with validated LLOQ was sensitive enough to cover all the *in vivo* plasma samples.

### 2.6.2 Linearity

In order to evaluate the linearity, six NDSM concentrations (3–1000 ng/mL) were calibrated and detected for six uninterrupted days. The linear equation was built up using least squares linear regression by plotting the peak area ratios of NDSM to IS on the ordinate (*Y*-axis) *versus* the concentration of NDSM on the abscissa (*X*-axis). Plasma samples spiked with NDSM at a final concentration of 3 ng/mL (LLOQ) represented the sensitivity of this method with the signal/noise (S/N) ≥ 10. The detection limit of NDSM was determined as 1 ng/mL (S/N ≥ 3).
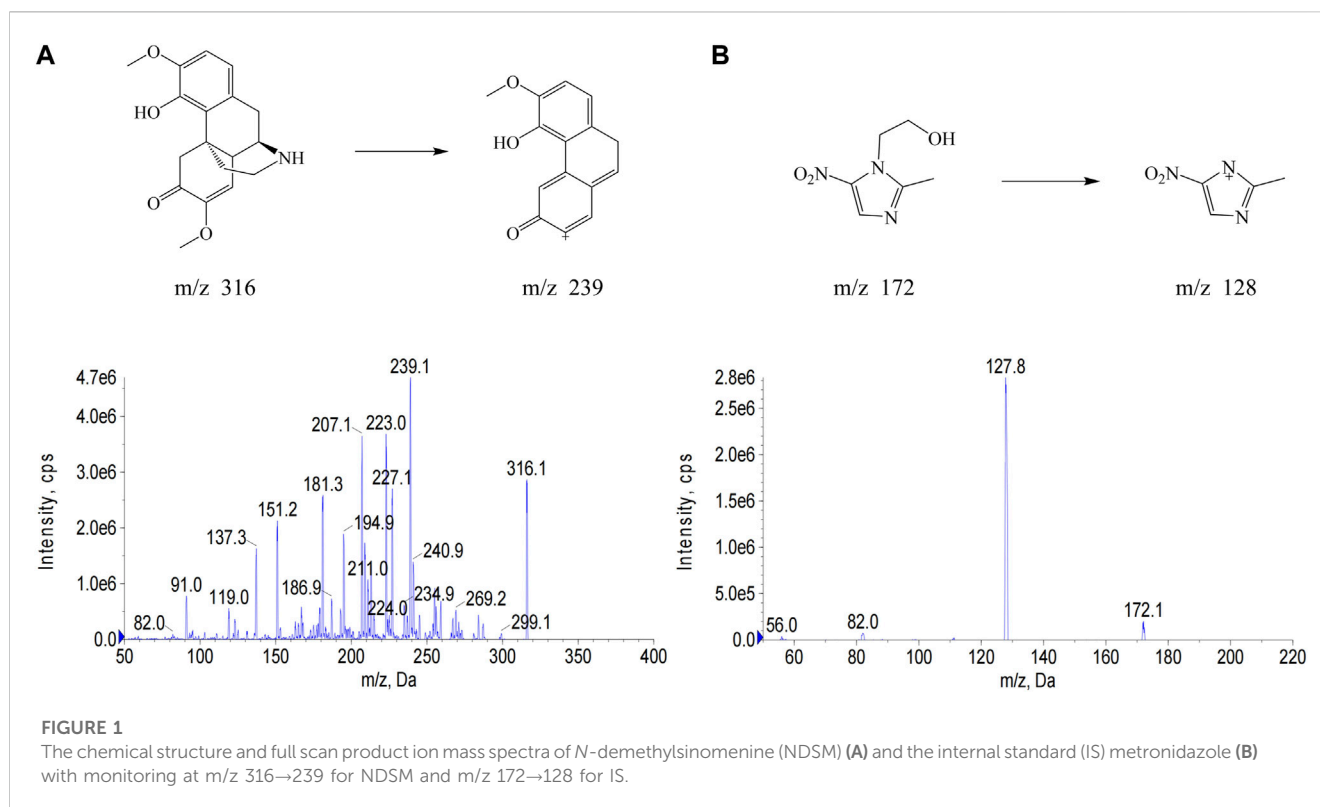
### 2.6.3 Precision and accuracy

To evaluate the precision and accuracy of the UPLC-MS/MS method, simulated plasma samples were analyzed at LLOQ and QC levels (3, 6, 60, and 800 ng/mL) with five replicates in each level on the same day and on three consecutive days, respectively. For LLOQ level, the precision (expressed as percent form of relative standard deviation, %RSD) must be within ±20%, and the accuracy (expressed as percent form of relative error, %RE) must be within ±20%. For QC levels, the precision should be within 15%, and the accuracy should range between −15% and 15%.

### 2.6.4 Recovery and matrix effect

The extraction recovery was tested by comparing the peak areas of NDSM from the extracted QC samples with those from the extracted blank plasma samples spiked with standard solutions at equivalent QC levels (6, 60, and 800 ng/mL). The matrix effect was investigated by comparing the peak areas from the extracted blank plasma samples spiked with standard solutions to those from methanol standard solutions at equivalent QC levels (6, 60, and 800 ng/mL). All QC samples were run in five replicates. The evaluation method for matrix effect and recovery of IS (30 ng/mL) was consistent with NDSM.

### 2.6.5 Stability

The stability of NDSM in the biological matrix was analyzed at QC levels under various storage conditions: untreated samples preserved at room temperature for 6 h (short-term stability), or in the −20°C for 30 d (long-term stability), or after three freeze-thaw cycles from −20°C to 25°C (freeze-thaw stability), and processed samples in the 4°C autosampler for 24 h (autosampler stability). Five independent samples were prepared for each concentration, and the %RSD and %RE were calculated. The judgment that samples were stable could be made if the deviation between the measured concentration and the nominal concentration was within 15.0%.

**FIGURE 1**
The chemical structure and full scan product ion mass spectra of *N*-demethylsinomenine (NDSM) **(A)** and the internal standard (IS) metronidazole **(B)** with monitoring at m/z 316→239 for NDSM and m/z 172→128 for IS.

### 2.6.6 Dilution integrity

Simulated plasma samples were prepared at a concentration of 2000 ng/mL, which was higher than the upper limit of quantification (ULOQ). The simulated plasma samples were diluted with blank rat plasma. The precision and accuracy of the diluted samples were not affected.

## 2.7 Pharmacokinetic application

To evaluate the bioavailability and pharmacokinetic profiles of NDSM, the plasma concentration of NDSM was measured after a single oral or intravenous administration at different dose levels. Six groups of rats were allocated randomly, each consisting of six rats, three male and three female, by oral gavage (10, 20, 40 mg/kg) or intravenous injection (0.5, 1, 2 mg/kg), respectively. Blood samples (approximately 0.4 mL) were collected from the tail vein into anticoagulant tubes at 0.083, 0.167, 0.333, 0.75, 1, 2, 3, 4, 6, 8, 12, and 24 h after intragastric administration (*i.g.*), and at 0.033, 0.116, 0.25, 0.5, 0.75, 1, 1.5, 2, 4, 6, and 8 h after intravenous administration (*i.v.*). According to the results from the concentration-dependent time curves obtained from our preliminary experiment, we designed this blood collection schedule to include all the absorption, distribution, and elimination phases. During the blood collection, the internal blood volume of rats was maintained by intravenously injecting 1 mL of normal saline to rats every three sampling intervals. Blood samples were centrifuged at 4000 rpm for 10 min, and then plasma supernatants were stored at −20°C.
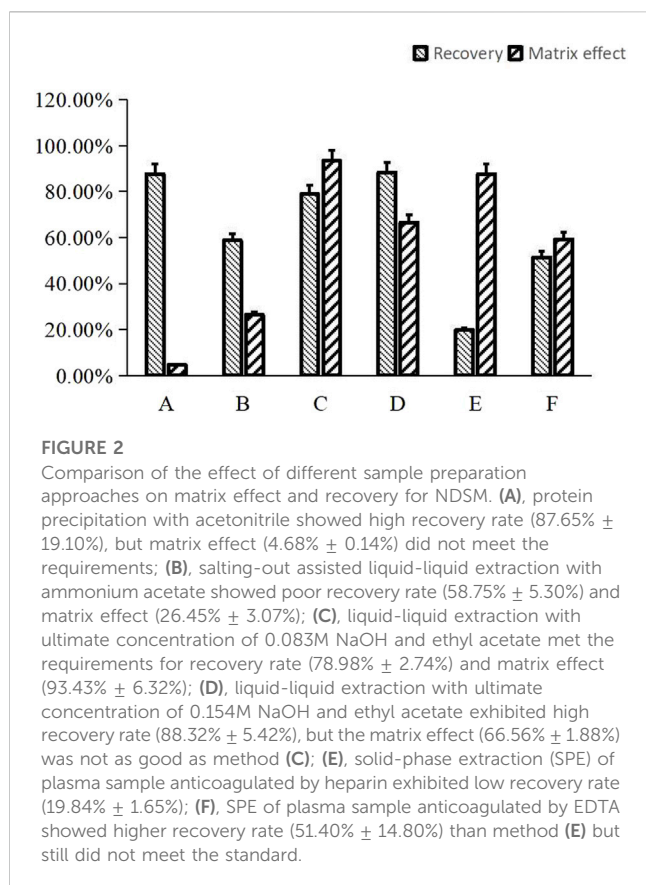
The pharmacokinetics parameters were calculated by the PKSolver software with a non-compartmental model (Zhang et al., 2010). The oral absolute bioavailability was calculated according to a previous report (Zheng et al., 2022). Statistical analyses were performed by one-way analysis of variance (ANOVA) followed by Tukey's *post hoc* analysis using GraphPad Prism 8.4 Software (San Diego, CA).

## 3 Results and discussion

## 3.1 Method development and optimization

### 3.1.1 Mass parameters and chromatography conditions

In this study, metronidazole, which also has nitrogen-containing heterocycles, was selected as the IS to avoid the interference of NDSM metabolites. The quasi-molecular ion (Q1 scan mode) and the major product ion fragments (MS2 scan mode) of NDSM and IS were obtained by injecting their net standard solution in methanol into the mass spectrometer coupled with electrospray ion source (Figure 1). The MRM with the transitions at m/z of 316→239 and 172→128 were selected for quantification of NDSM and IS, respectively, owing to their good separation and better peak intensity. Better peak shape and suitable retention time were obtained while the mobile phase was 10 mM ammonium acetate containing 0.35% acetic acid and acetonitrile. The total running time was 6 min, which was relatively quick and could be suitable for the detection of a large number of samples.

**FIGURE 2**
Comparison of the effect of different sample preparation approaches on matrix effect and recovery for NDSM. **(A)**, protein precipitation with acetonitrile showed high recovery rate (87.65% ± 19.10%), but matrix effect (4.68% ± 0.14%) did not meet the requirements; **(B)**, salting-out assisted liquid-liquid extraction with ammonium acetate showed poor recovery rate (58.75% ± 5.30%) and matrix effect (26.45% ± 3.07%); **(C)**, liquid-liquid extraction with ultimate concentration of 0.083M NaOH and ethyl acetate met the requirements for recovery rate (78.98% ± 2.74%) and matrix effect (93.43% ± 6.32%); **(D)**, liquid-liquid extraction with ultimate concentration of 0.154M NaOH and ethyl acetate exhibited high recovery rate (88.32% ± 5.42%), but the matrix effect (66.56% ± 1.88%) was not as good as method **(C)**; **(E)**, solid-phase extraction (SPE) of plasma sample anticoagulated by heparin exhibited low recovery rate (19.84% ± 1.65%); **(F)**, SPE of plasma sample anticoagulated by EDTA showed higher recovery rate (51.40% ± 14.80%) than method **(E)** but still did not meet the standard.

## 3.1.2 Comparison of the performance of sample preparation approaches

Endogenous compounds present in the biological matrix, such as phospholipids, proteins, and salts, can co-elute with the target analytes, and can interfere with mass spectrometric ionization, leading to ion enhancement or suppression (Desfontaine et al., 2018). We compared protein precipitation methods with methanol or acetonitrile (Wawrzyniak et al., 2018), salting-out assisted liquid-liquid extraction with ammonium acetate (Li et al., 2021), liquid-liquid extraction with ethyl acetate (Bao et al., 2017; Kanu, 2021), and solid-phase extraction (SPE) with C18 column (Lin et al., 2021).

After protein precipitation by adding three times the volume of methanol or twice the volume of acetonitrile to the simulated plasma sample containing IS, the extraction recovery rates of NDSM were higher than 95%, but both showed obvious suppressive matrix effect (4.68%), which led to poor sensitivity and so could not meet the requirements.

SPE is one of the key technologies for purifying complex biological fluids that can achieve good matrix effects (Lin et al., 2021). Acetonitrile containing 0.35% acetic acid was chosen as the eluent for C18 SPE column (Welch, Shanghai, China) to improve the elution capacity. Under a vacuum solid-phase extraction device (Merck, United States), we found that slowing down the elution rate and increasing the elution capacity of eluent could be beneficial for improvement of recovery, but it still could not achieve good extraction recovery (<60%).

Liquid-liquid extraction is a simple method with excellent extraction performance. In recent years, water-soluble solvent-assisted LLE methods, in which salts or sugars rather than hydrophobic solvents are used to treat biological samples, have been developed (Zhang et al., 2009). However, corrosion and clogging of mass spectrometry equipment caused by salt or sugar crystallization cannot be ignored. Compared to nonvolatile salts such as phosphate, this experiment used mass spectrometry-friendly ammonium acetate salting out assisted liquid-liquid extraction, but it was not effective in improving the recovery and matrix effect.

Previous studies have indicated that the addition of NaOH to plasma samples can slightly enhance the recovery of alkaloids (Xu et al., 2013). In this paper, 10 μL or 20 μL of 1 M NaOH was added into 100 μL plasma samples plus 10 μL IS solution to yield the ultimate concentration of 0.083 M or 0.154 M NaOH, then under these cases the recovery rates and matrix effects of NDSM were measured and compared. Finally, the results showed that twice liquid-liquid extraction using ethyl acetate to extract solvent when the plasma sample contained about 0.083 M NaOH can simultaneously achieve great recovery rate (78.98%) with no obvious matrix effect (93.43%), which met the requirements of detection (Figure 2).

## 3.2 Method validation

### 3.2.1 Selectivity, specificity, and sensitivity

The chromatograms of blank plasma, blank plasma spiked with NDSM at the LLOQ level and IS, and rat plasma samples after oral administration of NDSM (20 mg/kg) were demonstrated in Figure 3. No endogenous interference in the plasma was observed at the retention time of NDSM and IS, and the peak area of the blank signal recorded at abovementioned retention times was less than 5% that of NDSM (LLOQ level) and IS (30 ng/mL), showing good selectivity and specificity. So, the LLOQ was validated at 3 ng/mL, which was sensitive enough for the detection of the last time-point sample concentration.

### 3.2.2 Linearity and calibration curve

The standard curve exhibited superb linearity over the concentration range of 3–1000 ng/mL. The typical regression equation of the standard curve was Y = 0.00827X - 0.00652 (the correlation coefficient: 0.99955, weighting: 1/x).

### 3.2.3 Precision and accuracy

Table 1 summarized the results of intra-day and inter-day precision and accuracy of NDSM at the LLOQ and QC sample levels. The precision was expressed by %RSD, and the accuracy was represented by %RE. Both the %RSD and %RE values were below 15%, suggesting the outcomes were satisfactory.

### 3.2.4 Recovery and matrix effect

The matrix effect and extraction recovery for three QC samples of NDSM and IS were shown in Table 2. The findings demonstrated that the mean extraction recovery rate ranged from 73.55% to 81.88% for NDSM and was 94.19% for IS, suggesting that a high rate of extraction recovery was achieved. Importantly,
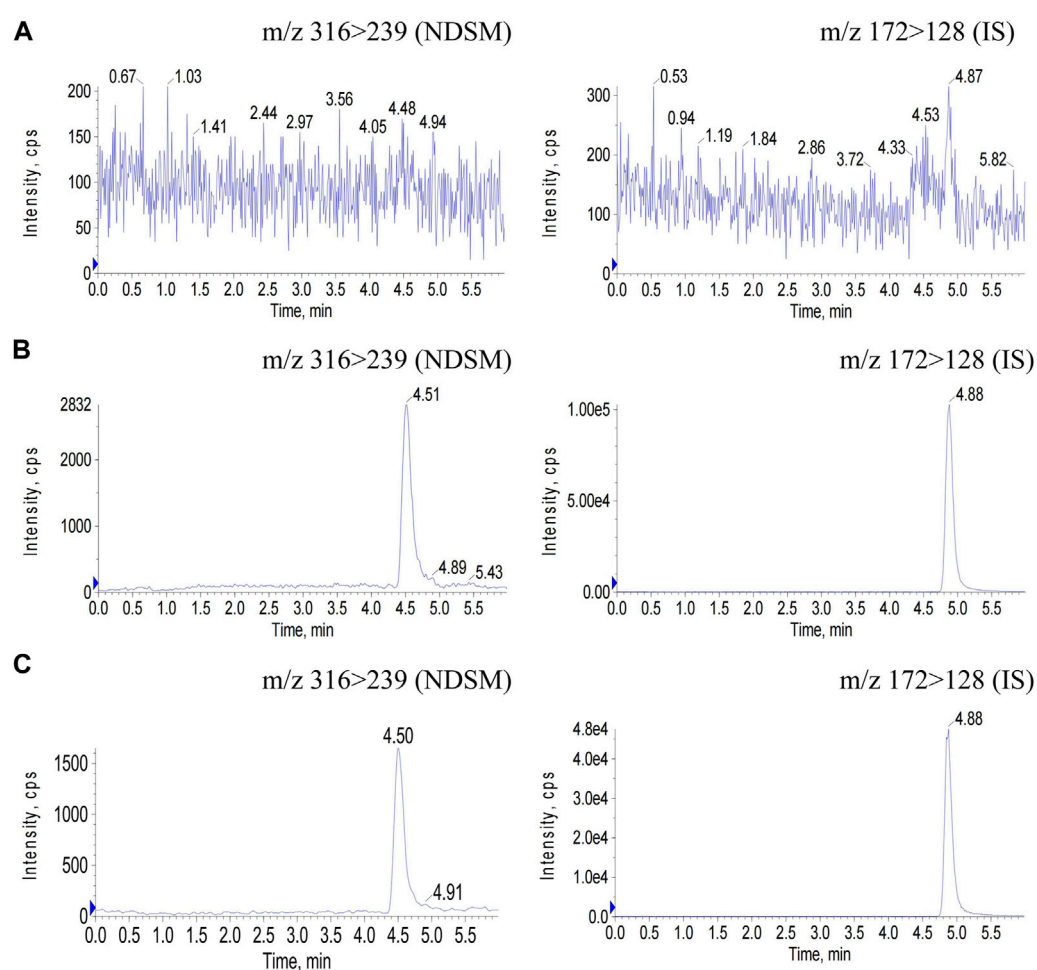
**FIGURE 3**
Chromatograms of NDSM (MRM 316/239) and IS (MRM 172/128) in rat plasma samples. **(A)** blank plasma sample; **(B)** blank plasma spiked with NDSM at the LLOQ level and IS; **(C)** plasma sample at 24 h after oral administration of NDSM (20 mg/kg). No interference peak in blank plasma samples was observed at the retention time of NDSM (4.5 min) and IS (4.8 min).

**TABLE 1 Precision and accuracy of NDSM in rat plasma.**

| QC conc. (ng/mL) | Intra-day (n = 5) | | | Inter-day (n = 15, 3 days) | | |
|---|---|---|---|---|---|---|
| | Mean ± SD ng/mL | Precision (RSD,%) | Accuracy (RE,%) | Mean ± SD ng/mL | Precision (RSD,%) | Accuracy (RE,%) |
| 3 (LLOQ) | 3.30 ± 0.33 | 10.05 | 9.93 | 3.25 ± 0.41 | 12.52 | 8.43 |
| 6.00 | 5.52 ± 0.42 | 7.68 | −7.92 | 6.44 ± 0.71 | 10.96 | 7.31 |
| 60.00 | 62.43 ± 3.60 | 5.77 | 4.04 | 59.87 ± 4.20 | 7.01 | −0.22 |
| 800.00 | 820.68 ± 29.51 | 3.60 | 2.58 | 787.65 ± 54.51 | 6.92 | −1.54 |

the extraction efficiency was independent of concentration and the precision was 2.41%–7.59% for NDSM and 2.38% for IS, suggesting it was stable and reproducible. Meanwhile, the mean matrix effect ranged from 92.95% to 103.96% for NDSM and was 89.73% for IS, which suggested no notable matrix effect on the determination.

### 3.2.5 Stability

The stability of short-term, long-term, freeze-thaw, and autosampler conditions was shown in Table 3. The accuracy (% RE) and precision (%RSD) of the stabilities were well within the acceptable limit (±15%), suggesting that there are no obvious problems in stability under the test conditions.

TABLE 2 Extraction recovery and matrix effect of NDSM (n = 5).

| | QC conc. (ng/mL) | Extraction recovery | | Matrix effect | |
|---|---|---|---|---|---|
| | | Mean ± SD (%) | RSD (%) | Mean ± SD (%) | RSD (%) |
| NDSM | 6.00 | 73.55 ± 2.75 | 3.74 | 97.65 ± 10.73 | 10.99 |
| | 60.00 | 78.44 ± 1.89 | 2.41 | 92.95 ± 7.78 | 8.37 |
| | 800.00 | 81.88 ± 6.21 | 7.59 | 103.96 ± 2.78 | 2.68 |
| IS | 30.00 | 94.19 ± 2.24 | 2.38 | 89.73 ± 0.42 | 0.47 |

TABLE 3 Stability data of NDSM in rat plasma (n = 5).

| Conditions | QC conc. (ng/mL) | Mean ± SD ng/mL | Precision (RSD,%) | Accuracy (RE,%) |
|---|---|---|---|---|
| Short-term stability (at room temperature for 6 h) | 6.00 | 5.53 ± 0.43 | 7.80 | −7.75 |
| | 60.00 | 57.39 ± 1.04 | 1.81 | −4.35 |
| | 800.00 | 761.50 ± 43.19 | 5.67 | −4.81 |
| Autosampler stability (processed samples at 4 °C autosampler for 24 h) | 6.00 | 6.57 ± 0.31 | 4.79 | 9.39 |
| | 60.00 | 63.62 ± 3.59 | 5.64 | 6.03 |
| | 800.00 | 821.64 ± 63.04 | 7.67 | 2.70 |
| Long-term stability (at −20 °C for 30 days) | 6.00 | 5.67 ± 0.72 | 12.74 | −5.46 |
| | 60.00 | 57.37 ± 2.72 | 4.75 | −4.38 |
| | 800.00 | 814.75 ± 33.02 | 4.05 | 1.84 |
| Freeze-thaw stability (3 cycles) | 6.00 | 5.74 ± 0.76 | 13.26 | −4.34 |
| | 60.00 | 57.51 ± 1.66 | 2.88 | −4.16 |
| | 800.00 | 793.01 ± 28.26 | 3.56 | −0.87 |

### 3.2.6 Dilution integrity and residue effect

The dilution integrity was measured when the plasma concentration of the *in vivo* sample was higher than the upper limit of quantification (ULOQ, 1000 ng/mL) of this method. The accuracy (%RE) and precision (%RSD) of the dilution integrity both were less than 15%, which met the requirements of quantitation. Furthermore, no obvious residue effect was observed when a blank sample was loaded after the calibration sample with the highest concentration.

## 3.3 Pharmacokinetics and bioavailability of NDSM

The UPLC-MS/MS method was developed and applied to study the pharmacokinetics of NDSM after intragastric administration (*i.g.*) and intravenous administration (*i.v.*) in rats. In our previous reports, intraperitoneal injection (*i.p.*) of 20 mg/kg NDSM exhibited significant antinociceptive effects against postoperative pain (Ou et al., 2018) and neuropathic pain (Zhou et al., 2021). In this study, three dosage levels of 10, 20, and 40 mg/kg were selected for *i. g.* administration. In a preliminary study, we found that the plasma

concentration of many *in vivo* samples exceeded ULOQ (1000 ng/mL) if intravenous dosage was higher than 2 mg/kg. Thus, we chose three dosage levels at 0.5, 1, and 2 mg/kg for intravenous pharmacokinetic study.

Figure 4 presented the average plasma concentration-time profiles and Table 4 summarized the main pharmacokinetic parameters of the non-compartment model for NDSM. In these concentration-time curves, the ratio of $AUC_{0-t}$ to $AUC_{0-\infty}$ was greater than 90% and the concentration of the last time point sample was under 1/10 of $C_{max}$, denoting that sampling schedule was appropriate and $AUC_{0-\infty}$ was reliable.

The pharmacokinetic profiles after *i. v.* administration at dosage of 0.5, 1, and 2 mg/kg showed similar average elimination half-life ($T_{1/2Z}$ of 1.55–1.73 h), mean residence time (MRT of 1.52–1.81 h), volume of distribution ($V_Z$ of 5.62–8.07 L/kg), and systemic clearance ($CL_Z$ of 2.51–3.34 L/kg/h), which had no significant differences between different dosage levels ($p > 0.05$). Similarly, the average elimination half-life ($T_{1/2Z}$ of 2.92–4.23 h) and mean residence time (MRT of 5.21–6.30 h) of the pharmacokinetic curves after oral administration of 10, 20, and 40 mg/kg also had no significant differences between different dosage levels ($p > 0.05$). We also analyzed the relationship of
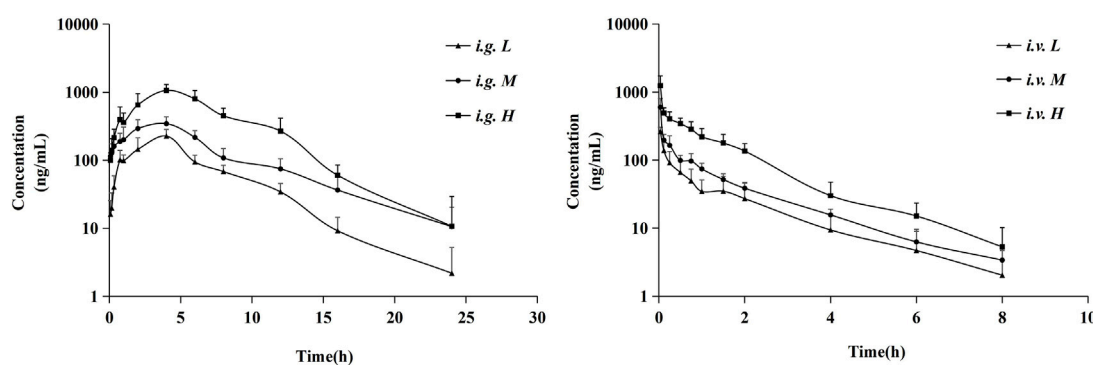
**FIGURE 4**
Mean plasma concentration profiles of NDSM after oral administration of 10 mg/kg (*i.g.* L), 20 mg/kg (*i.g.* M), and 40 mg/kg (*i.g.* H) and intravenous administration of 0.5 mg/kg (*i.v.* L), 1 mg/kg (*i.v.* M), and 2 mg/kg (*i.v.* H) (mean ± SD, n = 6). More details can be obtained in Table 4.

**TABLE 4 The estimated mean pharmacokinetic parameters of NDSM after oral or intravenous administration (mean ± SD, n = 6).**

| Parameters (unit) | Oral administration | | | Intravenous administration | | |
|---|---|---|---|---|---|---|
| | 10 mg/kg | 20 mg/kg | 40 mg/kg | 0.5 mg/kg | 1 mg/kg | 2 mg/kg |
| $C_{max}$ (ng/mL) | 226.42 ± 56.77 | 345.30 ± 89.68 | 1063.07 ± 242.20 | - | - | - |
| $C_{2\ min}$ (ng/mL) | - | - | - | 262.33 ± 42.62 | 598.98 ± 201.02 | 1243.18 ± 483.02 |
| $T_{max}$ (h) | 3 ± 0 | 3 ± 0 | 3 ± 0 | - | - | - |
| $T_{1/2Z}$ (h) | 3.45 ± 2.59 | 4.30 ± 1.12 | 2.92 ± 1.12 | 1.73 ± 0.71 | 1.70 ± 0.38 | 1.55 ± 0.76 |
| $AUC_{(0-t)}$ (ng/mL*h) | 923.80 ± 163.96 | 1958.50 ± 517.98 | 5416.40 ± 1100.90 | 176.03 ± 82.48 | 301.90 ± 54.87 | 828.34 ± 209.16 |
| $AUC_{(0-\infty)}$ (ng/mL*h) | 954.70 ± 163.98 | 2033.39 ± 573.54 | 5583.96 ± 1203.10 | 185.52 ± 85.74 | 310.99 ± 56.69 | 843.11 ± 215.07 |
| $AUC_{(0-t)}/AUC_{(0-\infty)}$ | 0.97 ± 0.02 | 0.97 ± 0.03 | 0.97 ± 0.02 | 0.94 ± 0.06 | 0.97 ± 0.02 | 0.98 ± 0.02 |
| MRT (h) | 5.21 ± 1.61 | 6.30 ± 1.48 | 5.35 ± 1.35 | 1.81 ± 0.67 | 1.71 ± 0.38 | 1.52 ± 0.36 |
| $V_Z$ (L/kg) | - | - | - | 7.99 ± 5.78 | 8.07 ± 1.98 | 5.62 ± 3.63 |
| $CL_Z$ (L/h/kg) | - | - | - | 3.26 ± 1.51 | 3.34 ± 0.83 | 2.51 ± 0.67 |
| F (%) | 26.24% ± 4.91% | 32.44% ± 6.73% | 32.69% ± 7.15% | - | - | - |

AUC from zero time to infinite ($AUC_{0-\infty}$) *versus* dose after intravenous and oral administration by linear regression analysis using GraphPad Prism 8.4 Software. As shown in Figure 5, results showed that the regression equation of AUC *versus* dose for intravenous administration was Y = 451.8X - 80.54 ($r^2$ = 0.9768, p = 0.0973), as well as Y = 157.6X - 820.6 ($r^2$ = 0.9768, p = 0.0693) for oral administration. According to the correlation coefficients ($r^2$) > 0.95 and the associated values of p > 0.05, it indicated a linear relationship between AUC and dose (Srinivas NR., 2015). These results indicated that the half-life of NDSM was independent of the dosage and did not extend with the increase of the dosage, while $AUC_{0-\infty}$ increased in proportion to the dose, suggesting that the elimination of NDSM was rapid and consistent with the linear kinetic characteristics.

The volume of distribution ($V_Z$ of 5.62–8.07 L/kg) far exceeding the total body fluid volume (0.6 L/kg) of rats (Zheng et al., 2022) demonstrated that the tissue distribution and extravascular uptake

of NDSM was extensive. The total clearance ($CL_Z$ of 2.51–3.34 L/kg/h) of NDSM was close to the rat hepatic flow velocity (3.3 L/kg/h) (Zheng et al., 2022), suggesting a quick clearance rate in rats.

The oral absolute bioavailability of 10, 20, and 40 mg/kg NDSM was calculated as 26.24% ± 4.91%, 32.44% ± 6.73%, and 32.69% ± 7.15%, respectively. The mean oral absolute bioavailability of NDSM was 30.46%, suggesting its suboptimal oral absorption. Additionally, NDSM showed a consistent time for peak plasma concentration ($T_{max}$) of 3 h after oral administration at the abovementioned three dosage levels. The oral half-life of NDSM (2.92–4.23 h) is longer than that of intravenous injection (1.55–1.73 h), which may be tentatively explained by the deconjugation of NDSM glucuronide through the enterohepatic circulation (Ohtani et al., 1994). In a previous study, the $T_{max}$, $T_{1/2}$ and oral bioavailability of rats after a single oral administration of 90 mg/kg sinomenine were 0.66h, 5.5h, and 79.6%, respectively, which demonstrated that sinomenine has fast oral absorption and
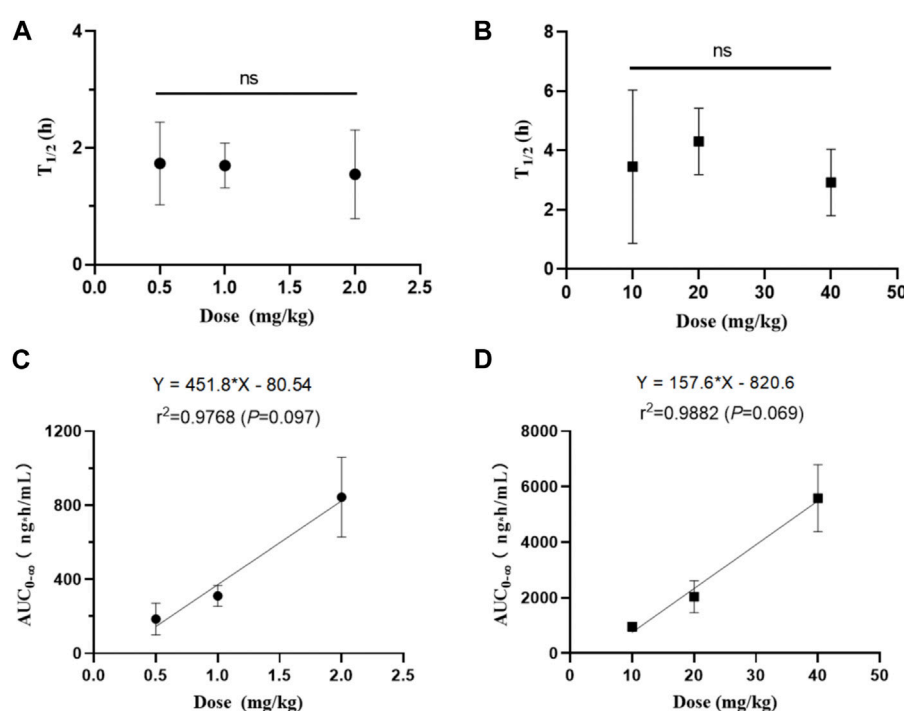
**FIGURE 5**
The relationship between half-life ($T_{1/2z}$) and dose of NDSM after single intravenous **(A)** and oral administration **(B)**, and the relationship between the area under the plasma concentration-time curve (AUC) and dose of NDSM after single intravenous **(C)** and oral administration **(D)** (mean $\pm$ SD, n = 6). The word "ns" indicated no differences for the half-life among the three dose levels ($p > 0.05$). The regression equation of AUC from zero to infinite ($AUC_{0-\infty}$) *versus* dose was Y = 451.8X - 80.54 ($r^2 = 0.9768$, $p = 0.0973$) for intravenous administration, and Y = 157.6X - 820.6 ($r^2 = 0.9768$, $p = 0.0693$) for oral administration. These results indicated that the half-life of NDSM was independent of the dosage and did not extend with the increase of the dosage, while $AUC_{0-\infty}$ increased in proportion to the dose.

high oral bioavailability (Liu et al., 2005a). Based on the longer half-life, a single oral administration of sinomenine (150 mg/kg) can maintain the effective drug concentration in rat plasma for a long time, but many adverse reactions were observed around 60 min after drug administration (Liu et al., 2005b). The studies on the metabolism and excretion of sinomenine found that sinomenine experienced phase I biotransformation and active hepatobiliary excretion, which was mainly regulated by P-glycoprotein (Tsai and Wu, 2003). NDSM, a phase I metabolite of sinomenine in urine, had a longer $T_{max}$ (3 h) and a shorter $T_{1/2Z}$ (2.92–4.23 h) than sinomenine after oral administration. Furthermore, the oral bioavailability of NDSM was less than half that of sinomenine. These changes may be due to the fact that the polarity and hydrophilicity was enhanced when sinomenine was metabolized to be NDSM. It was reported that sinomenine could not be transformed to demethylated metabolites by intestinal microbes *in vitro* due to its benzazepine structure (He et al., 2017). Whether the transmembrane absorption of NDSM in the stomach is less than that of sinomenine needs further investigation.

In addition, no gender differences were found in rats after intravenous or oral administration of NDSM (see Supplementary Tables S2–S7).

# 4 Conclusion

In this study, for the first time we have reported a rapid, simple, and sensitive UPLC-MS/MS method for the quantification of *N*-demethylsinomenine (NDSM) in rat plasma. Metronidazole was selected as IS to avoid confusion with potential metabolites and analogues of NDSM, improving the confidence of the assay. The method has a good linear relationship in the concentration range of 3–1000 ng/mL, while the LLOQ is 3 ng/mL. The method also meets the requirements in precision, accuracy, selectivity, and stability. The recovery rate and matrix effect can be satisfied by LLE with ethyl acetate twice. The method has been successfully applied to the preclinical pharmacokinetic study of NDSM in rats. By comparing AUC data from oral and intravenous administration, the mean oral absolute bioavailability of NDSM is determined as 30.46%. The current results provide useful data for further development of NDSM as a potential clinical candidate for the management of chronic pain.

# Data availability statement

The raw data supporting the conclusion of this article will be made available by the authors, without undue reservation.

## Ethics statement

The animal study was reviewed and approved by the Institutional Animal Care and Use Committee of Nantong University (protocol code S20200323-191 and date of approval is 10 March 2020).

## Author contributions

Conceptualization, QZ; data curation, LY, XQ, and YF; formal analysis, LY, XQ, and QZ; funding acquisition, QZ, J-XL, and J-JL; investigation, LY, XQ, and YF; methodology, LY, XQ, YF, YY, X-DZ, QW, and LW; project administration, QZ; resources, J-JL; software, WR; supervision, J-XL; validation, J-JL, WR, and J-XL; writing—original draft, LY; writing—review and editing, QZ. All authors contributed to the article and approved the submitted version.

## Funding

## Acknowledgments

## Conflict of interest

The authors declare that the research was conducted in the absence of any commercial or financial relationships that could be construed as a potential conflict of interest.

## Publisher's note

All claims expressed in this article are solely those of the authors and do not necessarily represent those of their affiliated organizations, or those of the publisher, the editors and the reviewers. Any product that may be evaluated in this article, or claim that may be made by its manufacturer, is not guaranteed or endorsed by the publisher.

## Supplementary material

The Supplementary Material for this article can be found online at: https://www.frontiersin.org/articles/10.3389/fchem.2023.1222560/full#supplementary-material

## References

Attal, N., Bouhassira, D., and Baron, R. (2018). Diagnosis and assessment of neuropathic pain through questionnaires. *Lancet Neurol.* 17 (5), 456–466. doi:10.1016/S1474-4422(18)30071-1

Bao, B. H., Kang, A., Zhao, Y., Shen, Q., Li, J. S., Di, L. Q., et al. (2017). A selective HPLC-MS/MS method for quantification of SND-117 in rat plasma and its application to a pharmacokinetic study. *J. Chromatogr. B Anal. Technol. Biomed. Life Sci.* 1052, 60–65. doi:10.1016/j.jchromb.2017.03.008

Cheng, W. M., Qiu, F., and Yao, X. S. (2007). Three major urinary metabolites of sinomenine in rats. *J. Asian Nat. Prod. Res.* 9 (1), 13–18. doi:10.1080/10286020500289444

Desfontaine, V., Capetti, F., Nicoli, R., Kuuranne, T., Veuthey, J. L., and Guillarme, D. (2018). Systematic evaluation of matrix effects in supercritical fluid chromatography versus liquid chromatography coupled to mass spectrometry for biological samples. *J. Chromatogr. B Anal. Technol. Biomed. Life Sci.* 1079, 51–61. doi:10.1016/j.jchromb.2018.01.037

Gao, T., Hao, J., Wiesenfeld-Hallin, Z., Wang, D. Q., and Xu, X. J. (2013). Analgesic effect of sinomenine in rodents after inflammation and nerve injury. *Eur. J. Pharmacol.* 721 (1-3), 5–11. doi:10.1016/j.ejphar.2013.09.062

Gao, T., Shi, T., Wang, D. Q., Wiesenfeld-Hallin, Z., and Xu, X. J. (2014). Repeated sinomenine administration alleviates chronic neuropathic pain-like behaviours in rodents without producing tolerance. *Scand. J. Pain* 5 (4), 249–255. doi:10.1016/j.sjpain.2014.05.006

Harirforoosh, S., Asghar, W., and Jamali, F. (2013). Adverse effects of nonsteroidal antiinflammatory drugs: An update of gastrointestinal, cardiovascular and renal complications. *J. Pharm. Pharm. Sci.* 16 (5), 821–847. doi:10.18433/j3vw2f

He, C. Y., Fu, J., Shou, J. W., Zhao, Z. X., Ren, L., Wang, Y., et al. (2017). *In vitro* study of the metabolic characteristics of eight isoquinoline alkaloids from natural plants in rat gut microbiota. *Molecules* 22 (6), 932. doi:10.3390/molecules22060932

Hylands-White, N., Duarte, R. V., and Raphael, J. H. (2017). An overview of treatment approaches for chronic pain management. *Rheumatol. Int.* 37 (1), 29–42. doi:10.1007/s00296-016-3481-8

Kadian, N., Raju, K. S., Rashid, M., Malik, M. Y., Taneja, I., and Wahajuddin, M. (2016). Comparative assessment of bioanalytical method validation guidelines for pharmaceutical industry. *J. Pharm. Biomed. Anal.* 126, 83–97. doi:10.1016/j.jpba.2016.03.052

Kanu, A. B. (2021). Recent developments in sample preparation techniques combined with high-performance liquid chromatography: A critical review. *J. Chromatogr. A* 1654, 462444. doi:10.1016/j.chroma.2021.462444

Li, M., Wang, H., Huan, X., Cao, N., Guan, H., Zhang, H., et al. (2021). Simultaneous LC-MS/MS bioanalysis of alkaloids, terpenoids, and flavonoids in rat plasma through salting-out-assisted liquid-liquid extraction after oral administration of extract from tetradium ruticarpum and Glycyrrhiza uralensis: A sample preparation strategy to broaden analyte coverage of herbal medicines. *Anal. Bioanal. Chem.* 413 (23), 5871–5884. doi:10.1007/s00216-021-03568-1

Lin, H., Chen, X., Ma, J., Zhang, X., Li, T., Zhang, Y., et al. (2021). Determination of propofol in human plasma with C18 pipette-tip based solid-phase extraction followed by liquid chromatography atmospheric-pressure chemical ionization tandem mass spectrometry analysis. *J. Pharm. Biomed. Anal.* 193, 113714. doi:10.1016/j.jpba.2020.113714

Liu, Z. Q., Chan, K., Zhou, H., Jiang, Z. H., Wong, Y. F., Xu, H. X., et al. (2005a). The pharmacokinetics and tissue distribution of sinomenine in rats and its protein binding ability *in vitro*. *Life Sci.* 77 (25), 3197–3209. doi:10.1016/j.lfs.2005.05.054

Liu, Z. Q., Zhou, H., Liu, L., Jiang, Z. H., Wong, Y. F., Xie, Y., et al. (2005b). Influence of co-administrated sinomenine on pharmacokinetic fate of paeoniflorin in unrestrained conscious rats. *J. Ethnopharmacol.* 99 (1), 61–67. doi:10.1016/j.jep.2005.01.052

Ohtani, M., Kotaki, H., Uchino, K., Sawada, Y., and Iga, T. (1994). Pharmacokinetic analysis of enterohepatic circulation of buprenorphine and its active metabolite, norbuprenorphine, in rats. *Drug Metab. Dispos.* 22 (1), 2–7.

Ou, Y., Su, M., Ling, Y., Wei, Q., Pan, F., Li, J., et al. (2018). Anti-allodynic effects of N-demethylsinomenine, an active metabolite of sinomenine, in a mouse model of postoperative pain. *Eur. J. Pharmacol.* 823, 105–109. doi:10.1016/j.ejphar.2018.01.044

Pertovaara, A. (2014). Sinomenine against neuropathic pain hypersensitivity. *Scand. J. Pain* 5 (4), 248. doi:10.1016/j.sjpain.2014.08.002

Singh, S. S. (2006). Preclinical pharmacokinetics: An approach towards safer and efficacious drugs. *Curr. Drug Metab.* 7 (2), 165–182. doi:10.2174/138920006775541552

Srinivas, N. R. (2015). Therapeutic drug monitoring of cyclosporine and area under the curve prediction using a single time point strategy: Appraisal using peak concentration data. *Biopharm. Drug Dispos.* 36 (9), 575–586. doi:10.1002/bdd.1967

Szigethy, E., Knisely, M., and Drossman, D. (2018). Opioid misuse in gastroenterology and non-opioid management of abdominal pain. *Nat. Rev. Gastroenterol. Hepatol.* 15 (3), 168–180. doi:10.1038/nrgastro.2017.141

Treede, R. D., Rief, W., Barke, A., Aziz, Q., Bennett, M. I., Benoliel, R., et al. (2019). Chronic pain as a symptom or a disease: The IASP classification of chronic pain for the international classification of diseases (ICD-11). *Pain* 160 (1), 19–27. doi:10.1097/j.pain.0000000000001384

Tsai, T. H., and Wu, J. W. (2003). Regulation of hepatobiliary excretion of sinomenine by P-glycoprotein in Sprague-Dawley rats. *Life Sci.* 72 (21), 2413–2426. doi:10.1016/s0024-3205(03)00118-8

Wawrzyniak, R., Kosnowska, A., Macioszek, S., Bartoszewski, R., and Jan, M. M. (2018). New plasma preparation approach to enrich metabolome coverage in untargeted metabolomics: Plasma protein bound hydrophobic metabolite release with proteinase K. *Sci. Rep.* 8 (1), 9541. doi:10.1038/s41598-018-27983-0

Xu, H., Li, Q., Yin, Y., Lv, C., Sun, W., He, B., et al. (2013). Simultaneous determination of three alkaloids, four ginsenosides and limonin in the plasma of normal and headache rats after oral administration of Wu-Zhu-Yu decoction by a novel ultra fast liquid chromatography-tandem mass spectrometry method: applicatio: Application of 4000Qtrap MS/MS system. *J. Mass Spectrom.* 48 (4), 519–532. doi:10.1002/jms.3183

Yi, L., Liang, Z. T., Peng, Y., Yao, X., Chen, H. B., and Zhao, Z. Z. (2012). Tissue-specific metabolite profiling of alkaloids in Sinomenii Caulis using laser microdissection and liquid chromatography-quadrupole/time of flight-mass spectrometry. *J. Chromatogr. A* 1248, 93–103. doi:10.1016/j.chroma.2012.05.058

Zhang, J., Wu, H., Kim, E., and El-Shourbagy, T. A. (2009). Salting-out assisted liquid/liquid extraction with acetonitrile: A new high throughput sample preparation technique for good laboratory practice bioanalysis using liquid chromatography-mass spectrometry. *Biomed. Chromatogr.* 23 (4), 419–425. doi:10.1002/bmc.1135

Zhang, Y., Huo, M., Zhou, J., and Xie, S. (2010). PKSolver: An add-in program for pharmacokinetic and pharmacodynamic data analysis in Microsoft Excel. *Comput. Methods Programs Biomed.* 99 (3), 306–314. doi:10.1016/j.cmpb.2010.01.007

Zhang, Y. S., Han, J. Y., Iqbal, O., and Liang, A. H. (2018). Research advances and prospects on mechanism of sinomenin on histamine release and the binding to histamine receptors. *Int. J. Mol. Sci.* 20 (1), 70. doi:10.3390/ijms20010070

Zhao, X. X., Peng, C., Zhang, H., and Qin, L. P. (2012). Sinomenium acutum: A review of chemistry, pharmacology, pharmacokinetics, and clinical use. *Pharm. Biol.* 50 (8), 1053–1061. doi:10.3109/13880209.2012.656847

Zheng, M. C., Tang, W. T., Yu, L. L., Qian, X. J., Ren, J., Li, J. J., et al. (2022). Preclinical pharmacokinetics and bioavailability of oxypeucedanin in rats after single intravenous and oral administration. *Molecules* 27 (11), 3570. doi:10.3390/molecules27113570

Zhou, Z., Qiu, N., Ou, Y., Wei, Q., Tang, W., Zheng, M., et al. (2021). N-Demethylsinomenine, an active metabolite of sinomenine, attenuates chronic neuropathic and inflammatory pain in mice. *Sci. Rep.* 11 (1), 9300. doi:10.1038/s41598-021-88521-z

Zhu, Q., Sun, Y., Mao, L., Liu, C., Jiang, B., Zhang, W., et al. (2016). Antinociceptive effects of sinomenine in a rat model of postoperative pain. *Br. J. Pharmacol.* 173 (10), 1693–1702. doi:10.1111/bph.13470

# Synthesis, characterization, and anti-cancer potential of novel p53-mediated Mdm2 and Pirh2 modulators: an integrated *In silico* and *In vitro* approach

Sarfaraj Niazi[1], C. P. Kavana[2], H. K. Aishwarya[3], Chandan Dharmashekar[2], Anisha Jain[3], Tanveer A. Wani[4], Chandan Shivamallu[2]*, Madhusudan N. Purohit[1]* and Shiva Prasad Kollur[5]*

[1]Department of Pharmaceutical Chemistry, JSS College of Pharmacy-Mysuru, JSS Academy of Higher Education and Research, Mysuru, India, [2]Department of Biotechnology and Bioinformatics, JSS Academy of Higher Education and Research, Mysuru, India, [3]Department of Microbiology, JSS Academy of Higher Education and Research, Mysuru, India, [4]Department of Pharmaceutical Chemistry, College of Pharmacy, King Saud University, Riyadh, Saudi Arabia, [5]School of Physical Sciences, Amrita Vishwa Vidyapeetham, Mysuru Campus, Mysuru, India

**Introduction:** Leukemia is a global health concern that requires alternative treatments due to the limitations of the FDA-approved drugs. Our focus is on p53, a crucial tumor suppressor that regulates cell division. It appears possible to stabilize p53 without causing damage to DNA by investigating dual-acting inhibitors that target both ligases. The paper aims to identify small molecule modulators of Mdm2 and Pirh2 by using 3D structural models of p53 residues and to further carry out the synthesis and evaluation of hit candidates for anti-cancer potency by *in vitro* and *in silico* studies.

**Methods:** We synthesized structural analogues of MMs02943764 and MMs03738126 using a 4,5-(substituted) 1,2,4-triazole-3-thiols with 2-chloro N-phenylacetamide in acetone with derivatives of PAA and PCA were followed. Cytotoxicity assays, including MTT, Trypan Blue Exclusion, and MTS assays, were performed on cancer cell lines. Anti-proliferation activity was evaluated using K562 cells. Cell cycle analysis and protein expression studies of p53, Mdm2, and Pirh2 were conducted using flow cytometry.

**Results:** As for results obtained from our previous studies MMs02943764, and MMs03738126 were selected among the best-fit hit molecules whose structural analogues were further subjected to molecular docking and dynamic simulation. Synthesized compounds exhibited potent anti-proliferative effects, with PAC showing significant cytotoxicity against leukemia cells. PAC induced cell cycle arrest and modulated p53, Mdm2, and Pirh2 protein expressions in K562 cells. Molecular docking revealed strong binding affinity of PAC to p53 protein, further confirmed by molecular dynamics simulation.

**Discussion:** The study presents novel anticancer compounds targeting the p53 ubiquitination pathway, exemplified by PAC. Future perspectives involve further optimization and preclinical studies to validate PAC's potential as an effective anticancer therapy.

# 1 Introduction

Cancer stands as a predominant global cause of mortality, wsitnessing a surge in affected individuals worldwide in recent years. This surge imposes substantial financial, emotional, and physical burdens on individuals, families, communities, and healthcare systems. Among the myriad forms of cancer, leukemia is anticipated to rank as the 11th most prevalent in terms of both incidence and cancer-related mortality. The hematologic malignancy arises from disrupting blood cell production in the bone marrow, where stem cells mature into red and white blood cells and platelets, (Prager et al., 2018). The uncontrolled proliferation of aberrant blood cells impedes the normal developmental process. The etiology of most leukemias remains largely spontaneous, with elusive causative factors. However, scientific investigations indicate a frequent association between these cancers and genetic abnormalities, immunosuppression, as well as exposure to risk factors such as ionizing radiation, carcinogenic chemicals, and oncogenic viruses (Hassan and Seno, 2020). Leukemia is commonly addressed through therapeutic modalities such as chemotherapy, targeted therapy, and stem cell transplantation. Additionally, ongoing research explores the potential of immunotherapy and emerging treatments in leukemia management. Despite the availability of FDA-approved treatments for leukemia, these therapies often result in adverse effects, including fatigue, edema, and muscle cramps. Notable treatments include APR-246 (Eprenetapopt), Nutlins (e.g., RG7112), and Idasanutlin (RG7388).Long-term use of these drugs can lead to hepatic and cardiac problems. Based on their unique mechanisms of action, anticancer drugs have been categorized into four groups: monoclonal antibodies, hormones, anti-tubulin and DNA-interactive hybrids, and antimetabolites. In the ongoing search for less harmful and more effective leukemia treatment strategies, additional therapeutic tumor suppressor paths must be explored (Marei et al., 2021).

Tp53 is known as a tumor suppressor, p53 is useful when it is activated in response to various cellular stressors such as DNA damage or oncogene activity. When it comes to cancer, proper regulation of p53 is essential because it is essential in limiting the unchecked proliferation and survival of cells containing genetic damage or mutations. p53 acts as a protective mechanism, limiting the unregulated proliferation of cells containing genomic defects that may eventually lead to cancer by coordinating cell cycle arrest, DNA repair, and apoptosis (Dittmar and Winklhofer, 2020). The canonical homo-tetrameric p53α protein, widely recognized as the "Guardian of the genome," emerges as a formidable tumor suppressor encoded by the Tp53 gene. p53 is a transcription factor that regulates numerous cell cycle pathways with previously unheard-of potency in the complex field of leukemia. Its profound ability to regulate essential cellular functions, maintain genomic integrity, and delay the onset of carcinogenesis,

makes it indispensable in the context of leukemia. p53 is a major molecular actor that protects cellular homeostasis, and it plays an important function in the treatment of leukemia. There are more than 500 known p53 DNA response elements (REs), which are 20-base pair sequences found in the promoter and enhancer regions of genes (Dittmar and Winklhofer, 2020). These REs are essential for interpreting the complex binding patterns of p53 and coordinating a range of cellular responses that impact outcomes including cell destiny, differentiation, DNA repair, and other physiological processes under stress conditions. The intricate network that controls the Tp53 gene family is influenced by microRNAs (miRNAs), which are crucial for maintaining the integrity of the genome. About 60% of coding genes are regulated by miRNAs, which have an impact on mRNA stability and translation. Research indicates that there is an increasing number of miRNAs that either directly or indirectly affect the Tp53 gene family. This intricate circuitry is mostly responsible for tumor prevention and is genetically modifiable. While treatment alternatives using miRNAs could be effective in fighting cancer, they are plagued by problems including poor cellular uptake, which emphasizes the need for efficient delivery methods and close observation for any side effects. This work focuses on the control of p53, which is regulated by several significant post-translational modifications, including phosphorylation and ubiquitination (Shin, 2023; Li and Zhang, 2022). Phosphorylation activates p53 and modifies its structural makeup, whereas ubiquitination is a more complex process that occurs only at lysine residues and impacts the fate of the substrate protein by forming polyubiquitin chains with distinct effects. It is challenging yet essential to comprehend the intricate interactions between p53 and various ubiquitinating E3 ligases, such as Mdm2 and Pirh2, to create effective anticancer drugs (Daks et al., 2022). Even though little research has been done on specific proteins like p53, Mdm2, and Pirh2, a deeper understanding of the protein-protein interaction network offers crucial insights into putative druggable hot spots, facilitating the development of novel modulators for therapeutic interventions against cancer (Daver et al., 2023). The development of dual-acting inhibitors that target both Mdm2 and Pirh2 E3(Ub)-ligases, with a focus on their promiscuous binding, can help overcome resistance and have a synergistic effect on p53 stabilization (Li et al., 2021). The potential of this method for treating cancer without causing DNA damage. This research aims to exploit a variety of chemical libraries and computational drug discovery techniques to create and identify small compounds that target the interactions between Pirh2 and Mdm2-p53.

The *in silico* results obtained from your previous studies Niazi and Purohit, 2015 were taken into consideration for synthesizing the potential anti-cancer molecules were synthesized using the standard protocol (Haronikova et al., 2021). Therefore, in the present investigation we synthesized structural analogues of MMs02943764 and MMs03738126 using a 4,5-(substituted) 1,2,4-triazole-3-thiols with 2-chloro N-phenylacetamide in

TABLE 1 Molecular physicochemical properties calculated for the synthesised 1, 2, 4-triazole analogues of PAA and PCA.

| Compound code | miLogP | TPSA (A²) | No. of atoms | HBA | HBD | Lipinski's violations | Rotatable bonds | Volume (A³) |
|---|---|---|---|---|---|---|---|---|
| PAC, 8(a) | 4.89 | 69.05 | 31 | 6 | 1 | 1 | 8 | 380.96 |
| PAA, 8(e) | 4.21 | 69.05 | 30 | 6 | 1 | 0 | 8 | 367.43 |

acetone with derivatives of PAA and PCA were characterized by employing infrared (IR), 1H nuclear magnetic resonance (NMR) and Mass spectral studies. The aim of this study is to identify small molecule modulators capable of targeting Mdm2 and Pirh2, two critical regulators of the tumor suppressor protein p53, utilizing 3D structural models of specific p53 residues. Further synthesized compounds were subjected to *in vitro* activities to evaluate their cytotoxicity profile. A computational docking method and molecular dynamics (MD) simulations are used to validate and modify promising hit candidate, ensuring their structural stability and potential efficacy of a synthesized compound (Devi et al., 2022).

# 2 Materials and methods

## 2.1 Chemicals

Chemical agents used in the present study included (DMEM and DMSO; S.D. Fine chemicals Ltd., Bengaluru, India), (Trypsin-EDTA Solution; SRL Chemicals, Mumbai, India), (FBS; Sigma, Bengaluru, India), (Camptothecin; Sigma, Bengaluru, India), (Antibodies; Abcam, Waltham, Boston, United States), (37°C incubator with humidified atmosphere of $CO_2$; Healforce, China), (Cell line: K562—procured from NCCS, Pune, India). HT microplate spectrophotometer reader was purchased from BioTek (Gujarat, India).

## 2.2 Synthesis of structural analogues of the MMs02943764 and MMs03738126

The structural analogues of MMs02943764 and MMs03738126 consisting of 1, 2, 4 triazole scaffold derived from molecular docking were synthesized as per the Scheme-1 and molecular physicochemical properties of 1, 2, 4-triazole derivatives are presented in (Table 1).

### 2.2.1 General experimental procedure for synthesizing 2-(4, 5-substituted) 1, 2, 4-triazole-3-ylthio)-N-(p-substituted)-phenyl acetamide derivatives of PAA and PCA

To a solution of appropriate 4, 5-(substituted) 1, 2, 4-triazole-3-thiols, (0.001 mol) in 30 mL acetone, appropriate 2-chloro N-phenylacetamide, (0.001 mol) was added. The mixture was vortexed under reflux condition for 3–5 h in the presence of anhydrous $K_2CO_3$ (0.005 mol, 0.69 g). The reaction was monitored by TLC using a mixture of ethyl acetate and hexane in 1:1 ratio as the mobile phase. The reaction mixture was filtered and poured into a beaker containing ice cubes. The precipitate formed was filtered, rinsed with cold water and recrystallized from ethanol to obtain

2-(4, 5substituted)-1, 2, 4-triazole-3-ylthio)-N-(p-substituted)-phenyl acetamide derivatives (Ali et al., 2021).

## 2.3 Characterization of synthesized compounds

Perkin Elmer FT-IR type 1650 spectrophotometer was used to record the infrared spectra of the synthesized compounds within the range of 4000–400 $cm^{-1}$ considering the Potassium bromide pellets. The 1H-NMR was analyzed using a Bruker AV-500 spectrometer and DMSO-$d_6$ was used as a solvent and tetramethylsilane was used as internal standard. The mass spectroscopy of synthesized compounds was analyzed using Agilent technologies (HP) 5973 mass spectrometer with an ionization potential of 70 eV.

## 2.4 Cytotoxicity assay

### 2.4.1 MTT assay

The evaluation of cytotoxicity was performed using MTT assay. The K562 cells were plated in a 96-well culture plate with various concentrations (25 μM–160 μM) of the methanol extract and fractions. The cultured plates were incubated for 24, 48, and 72 h at 37°C and 5% $CO_2$. Following incubation, 20 μL MTT solution in phosphate-buffered saline (PBS) was added to each well at a final concentration of 0.5 mg/mL followed by further incubation for 3 h at 37°C. The medium was then removed, and 100 μL DMSO was added to each well for solubilizing the formazan. The absorbance was measured at 490 nm (630 nm as a reference) using an ELISA reader (SkanIt™ Software, Microplate Readers, Thermo Fisher Scientific). Three independent experiments were carried out, and 8 replicates were taken for each experiment. The concentration of the methanol extract and fractions which resulted in a 50% reduction of cell viability, the half maximal inhibitory concentration (IC50 value), was calculated using the following formula: % inhibition = (control abs - sample abs)/(control abs) × 100. Paclitaxel was used as a positive control at the concentration of 0.2–50 μg/mL (Ghasemi et al., 2021).

### 2.4.2 Trypan blue exclusion assay

To evaluate the antiproliferative effects of the novel PAC and PAA compound, the trypan blue exclusion assay was performed. Cell K562 were seeded into 12-well plates at a density of $2 \times 10^4$ cells/well. After 24 h, cells were exposed to the tested compounds at concentrations corresponding to their respective IC50 values and then incubated for 72 h. Subsequently, cells were harvested and centrifuged at 500 $g$ for 5 min. Following centrifugation, the supernatant was discarded, and the cell sediment was dissolved in 0.2 mL of PBS. Next, 10 μL of the cell solution was mixed with 10 μL of trypan blue dye. Cell counting was performed using an automatic cell

counter (Countessa). The data obtained were expressed as the mean ± standard deviation (SD), and the mean percentage of viable cells was calculated from three independent experiments, each performed in triplicate (Tavares-Carreón et al., 2020).

### 2.4.3 MTS assay

The cytotoxicity of synthesized compounds was evaluated by MTS assay using the K562 cancer cell line. The cancer cells were cultured in DMEM (Gibco, United States) supplemented with 10% FBS (Gibco, United States) at 37°C with 5% $CO_2$. Briefly, a total of 2000 K562 cells for each well were cultured overnight in a 96-well plate. Then, the novel PAC and PAA compound or Doxorubicin were added to each well at varied concentrations (0.01 μM, 0.1 μM, 1 μM, 10 μM, 100 μM). After 4 days, MTS and PMS were added to the cell culture and incubated at 37°C for 2–3 h. The absorbance was measured at 490 nm to quantify the viable cells. The growth ratio of treated cells was calculated by comparing the absorbance to the non-treated cells (Ma et al., 2022).

## 2.5 Anti-proliferation activity

The K562 cells ($1 \times 10^6$ cells/well) were procured from ATCC. The stock cells were cultured in DMEM which is supplemented with inactivated FBS (10%), penicillin (1%; 100 IU/mL), and streptomycin (100 μg/mL) was added in a humidified atmosphere containing $CO_2$ (5%) at 37°C until confluent. The cells are dissociated with TPVG solution having a composition of trypsin (0.2%), EDTA (0.02%), and glucose (0.05%) dissolved in PBS. The viability of the cells is then checked using trypan blue and centrifuged. Further, $5.0 \times 10^4$ cells/well were seeded in a 96 well plate and finally incubated for 24 h in $CO_2$ (5%) incubator at 37°C.

The monolayered cell culture was trypsinised. The cell count was brought to $5.0 \times 10^5$ cells/mL by using the medium containing 10% FBS. Next, 100 μL of diluted cell suspension was added to each well of the microtiter plates. After 24 h, when the monolayer is formed, the supernatant is removed. 100 μL of different experimental compounds added to the wells containing the monolayer. These plates were kept for incubation in $CO_2$ (5%) incubator for 24 h at 37°C and cells will be periodically checked for physical changes such as granularity, shrinkage, and swelling. After 24 h of incubation, the sample solution was removed from the wells. 100 μL of MTT (5 mg/10 mL of MTT in PBS) was added to the wells. The plates were gently shaken and incubated for 4 h at 37°C under the $CO_2$ (5%) environment. The supernatant was removed and DMSO (100 μL) was added. The plates were again gently shaken to solubilize the formazan produced in the viable cells. The absorbance values were taken from the microplate reader at a wavelength of 590 nm. The percentage growth inhibition has been calculated as per the protocol (Tian et al., 2022).

## 2.6 Cell cycle analysis by flow cytometry

To analyze the cell cycle phase distribution, K562 cells ($1 \times 106$ cells/well) were seeded in a 6- well plate for 48 h and then exposed to the experimental compounds (PAC (68.44 μM) and standard drug, Calprotectin (25 μM)) and control. After incubation for 48 h, the untreated and treated cells were rinsed 2x with PBS. The cells are then fixed in 70% ethanol at −20°C for 30 min. The fixed

cells were again washed with PBS and 50 μL of RNase solution was added. 400 μL of PI solution/million cells added directly to the cell's RNase A suspension. Mixed well and incubated for 20–30 min at room temperature in the absence of light. The cell cycle was measured with BD FACSCalibur™ and the percentages of cells (10,000 cells in total) in the different phases (G1, S, and G2) were calculated by the Cell Quest software (BD Biosciences) (Bunney et al., 2017).

## 2.7 p53, Mdm2, and Pirh2 protein expression studies using flow cytometry

The K562 cells ($1 \times 10^6$ cells/well) was seeded in a 6-well plate and incubated under $CO_2$ atmosphere at 37°C for 24 h. After 24 h, the cells were cultured in a medium containing required concentrations of experimental compounds and controls for 24 h. Cells were then washed twice with PBS and 200 μL of trypsin-EDTA solution was added. The mixture was then incubated at 37°C for 3–4 min. To this, 2 mL culture medium was added, and the cells were harvested directly into the 12 × 75 mm polystyrene tubes followed by centrifugation and 1xPBS wash. PBS was decanted completely, and the cells were fixed with 70% chilled ethanol followed by incubation at −20°C for 30 min 20 μL of primary antibody (p53/Mdm2/Pirh2) was added (Parrales et al., 2016). The cells were washed with 2xPBS and treated with 20 μL of secondary fluorescent antibody Phycoerythrin (PE) and incubated for 30 min at room temperature in dark condition. The cells were then rinsed with 1xPBS to remove unbound secondary antibody and re-suspended in the 0.5 mL of PBS. The cells were analyzed for p53, Mdm2, and Pirh2 proteins expression by using BD FACSCalibur™. At least ten thousand cells were counted for each sample (Bunney et al., 2017).

## 2.8 Computational analysis

### 2.8.1 Ligand preparation

The 3D structures of the predicted bioactive ligand (PAC) were meticulously prepared utilizing the Ligand Prep module within the Schrödinger suite. Through this process, the ligands were subjected to minimization procedures to optimize their conformations. The resulting refined ligands were subsequently assessed for their binding affinity through molecular docking analyses (Bunney et al., 2017).

### 2.8.2 Protein preparation and binding site analysis

The Structure of Human MDM2 Protein (PDB ID: 3LBK) was retrieved from the Protein Data Bank and prepared using Maestro's Protein Preparation Wizard. This involved meticulous refinement, including the removal of atomic clashes, water molecules, and unnecessary atoms, as well as the addition of missing atoms and hydrogen. The Sitemap tool in Maestro was then employed to generate the binding site, facilitating precise analysis of potential targets within the TP53 pathway. These procedures, employing advanced computational tools, establish a robust foundation for elucidating protein interactions and exploring therapeutic strategies within the TP53 pathway (Hatami et al., 2023).

TABLE 2 Experimental physical data of the synthesized 1, 2, 4 triazole.

| Compound code | Molecular formula ($^S$) | M.W (gm) | M.P. (°C) | $R_f$ | % yield |
|---|---|---|---|---|---|
| PAC, 8(a) | $C_{25}H_{24}N_4O_3$ | 450.94 | 164 | 0.37 | 41.73 |
| PAA, 8(e) | $C_{23}H_{20}N_4O_2$ | 416.00 | 111 | 0.34 | 58.32 |
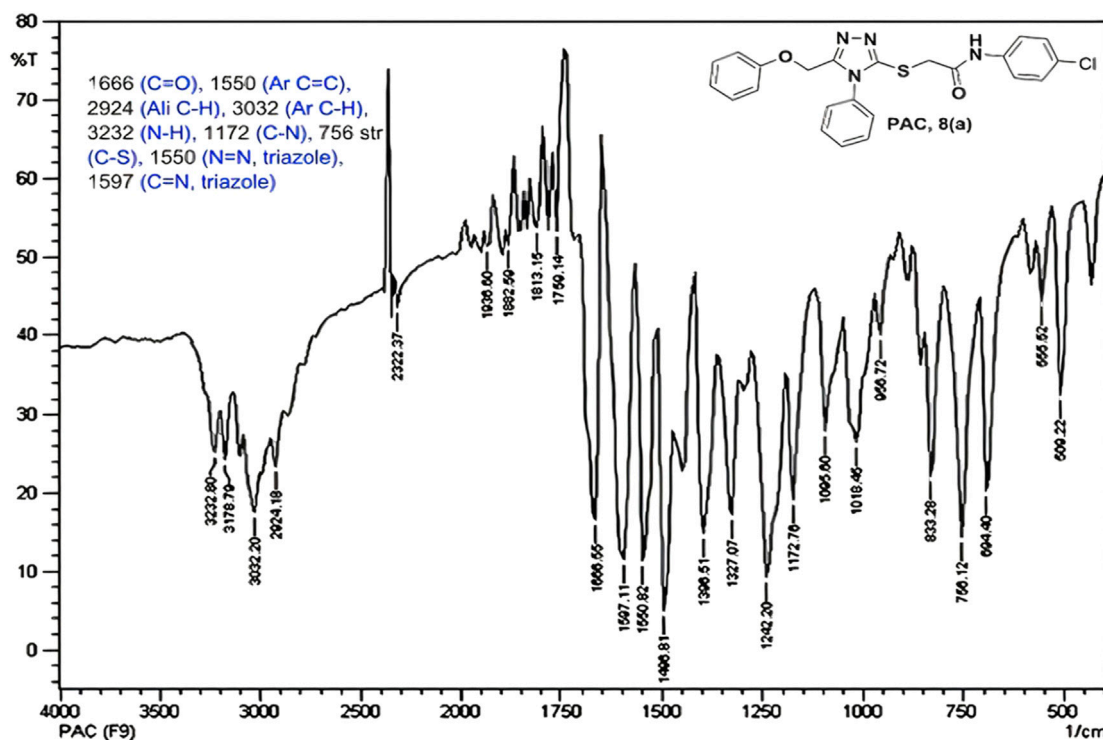


**FIGURE 1**
IR spectrum of PAC.

## 2.8.3 Molecular docking

The docking study utilized the Glide (Grid-based Ligand Docking with Energetics) protocol, as described by Friesner et al., in 2004. A two-tier docking approach was employed, involving standard precision (SP) and extra precision (XP). The compounds were docked using Glide, and the resulting conformers were systematically evaluated using the Glide score reprise (Ban et al., 2018).

## 2.8.4 Molecular dynamic simulation

The compounds underwent filtration based on criteria such as Glide score (Kcal/mol), protein-ligand non-bonded interactions, ligand-active site complementarity, and a review of relevant literature. The top complex, selected through this screening process, underwent further scrutiny via MD Simulations utilizing the Desmond module within the Schrödinger Suite 2022-23 (https://newsite.schrodinger.com/platform/products/maestro/). The analysis aimed to evaluate intermolecular interactions and the stability of the complex across varying time scales. For system construction, the TIP3P solvent model and an orthorhombic water box shape were chosen, with the addition of counter ions for system neutralization. The resulting model system was loaded into the molecular dynamics work panel, and the simulation run time was set at 200 ns. Post-simulation, the complexes were analyzed

using the simulation interaction diagram panel within the Desmond module (Du et al., 2016; Kaushik et al., 2018).

## 2.9 Statistical analysis

All experiments were conducted in triplicate, data were presented as mean ± standard error of the mean (SEM). Student's t-test was employed for comparing between two groups in the *in vitro* assay. To assess the statistical significance of the data, one-way analysis of variance (ANOVA) was utilized, with a significance level set at $p < 0.05$. Statistical analysis was performed using GraphPad Prism 8.0 (Aly et al., 2020).

# 3 Results and discussion

## 3.1 Synthesis and characterization of compounds consisting of 1, 2, 4triazole scaffolds of PAA and PAC

The free mercapto group present in the 1,2,4-triazole intermediate readily reacts with appropriate chloroacetamide under dry conditions
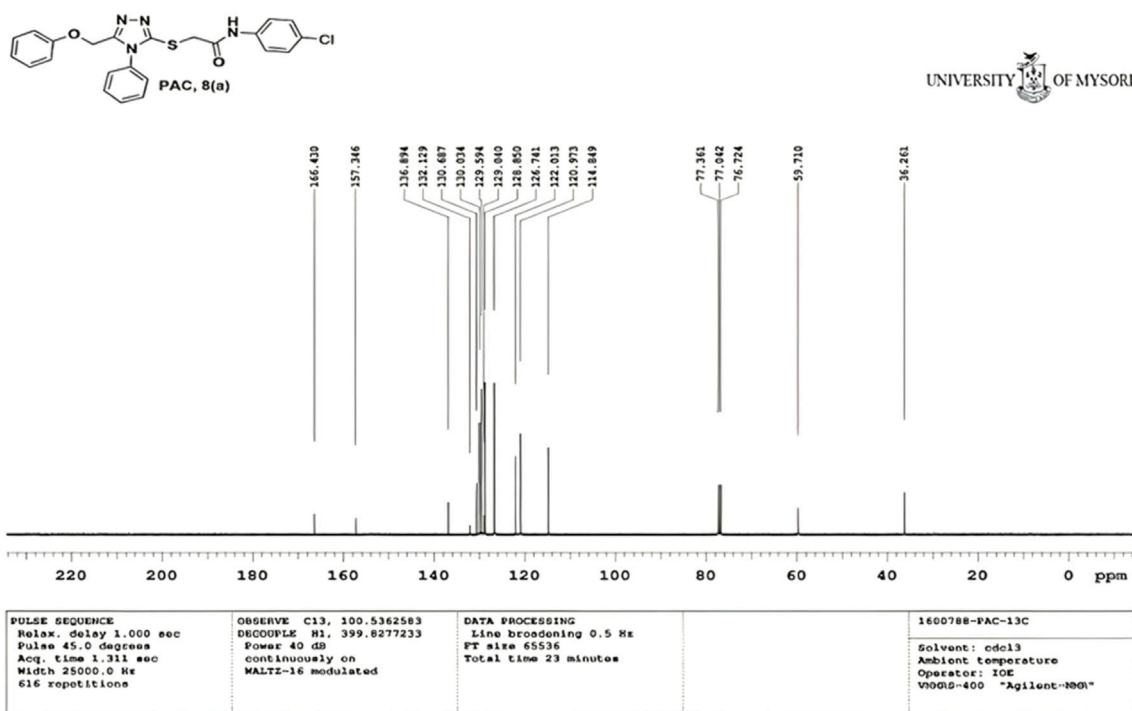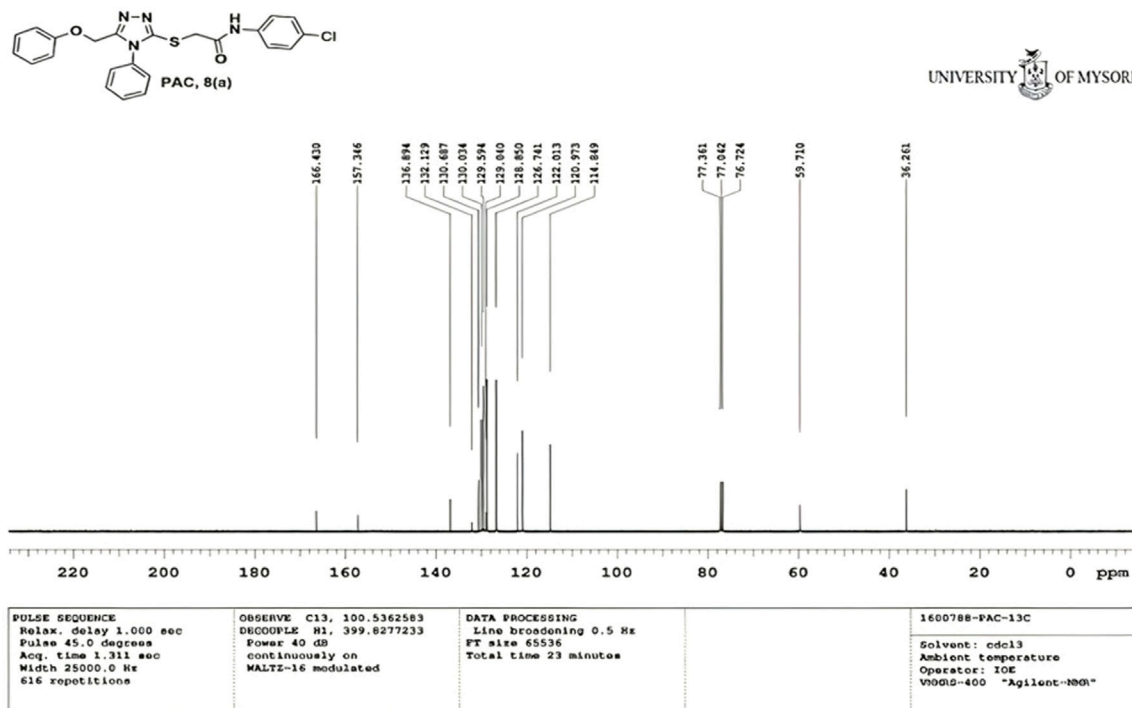
**FIGURE 2**
^{1}H NMR spectrum of PAC.



**FIGURE 3**
^{13}C NMR spectrum of PAC.

**FIGURE 4**
Mass spectrum of PAC.



**FIGURE 5**
^{1}H NMR spectrum of PAA.

to yield the final compounds of PAA and PAC. The synthesized compounds of PAA and PAC were characterized by determining physical constants (Rf values and melting points) and different spectroscopic methods such as IR, ^{1}H NMR, 13C NMR, Mass spectroscopy and single crystal XRD. The experimental physical data of the synthesized compounds of PAA and PAC is provided in Table 2 and the calculated values of molecular physicochemical properties are shown in Table 1 (see materials and methods section).

IR spectra of all the synthesized compounds of PAA and PAC showed stretching absorption bands around regions 1550–1570 cm$^{-1}$

due to N=N and 1560–1640 cm$^{-1}$ due to C=N functions confirming the presence of 1,2,4-triazole ring. The absence of absorption band around 2576 cm$^{-1}$ which corresponds to–SH group and retaining of absorption band −750 cm$^{-1}$ corresponded to C-S function confirms the coupling of triazole ring with acetamides via. reactive -SH group. The spectral characterization by ^{1}H NMR spectra of all the synthesized compounds of PAA and PAC showed the chemical shift signals in the range of δ 6.77–6.9 ppm (Ar-H) resonated as multiplet for aromatic protons. The NH proton corresponded to the amide group resonated as a singlet and showed the chemical shift signal around 10.3 ppm.
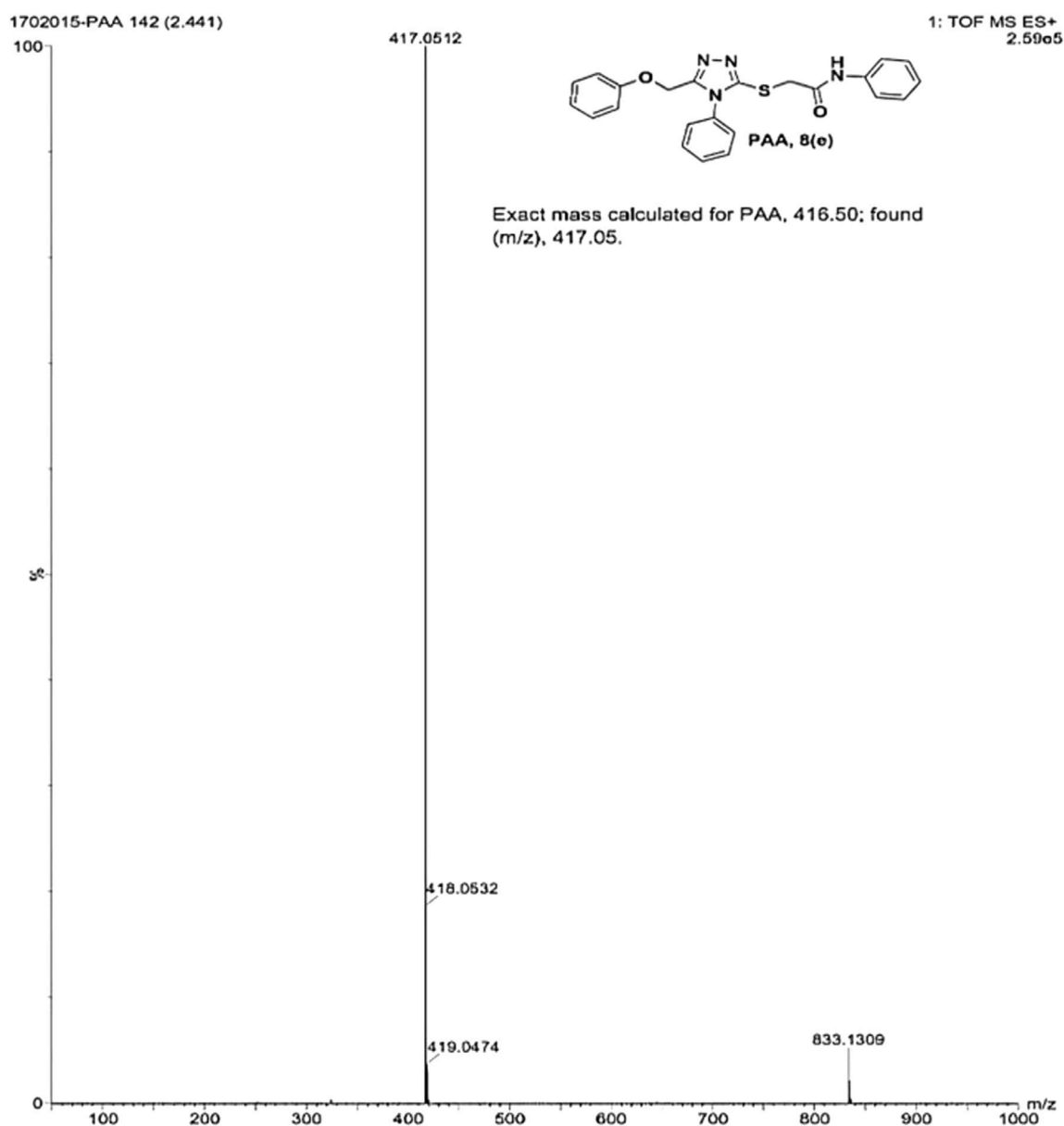
**FIGURE 6**
Mass spectrum of PAA.
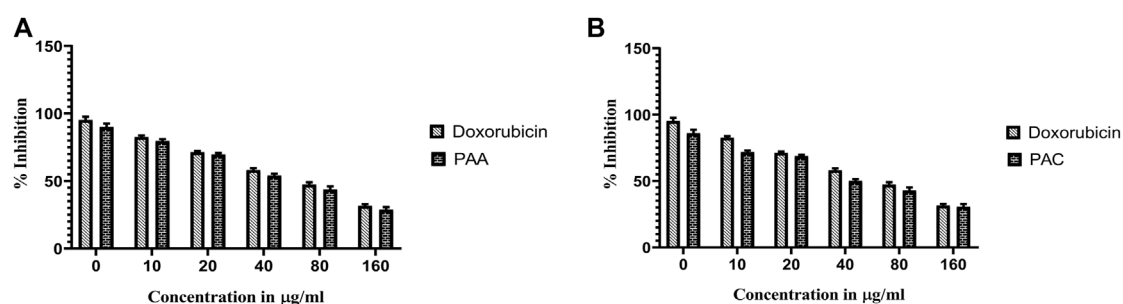


**FIGURE 7**
The cell viability inhibition of K562 cell lines against PAC and PAA synthesized compounds for about 48 h using MTT assay. The cell viability inhibition of K562 cell lines upon treatment of **(A)** PAC and **(B)** PAA in concentration dependent manner for about 48 h using MTT assay. One-way ANOVA followed by Dunnett's multiple comparison test was used to identify significant differences by multiple comparisons. Data are expressed as mean $\pm$ SEM (n = 3), ****$p < 0.0001$ represents the comparison between respective groups with doxorubicin.

TABLE 3 Results of antiproliferation activity of selected compounds performed on the MCF 7, Reh, Nalm6, K562 cell lines.

| Compound code | K562 IC50(µM48 h) |
|---|---|
| Control | - |
| PAC | 35.264 |
| PAA | 54.40 |

Also, the chemical shift signals at δ 4.1 ppm and δ 5.0 ppm resonated singlet peaks corresponded to that of α-proteins $S-CH_2-$ C=O and $O-CH_2-C=N$ respectively. Mass spectrum of the compounds of PAA and PAC showed intense molecular ion peak $[M]^+$ and $[M+1]^+$ peak for chloro-substituted compounds which are consistent to with respective molecular weights. All the screenshots of the spectral data collected for the compounds of PAA and PAC are provided as Figures 2–7. Analysis of overall spectroscopic data for the compounds of PAA and PAC suggests the formation of desired chemical scaffolds (Table 2) (Volkov et al., 2022).

N-(4-chloro phenyl)-2-((5-(phenoxy methyl)-4-phenyl-4H-1, 2, 4-triazol-3 yl)thio) acetamide (8a; PAC): IR (vmax, cm$^{-1}$): 1666 (C=O), 2924 (Ali C-H), 3032 (Ar C-H), 3232 (N-H), 1172 (C-N), 756 str (C-Cl), 1550 (N=N, triazole), 1597 (C=N, triazole); $^1$H NMR (400 MHz, CDCl3) δ 10.482 (s, -NH-, $^1$H), 7.561-6.844 (m, Ar-CH-, 14H), 5.053 (s, O-CH2-, 2H) 3.962 (s, S-CH2-, 2H); 13C NMR (100 MHz, CDCl3) δ 166.43, 157.34, 136.89, 132.12, 130.68, 130.03, 129.59, 129.07, 128.85, 126.74, 122.01,120.97, 114.84, 59.71, 36.26; Mass: Exact mass calculated for $C_{23}H_{19}C_lN_4O_2S$, 450.09; found (m/z), 451.13 $[M + H]^+$ (Figures 1–4).

2-((5-(phenoxy methyl)-4-phenyl-4H-1, 2, 4-triazol-3-yl)thio)-N-phenyl acetamide (8e; PAA): IR (vmax, cm$^{-1}$): 1666 (C=O), 1550 (Ar C=C), 2931 (Ali C-H), 3055 (Ar C-H), 3240 (N-H), 1172 (C-N),763 str (C-S), 1550 (N=N, triazole), 1597 (C=N, triazole); $^1$H-NMR (400 MHz, DMSO-d6) δ 10.323 (s,-NH-, $^1$H), 7.533–6.816 (m, Ar-CH-, 15H), 5.048 (s, O-CH2-, 2H), 4.162 (s, S-CH2-, 2H); Mass: Exact mass calculated for $C_{23}H_{20}N_4O_2S$, 416.50; found (m/z), 417.05 [M+] (Figures 5, 6).

## 3.2 *In vitro* evaluation

### 3.2.1 MTT assay

The cytotoxicity active of the synthesized PAC and PAA compounds was tested against K562 cell lines using MTT assay. As shown is Figure 7 the PAC shows the better cytotoxic effect when compared to PAA and standard drug doxorubicin in a concentration and time—dependent manner with 48 h of exposure. The results
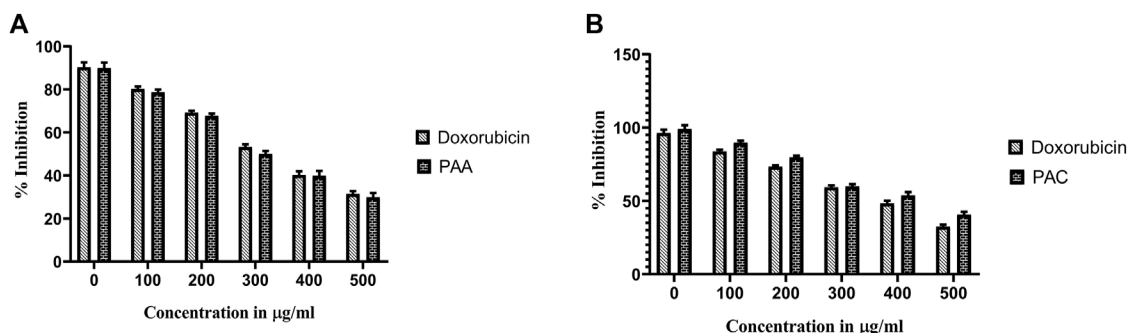


FIGURE 8
The effect of synthesised PAC (A) and PAA (B) compounds upon K562 cell lines on total cell number and viability (%) was measured by trypan blue assay. One-way ANOVA followed by Dunnett's multiple comparison test was used to identify significant differences by multiple comparisons. Data are expressed as mean $\pm$ SEM (n = 3), ****$p < 0.0001$ represents the comparison between respective groups with doxorubicin.
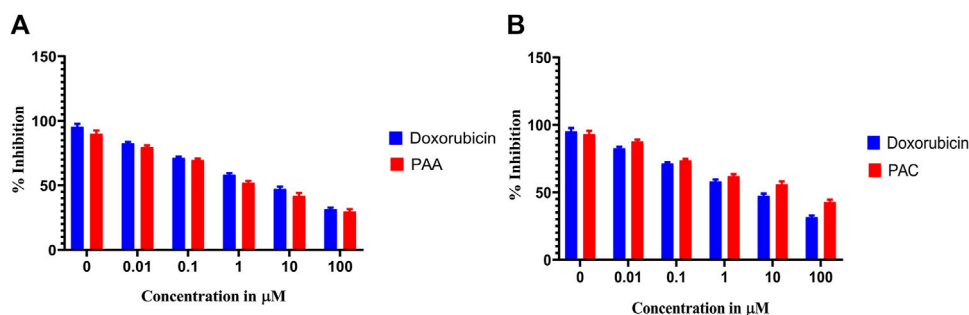


FIGURE 9
The cell viability inhibition of K562 cell lines against PAC and PAA synthesized compounds for about 48 h using MTS assay. The cell viability inhibition of K562 cell lines upon treatment of (A) PAC and (B) PAA in concentration dependent manner for about 48 h using MTT assay. One-way ANOVA followed by Dunnett's multiple comparison test was used to identify significant differences by multiple comparisons. Data are expressed as mean $\pm$ SEM (n = 3), ****$p < 0.0001$ represents the comparison between respective groups with doxorubicin.
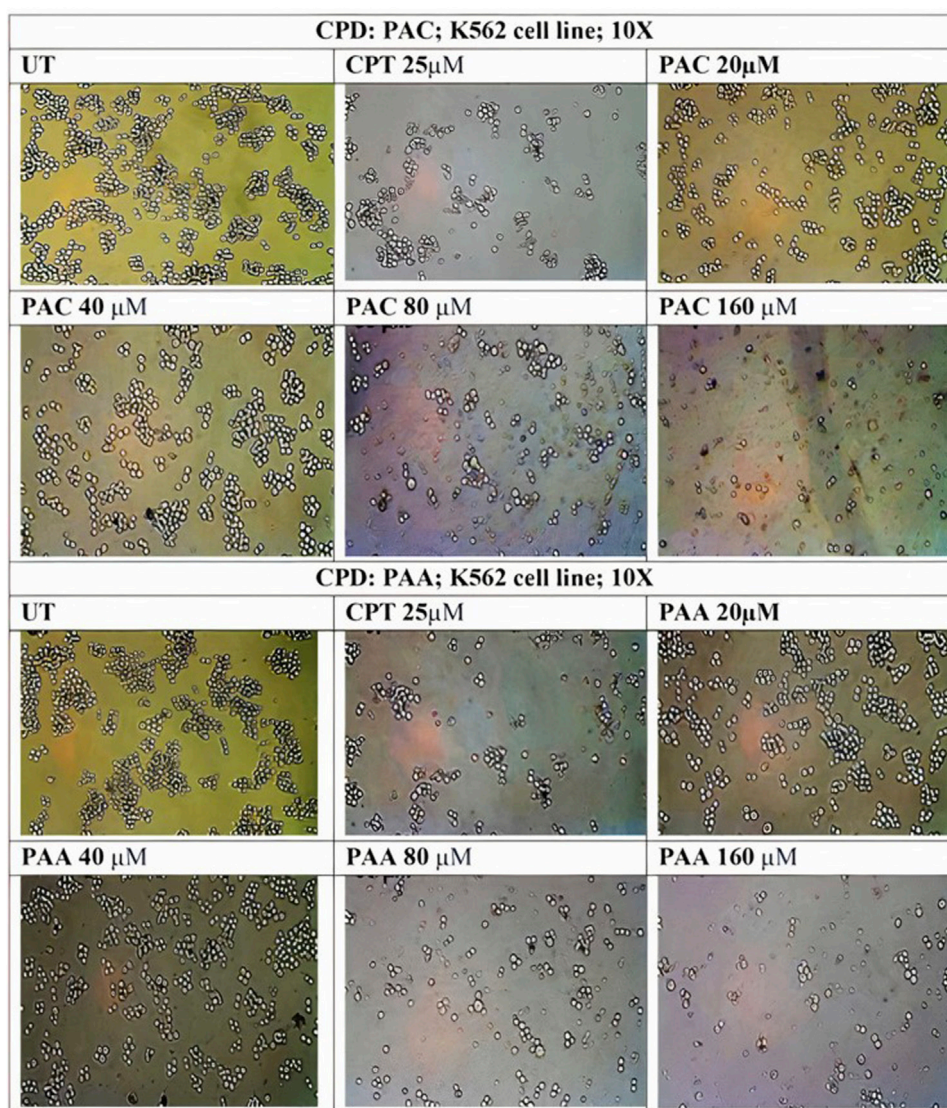
**FIGURE 10**
Photomicrographic images of untreated K562 colonies and the drug treatment induced inhibition of proliferation and subsequent inhibition of growth in K562 cells as obtained from MTS assay. Both **(A)** PAC and **(B)** PAA induced the dose dependent inhibition of proliferation in K562 human leukaemia cell lines.

confirm that, upon increase in concentration up to 160 μg/mL could decrease the cell viability (<0.05).

### 3.2.2 Trypan blue exclusion assay

Trypan Blue Exclusion Assay was used to analyse the total viability of cells after exposure of PAC and PAA compound upon IC50 concentration of MTT assay (Table 3). K562 cells were incubated for about 72 h. The PAA compound and standard drug doxorubicin done not show any significantly affect, whereas PAC compounds shows better cell inhibition as shown in Figure 8.

### 3.2.3 MTS assay

Cytotoxicity active of the synthesized compounds was evaluated by MTS assay using the K562 cancer cell line. The PAC treatment has

caused a dramatic fall in the expression levels of both Mdm2 and Pirh2 oncoproteins as compared to the untreated K562 cells. As shown in Figures 9, 10 the PAC shows the better cytotoxic effect when compared to PAA and standard drug doxorubicin in a concentration and time—dependent manner with 48 h of exposure. The results confirm that, upon increase in concentration up to 100 μg/mL could decrease the cell viability (<0.05) (Jiao et al., 2020).

## 3.3 Cell cycle study: PAC induces K562 cell cycle arrest predominantly at the SubG0/G1 and S phases

Since PAC exhibited relatively better anti-proliferation activity in all the tested cancer cell lines, therefore, it was further selected for cell cycle

TABLE 4 Description of the different cancer cell lines used to test anti-proliferation activity.

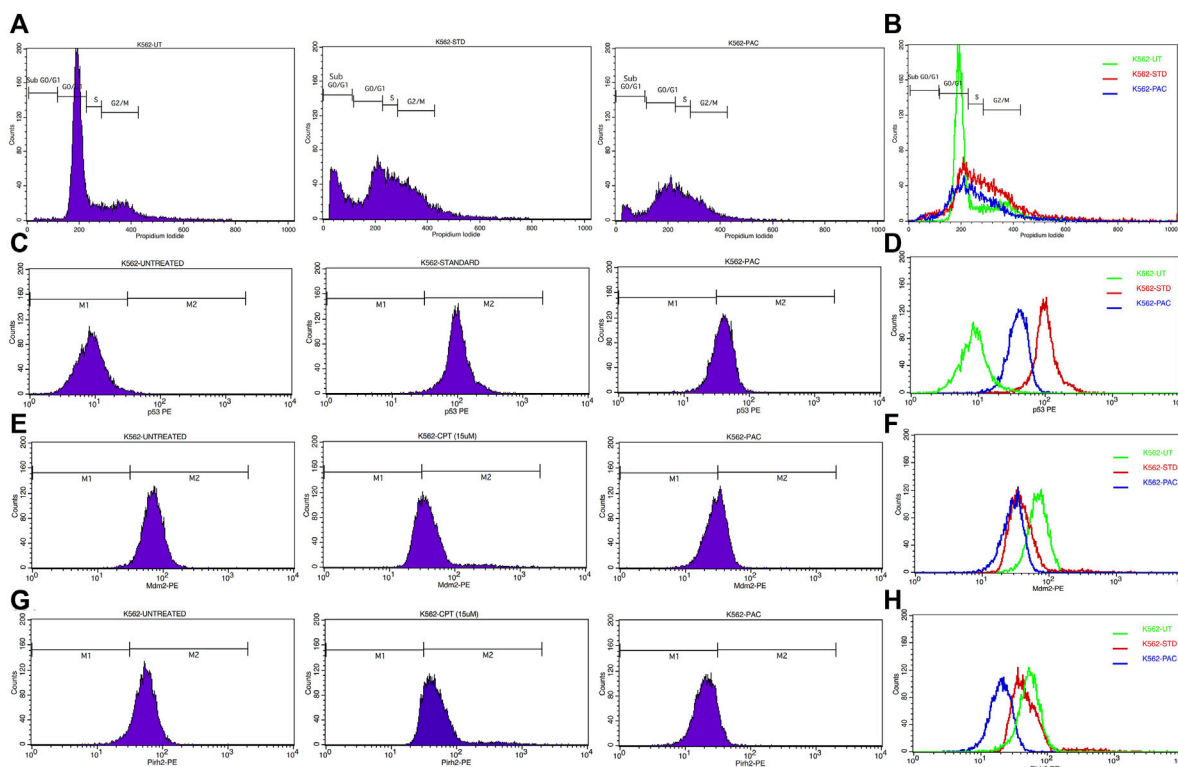| Cell line | ATCC | Cancer type | TP53 status | p53 variant | TP53_Allele type | Comments |
|-----------|------|-------------|-------------|-------------|------------------|----------|
| **K562** | CCL-243™ | Myeloid erythrocytic leukemia cell line | c.406 407ins1 | p. Q136fs* 13 (sourced from COSMIC database) | Homozyg ous | p53-null Consists of mdm2 SNP309 T/G allele No overexpression of Mdm2 |



**FIGURE 11**
**(A)** CPT and PAC induced K562 cell cycle arrest. Both the synthesized compounds, CPT and PAC were treated against K562 cell lines with different concentrations for about 48 h. The degraded cells were recounted with PI stain during sub G0/G1, S, and G2/M phase using flow cytometry.**(B)** Overlay graphs showing the DNA content of cell cycle progression in K562 leukaemia cells of control (untreated), CPT, and PAC treated groups. The percentage content of DNA in various phases of the cell cycle (G1, S, G2/M and subG1 phase) after 48 h of incubation have been analysed by using Cell Quest software (BD Biosciences). Left panels **(C,E, G)** histograms and the right panels **(D,F, H)** overlay graphs of flow cytometric analysis of p53, Mdm2 and Pirh2 protein expression in K562 cells.

studies. The cell cycle study was conducted on K562 cells in order to decipher the growth phase which is prone to the PAC treatment. The results indicated that the higher percentage of K562 cells are arrested at SubG0/G1 and S phases as evident. A marked increase in the percentage of gated cell populations which are in SubG0/G1, S and G2 phases was detected as compared to that in control K562 p53 null cells. This implies that PAC induces cell cycle arrest predominantly at the SubG0/G1, S and G2 phases. This also suggests an increased level of p53 due to inhibition of Mdm2/Pirh2 by PAC in K562 p53 null cells has occurred thus blocking cell cycle progression since p53 also acts at the G1 checkpoint during G1/S transition phase of the cell cycle and induces the expression of cyclin-dependent kinase (cdk) inhibitor. The cdk inhibitor inactivates the Cdk-G1/S cyclin complex, which later blocks cell cycle progression. These facts suggest that PAC rescues p53 by inhibiting ubiquitination by Mdm2/Pirh2 in K562 p53 null cells (Sane and Rezvani, 2017).

Whereas, in case of cells treated with Camptothecin (CPT; 25 µM), the highest percentage of cells got arrested during G2/M phase (30%) which suggests CPT induces arrest G2/M phase of the cell cycle by a distinct mechanism.

## 3.4 Flow cytometric analysis revealed PAC induces expression of p53 and suppress Mdm2 and Pirh2 proteins expressions

Since PAC and its analogues have been designed *in silico* to modulate the ubiquitination of p53 by both Mdm2 and Pirh2 E3 enzymes, hence its impact on the expression levels of p53, Mdm2 and Pirh2 proteins have been studied by flow cytometry. The expression levels of p53 and Mdm2 and Pirh2 proteins were measured in K562 cells under control and treated conditions. In the histogram graphs Figures 5C–H, the
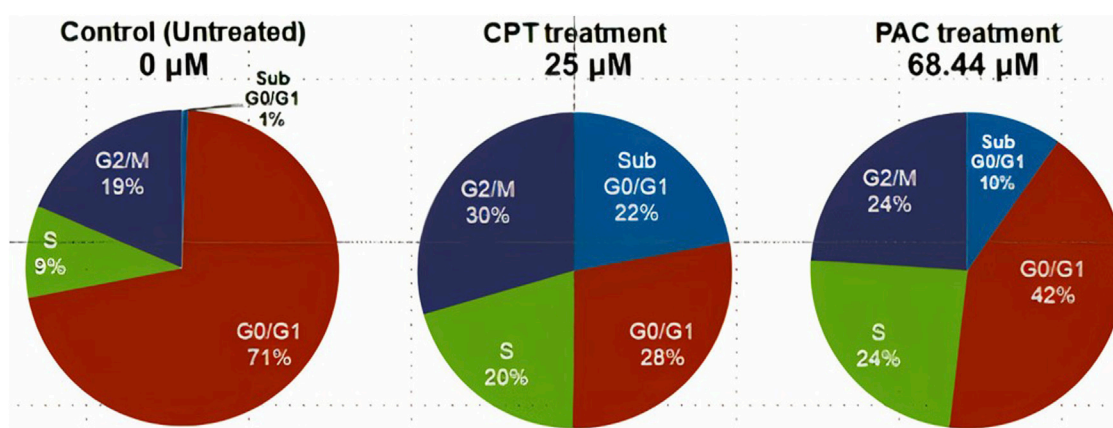
**FIGURE 12**
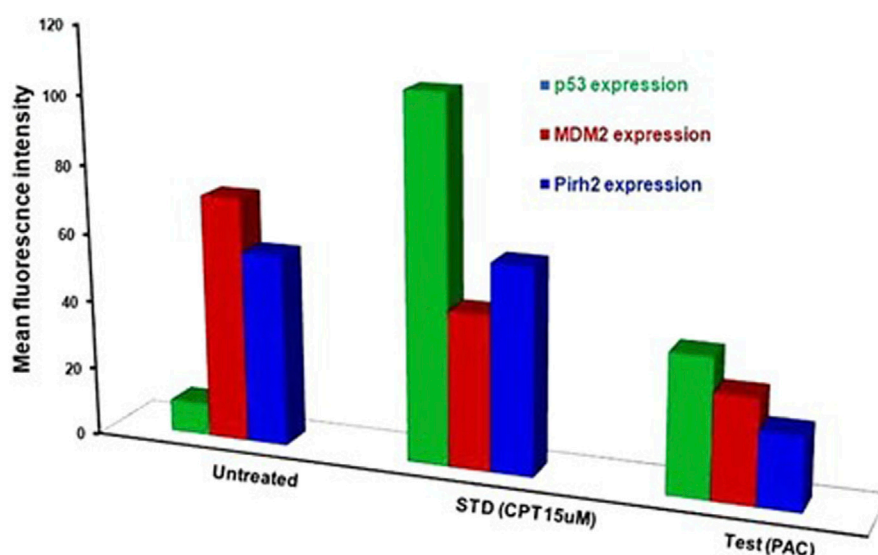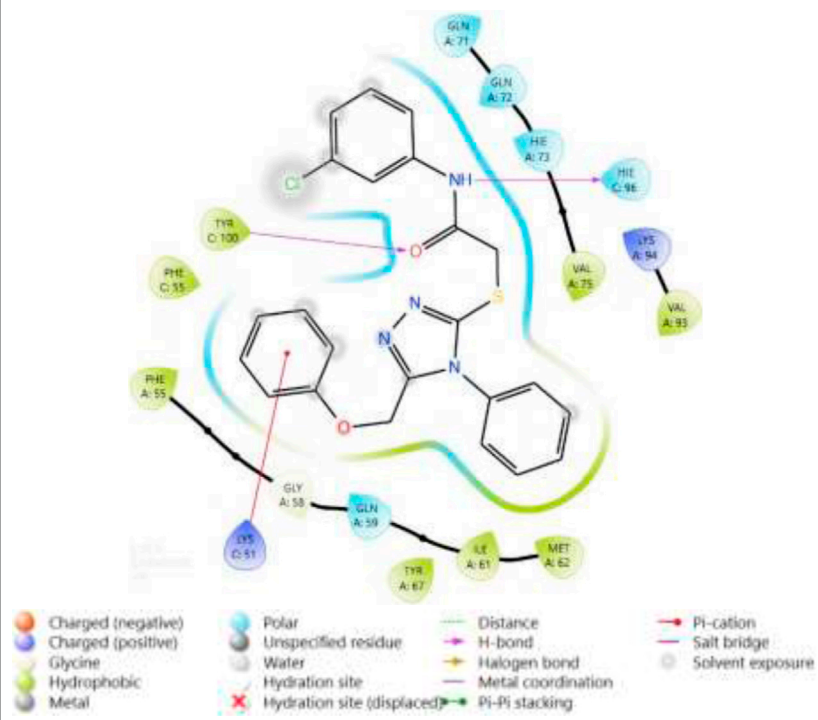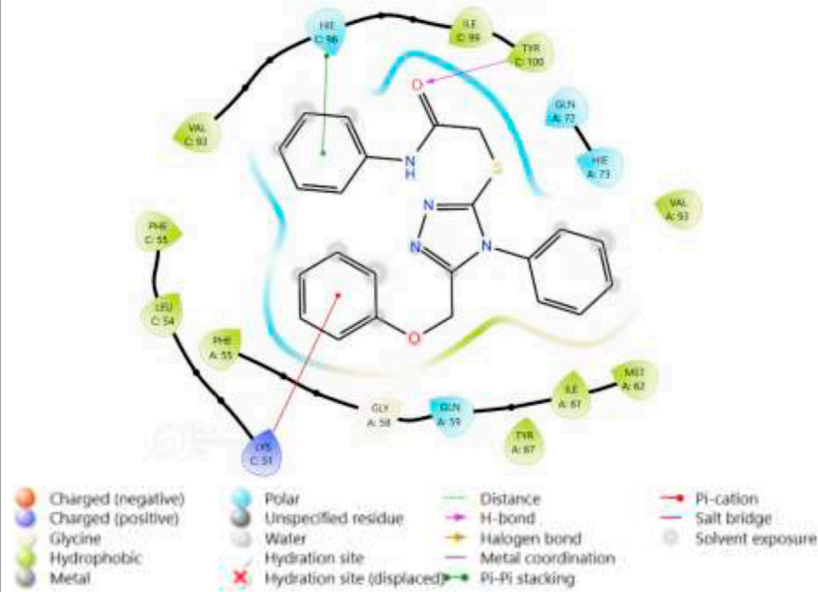Pie charts illustrating the percentage of gated cells at SubG0/G1, G0/G1, S and G2/M.



**FIGURE 13**
Histograms representing the flow cytometric analysis of p53, Mdm2 and Pirh2 expression levels in control, K562 cells treated with an IC50 concentration of test compound (PAC) and CPT (15 μM). phase of K562 cell proliferation under treated (CPT and PAC) and control conditions.

M1 region represents lower expression levels of p53, Mdm2, and Pirh2 protein while the M2 region represents normal to high expression levels.

Generally, K562 cells express a negligible amount of p53, and the results obtained from the flow cytometric analysis has also indicated the lower expression of the p53 tumour suppressor protein under control conditions. Interestingly, exposure of the K562 cells to the indicated concentrations of CPT (reference) and PAC has caused a dramatic increase in the p53 levels. Quantitatively, the exposure of K562 cells to CPT, which is a topoisomerase inhibitor derived from natural source, has triggered ~10 folds rise in the p53 level, while the PAC treatment has caused ~4-fold rise in the p53 levels (Figure 7).

Generally, the expression level of Mdm2 is not affected in K562 cancer cells (Table 4), and the status Pirh2 expression in K562 cancer cell lines has not been documented till date. However, Mdm2 serves as a primary negative regulator of p53 expression whereas Pirh2 serves as secondary. Hence, it may be presumed that the expression level of Mdm2 is slightly high as compared to the Pirh2. In an agreement, the flow cytometric analysis indicated that Mdm2 expression was slightly high when compared to Pirh2 in control group of K562 cell population (see Figures 11E–H, 13), which reinforces the notion that Mdm2 is a primary negative regulator of p53. On the other hand, CPT, a reference molecule which is a topoisomerase inhibitor, has less influence on Mdm2 and Pirh2 expressions in K562 cells. Strikingly, the PAC treatment has caused a dramatic fall in the expression levels of both Mdm2 and

**TABLE 5 2D interaction diagram of the Ligands with their interactions with the protein 3LBK.**

| Ligands | Two-dimensional inter-molecular interaction | Docking score | Active site residues |
|---|---|---|---|
| PAC |  | −8.574 | HIE96, TYR100 |
| PAA |  | −7.096 | TYR100 |

Pirh2 oncoproteins as compared to the untreated K562 cells (see Figure 7). These data partly suggest that PAC inhibits Mdm2 and Pirh2 oncoproteins which resulted in the rise in p53 tumour suppressor protein in K562 cells. On the other hand, the induction of p53 levels by CPT in K562 p53 null cells may be due to distinct mechanisms. Results of the overall *in-vitro* analysis suggest that PAC exhibited good anticancer activity against all the tested cancer cell lines. Enzyme binding studies are required to further validate the Mdm2 and Pirh2 promiscuous binding nature of PAC and its analogs. (Figures 11–13) (Astalakshmi et al., 2022).

## 3.5 Molecular docking

Through our molecular docking experiment, we discovered that PAC is efficient. As a result, PAC had the highest ratings for Glide (−8.312 kcal/mol) and binding affinity −49.601 kcal/mol). The docked complex analysis revealed that the residues HIE96, TYR100 bonded with hydrogen bonding. Lys 173 was interacting with the ligand at the hydration site The Glide ratings for PAA were −7.216 kcal/mol, and the binding affinity was recorded as −42.371 kcal/mol. Analysis of the docked complex indicated
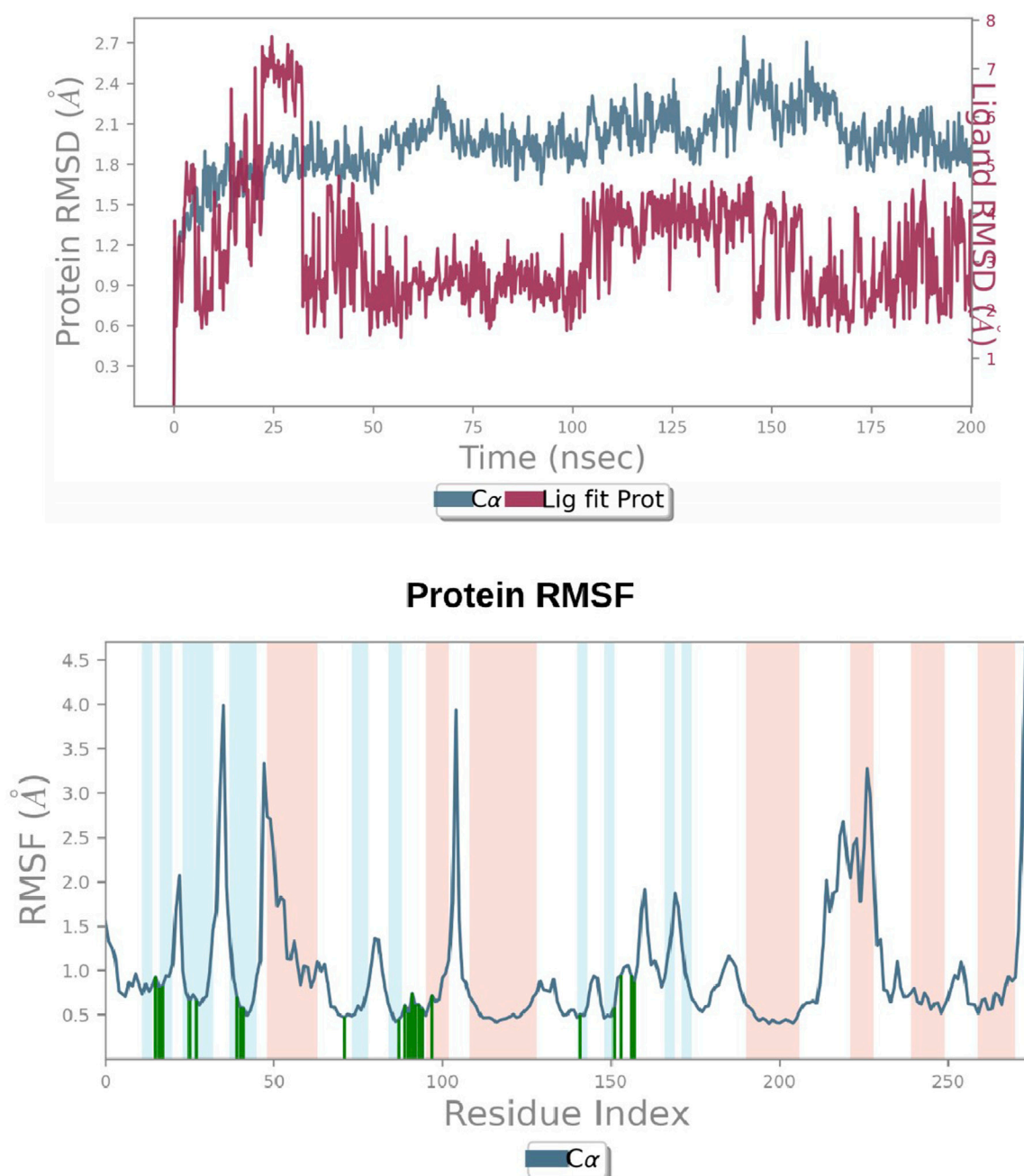
**FIGURE 14**
**(A)** RMSD graphs of Receptor-ligand complexes in MD simulations. **(B)** RMSF plot of Protein.

the occurrence of hydrogen bonding between PAA and the residues TYR100 exhibited superior docking scores and binding affinity compared to PAA. Consequently, additional investigations and studies were conducted specifically focusing on PAC. (Table 5) (Vettoretti et al., 2016).

## 3.6 Molecular dynamic simulation

A simulation study was conducted using molecular dynamics (MD) to confirm the stability of the receptor-ligand complex, validate

the predicted binding mode, and examine potential interactions. These aspects had been previously investigated through Glide XP docking. In the present investigation, we ran a 200 ns MD simulation of the PAC—3LBK complex. This extended simulation duration enabled the examination of molecular and atomic-level changes crucial for understanding the stability of the protein-ligand complex and the dynamic behavior of the ligand. Using the Desmond tool from the Schrödinger suite, a 200 ns simulation was conducted, and resulting trajectories were analyzed with the simulation interaction diagram panel to comprehend deviation fluctuation and intermolecular interactions. The root mean square

deviation (RMSD) value was calculated to assess the deviation in the protein's backbone throughout the 200 ns simulation period. The RMSD plot of the PAC—3LBK complexes are shown in Figure 12A, demonstrating slight conformational fluctuations in the complexes between 135 and 160 ns. RMSD levels range from 1.8 Å to 2.7 Å Around 8 Å. Similarly, there was a modest fluctuation in the ligand RMSD between 0 ns and 30 ns, with RMSD ranging from 0.6A to 2.7 around 2.1 Å. Despite these variations, the PAC—3LBK complex remained stable. The Root Mean Square Fluctuations (RMSF) aid in characterizing local protein alterations. These variations were used to identify the residue in the complex that contributes to structural fluctuations. The region of proteins was represented by peaks that vary throughout the process of simulation. The N and C terminal of protein tails changes more when compared to any other regions of protein. The alpha helices and beat chain are stronger than the unstructured regions of the protein and hence they alter less when compared to loop regions. The alpha and beat regions are represented in red and blue color. These regions were specified by helices or strands that continue 70% of simulation time. The proteins that are interacted with ligand are represented in green color with slight fluctuations, conforms the protein ligand complex are stable. (Figures 14A, B) (Li and Zhang, 2022).

## 4 Conclusion

In conclusion, our research focuses on developing and testing new anticancer drugs based on a 1,2,4-triazole scaffold. These chemicals were painstakingly crafted to alter the ubiquitination of the tumour suppressor protein p53, which is regulated by the E3 ubiquitin ligases Mdm2 and Pirh2. Notably, the principal chemical, PAC, demonstrated significant anti-proliferative effects across a range of cancer cell lines, with a particularly strong effect on leukemia cells. PAC modulates p53-mediated pathways by inhibiting Mdm2 and Pirh2, leading to the stabilization of p53.PAC promotes cell cycle arrest at the SubG0/G1, S, and G2 phases, indicating its ability to disturb normal cell cycle progression, according to cell cycle analyses. According to flow cytometry studies, PAC increases p53 expression while decreasing Mdm2 and Pirh2 levels in K562 cancer cells. A molecular dynamics simulation of PAC with the TP53 protein revealed sustained connections lasting 200 ns, highlighting its potential as a powerful anticancer therapy. Our complete technique combines manual design, organic synthesis, *in vitro* testing, and molecular dynamics modelling. This multidisciplinary strategy attempts to identify and characterize novel chemicals for cancer therapy. The compounds were created without the use of artificial intelligence, and the study highlights PAC's potential as a game-changing anticancer treatment due to its multifaceted impact on cell cycle regulation and molecular interactions. This work contributes to the larger goal of producing effective and tailored cancer medicines, highlighting the need of varied approaches in drug discovery and development.

## Data availability statement

The original contributions presented in the study are included in the article/Supplementary Material, further inquiries can be directed to the corresponding authors.

## Ethics statement

Ethical approval was not required for the studies on animals in accordance with the local legislation and institutional requirements because only commercially available established cell lines were used.

## Conflict of interest

The authors declare that the research was conducted in the absence of any commercial or financial relationships that could be construed as a potential conflict of interest.

## Publisher's note

All claims expressed in this article are solely those of the authors and do not necessarily represent those of their affiliated organizations, or those of the publisher, the editors and the reviewers. Any product that may be evaluated in this article, or claim that may be made by its manufacturer, is not guaranteed or endorsed by the publisher.

# References

Ali, S. A. A., Khan, D., Naqvi, A., Faleh Al-Blewi, F., Rezki, N., et al. (2021). Design, synthesis, molecular modeling, anticancer studies, and density functional theory calculations of 4-(1,2,4-triazol-3-ylsulfanylmethyl)-1,2,3-triazole derivatives. *ACS Omega* 6 (1), 301–316. doi:10.1021/acsomega.0c04595

Aly, A. A., Alaa, A. H., Makhlouf, M. M., Bräse, S., Aly, A. A., Hassan, A. A., et al. (2020). *Activities of drugs*.

Astalakshmi, N., Gokul, T., Gowri Sankar, K. B., Nandhini, M., Hari Hara Sudhan, M. R., Gowtham, S., et al. (2022). Over view on molecular docking: a powerful approach for structure based drug discovery. *Int. J. Pharm. Sci. Rev. Res.* 77 (2), 146–157. doi:10.47583/ijpsrr.2022.v77i02.029

Ban, T., Ohue, M., and Akiyama, Y. (2018). Multiple grid arrangement improves ligand docking with unknown binding sites: application to the inverse docking problem. *Comput. Biol. Chem.* 73, 139–146. doi:10.1016/j.compbiolchem.2018.02.008

Daks, A., Fedorova, O., Parfenyev, S., Nevzorov, I., Shuvalov, O., and Barlev, N. A. (2022). The role of E3 ligase Pirh2 in disease. *Cells* 11 (9), 1515–1523. doi:10.3390/cells11091515

Daver, N. G., Iqbal, S., Renard, C., Chan, R. J., Hasegawa, K., Hu, H., et al. (2023). Treatment outcomes for newly diagnosed, treatment-naïve TP53-mutated acute myeloid leukemia: a systematic review and meta-analysis. *J. Hematol. Oncol.* 16 (1), 19–14. doi:10.1186/s13045-023-01417-5

Devi, J., Kumar, S., Kumar, B., Asija, S., and Kumar, A. (2022). Synthesis, structural analysis, *in vitro* antioxidant, antimicrobial activity and molecular docking studies of transition metal complexes derived from Schiff base ligands of 4-(benzyloxy)-2-hydroxybenzaldehyde. *Res. Chem. Intermed.* 48 (4), 1541–1576. doi:10.1007/s11164-021-04644-y

Dittmar, G., and Winklhofer, K. F. (2020). Linear ubiquitin chains: cellular functions and strategies for detection and quantification. *Front. Chem.* 7, 915–916. doi:10.3389/fchem.2019.00915

Du, X., Yi, Li, Xia, Y. L., Ai, S. M., Liang, J., Peng, S., et al. (2016). Insights into protein–ligand interactions: mechanisms, models, and methods. *Int. J. Mol. Sci.* 17 (2), 1–34. doi:10.3390/ijms17020144

Ghasemi, M., Turnbull, T., Sebastian, S., and Kempson, I. (2021). The mtt assay: utility, limitations, pitfalls, and interpretation in bulk and single-cell analysis. *Int. J. Mol. Sci.* 22 (23), 12827. doi:10.3390/ijms222312827

Haronikova, L., Bonczek, O., Zatloukalova, P., Kokas-Zavadil, F., Kucerikova, M., Coates, P. J., et al. (2021). Resistance Mechanisms to Inhibitors of P53-MDM2 Interactions in cancer therapy: can we overcome them? Cellular and molecular biology letters. *Biomed. Cent.* 26, 53. doi:10.1186/s11658-021-00293-6

Hassan, G., and Seno, M. (2020). Blood and cancer: cancer stem cells as origin of hematopoietic cells in solid tumor microenvironments. *Cells* 9 (5), 1293. doi:10.3390/cells9051293

Hatami, S., Sirous, H., Karim, M., Najafipour, A., and Fassihi, A. (2023). Preparing a database of corrected protein structures important in cell signaling pathways. *Res. Pharm. Sci.* 18 (1), 67–78. doi:10.4103/1735-5362.363597

Jiao, R., Xu, F., Huang, X., Li, H., Liu, W., Cao, H., et al. (2020). Antiproliferative chromone derivatives induce K562 cell death through endogenous and exogenous pathways. *J. Enzyme Inhibition Med. Chem.* 35 (1), 759–772. doi:10.1080/14756366.2020.1740696

Kaushik, A. C., Kumar, S., Wei, D. Q., and Sahi, S. (2018). Structure based virtual screening studies to identify novel potential compounds for GPR142 and their relative dynamic analysis for study of type 2 diabetes. *Front. Chem.* 6, 23–14. doi:10.3389/fchem.2018.00023

Li, Q., and Zhang, W. (2022). Progress in anticancer drug development targeting ubiquitination-related factors. *Int. J. Mol. Sci.* 23 (23), 15104–15115. doi:10.3390/ijms232315104

Li, Y., Cui, K., Zhang, Q., Li, Xu, Lin, X., Tang, Yi, et al. (2021). FBXL6 degrades phosphorylated P53 to promote tumor growth. *Cell Death Differ.* 28 (7), 2112–2125. doi:10.1038/s41418-021-00739-6

Ma, W., Zhu, M., Wang, Bo, Gong, Z., Du, X., Yang, T., et al. (2022). Vandetanib drives growth arrest and promotes sensitivity to imatinib in chronic myeloid leukemia by targeting ephrin type-B receptor 4. *Mol. Oncol.* 16 (14), 2747–2765. doi:10.1002/1878-0261.13270

Marei, H. E., Althani, A., Afifi, N., Hasan, A., Caceci, T., Pozzoli, G., et al. (2021). P53 signaling in cancer progression and therapy. *Cancer Cell Int.* 21 (1), 703–715. doi:10.1186/s12935-021-02396-8

Niazi, S., and Purohit, M. (2015). Rational design of promiscuous binding modulators of P53 inducing E3(ub)-ligases (Mdm2 and Pirh2) as anticancer agents: an *in silico* approach. *Med. Chem. Commun.* 6 (11), 1959–1968. doi:10.1039/C5MD00319A

Parrales, A., Ranjan, A., Iyer, S. V., Padhye, S., Weir, S. J., Roy, A., et al. (2016). DNAJA1 controls the fate of misfolded mutant p53 through the mevalonate pathway. *Nat cell biol.* 18 (11), 1233–1243. doi:10.1038/ncb3427

Prager, G. W., Braga, S., Bystricky, B., Qvortrup, C., Criscitiello, C., Esin, E., et al. (2018). Global cancer control: responding to the growing burden, rising costs and inequalities in access. *ESMO Open* 3 (2), e000285. doi:10.1136/esmoopen-2017-000285

Sane, S., and Rezvani, K. (2017). Essential roles of E3 ubiquitin ligases in P53 regulation. *Int. J. Mol. Sci.* 18 (2), 442. doi:10.3390/ijms18020442

Shin, D. Y. (2023). TP53 mutation in acute myeloid leukemia: an old foe revisited. *Cancers* 15 (19), 4816–16. doi:10.3390/cancers15194816

Tavares-Carreón, F., Torre-Zavala, S.De La, Arocha-Garza, H. F., Souza, V., Galán-Wong, L. J., and Avilés-Arnaut, H. (2020). *In vitro* anticancer activity of methanolic extract of granulocystopsis sp., a microalgae from an oligotrophic oasis in the chihuahuan desert. *PeerJ* 2020 (3), 1–21. doi:10.7717/peerj.8686

Bunney, P. E., Zink, A., Holm, A., Billington, C., and Kotz, C. (2017). Orexin activation counteracts decreases in nonexercise activity thermogenesis (NEAT) caused by high-fat diet. *Physiology Behav.* 176 (10), 139–148. doi:10.1016/j.physbeh.2017.03.040

Tian, Z., Yang, L., Huang, M., Sun, C., Chen, M., Zhao, W., et al. (2022). Antitumor activity and mechanism of action of the antimicrobial peptide AMP-17 on human leukemia K562 cells. *Molecules* 27 (22), 8109–8117. doi:10.3390/molecules27228109

Vettoretti, G., Moroni, E., Sattin, S., Tao, J., Agard, D. A., Bernardi, A., et al. (2016). Molecular dynamics simulations reveal the mechanisms of allosteric activation of hsp90 by designed ligands. *Sci. Rep.* 6 (April), 23830–23913. doi:10.1038/srep23830

Volkov, P. A., Khrapova, K. O., Telezhkin, A. A., Trofimov, B. A., Bidusenko, I. A., and Albanov, A. I. (2022). *Short note*.

# Frontiers in
# Chemistry

Explores all fields of chemical science across the periodic table

Advances our understanding of how atoms, ions, and molecules come together and come apart. It explores the role of chemistry in our everyday lives - from electronic devices to health and wellbeing.

## Discover the latest Research Topics

See more →

**Frontiers**

Avenue du Tribunal-Fédéral 34
1005 Lausanne, Switzerland
frontiersin.org

**Contact us**

+41 (0)21 510 17 00
frontiersin.org/about/contact



frontiers

**Frontiers in Chemistry**

frontiers | Research Topics